

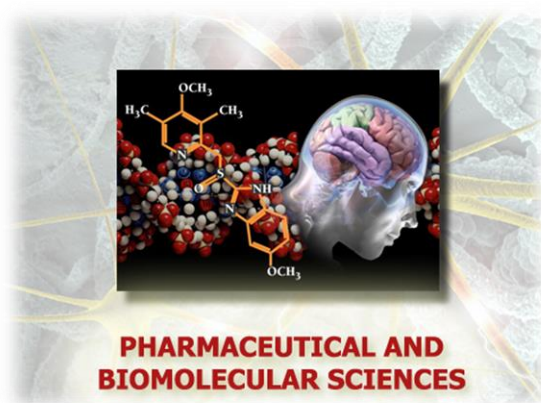
Università degli Studi di Torino



**Scuola di Dottorato in Scienze della Natura e
Tecnologie Innovative**

**Dottorato in Scienze Farmaceutiche e
Biomolecolari**

XXXIII ciclo



***Nanomaterials for the treatment of collagen-based
industrial products***

Candidata: Erica Rebba

Tutor: Prof.ssa Gloria Berlier

Università degli Studi di Torino



**Dottorato in
Scienze Farmaceutiche e Biomolecolari**

**Tesi svolta presso il
Dipartimento di Chimica**

CICLO: XXXIII

TITOLO DELLA TESI:

Nanomaterials for the treatment of collagen-based industrial products

TESI PRESENTATA DA: Erica Rebba

TUTOR(S): Prof.ssa Gloria Berlier

COORDINATORE DEL DOTTORATO: Prof.ssa Roberta Cavalli

ANNI ACCADEMICI: 2017-2020

SETTORE SCIENTIFICO-DISCIPLINARE DI AFFERENZA*: CHIM/02

A Gianmario

*“Insegnami la dolcezza ispirandomi la carità,
insegnami la disciplina dandomi la pazienza e
insegnami la scienza illuminandomi la mente.”*

Sant'Agostino

TABLE OF CONTENTS

Abstract	5
1. INTRODUCTION	7
1.1 BACKGROUND AND CHALLENGE	7
1.2 AN INSIGHT ON WATERPROOF AND FIREPROOF AGENTS: ENVIRONMENTAL CONCERNS AND POSSIBLE SUSTAINABLE STRATEGIES	11
1.3 AIM AND ORGANIZATION OF THE WORK.....	19
Bibliographic References	20
2. WATERPROOFING ASPECTS	24
2.1 MATERIALS AND METHODS.....	24
2.1.1 Materials.....	24
2.1.1.1. Synthesis of m-SiO ₂	25
2.1.2 Methods	29
2.1.2.1 Infrared (IR) spectroscopy on non-functionalized and functionalized nanomaterials in controlled atmosphere	29
2.1.2.2 Attenuated Total Reflectance (ATR) IR spectroscopy - Cylindrical Internal Reflectance (CIR) cell.....	30
2.1.2.3 SS-NMR analysis	31
2.1.2.4 Near-infrared spectroscopy.....	31
2.1.2.5 Specific Surface Area (SSA _{BET}) and Thermogravimetric Analysis (TGA)	31
2.1.2.6 Microgravimetric and Adsorption Microcalorimetric Measurements	32
2.1.2.7 Contact Angle Measurements	33
2.1.2.8 FESEM	33
Bibliographic References	34
2.2 THE FUNCTIONALIZATION OF ALUMINA NANOPARTICLES: AN EXISTING PROTOCOL AS THE STARTING POINT.....	35
2.2.1 Procedure of functionalization	35
2.2.2 Study of isostearic acid carboxylic groups: -COOH and -COO ⁻ forms	36
2.2.3 First evidence of the presence of ISOST on alumina surface: IR spectroscopy.....	37
2.2.4 The grafting density through IR spectroscopy using a non-conventional mixture method and confirmation from TGA – evaluation of the hydrophobicity with contact angle measurements.....	42
Bibliographic References	46
2.3 SILICA INSTEAD OF ALUMINA: NEW PROCEDURES OF FUNCTIONALIZATION WITH ISOSTEARIC ACID	47
2.3.1 The surface of silica	47
2.3.2 Procedure of functionalization with APTS.....	52
2.3.3 Evidence and quantification of amine groups on surface	54

2.3.4 Procedure of functionalization with isostearic acid: first approach based on the activation of carboxylic groups in ester compounds.....	61
2.3.5 Evidence of the presence of isostearic acid on silica surface and evaluation of hydrophobicity: IR spectroscopy, SS-NMR and Contact Angle measurements	63
2.3.6 Improvement of functionalization with isostearic acid: modification of isostearic acid into acyl chloride compound.....	68
2.3.7 Evaluation of the effectiveness of functionalization and grafting density: IR spectroscopy, SS-NMR and contact angle measurements	71
Bibliographic References	76
2.4 A COMPARISON BETWEEN ALUMINA AND SILICA MATERIALS: BEHAVIOUR TOWARDS LIQUID WATER AND WATER VAPOURS	77
2.4.1 On the origin of superhydrophobic surfaces.....	77
2.4.2 Interaction of pristine and functionalized nanoparticles with water vapor: microgravimetric analysis, Near-IR spectroscopy, and microcalorimetric analysis.....	78
2.4.3 Interaction of pristine and functionalized nanoparticles with liquid water: evidence of superhydrophobicity	90
2.4.4 A proposal of explanation: the study of the chemical structure of hydrophobic agents.....	93
Bibliographic References	97
2.5 A FURTHER IMPROVEMENT OF FUNCTIONALIZATION OF SILICA NANOPARTICLES: THE USE OF ACETIC ACID	98
2.5.1 Procedure of functionalization	98
2.5.2 Evidence of the effectiveness of functionalization: IR spectroscopy and Contact Angle measurements.....	100
2.5.3 Microgravimetric analysis: study of the adsorption capacity towards water vapours	102
2.5.4. A possible explanation of the high water adsorption capacity after functionalization: SS-NMR studies.....	103
Bibliographic References	106
2.6 APPLICATION OF HYDROPHOBIC MATERIALS ON LEATHER SAMPLES	107
2.6.1 Deposition of alumina nanoparticles using the spray technology – characterization of treated leather samples with SEM-EDS analyses	107
2.6.2 Deposition of commercial hydrophobic silica using a new technology: Roll Coater – characterization of treated leather samples with SEM-EDS analyses.....	111
Bibliographic References	115
3. FIREPROOFING ASPECTS	116
3.1 MATERIALS AND METHODS.....	116
3.1.1 Materials.....	116
3.1.2 Methods	117
3.1.2.1 XRD analysis.....	117
3.1.2.2 TEM measurements.....	117
3.1.2.3 Leather treatments - tanning with OSA and re-tanning with nano-HA.....	117

3.1.2.4 Shrinkage temperature.....	118
3.1.2.5 Micro-DSC analysis	118
3.1.2.6 NMR-MOUSE (Nuclear Magnetic Resonance – MOBILE Universal Surface Explorer).....	118
3.1.2.7 SEM measurements.....	119
Bibliographic references.....	120
3.2 THE PRODUCTION OF NANO-HYDROXYAPATITE (nano-HA) AS FLAME RETARDANT AGENT	121
3.2.1 Characterization of the prepared nano-HA.....	121
3.2.2 Life Cycle Assessment (LCA) at lab-scale: assessment of the sustainability of nano-HA production	123
Bibliographic references.....	130
3.3 A SUSTAINABLE ALTERNATIVE IN THE TANNING PROCESS AND APPLICATION OF NANOMATERIALS ON LEATHER.....	131
3.3.1 Oxidized sodium alginate (OSA) as a sustainable tanning agent.....	131
3.3.2 Application of nano-TiO ₂ , nano-SiO ₂ and nano-HA on leather tanned with OSA: SEM-EDS analysis	135
3.3.3 Assessment of thermal capacity of treated leather samples: micro-DSC analysis.....	138
3.3.4 Study of the interaction between nano-HA and leather: ATR and NMR-MOUSE analyses	140
Bibliographic References	142
3.4 INDUSTRIAL SCALE-UP OF NANO-HA PRODUCTION	143
3.4.1 Preparation and characterization of nano-HA at industrial scale	143
3.4.2 Application of nano-HA at industrial scale on leather samples and preliminary fire-resistance tests	145
Bibliographic References	148
General conclusions	149
Publications and congress & conference participation	
Acknowledgement	
Appended papers	

Abstract

This PhD study has been focused on the preparation and characterization of nanomaterials as sustainable alternatives to the conventional waterproof and fireproof agents used in leather treatment. In the last years, the leather industry has significantly contributed to the circular economy; in fact, leather derives from the conversion of food industries residues, transforming wastes into added value goods. Nevertheless, the tanning industry employs a huge number of dangerous chemicals to give special characteristics to leather that could represent a risk for animal and human health.¹ The growing awareness of environmental issues and social challenges of leather production are strongly pushing the tanning industry to develop sustainable technologies.

In this context, one of the major challenges for the tanning industry is to substitute the already applied non-sustainable substances used to fulfill the request of water-repellent and fire-resistance leather products. In particular, perfluoroalkylated substances (PFAS) are the most used compounds to reduce the natural hydrophobicity of leather; several studies reported the persistence of PFAS in the environment, their ability to accumulate in human body and cause dangerous diseases,² prompting European authorities to restrict their use in new consumer goods.³

In this respect, the possibility to exploit the nanomaterials as the eco-friendly alternatives came into a spotlight.^{4, 5}

The first part of this research work is based on the preparation of nanoparticles functionalized with highly branched alkyl chains to obtain hydrophobic surfaces and their further application for leather coating.

Since silica nanoparticles are already used in the leather finishing process, they may play an additional role upon functionalization. The characterization of functionalized silica nanoparticles was carried out by two different approaches and points of view. Water sessile drop contact angle measurements were used to monitor water-repellency at the macroscopic level. On the other hand, the complementary combination of infrared spectroscopy, microgravimetric, and microcalorimetric analyses allowed to describe the surface interaction with water vapour in controlled atmosphere at the molecular level.

The second part of the work is related to fireproofing aspects, taking into account the environmental concern in the use of brominated flame-retardants (BFRs), consisting of a mixture of chemicals based on organic bromine compounds, as conventional fire-resistance agents.

These substances whether in use or waste, pollute air, soil, and water.⁶ Some toxicological studies on BFRs were carried out in recent years, reporting diseases in aquatic species and damage to several major organs.^{7, 8}

The increased restrictions in their use in manufacturing processes stimulated the thinking about sustainable, non-toxic, and safer replacements. In this respect, several available inorganic nanomaterials, i.e. nano-hydroxyapatite (nano-HA), nano-TiO₂ and nano-SiO₂ are studied and tested as fire-resistance agents in leather treatment instead of BFRs. The objective was to develop a tanning technology able to provide leather with improved flame resistance, a mandatory requirement for automotive leather.

This work involved a detailed characterization of dimensional, morphological and surface features of nanomaterials by several complementary techniques (HR-TEM, SSA_{BET}, FT-IR, TGA, microgravimetry), and the investigation at molecular level of the interaction of nanomaterials with

leather by SEM-EDS, FT-IR, NMR-MOUSE and micro-DSC. Further, the development of the detailed protocol of the production of nano-HA at laboratory scale with a reproducible method allowed to evaluate environmental impacts and damages of the synthesis of nano-HA at laboratory scale through Life Cycle Assessment, in collaboration with the Management Department of University of Torino.

A side part of this project was focused on the development of an alternative to chrome-tanning; chromium (III), present in salts used for tanning, can be converted into chromium (VI) in the production, but also in the manufactured leather, in particular during the burning of waste leather products.⁹

Oxidized sodium alginate (OSA) as a sustainable tanning agent could act as a crosslinker between collagen fibers, increasing the stability of the leather: collagen becomes less susceptible to hydrolysis and the leather more resistant to shrinkage when subjected to heat. This part of the work was carried out in collaboration with the Institute for Textiles and Leather of Bucharest.

Bibliographic References

1. Sreeram, K. J.; Ramasami, T., Sustaining tanning process through conservation, recovery and better utilization of chromium. *Resources, Conservation and Recycling* **2003**, *38* (3), 185-212.
2. Mastrantonio, M.; Bai, E.; Uccelli, R.; Cordiano, V.; Screpanti, A.; Crosignani, P., Drinking water contamination from perfluoroalkyl substances (PFAS): an ecological mortality study in the Veneto Region, Italy. *European Journal of Public Health* **2018**, *28* (1), 180-185.
3. ECHA, E. C. A., Perfluoroalkyl chemicals, <https://echa.europa.eu/it/hot-topics/perfluoroalkyl-chemicals-pfas>.
4. Shi, J.; Wang, C.; Ngai, T.; Lin, W., Diffusion and Binding of Laponite Clay Nanoparticles into Collagen Fibers for the Formation of Leather Matrix. *Langmuir* **2018**, *34* (25), 7379-7385.
5. Wang, Z.; Yang, W.; Sun, F.; Zhang, P.; He, Y.; Wang, X.; Luo, D.; Ma, W.; Sergio, G.-C., Construction of a superhydrophobic coating using triethoxyvinylsilane-modified silica nanoparticles. *Surface Engineering* **2018**, *35* (5), 418-425.
6. Eze, C. T.; Michelangeli, F.; Otitoloju, A. A.; Eze, O. O.; Ibraheem, O.; Ogbuene, E. B.; Ogunwole, G. A., Occurrence of chemical pollutants in major e-waste sites in West Africa and usefulness of cytotoxicity and induction of ethoxyresorufin-O-deethylase (EROD) in determining the effects of some detected brominated flame retardants and e-waste soil-derived extracts. *Environmental Science and Pollution Research* **2020**.
7. Chen, X.; Guo, W.; Lei, L.; Guo, Y.; Yang, L.; Han, J.; Zhou, B., Bioconcentration and developmental neurotoxicity of novel brominated flame retardants, hexabromobenzene and pentabromobenzene in zebrafish. *Environmental Pollution* **2021**, *268*, 115895.
8. Zhao, X.; Chen, T.; Yang, B.; Wang, D.; Sun, W.; Wang, Y.; Yang, X.; Wen, S.; Li, J.; Shi, Z., Serum levels of novel brominated flame retardants (NBFRs) in residents of a major BFR-producing region: Occurrence, impact factors and the relationship to thyroid and liver function. *Ecotoxicology and Environmental Safety* **2021**, *208*, 111467.
9. Covington, A. D., *Tanning Chemistry: The Science of Leather* **2009**.

1. INTRODUCTION

1.1 BACKGROUND AND CHALLENGE

The leather industry, based on the conversion of food industry's waste material into useful manufactured products provides a large number of consumer goods, either for technical or daily use.¹ In order to transform a raw hide into leather, several steps are involved in leather production processes; the number of steps depends on the desired leather type. Each step is fundamental to reach a high level of quality of the produced leather.

A scheme summarizing the different steps of leather production is reported in Fig. 1.1.1, with a brief explanation for each step, and particular attention on the produced wastewater and solid waste.

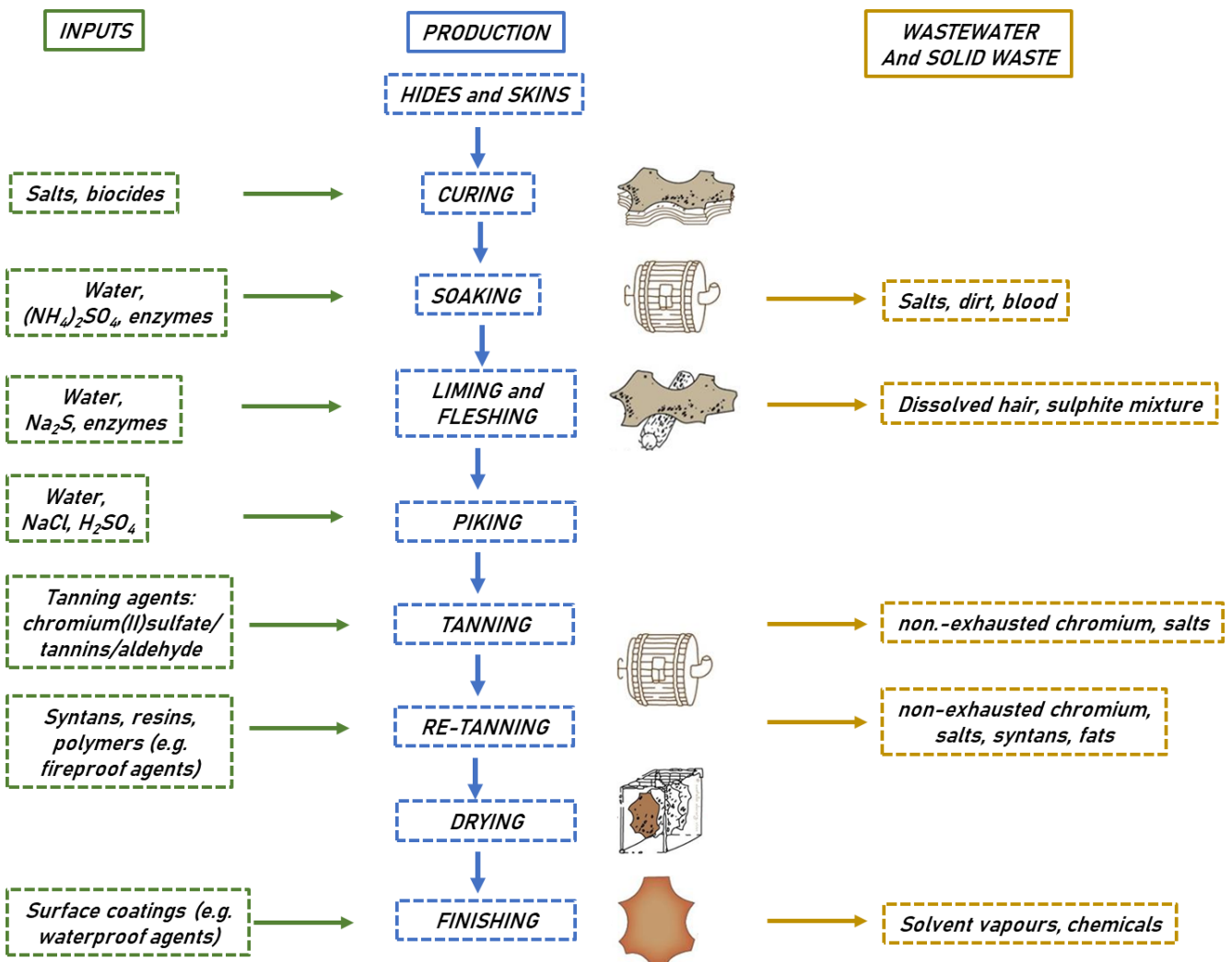


Figure 1.1.1. Scheme of leather production with inputs for each step and produced wastewater and solid waste after treatments.

The first step is the *curing*, the salt conservation treatment, that removes water from raw hides to preserve them from deterioration. Biocides can be also used for the preservation of skins. The cured hides are then soaked in water (*soaking*). The salts and dirt from the previous step are removed, and the hides regain their original softness. This step could last for some hours or several days, depending on the volume of the salts used and the dehydration of the skin. After this step, a consistent amount of water containing salts, dirt and blood represents the waste.

The *liming*, using a sulphite-based mixture, removes the hair from the hides; moreover, the chemical bonds between collagen fibers are broken, in a controlled way, due to an alkaline swelling of the skin.

The mechanical step of *fleshing*, using a sharp and curved blade, removes any excess of fleshy tissue from the back side and fat layers remained after the previous step. Some enzymes can be added after this step and the pelt becomes flat, relaxed, and clean.

The *picking* process is a preparation step, involving the addition of weak acid and salts solutions before the tanning step.

The most important step in the leather production is the *tanning*.^{2, 3} During this process, the hide becomes leather, thanks to the use of tanning agents. From the molecular point of view, this step involves a reaction with the exposed groups of collagen, as depicted in Fig. 1.1.2 and described in the following.⁴

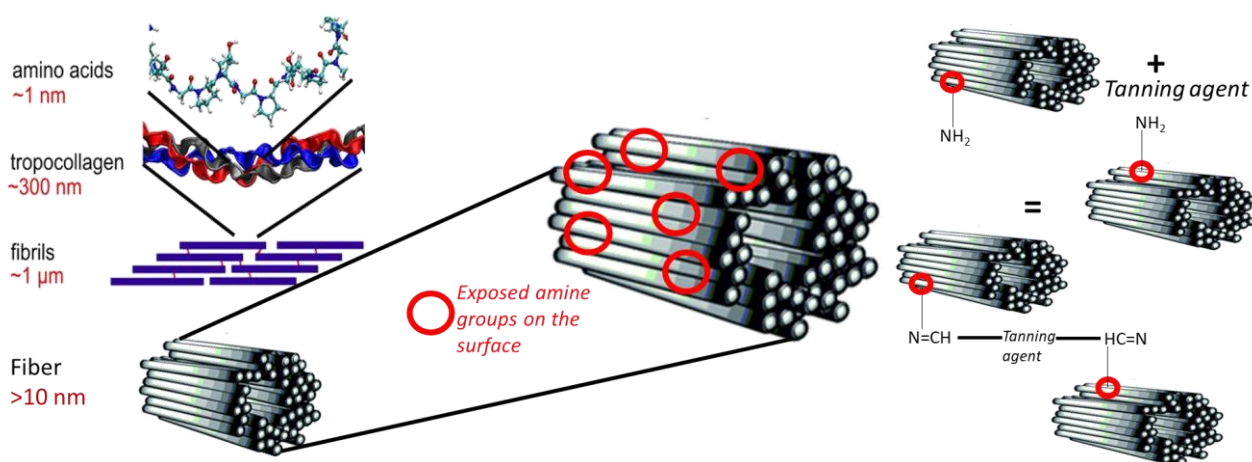


Figure 1.1.2. Collagen structure and the mechanism of the tanning step for the crosslinking of collagen fibers.

Collagen is composed of different amino acids, the most common are glycine, proline, hydroxyproline and hydroxylysine. Usually they form repeating (Gly-Pro-Y) or (Gly-X-Hyp) triad in each chain, and the most common triplet in collagen is Pro-Hyp-Gly, that forms the 10% of the total sequence and a stable triple helix. The tropocollagen consists of a single collagen molecule and its organization results in fibrils structures that can form fibers. The exposed amine groups of the final residues of amino acid triads on the surface could act as crosslinks towards tanning agents. The formation of a stable bond between collagen fibers thanks to tanning makes it less susceptible to putrefaction and hydrolysis because the fibers denature when the water bound in them is released. Moreover, it becomes much resistant to shrinkage when subjected to heat.

Several types of tanning agents are currently used to satisfy these characteristics. The most used are chrome tanning, vegetal tanning, synthetic tanning and tanning with fats and oils.

Chrome tanning, performed by using chromium (III) salt, is used in around 85% of global leather production.³ The skin does not adsorb all the chromium salts used for tanning, and the wastes related to this step contains high amounts non-exhausted chromium (III), that can be converted in chromium (VI) due to mistakes in the production. Chromium (VI) can also emerge later in the manufactured leather. Moreover, the chemistry of chrome-process also highlights the potential

dangers in burning waste leather products: the fly ash that contains Cr (VI) represents a high risk for the environment.⁵

This compound is also harmful to health, and in the last years several alternatives for chrome tanning have been tested. Although the production of leather without the use of chromium is more complex, several works based on the use of sustainable alternative for the production of FOC- (free of chrome) and FOM- (free of metals) leather have appeared.⁶⁻⁸

Vegetable tanning agents are based on tannins found naturally in plants; they derive from wood, bark, leaves, roots etc.,⁹ which are water-soluble, non-crystalline ingredients of plant matter. Oak and spruce bark, quebracho, tara pods, olive leaves, rhubarb roots or mimosa are the most used. The use of synthetic tanning agents (i.e. glutaraldehyde, phenols, and acrylates) results in soft leathers. These substances are usually employed in a combined tanning process with either chrome or vegetable tanning.

One of the disadvantages in the use of FOC and FOM leather is the sensitivity to moisture and heat. The water, penetrating in the pores of the leather, could start boiling when subjected to heat, and the leather becomes much more solid and it can shrink.

The *retanning* process is necessary to reach the desired characteristics when the primary tanning is not effective enough. Moreover, in this step other materials can be added, in order to increase the thermal stability of the leather or to impart qualities such as dyeability, fine quality and stability of the exposed surface (grain). Nanomaterials can be used in this step, thanks to their ability to penetrate into the fibers and interact with them which could increase the thermal stability of the leather^{10, 11} and improve its properties.¹²

After the procedures of splitting, shaving and neutralization of leather (to uniform the thickness and to remove residual chemicals), the *drying* step allows to remove 10-20% of water content from leather. The *finishing* process depends on the required specifications: pigmentation, pressing, ironing, embossing, adjusting of gloss level, waterproofing, etc. The type and the amount of waste in this step is related to the final characteristics required for leather.

The explanation of the entire scheme of leather production gives an idea of the huge number of solvents, hazardous chemicals and dangerous substances used in several steps, with a consequent production of waste that can represent a high risk for the environment and for animal and human health.¹³ In the last years, the European Commission along with different associations and organizations are working to promote the use of cleaner production technologies while keeping and improving the quality of products and processes.¹⁴ Imposed restrictions in the use of the most dangerous substances, reported in the regulations of Registration, Evaluation, Authorization and Restriction of Chemicals (REACH), are hitting new highs every day, encouraging different countries to prohibit their use in new manufactured goods. This stimulates a constant research and development work in the application of new sustainable alternatives that can improve environmental performances with the activation of several funding programs not only from government institutions, but also from private companies.

The Confederation of National Associations of Tanners and Dressers of the European Community (COTANCE)¹⁵ is the representative association of the European Leather Industry. This organization was established in order to promote the interests of the European tanning industry at international level. Europe has always played a primary role in this sector, with one of the bigger markets of leather goods and about 25% of the world's leather production.

Different products and industrial processes are involved in the leather industry, also thanks to the long tradition of producing all kinds of leather (e.g. bovine, calf, sheep and goat leather), that contribute to the successful production of furniture, footwear and clothing. The expertise in the processing of leather and the high quality of the products explain the endlessly strong demand on international markets, reported in many articles published by COTANCE.¹⁵

From the last data provided by European Commission,¹⁴ the leather sector includes about 36,000 companies and creates a turnover of € 48 billion. These enterprises employ around 435,000 people. In the last Manifesto published after the European Social Dialogue project “A future for European Leather!”¹⁶ managed by COTANCE and IndustriALL¹⁷ in 2016, different aspects on leather production were analysed, with a particular attention on the environmental matters.

Rawhide is a by-product of food industry, in particular animal farming; since tanning is the recycling of animal-by-products into leather and it is possible to find a suitable recovery and destination of use of the solid waste from its production, the European Commission believes that there is a large potential for circular economy action¹⁸ also in this sector and different research works are published in this respect.^{19, 20}

In December 2020, COTANCE and IndustriALL presented the Social and Environmental Report 2020, where the image of European leather as a modern and sustainable industry is reported, based on the progress achieved by the sector in the last years. Noteworthy in this regard, the improvement of innovation and performances are placed at the center of the Europe 2020 strategy,²¹ resulting in Horizon 2020 as a funding program; the key directions are the promotion of a smart, sustainable and inclusive growth.

In the light of the foregoing, this PhD project was born in 2017, thanks to the collaboration of Prof. Gianmario Martra at the Department of Chemistry of University of Torino with several institutions in the framework of different international and regional projects: NoPFA - Prodotti e Processi Sostenibili per le Industrie Conciarie tramite Uso di **Nanomateriali** per la Sostituzione di Sostanze **PerFluorurate Alchilate** per la Impermeabilizzazione (Sustainable Products and Processes for Tanning Industries Using Nanomaterials for the Replacement of Perfluorurate Alkylated Substances for Waterproofing), funded by Piedmont Region, InSuLA - **Innovative Materials and Technologies for Sustainable Leather Manufacturing for Automotive** (MANUNET transnational call 2017, funded by FINPIEMONTE) and NanoSusLeather - **Nanomaterials for Sustainable Leather Products** (funded by Compagnia di San Paolo).

KEMIA TAU company, a top-level Italian player in the business of chemicals for leather tanning and finishing, played an active and leading role in these projects, starting collaborations with a number of institutions with different area of expertise: the Institute for Textiles and Leather located in Bucharest, for leather processes at micro-pilot level, the Department of Chemistry possessing expertise in the preparation and characterization of nanomaterials at laboratory scale, and the Management Department experienced into Life-Cycle Assessment (LCA) and Life Cycle Cost Analysis (LCCA) of innovative manufacturing processes.

The starting point of the project was the evidence of the potential of nanomaterials, also combined with polymers to form composites, in ‘greening’ leather making processes. Different research works have demonstrated quite recently, good promises in this field.²²⁻²⁵

The decrease of the environmental impact of tanning/retanning and leather finishing are pursued by investigating the most impactful leather treatments. The selected innovative tools for contributing to the sustainable innovation in Europe tannery and leather finishing technology are the following:

- the use of nanomaterials as *waterproofing agents* for the substitution of the already applied perfluoroalkyl substances (PFAS) in hydrophobic coatings for leather, starting from the possibility to functionalized nanoparticles (e.g. silica) with non-fluorinated hydrophobic molecules.²⁶
- the application of nanocomposites based on nano-hydroxyapatite (nano-HA), nanoclays, nano-SiO₂ and nano-TiO₂ as the main constituents for the *flame resistance* behaviour²⁷⁻²⁹ instead of brominated (PBB, PBDE, HBCD) flame retardants, which were shown to be persistent in the environment and toxic for animals and humans.³⁰
- the employment of inorganic fillers such as nanoclays and nano-HA allowing to decrease the amount of synthetic tannins used in the tanning/retanning process, typically phenol-formaldehyde-based resins; the innovative aspect is the development of *new knowledge based organic tanning agent* (KTA) from alginate as a sustainable alternative to formaldehyde (FA) and glutaraldehyde (GA) which were shown to have adverse health effects on humans and contribute to greenhouse gas emission as petroleum-derived chemicals.^{31, 32} This part of the work was carried out in collaboration with the Institute for Textiles and Leather of Bucharest.

The core of this PhD project regards the first two challenges, and the state-of-the-art of waterproof and fireproof agents and technologies are reported in the following section.

1.2 AN INSIGHT ON WATERPROOF AND FIREPROOF AGENTS: ENVIRONMENTAL CONCERNS AND POSSIBLE SUSTAINABLE STRATEGIES

The main challenge of this project is to find a sustainable alternative to dangerous substances applied to give specific properties to leather, in order to combine desired technological and aesthetic standards: waterproofing and flame resistance are two of those attributes.

Nowadays, the required *hydrophobic behaviour* of a variety of consumer goods is satisfied by employment of perfluoroalkyl substances (PFAS). The textile and leather industries use PFAS to impart waterproof and grease-repellent characteristics to final products, such as technical boots, shoes and jackets.³³ However, the types of PFA-containing products are extremely varied and are involved in many industrial and commercial applications, not only in the leather industry (Fig. 1.2.3).³⁴



Figure 1.2.3. Scheme of the principal PFAS-containing products of daily-use.

In the Fig. 1.2.3, the most common uses of PFAS are reported:³⁵

- in the food-packaging industry, to obtain waterproof and greaseproof papers. Packaging involves food contact paper such as plates, popcorn bags, pizza boxes;
- the production of pesticides requires the use of PFAS as dispersants and wetting agents for herbicides and to facilitate spraying and penetration in insecticides;
- inside the paints, PFAS are used to reduce surface tension for substrate wetting, levelling, and increasing gloss and antistatic properties;
- in the photographic field, PFAS are involved in manufacturing film, paper, and plates as dirt rejecters and friction control agents and to reduce surface tension and static electricity.

The PFAS terms refers to more than 4000 substances,³⁴ consisting of a carbon backbone with fluorine atoms attached to alkyl chains of different lengths (Fig. 1.2.4). The shorter chains can be more persistent in the environment, while the longer ones are not very stable and with degradation they could transform in shorter chains.

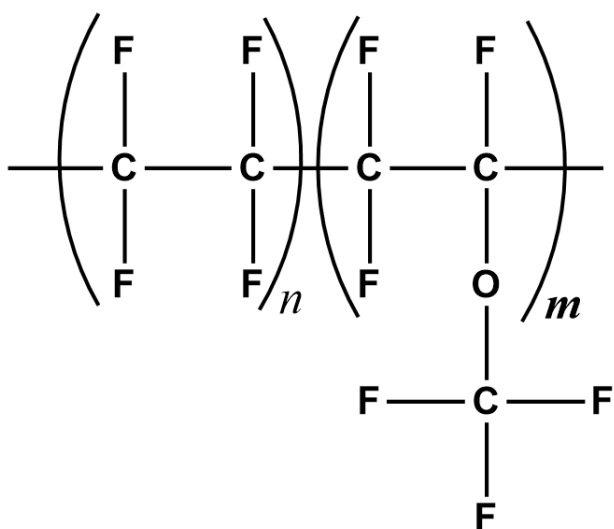
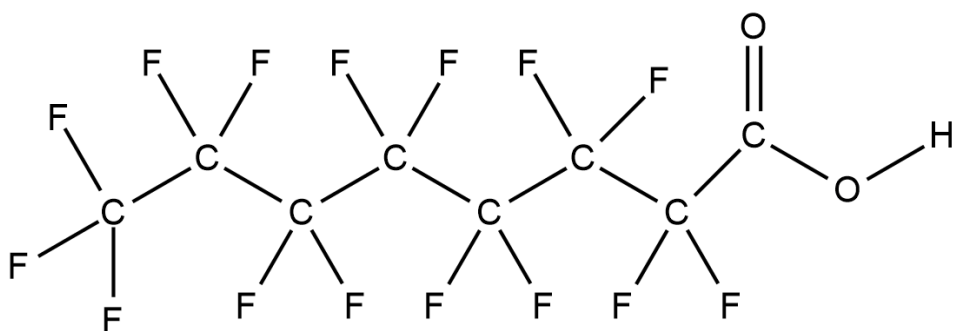
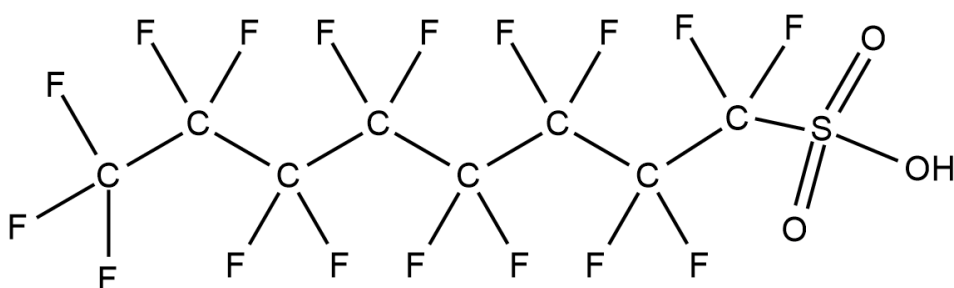


Figure 1.2.4. Chemical structure of PFAS.

The two most known PFAS are perfluorooctanoic acid (PFOA) and perfluorooctanesulfonate (PFOS), reported in Fig. 1.2.5.³⁶ These compounds are detected in epidemiological studies, and they are responsible for changes in hormonal balance and thyroid function.³⁴



PFOA



PFOS

Figure 1.2.5. Chemical structures of Perfluorooctanoate (PFOA) and Perfluorooctane sulfonate (PFOS).

The potential human risk of these substances led to the inclusion, since 2009, of PFOS and its derivatives in the International Stockholm Convention, to avoid their use. Moreover, they have been restricted in the EU for more than ten years, under the EU's Persistent Organic Pollutants (POPs) Regulation.³⁷ Mixtures of PFAS are detected in air, soil and water, and many research works reported the worrying situation in different parts of the world.^{34, 38, 39}

Different routes on the release of PFAS to the environment exist; the air pollution from landfills is detected in different plant leaves,⁴⁰ acting as a kind of passive monitoring tool. The landfills are not the only source of PFAS air emission, but several studies reported the pollution also from the aeration step employed in wastewater treatments.³⁴

The industrial discharges are responsible for the water pollution; rivers and lakes can leach these compounds into soil and affect the organisms living in those areas, even with food that is grown from this contaminated land. In September 2020, the EFSA (European Food Safety Authority) established a new maximum level for the main perfluoroalkyl substances accumulated in the body, based on the risks to people's health from the presence of PFAS in food.³⁷ In Italy, Veneto is the most contaminated region by PFAS; the high concentration of chemical industries, textiles and leather factories led to excessive levels of PFAS detected in surface freshwater and groundwater.³⁹ Since PFAS are persistent organic substances that can accumulate in the human body through inhalation, water and food ingestion, several studies have reported the relationship between the high level of PFAS concentration in the environment and the diseases found in local people. The higher relative risks (RRs) are detected for general mortality, diabetes, cerebrovascular and Alzheimer's diseases and myocardial infarction for males; kidney and breast cancer and Parkinson's disease are the most common pathology in females.⁴¹

Moreover, for pregnant women, the risks include the possibility to transfer PFAS to the fetus through placenta and from maternal blood to breast milk to babies; these could have a relationship with a variety of growth disorders of new-borns in contaminated areas of Veneto region.⁴² Despite the fact that in Italy (and Europe) no restriction in the limits of PFAS in water were imposed until the new European directive of 2020,³⁷ Veneto region in 2014, with the National Institute of Health, has started to fix maximum level on PFAS concentration in drinking water.³⁹

Conventional ways to remove the PFAS from wastewater are not effective,³⁴ and the only solution is to ban their use in new consumer goods. For this purpose, the manufacturing and use of different PFAS is being restricted under REACH, and from 1 October 2021 the ECHA, under request of the European Commission, will prepare a restriction proposal for PFAS in firefighting foams.³⁷ On such a basis, the most recent research works are moving towards the study of new sustainable products for different applications without the use of fluorinated compounds.

The recent trends are the use of nanomaterials for the production of hydrophobic coatings, for the lower cost in the production and the simple application methods on different substrates. In particular, modified silica nanoparticles were studied as hydrophobic and/or self-cleaning layers for clothes, shoes, paper, glass and other consumer goods of industrial interest.⁴³ Moreover, several studies regarding the possibility to employ nanoparticles in order to satisfy waterproof qualities also in leather treatments are reported.⁴⁴

Although the wide employment of fluor-alkylsilane modified nanoparticles as waterproof coating,⁴⁵⁻⁴⁷ especially at the beginning of the research in this field, recent studies are heading towards fluorine-free compounds for the functionalization of silica surface using various surface

modifiers based on alkylsilane molecules with different alkyl chains length and branching moieties.⁴⁸⁻⁵⁰

The most required characteristic of waterproof coatings for consumer goods is the superhydrophobicity. While the deposition of a droplet on a hydrophobic surface generates an angle between the liquid-solid and liquid-vapor interface (called contact angle) between 90° and 150° , superhydrophobic materials show contact angles greater than 150° (Fig. 1.2.6).⁵¹

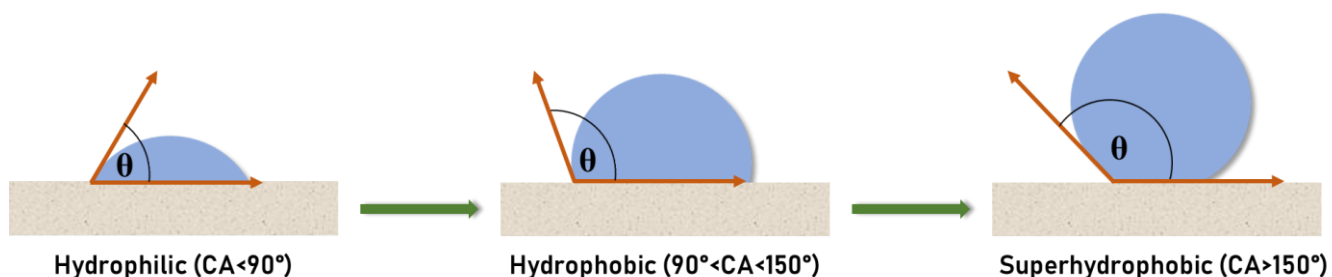


Figure 1.2.6. Scheme of water droplet contact angle at different levels of wettability.

The basic principles of the high water contact angle and the self-cleaning properties of superhydrophobic materials are well-known in nature, with the so-called “Lotus effect”.⁵² Most of the research works based on the production of superhydrophobic coatings are inspired by the characteristics of lotus leaves; in fact, they naturally combine the low-surface energy with the exhibition of micro-nano- hierarchical structures on the surface, forming roughness grooves, that can trap air and thus, they are able to protect the surface from water (Fig. 1.2.7).

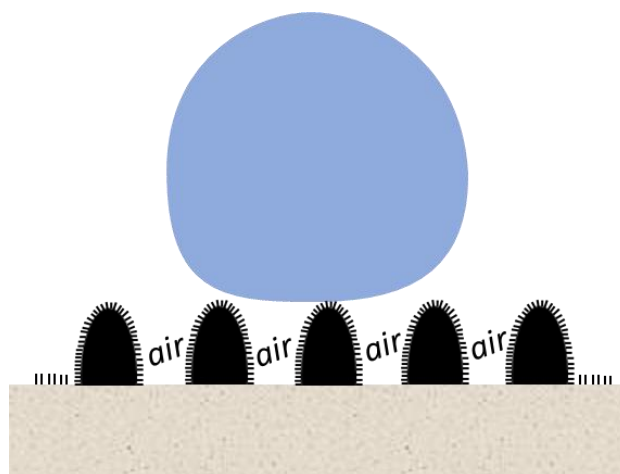


Figure 1.2.7. Schematic representation of the contact between a water droplet and nano- and micro-hierarchical structures on a superhydrophobic surface.

To mimic this effect, a variety of surface modification strategies and several molecules exposing hydrophobic moieties are employed in the preparation of water-repellent coatings with low-surface energy and high roughness.^{50, 53, 54}

Potential obstacles in the supply of some commercially available materials for the functionalization of silica nanoparticles and the required precaution to avoid health risks for the workers in the use

of some kind of hazardous alkylsilanes,⁵⁵ led the exploitation of some new and safe strategies for the production and application of hydrophobic nanoparticles.^{26, 48} The use of a safe and non-toxic molecule for the functionalization of silica surface, like isostearic acid, and the potential simple application on leather samples, allows to place this PhD project in this innovative and sustainable field of research.

Moving on to *fireproofing* aspects, the environmental concern is again the key point. In the past few decades, the flame resistance of a variety of products has been provided by the use of brominated flame retardants (BFRs), consisting of a mixture of chemicals based on organic bromine compounds. The European Food Safety Authority (EFSA)⁵⁶ reported five main groups of BFRs of industrial interest (Fig. 1.2.8):

- *Polybrominated diphenyl ethers* (PBDEs), found in plastic materials, textiles and leather industries, and electronic equipment;
- *Hexabromocyclododecanes* (HBCDs), usually employed for thermal insulation of buildings;
- *Tetrabromobisphenol A* (TBBPA-A), for printed circuit boards and TVs;
- *Polybrominated biphenyls* (PBBs), applied in plastic foams, monitors, textiles;
- Other BFRs.

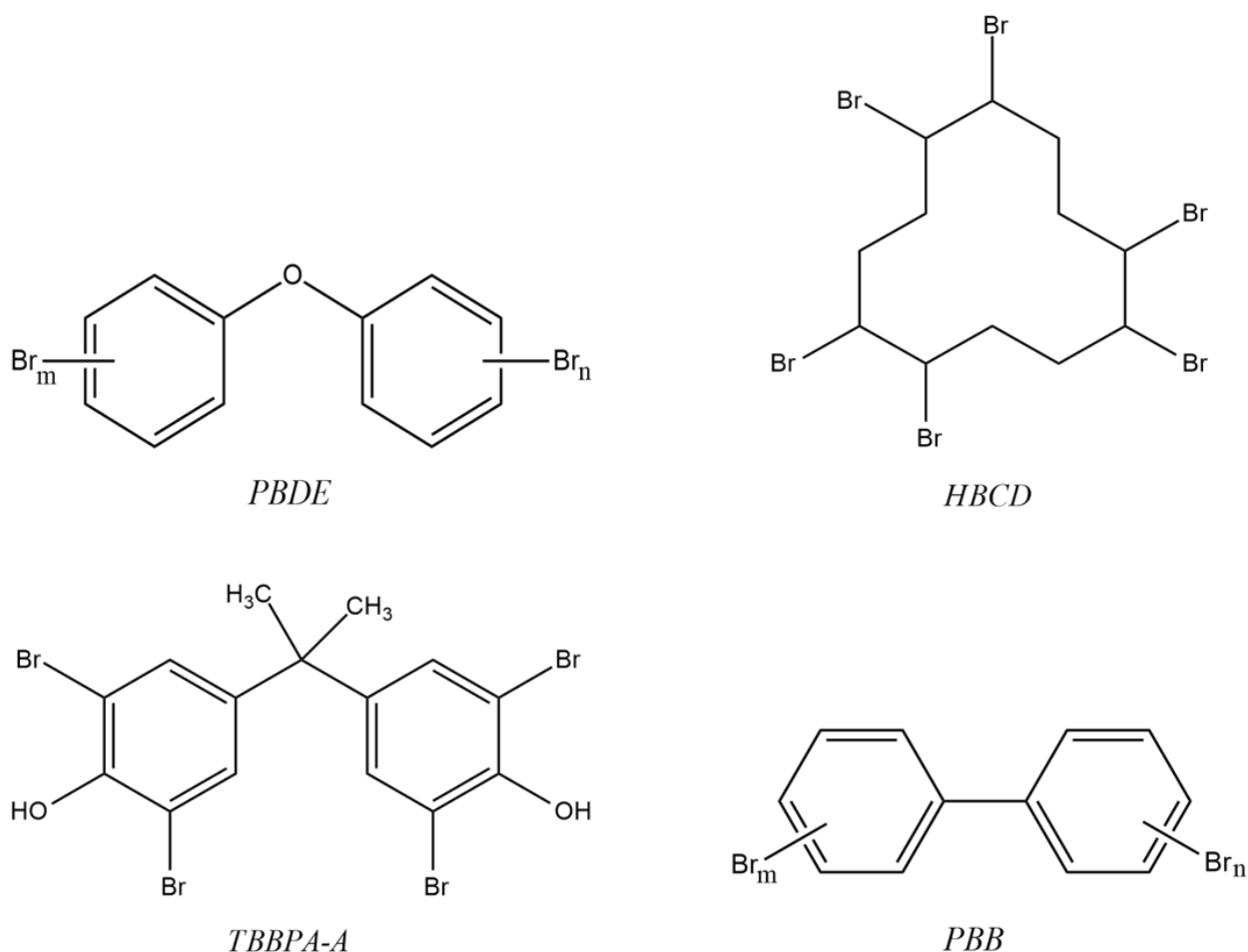


Figure 1.2.8. Chemical structures of the most used BFRs groups in industrial processes: PBDE (*Polybrominated diphenyl ether*); HBCD (*Hexabromocyclododecane*); TBBPA-A (*Tetrabromobisphenol A*); PBB (*Polybrominated biphenyls*).

The imposed limits for BFRs, either in products⁵⁷ and in food chains⁵⁶ of the already mentioned “traditional” brominated flame retardants (BRFs), led to a progressive substitution with alternatives, the novel flame retardants (NBFRs), with a global production around 100,000 tons. The most used NBFRs (Fig. 1.2.9) are *tris(2,3-dibromopropyl) phosphate* (TDBPP), *2,2-Bis(bromomethyl)-1,3-propanediol* (DBNPG) *hexabromobenzene* (HBB) and *pentabromobenzene* (PBB). They have been widely used in polymeric materials, household furniture, and electronic devices.⁵⁸

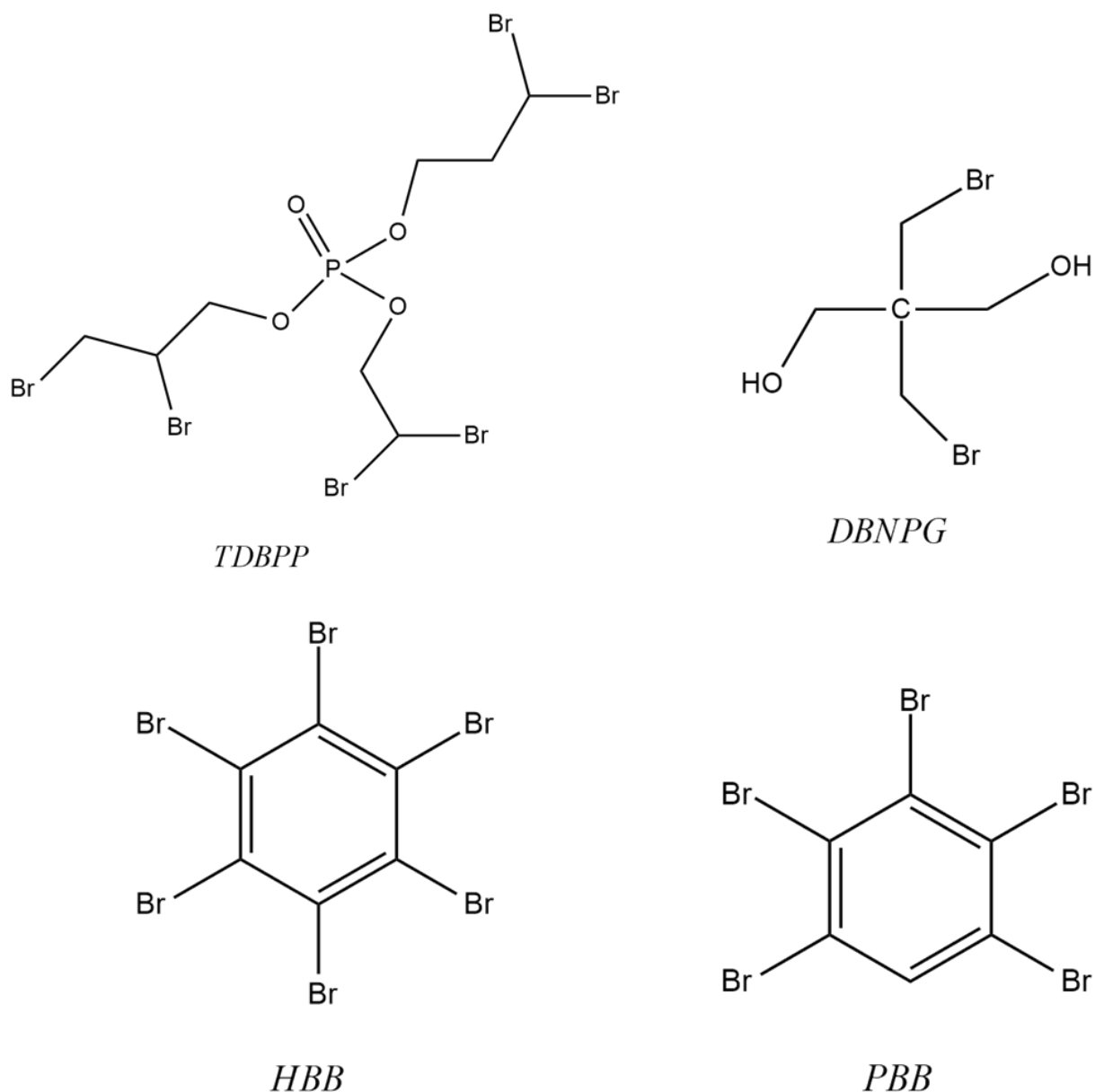


Figure 1.2.9. Chemical structures of some novel BFRs (NBFRs): TDBPP (*tris(2,3-dibromopropyl) phosphate*); DBNPG (*2,2-Bis(bromomethyl)-1,3-propanediol*); HBB (*hexabromobenzene*) and PBB (*pentabromobenzene*).

Although the time-limited toxicological studies on NBFRs, several new research works are published in this respect, reporting CNS development disease in embryos of aquatic species⁵⁸ and liver injury indicators in exposed population.⁵⁹

One of the recent issues in the use of BFRs is linked to environmental pollution during recycling processes. Chemical pollutants in consumer goods are released into the environment with a subsequent contamination of air, soil, and water. A recent study reported the environmental concern especially for electronic waste, in which brominated compounds are used to protect electronic parts against fire damage.⁶⁰ The relevant risks for the environment and human's health in the use of BFRs⁶¹ has shifted the attention on the possibility to employ bromine-free and halogen-free compounds as flame retardants agents.^{62, 63}

Flame retardants (FRs) are employed also in the field of tanneries, especially for leather intended to seat covers for aircrafts, cars, and theatres; the mechanism of FRs in terms of flame propagation and flame retardancy is reported.⁶⁴

The role of flame-retardant agents during the heat decomposition results in the consumption of oxygen, with the formation of compounds between the FR and the oxygen in air to form water and nitrogen oxides. In this way, there is a dilution of the oxygen concentration and a good flame-retardant efficiency. Moreover, it is possible to take advantage of the formation of hydrogen bonds between hydroxyl groups of FRs and functional groups of amino acids of collagen that improve the tanning effect and so the FR acts as a crosslinker between collagen fibers. The increase of tanning results in an increase of heat stability of leather.

In order to reach comparable performances without the use of chemicals, recent research works have reported the possibility of using also nanomaterials as flame-retardants.^{27, 65} Nanomaterials can form a sort of "grid" in leather, if they are properly distributed, preventing the breakdown of products that can release gas-phase combustible molecules.

The study of the affinity between leather and nanoclays, nanoparticles and nanocomposites was the starting point of the research in this field, and good evidence of the penetration and interaction of nanocomposites in leather matrix are reported.^{65,66} Although the potential beneficial in fireproofing qualities of consumer goods, avoiding the employment of bromine-containing flame-retardant agents, the research regarding the use of nanomaterials in this field is mostly related to the use of nanoclays.⁶⁷

Among nanomaterials, the attention was drawn to the hydroxyapatite (HA), a calcium phosphate similar to the mineral component of natural bone in morphology and composition.⁶⁸ The compatibility between hydroxyapatite and collagen, naturally exploited in bone biomineralization in human body,⁶⁹ led the use of HA, especially in the "nano" form for the better bioactivity, in biomedical applications like orthopedic and dental implant formulations.^{68, 70}

The nanomaterial was employed also as flame retardant agents in different fields, such as paper industry⁷¹ and in the treatment of wood ash for a new use application.²⁹ Despite several proofs about the effectiveness of nano-HA as flame retardant agent, the literature dealing with its use in leather treatments is not wide,^{10, 72} and one objective of this PhD work was to contribute into the increase of the knowledge in this field for the improvement of sustainability in leather production.

1.3 AIM AND ORGANIZATION OF THE WORK

On the basis of the state-of-the-art reported in the previous sections, the main target of this work is the development of new sustainable processes and non-toxic nanocomposites for waterproof and fireproof purposes.

This manuscript is divided in two main parts; the first one, concerning the preparation, characterization and application of nanoparticles functionalized with highly branched alkyl chains positively affecting the hydrophobic qualities of the surface, was organized following the temporal order of the study carried out in the past three years.

Starting from the reproduction of an existing protocol²⁶ based on the functionalization of alumina nanoparticles with commercial branched alkyl carboxylic acids (FINEOXOCOL, by Nissan Chemical America Corporation), the attention passed to silica nanoparticles. The advantages in the use of this kind of nanomaterial are, firstly, the possibility to link covalently the branched alkyl carboxylic acids to the silica surface functionalized with amino groups, definitely more robust than the Coulombic interaction between carboxylate groups and surface cations exploited for the surface functionalization of alumina nanoparticles. The second one was linked to sustainability: silica is already used in leather finishing process, to deliver softness, luster and abrasion resistance; the functionalization with hydrophobic moieties on the surface of the already applied material could avoid the use of another compound in the treatment to deliver additional waterproof qualities.

The hydrophobicity of the synthesized materials was studied by two different approaches and points of view. Contact angle measurements were used to monitor the repellence towards water droplets at the macroscopic level, while microgravimetric and microcalorimetric analyses allowed to characterize at the molecular level the adsorption capacity of the materials towards water vapour. The second part of the work is related to fireproofing aspects. The study is focused on the possibility to use safe and non-toxic nanocomposites based on nano-SiO₂, nano-TiO₂ and nano-HA as flame retardant agents in leather. In particular, the rationale for the last material is the intrinsic high affinity of this material for collagen, the main component of leather, spontaneously exploited by nature in the nanocomposite structure of bone tissue. The work has been focused on the production of nano-HA using a low-cost method, with attention to the reproducibility and the characteristics of the prepared material. The three nanomaterials were applied on leather, to test their effect on the thermal capacity of the product. Attention was focused on the interaction of nano-HA with leather, in relation to the observed superior thermal resistance.

Finally, a side part of this project was focused on the use of oxidized sodium alginate as a sustainable alternative to chrome-tanning, in tight collaboration with the Institute for Textiles and Leather of Bucharest.

Bibliographic References

1. Dixit, S.; Yadav, A.; Dwivedi, P. D.; Das, M., Toxic hazards of leather industry and technologies to combat threat: a review. *Journal of Cleaner Production* **2015**, *87*, 39-49.
2. BLC Leather Technology Centre Ltd <http://www.all-about-leather.co.uk/what-is-leather/how-is-leather-made.htm>
3. Colourlock https://www.leather-dictionary.com/index.php/Leather_production.
4. Domene, C.; Jorgensen, C.; Abbasi, S. W., A perspective on structural and computational work on collagen. *Phys Chem Chem Phys* **2016**, *18* (36), 24802-24811.
5. Covington, A. D., *Tanning Chemistry: The Science of Leather* **2009**.
6. Krishnamoorthy, G.; Sadulla, S.; Sehgal, P. K.; Mandal, A. B., Greener approach to leather tanning process: d-Lysine aldehyde as novel tanning agent for chrome-free tanning. *Journal of Cleaner Production* **2013**, *42*, 277-286.
7. Shi, J.; Puig, R.; Sang, J.; Lin, W., A comprehensive evaluation of physical and environmental performances for wet-white leather manufacture. *Journal of Cleaner Production* **2016**, *139*, 1512-1519.
8. Roig, M.; Segarra, V.; Bertazzo, M.; Martinez, M. A.; Ferrer, J.; Raspi, C., Chrome-free leather, tanned with oxazolidine. *Journal of AQEIC* **2012**, *63*, 101-109.
9. Kanth, S. V.; Venba, R.; Madhan, B.; Chandrababu, N. K.; Sadulla, S., Cleaner tanning practices for tannery pollution abatement: Role of enzymes in eco-friendly vegetable tanning. *Journal of Cleaner Production* **2009**, *17* (5), 507-515.
10. Selvaraju, S.; Ramalingam, S.; Rao, J. R., Preparation and application of biodegradable nanocomposite for cleaner leather processing. *Journal of Cleaner Production* **2017**, *158*, 225-232.
11. Kale, M. B.; Luo, Z.; Zhang, X.; Dhamodharan, D.; Divakaran, N.; Mubarak, S.; Wu, L.; Xu, Y., Waterborne polyurethane/graphene oxide-silica nanocomposites with improved mechanical and thermal properties for leather coatings using screen printing. *Polymer* **2019**, *170*, 43-53.
12. Ma, J.; Lv, X.; Gao, D.; Li, Y.; Lv, B.; Zhang, J., Nanocomposite-based green tanning process of suede leather to enhance chromium uptake. *Journal of Cleaner Production* **2014**, *72*, 120-126.
13. Sreeram, K. J.; Ramasami, T., Sustaining tanning process through conservation, recovery and better utilization of chromium. *Resources, Conservation and Recycling* **2003**, *38* (3), 185-212.
14. European Commission website https://ec.europa.eu/growth/sectors/fashion/leather/eu-industry_en
15. COTANCE <https://www.euroleather.com/>
16. AFFEL manifesto <http://www.euroleather.com/doc/AFFELmanifesto.pdf>.
17. IndustriALL www.industriall-union.org.
18. European Civil Society Strategy <https://fairtrade-advocacy.org/wp-content/uploads/2020/04/Civil-Society-European-Strategy-for-Sustainable-Textiles.pdf>
19. Moktadir, M. A.; Ahmadi, H. B.; Sultana, R.; Zohra, F.-T.; Liou, J. J. H.; Rezaei, J., Circular economy practices in the leather industry: A practical step towards sustainable development. *Journal of Cleaner Production* **2020**, *251*.
20. Sathish, M.; Madhan, B.; Raghava Rao, J., Leather solid waste: An eco-benign raw material for leather chemical preparation - A circular economy example. *Waste Manag* **2019**, *87*, 357-367.
21. IPEX EU document COM/2010/2020 FIN, at www.ipex-eu
22. Li, K.; Yu, R.; Zhu, R.; Liang, R.; Liu, G.; Peng, B., pH-Sensitive and Chromium-Loaded Mineralized Nanoparticles as a Tanning Agent for Cleaner Leather Production. *ACS Sustainable Chemistry & Engineering* **2019**, *7* (9), 8660-8669.
23. Raji, P.; Samrot, A. V.; Bhavya, K. S.; Sharan, M.; Priya, S.; Paulraj, P., Greener Approach for Leather Tanning Using Less Chrome with Plant Tannins and Tannins Mediated Nanoparticles. *Journal of Cluster Science* **2019**, *30* (6), 1533-1543.
24. Zhu, R.; Yang, C.; Li, K.; Yu, R.; Liu, G.; Peng, B., A smart high chrome exhaustion and chrome-less tanning system based on chromium (III)-loaded nanoparticles for cleaner leather processing. *Journal of Cleaner Production* **2020**, *277*.
25. Gao, D.; Wang, P.; Shi, J.; Li, F.; Li, W.; Lyu, B.; Ma, J., A green chemistry approach to leather tanning process: Cage-like octa(aminosilsesquioxane) combined with Tetrakis(hydroxymethyl)phosphonium sulfate. *Journal of Cleaner Production* **2019**, *229*, 1102-1111.

26. Alexander, S.; Eastoe, J.; Lord, A. M.; Guittard, F.; Barron, A. R., Branched Hydrocarbon Low Surface Energy Materials for Superhydrophobic Nanoparticle Derived Surfaces. *ACS Appl Mater Interfaces* **2016**, *8* (1), 660-6.
27. Dong, L.-Y.; Zhu, Y.-J., A New Kind of Fireproof, Flexible, Inorganic, Nanocomposite Paper and Its Application to the Protection Layer in Flame-Retardant Fiber-Optic Cables. *Chemistry – A European Journal* **2017**, *23* (19), 4597-4604.
28. Elbasuney, S.; Mostafa, H. E., Synthesis and surface modification of nanophosphorous-based flame retardant agent by continuous flow hydrothermal synthesis. *Particuology* **2015**, *22*, 82-88.
29. Akaki, T.; Maehara, H.; Tooyama, M., Development of wood and wood ash-based hydroxyapatite composites and their fire-retarding properties. *Journal of Wood Science* **2012**, *58* (6), 532-537.
30. Costa, L.; Giordano, G.; Tagliaferri, S.; Caglieri, A.; Mutti, A., Polybrominated diphenyl ether (PBDE) flame retardants: Environmental contamination, human body burden and potential adverse health effects. *Acta bio-medica : Atenei Parmensis* **2009**, *79*, 172-83.
31. Takigawa, T.; Endo, Y., Effects of Glutaraldehyde Exposure on Human Health. *Journal of occupational health* **2006**, *48*, 75-87.
32. Yi, Y. D.; Ding, W.; Wang, Y. N.; Shi, B., Determination of Free Formaldehyde in Leather Chemicals. *Journal of the American Leather Chemists Association* **2019**, *114* (10), 382-390.
33. Kotthoff, M.; Müller, J.; Jüring, H.; Schlummer, M.; Fiedler, D., Perfluoroalkyl and polyfluoroalkyl substances in consumer products. *Environmental Science and Pollution Research* **2015**, *22* (19), 14546-14559.
34. Stoiber, T.; Evans, S.; Naidenko, O. V., Disposal of products and materials containing per- and polyfluoroalkyl substances (PFAS): A cyclical problem. *Chemosphere* **2020**, *260*, 127659.
35. Kissa, E., *Fluorinated Surfactants and Repellents, Second Edition*. Taylor & Francis: **2001**.
36. Sinclair, G. M.; Long, S. M.; Jones, O. A. H., What are the effects of PFAS exposure at environmentally relevant concentrations? *Chemosphere* **2020**, *258*, 127340.
37. ECHA, E. C. A., Perfluoroalkyl chemicals, <https://echa.europa.eu/it/hot-topics/perfluoroalkyl-chemicals-pfas>.
38. Letcher, R. J.; Chu, S.; Smyth, S.-A., Side-chain fluorinated polymer surfactants in biosolids from wastewater treatment plants. *Journal of Hazardous Materials* **2020**, *388*, 122044.
39. Bertanza, G.; Capoferri, G. U.; Carmagnani, M.; Icarelli, F.; Sorlini, S.; Pedrazzani, R., Long-term investigation on the removal of perfluoroalkyl substances in a full-scale drinking water treatment plant in the Veneto Region, Italy. *Science of The Total Environment* **2020**, *734*, 139154.
40. Tian, Y.; Yao, Y.; Chang, S.; Zhao, Z.; Zhao, Y.; Yuan, X.; Wu, F.; Sun, H., Occurrence and Phase Distribution of Neutral and Ionizable Per- and Polyfluoroalkyl Substances (PFASs) in the Atmosphere and Plant Leaves around Landfills: A Case Study in Tianjin, China. *Environmental Science & Technology* **2018**, *52* (3), 1301-1310.
41. Mastrantonio, M.; Bai, E.; Uccelli, R.; Cordiano, V.; Screpanti, A.; Crosignani, P., Drinking water contamination from perfluoroalkyl substances (PFAS): an ecological mortality study in the Veneto Region, Italy. *European Journal of Public Health* **2018**, *28* (1), 180-185.
42. Manea, S.; Salmaso, L.; Lorenzoni, G.; Mazzucato, M.; Russo, F.; Mantoan, D.; Martuzzi, M.; Fletcher, T.; Facchin, P., Exposure to PFAS and small for gestational age new-borns: A birth records study in Veneto Region (Italy). *Environmental Research* **2020**, *184*, 109282.
43. Latthe, S. S.; Sutar, R. S.; Kodag, V. S.; Bhosale, A. K.; Kumar, A. M.; Kumar Sadasivuni, K.; Xing, R.; Liu, S., Self – cleaning superhydrophobic coatings: Potential industrial applications. *Progress in Organic Coatings* **2019**, *128*, 52-58.
44. Ma, J.; Zhang, X.; Bao, Y.; Liu, J., A facile spraying method for fabricating superhydrophobic leather coating. *Colloids and Surfaces A: Physicochemical and Engineering Aspects* **2015**, *472*, 21-25.
45. Zhou, H.; Niu, H.; Gestos, A.; Lin, T., Robust, Self-Healing Superamphiphobic Fabrics Prepared by Two-Step Coating of Fluoro-Containing Polymer, Fluoroalkyl Silane, and Modified Silica Nanoparticles. *Advanced Functional Materials* **2013**, *23*, 1664-1670.
46. Xu, L.; Karunakaran, R. G.; Guo, J.; Yang, S., Transparent, Superhydrophobic Surfaces from One-Step Spin Coating of Hydrophobic Nanoparticles. *ACS Applied Materials & Interfaces* **2012**, *4* (2), 1118-1125.

47. Tang, W.; Huang, Y.; Meng, W.; Qing, F.-L., Synthesis of fluorinated hyperbranched polymers capable as highly hydrophobic and oleophobic coating materials. *European Polymer Journal* **2010**, *46* (3), 506-518.
48. Ye, H.; Zhu, L.; Li, W.; Liu, H.; Chen, H., Constructing Fluorine-Free and Cost-Effective Superhydrophobic Surface with Normal-Alcohol-Modified Hydrophobic SiO₂ Nanoparticles. *ACS Applied Materials & Interfaces* **2016**, *9* (1), 858-867.
49. Li, J.; Wan, H.; Ye, Y.; Zhou, H.; Chen, J., One-step process to fabrication of transparent superhydrophobic SiO₂ paper. *Applied Surface Science* **2012**, *261*, 470-472.
50. Wang, Z.; Yang, W.; Sun, F.; Zhang, P.; He, Y.; Wang, X.; Luo, D.; Ma, W.; Sergio, G.-C., Construction of a superhydrophobic coating using triethoxyvinylsilane-modified silica nanoparticles. *Surface Engineering* **2018**, *35* (5), 418-425.
51. Ahmad, D.; van den Boogaert, I.; Miller, J.; Presswell, R.; Jouhara, H., Hydrophilic and hydrophobic materials and their applications. *Energy Sources, Part A: Recovery, Utilization, and Environmental Effects* **2018**, *40* (22), 2686-2725.
52. Marmur, A., The Lotus Effect: Superhydrophobicity and Metastability. *Langmuir* **2004**, *20* (9), 3517-3519.
53. Li, X. M.; Reinhoudt, D.; Crego-Calama, M., What do we need for a superhydrophobic surface? A review on the recent progress in the preparation of superhydrophobic surfaces. *Chem Soc Rev* **2007**, *36* (8), 1350-68.
54. Wang, N.; Tang, L.; Tong, W.; Xiong, D., Fabrication of robust and scalable superhydrophobic surfaces and investigation of their anti-icing properties. *Materials & Design* **2018**, *156*, 320-328.
55. Zettlemoyer, A. C.; Hsing, H. H., Water on silica and silicate surfaces. III. Hexamethyldisilazane-treated silica surfaces. *Journal of Colloid and Interface Science* **1976**, *55* (3), 637-644.
56. European Food Safety Authority (EFSA), B. F. R. <https://www.efsa.europa.eu/en/topics/topic/brominated-flame-retardants>.
57. DIRECTIVE 2003/11/EC OF THE EUROPEAN PARLIAMENT AND OF THE COUNCIL of 6 February 2003, Amending for the 24th time Council Directive 76/769/EEC relating to restrictions on the marketing and use of certain dangerous substances and preparations (pentabromodiphenyl ether, octabromodiphenyl ether). *Official Journal of the European Union* **2003**.
58. Chen, X.; Guo, W.; Lei, L.; Guo, Y.; Yang, L.; Han, J.; Zhou, B., Bioconcentration and developmental neurotoxicity of novel brominated flame retardants, hexabromobenzene and pentabromobenzene in zebrafish. *Environmental Pollution* **2021**, *268*, 115895.
59. Zhao, X.; Chen, T.; Yang, B.; Wang, D.; Sun, W.; Wang, Y.; Yang, X.; Wen, S.; Li, J.; Shi, Z., Serum levels of novel brominated flame retardants (NBFRs) in residents of a major BFR-producing region: Occurrence, impact factors and the relationship to thyroid and liver function. *Ecotoxicology and Environmental Safety* **2021**, *208*, 111467.
60. Eze, C. T.; Michelangeli, F.; Otitolaju, A. A.; Eze, O. O.; Ibraheem, O.; Ogbuene, E. B.; Ogunwole, G. A., Occurrence of chemical pollutants in major e-waste sites in West Africa and usefulness of cytotoxicity and induction of ethoxyresorufin-O-deethylase (EROD) in determining the effects of some detected brominated flame retardants and e-waste soil-derived extracts. *Environmental Science and Pollution Research* **2020**.
61. Darnerud, P., Toxic effects of brominated flame retardants in man and in wildlife. *Environment International* **2003**, *29* (6), 841-853.
62. El-Shafei, A.; ElShemy, M.; Abou-Okeil, A., Eco-friendly finishing agent for cotton fabrics to improve flame retardant and antibacterial properties. *Carbohydrate Polymers* **2015**, *118*, 83-90.
63. Arslan, F.; Dilsiz, N., Flame resistant properties of LDPE/PLA blends containing halogen-free flame retardant. *Journal of Applied Polymer Science* **2020**, *137* (32), 48960.
64. Duan, B.; Wang, Q.; Wang, X.; Li, Y.; Zhang, M.; Diao, S., Flame retardance of leather with flame retardant added in retanning process. *Results in Physics* **2019**, *15*, 102717.
65. Jiang, Y.; Li, J.; Li, B.; Liu, H.; Li, Z.; Li, L., Study on a novel multifunctional nanocomposite as flame retardant of leather. *Polymer Degradation and Stability* **2015**, *115*, 110-116.
66. Shi, J.; Wang, C.; Ngai, T.; Lin, W., Diffusion and Binding of Laponite Clay Nanoparticles into Collagen Fibers for the Formation of Leather Matrix. *Langmuir* **2018**, *34* (25), 7379-7385.

67. Ingraio, C.; Vesce, E.; Evola, R. S.; Rebba, E.; Arcidiacono, C.; Martra, G.; Beltramo, R., Chemistry behind leather: Life Cycle Assessment of nano-hydroxyapatite preparation on the lab-scale for fireproofing applications. *Journal of Cleaner Production* **2021**, *279*, 123837.
68. Wei, G.; Ma, P., Structure and Properties of Nano-Hydroxyapatite/Polymer Composite Scaffolds for Bone Tissue Engineering. *Biomaterials* **2004**, *25*, 4749-57.
69. Nudelman, F.; Pieterse, K.; George, A.; Bomans, P.; Friedrich, H.; Brylka, L.; Hilbers, P.; With, G.; Sommerdijk, N., The role of collagen in bone apatite formation in the presence of hydroxyapatite nucleation inhibitors. *Nature materials* **2010**, *9*, 1004-9.
70. Kalita, S. J.; Bhardwaj, A.; Bhatt, H. A., Nanocrystalline calcium phosphate ceramics in biomedical engineering. *Materials Science and Engineering: C* **2007**, *27* (3), 441-449.
71. Lu, B.-Q.; Zhu, Y.-J.; Chen, F., Highly Flexible and Nonflammable Inorganic Hydroxyapatite Paper. *Chemistry – A European Journal* **2014**, *20* (5), 1242-1246.
72. Ershad-Langroudi, A.; Mirmontahai, A., Thermal analysis on historical leather bookbinding treated with PEG and hydroxyapatite nanoparticles. *Journal of Thermal Analysis and Calorimetry* **2015**, *120* (2), 1119-1127.

2. WATERPROOFING ASPECTS

2.1 MATERIALS AND METHODS

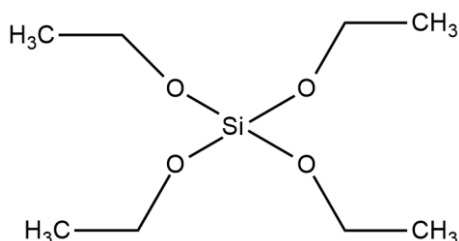
2.1.1 Materials

Different types of commercial nanoparticles, in a pristine or functionalized form, were used during this research work. The following materials were purchased from Evonik:

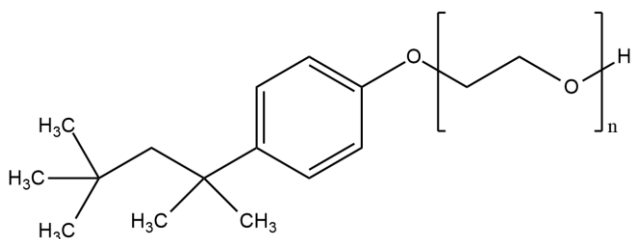
- *Aeroxide Alu C*, a highly dispersed fumed aluminum oxide, with high specific surface area and low water content. It was employed for the functionalization with a hydrophobic agent to obtain a hydrophobic surface.
- *Aeroxide Alu C 805*, a highly dispersed hydrophobic fumed aluminum oxide. It is functionalized with an unknown method using an organosilane (C8 type), in order to obtain a hydrophobic surface. This commercial hydrophobic material was employed for comparison with the functionalized alumina nanoparticles.
- *Aerosil OX50*, a hydrophilic pyrogenic silica, for the preliminary tests for the functionalization with APTS ((3-Aminopropyl) triethoxysilane).
- *Aerosil 300*, a hydrophilic fumed silica, used for the functionalization with hydrophobic agents to reach a high level of hydrophobicity.
- *Aerosil R 812 (AR812)*, high thickening fumed silica surface functionalized with HMDS (hexamethyldisilazane). It was employed for comparison with the functionalized silica nanoparticles.

The following reagents (purchased from Merck) were employed for the micro-emulsion synthesis of silica nanoparticles with controlled shape and size:

- *Tetraethyl orthosilicate (TEOS)*; siliceous precursor for nanoparticle synthesis, purity >97.5%, molecular weight of 208.33 g/mol.



- *TritonX-100*; laboratory grade, non-ionic surfactant, essential for the formation of micelles in the synthesis of silica nanoparticles. It has a molecular weight of 647 g/mol and it is a colourless viscous liquid.



- Other reagents (Merck) used in micro-emulsion synthesis are: *cyclohexane* (anhydrous, $\geq 99,5\%$) as non-polar phase and *deionized water* as polar phase; *n-hexanol* (anhydrous, $\geq 99\%$) used as co-surfactant and *ammonium hydroxide solution* (28% NH_3 in H_2O , $\geq 99,99\%$) as the basic catalyst for the initiation of the hydrolysis reactions of the siliceous precursor.

2.1.1.1. Synthesis of $m\text{-SiO}_2$

The following synthesis procedure proposed in the literature was used for the preparation of silica nanoparticles with a W/O microemulsion method.¹ 150 mL of cyclohexane, 36 mL of n-hexanol 37.7 g of Triton X-100 and 10.8 mL of deionized water were mixed and stirred at room temperature (r.t.) for 30 min, to form the microemulsion. Tetraethylorthosilicate (TEOS, 2 mL, 8.96 mmol) and NH_4OH (28-30%, 1.4 mL, 10.6 mmol) were added after 10 min of stirring, in order to start the hydrolysis and the condensation of TEOS. In this step micro-droplets of water are confined in the micelles of surfactant dispersed in the organic solvent, that is the majority component.

The system is dynamic, the droplets collide, merge and continuously reform in the order of nano/milliseconds; during this phase, the molecules dissolved in the micelles exchange. A first step involves the association of precursor molecules into the micelles, which begins with the formation of a small amount of the monosubstituted species that comes from the spontaneous hydrolysis of a -OR group (Fig. 2.1.1) and that is divided between the non-polar phase, where it is more soluble, and micelles.

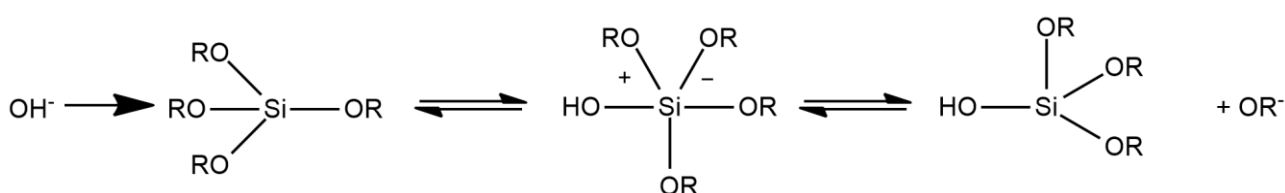
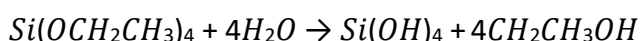
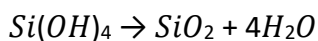


Figure 2.1.1. Mechanism of hydrolysis of a tetraalkoxysilane by nucleophilic substitution $\text{S}_{\text{N}}2$.

The intermediate has an amphiphilic character and tends to localize it at the level of the micellar wall, thus becoming more available for further hydrolysis reactions. Hydrolysis, after the formation of intermediate species, leads to the generation of tetrasubstituted monomer, silicic acid:



From this moment on, the hydrophilic species formed give way to condensation reactions, thus arriving at nucleation and growth processes:



Once reached a minimum concentration of monomers in the micelles, the nucleation phase begins, while the growth, which is a simultaneous process and in competition with nucleation, can occur by adding a monomer to an already formed nucleus or by condensation of two nuclei, with a mechanism both within the same micelle and between different micelles.

After 16h, addition of ethanol (80mL) stops the reaction and the precipitated nanoparticles are extracted and washed by cycles of centrifugation (10'000 rpm, 20 min, 25°C) and re-suspension with ethanol and deionized water, to remove surfactant molecules. This type of synthesis allows to obtain a fine control on the morphological and dimensional characteristics of the synthesized nanoparticles (called m-SiO₂), which are also well dispersed in water.

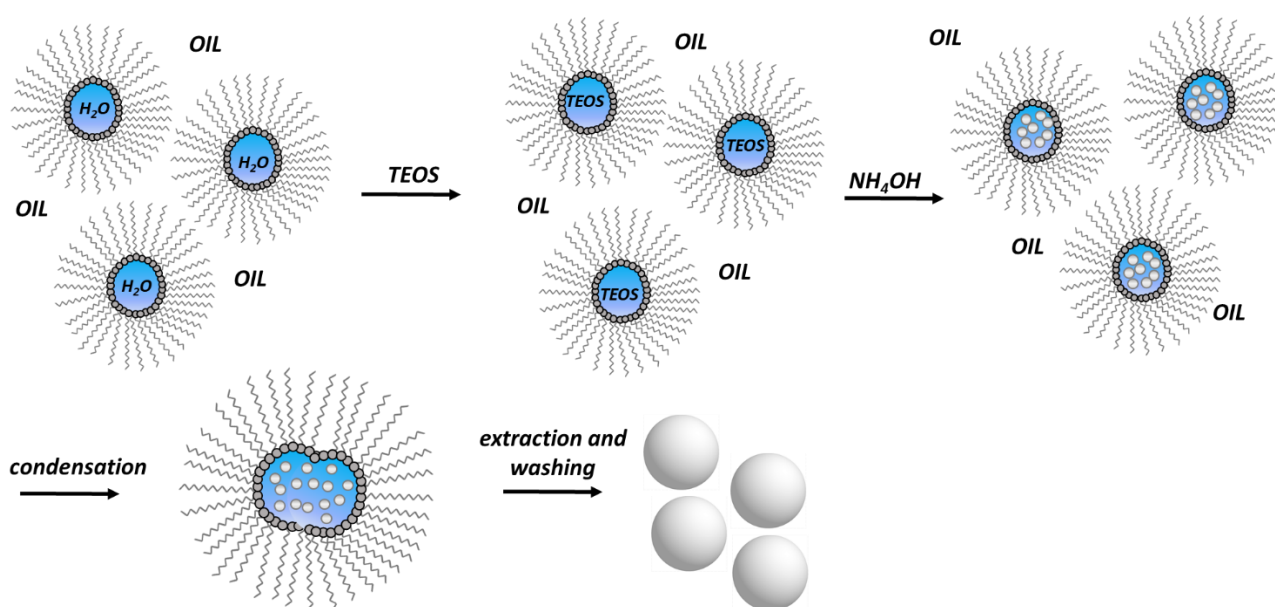


Figure 2.1.2. Scheme of the preparation of m-SiO₂ nanoparticles; hydrolysis occurs in the inverse W/O microemulsion in a basic environment and the nanoparticles are extracted after repeated washing cycles.

All the mentioned alumina and silica materials are in powder forms. The physico-chemical properties of interest for this work are reported in Table 2.1.1.

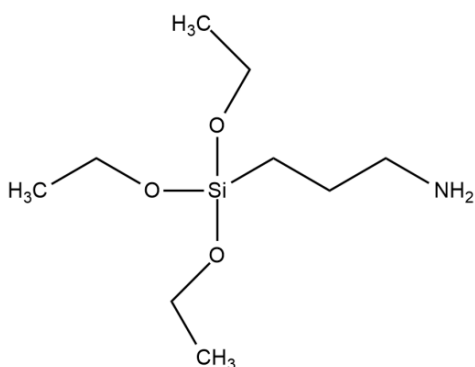
Table 2.1.1. Physico-chemical properties of alumina and silica materials used in this work.

Al_2O_3	SSA_{BET} (m^2/g)	Surface hydrophobic moieties density ($molec/nm^2$)	Mean size of primary particles (nm)
Alu C	100	–	13^2
Alu C 805	100	3	13^2

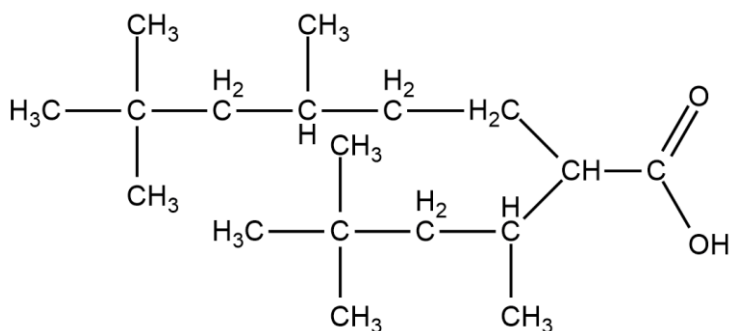
SiO_2	SSA_{BET} (m^2/g)	Surface silanol groups density ($SiOH/nm^2$) ²	Surface hydrophobic moieties density ($molec/nm^2$) ²	Mean size of primary particles (nm)
AOX50	50	1.6	–	40^3
A300	300	5.6	–	7^3
<i>m</i> - SiO_2	95	7.2	–	50
AR812	260	0.44^7	3.5^4	7^2

For the functionalization of nanoparticles different reagents were used:

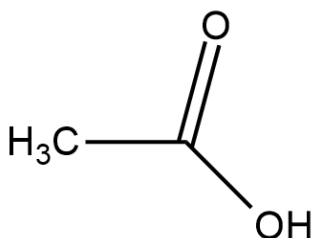
- (3-Aminopropyl)triethoxysilane (APTS, purity: 99%); nucleophilic reagent for surface functionalization of silica nanoparticles with amino groups ($-NH_2$); it was purchased by Merck; it has a molecular weight of 221.37 g/mol and a density of 0.946 g/ml.



- Isostearic acid (FINEOXOCOL); highly branched carboxylic acid ($iso-C_{17}H_{35}$)COOH; It was purchased from Nissan Chemical Corporation and the acid is a transparent, odorless and viscous liquid. The molecular weight is 284,4772 g/mol with a branching factor of 7.1. It was employed in the functionalization of alumina and silica nanoparticles for the hydrophobization of the surface.



- *Acetic acid* (glacial, $\geq 99.99\%$); it was purchased from Merck. It was used for the improvement of the hydrophobicity of the silica surface after functionalization with isostearic acid. The molecular weight is 60.05 g/mol.



- The following reagents and solvents for the reactions and washings were purchased from Merck: *N,N'*-Dicyclohexylcarbodiimide (99%), *N*-Hydroxysuccinimide (98%), hydrochloric acid (37%), *N,N*-Dimethylformamide (anhydrous, 99,8%) 2-propanol ($\geq 99\%$), ethanol (anhydrous), toluene (anhydrous, $\geq 99,8\%$) dichloromethane (anhydrous, $\geq 99,8\%$), methanol (anhydrous, $\geq 99,8\%$) and deuterated water (99.9 atom %D).

The *thionyl chloride* (97%), was purchased from Merck too, but it was subjected to a preliminary distillation for the purification, in order to avoid the presence of water during the reaction.

Milli-Q water was used for the functionalization, *distilled water* was used for washing.

For the sake of effectiveness and clarity, information on functionalization protocols used in this research work will be provided in the first part of the chapters dealing with each of them.

2.1.2 Methods

2.1.2.1 Infrared (IR) spectroscopy on non-functionalized and functionalized nanomaterials in controlled atmosphere

The bare and functionalized materials were pressed into self-supporting pellets, inserted in a gold frame, and then placed in properly designed cells equipped with CaF_2 windows for transmission measurements (Fig. 2.1.3). These can be connected to conventional high-vacuum lines allowing adsorption/desorption to be carried out *in situ*. The vacuum line consists of a system of Pyrex tubes connected to the pumping system that allows reaching a residual pressure of less than 10^{-5} mbar. The pumping system consists of a primary rotary pump and a turbomolecular pump connected in series.

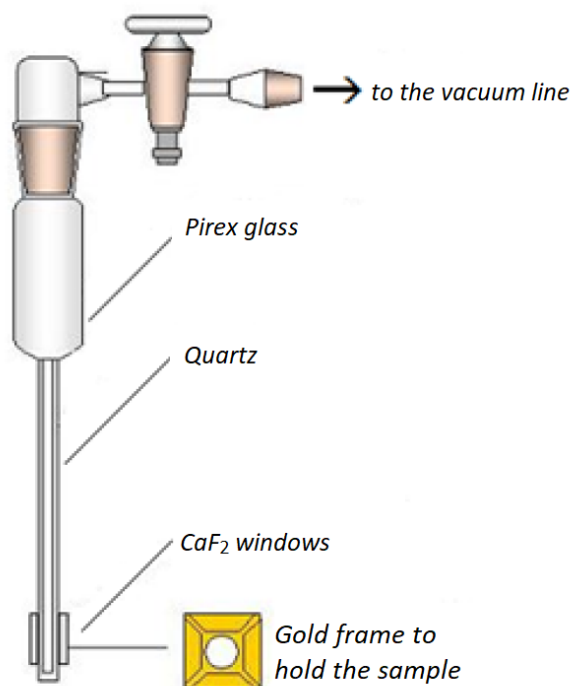


Figure 2.1.3. Scheme of vacuum cells for IR measurements in controlled atmosphere at room temperature.

The spectra were collected at beam temperature (b.t. ca. 323 K), in air and after outgassing that allows to remove water adsorbed on the surface, with a Bruker IFS28 spectrometer (resolution 4 cm^{-1} , DTGS detector), by accumulating 128 scans to obtain a good signal-to-noise ratio.

For silica, data were normalized to the intensity of the signals in the $2100\text{-}1700\text{ cm}^{-1}$ range due to a combination and overtone of vibration modes of bulk materials groups in order to render differences in intensity independent of differences in the thickness of the pellets. For comparative analysis of the intensity of surface species, the spectra of different materials were additionally normalized with respect to the specific surface area (SSA).

2.1.2.2 Attenuated Total Reflectance (ATR) IR spectroscopy - Cylindrical Internal Reflectance (CIR) cell

For the infrared analysis of isostearic acid (in liquid form) spectra were measured in ATR mode. ATR is based on the phenomenon of total internal reflection (Fig. 2.1.4) that occurs when an infrared beam enters a crystal with an angle of incidence at the interface greater than the critical angle. The interaction of the IR beam with a fully reflective surface causes the formation of an evanescent wave into the medium of lower refractive index (sample). The penetration depth depends on the wavelength, if the sample selectively absorbs radiation the beam loses energy at the wavelength at which the material absorbs. The crystals used in ATR cell have a very high refractive index and low solubility in water such as zinc selenide (ZnSe), germanium (Ge), and thallium/iodide (KRS-5), or carbon in the diamond crystalline form.⁵

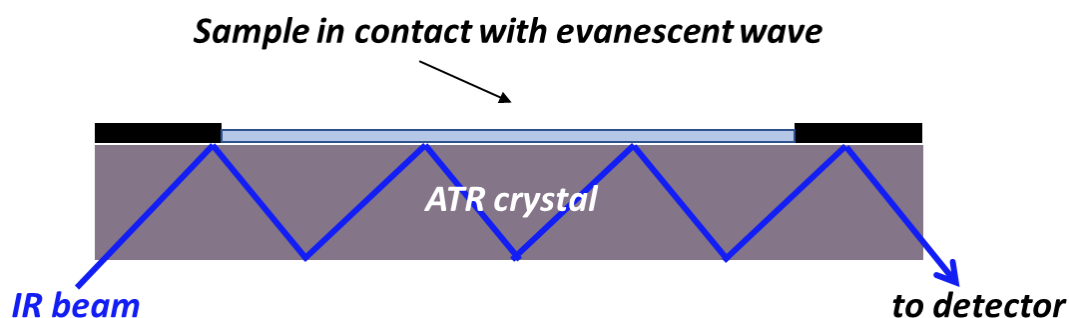


Figure 2.1.4. Schematic representation of a multiple reflection ATR system.

Spectra were collected with a Bruker IFS 28 spectrometer (resolution 4 cm^{-1} , MCT - Mercury Cadmium Telluride - detector) and a CIR cell was used for collection of the spectra (128 scans).

A Spectra Tech "CIRCLE" cell equipped with a zinc selenide⁵ crystal was used (Fig. 2.1.5). The evanescent wave extension represented by about $\frac{1}{2}$ of the incident λ , about $10\text{ }\mu\text{m}$. This has to be taken into consideration while filling the cell with the analyte. Practically, a suitable thickness for the ATR analysis corresponds to fill the cell covering the ZnSe crystal.

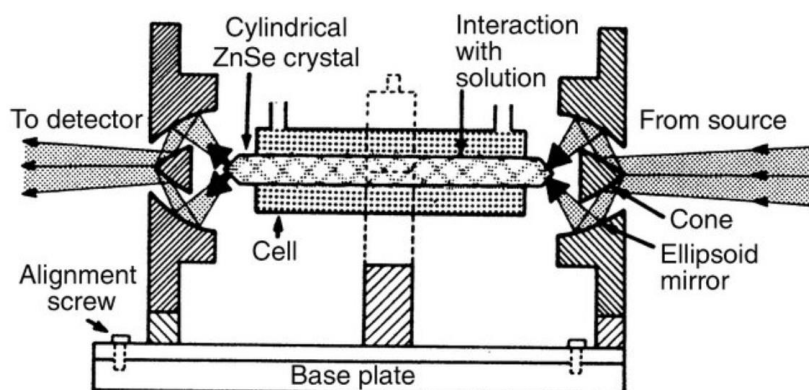


Figure 2.1.5. Scheme of the Cylindrical Internal Reflectance (CIR) cell.⁶

2.1.2.3 SS-NMR analysis

Solid-state NMR spectra were acquired with a Bruker Avance II 400 Ultra Shield instrument, operating at 400.23, 100.63 and 79.5 MHz, respectively for ^1H , ^{13}C and ^{29}Si nuclei.

For ^1H MAS spectra, the powder samples were packed into cylindrical zirconia rotors with a 2.5 mm outer diameter (o.d.) and a 14 μL volume. A certain amount of sample was collected from each batch and used without further preparations to fill the rotor. The spectra were acquired at room temperature at a spinning speed of 32 kHz using a depth sequence, with a 90° ^1H pulse of 2.5 μs , recycle delays of 1 or 4.5 s (for the sample A300-APTS-ISOST), a number of scans of 32 or 96 (for the sample A300-APTS-ISOST). The ^1H chemical shift scale was calibrated through the ^1H signal of external standard adamantane (at 1.87 ppm).

For ^{13}C and ^{29}Si spectra, the powder samples were packed into cylindrical zirconia rotors with a 4 mm o.d. and an 80 μL volume. A certain amount of sample was collected from each batch and used without further preparations to fill the rotor. ^{13}C CPMAS (Carbon-13 Cross-Polarization Magic Angle Spinning) spectra were acquired at room temperature at a spinning speed of 12 kHz, using a ramp cross-polarization pulse sequence with a 90° ^1H pulse of 3.6 μs , a contact time of 3 or 4 ms (for the sample A300-APTS-ISOST), an optimized recycle delay of 1.1 s, a number of scans in the range 63000-223000, depending on the sample. Direct-excitation ^{29}Si MAS spectra were acquired at room temperature at a spinning speed of 12 kHz, using a ^{29}Si 90° pulse of 6 μs , a recycle delay of 100 s and a number of scans in the range 600-1770, depending on the sample. The ^{13}C chemical shift scale was calibrated through the methylenic signal of external standard glycine (at 43.7 ppm). The ^{29}Si chemical shift scale was calibrated through the signal of external standard TMS (at 0 ppm).

2.1.2.4 Near-infrared spectroscopy

The study of the interaction, at molecular level, between water molecules and the nanoparticles surface (in pristine form or after functionalization) was carried out by Near-IR spectroscopy. The measurements were performed in diffuse reflectance mode, using a Varian Cary 5000 UV-Vis-NIR spectrophotometer equipped with an integrating sphere. The samples were put as a self-supporting pellet in a quartz cell directly connected to a vacuum line (residual pressure $<5 \times 10^{-4}$ mbar), in order to carry out the adsorption-desorption water sequences *in situ*. The spectra were recorded in the 8000-4000 cm^{-1} region.

2.1.2.5 Specific Surface Area (SSA_{BET}) and Thermogravimetric Analysis (TGA)

Specific surface areas were measured by N_2 adsorption-desorption isotherms at 77 K using a Micromeritics ASAP 2020 instrument and SSA was calculated by the Brunauer-Emmett-Teller (BET) method. Before measurements, the nanomaterials were outgassed at r.t until a residual pressure of ca. 0.02 mbar, for 10 hours.

TGA (TA Instruments SDT Q600) measurements were carried out on the commercial hydrophobic samples (AluC805 and AR812), in order to evaluate the grafting density of the hydrophobic molecules and on the functionalized samples (AluC-ISOST, A300-APTS and A300-APTS-ISOST) to confirm the grafting density calculated from the mixture method in IR measurements (see below). The samples were analysed in powder form and 10 mg aliquots were placed in the sample holder.

Measurements were performed under a constant air flux ($0.1 \text{ L}\cdot\text{min}^{-1}$) with a heating rate of $10 \text{ K}\cdot\text{min}^{-1}$ from 298 to 1273 K. The grafting density is calculated from equation (1):

$$\sigma^{graft} = \left(\frac{wt\%}{100 - wt\%} \right) \left(\frac{6.022 \cdot 10^{23}}{M_w \cdot SSA} \right) \quad (1)$$

Where $wt\%$ corresponds to the weight loss (%), calculated with the respect to the dry mass (that is subtracting the water loss measured below ca. $100 \text{ }^\circ\text{C}$); M_w is the mass weight of the functionalizing agents (g/mol); SSA is the specific surface area (m^2/g).

2.1.2.6 Microgravimetric and Adsorption Microcalorimetric Measurements

The microgravimetric measurements were carried out using a Hiden Intelligent Gravimetric Analyzer IGA002 instrument. The samples were introduced in the sample holder as broken pieces of a self-supporting pellet, heated at 30°C and outgassed overnight ($P \leq 10^{-4} \text{ mbar}$). The measurements were carried out admitting water vapour at 22 mbar, and then progressively decreasing the coverage and recording seven/eight pressure points. H_2O desorption/adsorption cycles were recorded twice for each sample (Fig. 2.1.6).

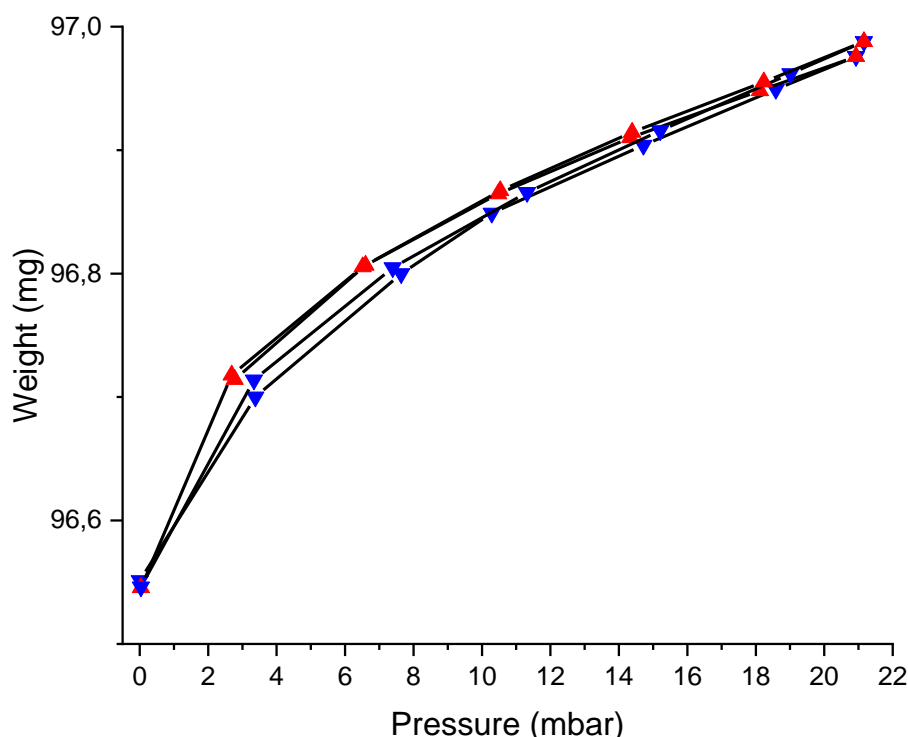


Figure 2.1.6. Example of microgravimetric measurements of water adsorption and desorption at 303K on silica. Isotherms with blue “>” are adsorption isotherms; red “<” are referred to desorption isotherms.

From each isotherms the number of water molecules per nm² at each pressure point are calculated. The average of the two measurements corresponds to the number shown in the histograms in the following (see chapter 2.4).

In order to calculate the heat of adsorption, microcalorimetric measurements were carried out using a heat-flow microcalorimeter (Calvet C80, Setaram, France) connected to a grease-free high-vacuum gas-volumetric glass apparatus (residual pressure $\leq 1 \times 10^{-6}$ Torr). The pressure was monitored by a Ceramicell 0-100 Torr gauge and a Ceramicell 0-1000 Torr gauge (by Varian), following a well-established procedure described in literature.⁷ Thanks to this procedure, it was possible to determine, for subsequent small increments of water, both adsorbed amounts (n_a) and integral heats evolved ($-Q_{int}$), as a function of the increasing equilibrium pressure. The calorimetric outputs ($-Q_{int}$) were converted into the differential enthalpy ($-q^{diff}$); the differential-heat plots were obtained by taking the middle point of the partial molar heats ($\Delta Q_{int}/\Delta n_a$, kJmol⁻¹) vs. n_a , the individual adsorptive doses, in order to evaluate the energy of interaction of the water molecules with the adsorption sites. The samples were introduced in a quartz cell as pieces of broken self-supporting pellets, connected to the vacuum line of the instrument for the activation under vacuum, at 30°C, overnight. Then the measurements were carried out *in situ*, admitting water vapor until 10 mbar, a conservative value for an effective use of the perfect gas law for data analysis.

2.1.2.7 Contact Angle Measurements

The contact angle measurements were performed to estimate the hydrophilicity/hydrophobicity of the studied materials. The experiments were carried out using a Kruss DSA100 instrument, through the sessile drop method (static contact angle) on self-supporting pellets of materials, pressed at ca. 1 ton. In order to perform reproducible measurements, the surface of the pellet should be as homogeneous as possible; therefore, the pellets were left under pressure for five minutes and then removed from the metal disks. The contact angle was measured by the Laplace-Young model using a drop shape analysis program, DSA3. The amount of water deposited on the surface for the measurement is $\sim 5 \mu\text{l}$.

2.1.2.8 FESEM

The images of the materials were acquired using a FEG-SEM S9000 by Tescan. The measurements were performed with a Schottky emitter, using a resolution of 0.7 nm at 15 keV and 1.4 nm at 1 keV; the probe current was setting at 10 pA and the electron beam energy at 5 keV. The analyses were carried out with an in-beam SE detector. The samples of pristine and functionalized nanomaterials were placed in the sample holder as self-supporting pellets as for contact angle measurements. The leather samples (ca. 1x1 cm) were analysed, for each treated leather sample, in different part: the grain, that is the exposed surface, the flesh, that is the back surface and the section, that represents the internal part of the sample.

Bibliographic References

1. Santra, S.; Zhang, P.; Wang, K.; Tapeç, R.; Tan, W., Conjugation of Biomolecules with Luminophore-Doped Silica Nanoparticles for Photostable Biomarkers. *Analytical Chemistry* **2001**, *73* (20), 4988-4993.
2. Bera, O.; Jovičić, M.; Pavličević, J.; Pilić, B., The influence of oxide nanoparticles on the kinetics of free radical methyl methacrylate polymerization in bulk. *Polymer Composites* **2013**, *34* (8), 1342-1348.
3. Petzold, G.; Rojas, R.; Mende, M.; Schwarz, S., Application Relevant Characterization of Aqueous Silica Nanodispersions. *Journal of Dispersion Science and Technology* **2009**, *30*, 1216-1222.
4. Degussa AG, D., Technical Bulletin Fine Particles. No. 18,. **1987**.
5. Stuart, B., *Infrared Spectroscopy*. John Wiley & Sons: **2015**; pp. 1-18.
6. Leclerc, D., Fourier Transform Infrared Spectroscopy in the Pulp and Paper Industry. In *Encyclopedia of Analytical Chemistry*, Meyers, R. A., Ed. John Wiley & Sons: **2000**; pp. 8361-8388.
7. Bolis, V.; Busco, C.; Aina, V.; Morterra, C.; Ugliengo, P., Surface Properties of Silica-Based Biomaterials: Ca Species at the Surface of Amorphous Silica As Model Sites. *The Journal of Physical Chemistry C* **2008**, *112* (43), 16879-16892.

2.2 THE FUNCTIONALIZATION OF ALUMINA NANOPARTICLES: AN EXISTING PROTOCOL AS THE STARTING POINT

2.2.1 Procedure of functionalization

The starting point of this first part of the research work was to reproduce an existing procedure reported in literature¹ based on the functionalization of alumina nanoparticles with a hydrophobic molecule, the isostearic acid, hereafter referred to as ISOST. The advantages are the commercial availability of nanomaterials (Aeroxide Alu C, Evonik), a functionalization method already developed at laboratory scale, and the possibility to carry out the applicative tests on leather samples (see chapter 2.6).

Different tests were carried out, starting from literature works, to optimize the functionalization procedure.^{2, 3} The investigated parameters were the amount of alumina nanoparticles (AluC) and ISOST used, temperature and time of the reaction (Table 2.2.1).

Table 2.2.1 Different parameters for the optimization of the functionalization of AluC with ISOST. The amount of isostearic acid was calculated by a molar ratio of 10:1 (470 mg) or 20:1 (940 mg) between ISOST and AluC, starting from the amount required to cover the surface with 1 ISOST/nm².

	Alumina NPs (gr)	Isostearic Acid (mg)	Toluene (mL)	Temperature (°C)	Time (hours)
1	1	470 (10:1)	100	125	16
2	1	470 (10:1)	100	125	96
3	1	940 (20:1)	100	125	16
4	1	940 (20:1)	50	125	16
5	2	940 (20:1)	200	125	16

Thermogravimetric analysis showed no significant differences in terms of grafting density in the different tests (see below). Procedure '5' was thus selected, as most effective in terms of time saving and amount of produced material from one batch. The equipment (Fig. 2.2.1) is composed of a round bottom flask, heated by a heating mantle, and connected to a condenser, cooled by water.

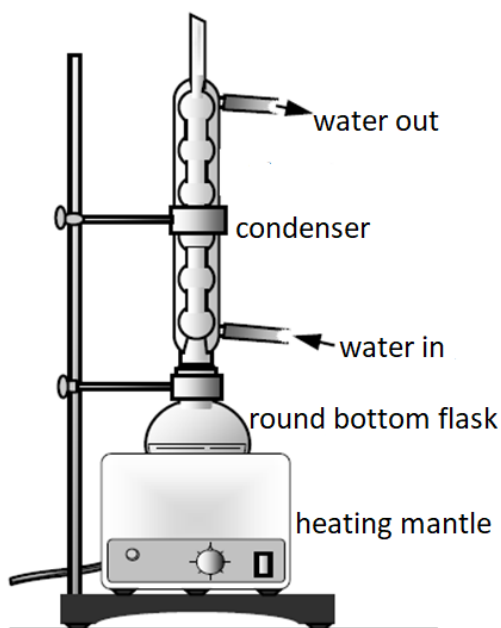


Figure 2.2.1. Reflux apparatus for the functionalization of AluC with ISOST.

AluC nanoparticles were put in the round bottom flask and refluxed overnight at $T=125^{\circ}\text{C}$ in toluene with ISOST. The functionalized nanoparticles (AluC-ISOST) were then centrifuged and washed in order to remove the excess of reagent and solvent with 2-propanol (2x50 mL, 10000 rpm, 10') and ethanol (1x50 mL, 10000 rpm, 10'); the washed nanoparticles were dried in oven at 50°C , overnight.

2.2.2 Study of isostearic acid carboxylic groups: $-\text{COOH}$ and $-\text{COO}^-$ forms

Before starting with the study of the interaction between ISOST and alumina surface, the spectra of ISOST functional groups in the $-\text{COOH}$ and $-\text{COO}^-$ form are reported, for comparison. The purpose of acquiring the spectrum of the isostearate form (COO^-) is to reproduce the mechanism of interaction between the molecule and the surface (alumina), that could act as a base towards the carboxylic groups of ISOST.

The spectrum of ISOST in the $-\text{COOH}$ form was acquired using the CIR cell as described in the chapter 2.1. On the other hand, for the isostearate form, the pH of the aqueous solution was brought to 12 adding NaOH, in order to deprotonate the carboxylic groups. The detailed assignment of bands appearing in the spectra is reported in Table 2.2.2 (see below).

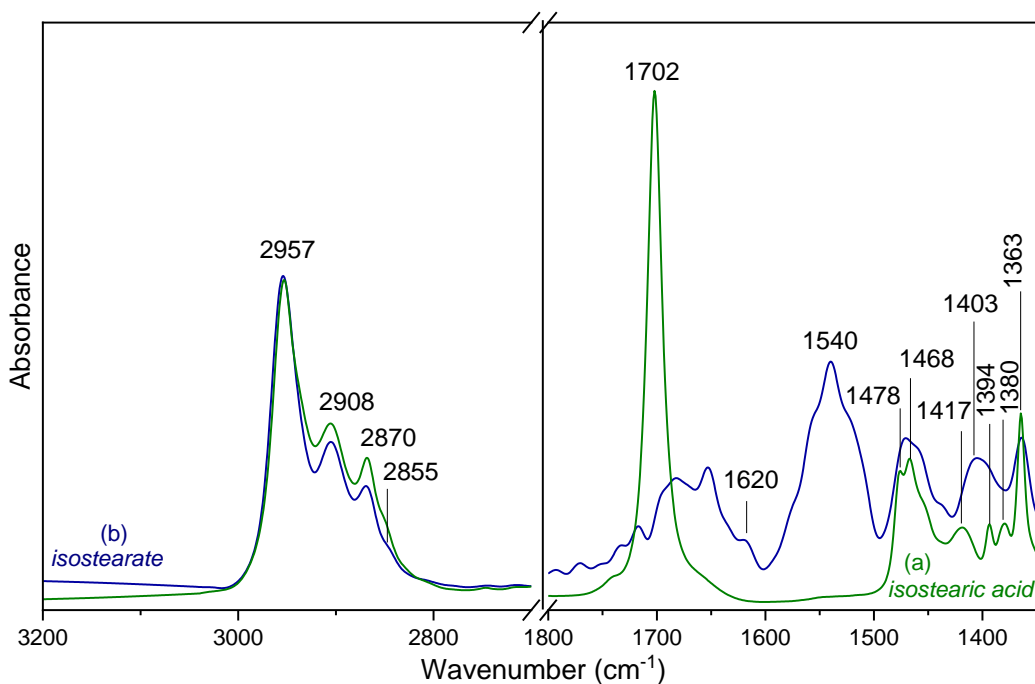


Figure 2.2.2. IR spectra of ISOST in the pure liquid form (isostearic acid, green spectrum (a)) and in basic aqueous solution (isostearate, blue spectrum (b)) in the 3200-1350 cm^{-1} range.

Focusing on the spectra of ISOST in the acid and isostearate forms, signals due to $-\text{CH}_x$ stretching (ν 3000-2800 cm^{-1}) and bending (δ , 1500-1350 cm^{-1}) modes appear almost equivalent in the two cases, whereas the main, expected difference is in the features due to the functional group. In the case of $-\text{COOH}$ form (spectrum a), the band at 1702 cm^{-1} is due to $\nu\text{C}=\text{O}$ mode, and the combination of the deformation (δ) mode of the $-\text{CH}$ moiety in α position to the carboxylic group with the $\delta\text{-COH}$ one results in the broad signal at 1417 cm^{-1} . Passing to the spectrum of the isostearate form (spectrum b), signals at 1540 and 1403 cm^{-1} are assignable to the asym and sym νCOO^- modes, respectively, while the broad and complex features spread over the 1700-1600 cm^{-1} range can be ascribed to the $\nu\text{C}=\text{O}$ mode of undissociated carboxylic groups (in equilibrium with the deprotonated ones)¹ H-bonded with water molecules and/or interacting with Na^+ cations introduced with the base. In both cases the interaction results in a decrease of the $\nu\text{C}=\text{O}$ frequency and the presence of a rich series of sub-bands can be related to local heterogeneity in solvation of both $-\text{COOH}$ moieties and $-\text{COOH}\cdots\text{Na}^+$ adducts.

2.2.3 First evidence of the presence of ISOST on alumina surface: IR spectroscopy

Information on chemical bonding of ISOST to AluC nanoparticles was obtained by IR spectroscopy. In order to verify the complete/incomplete desorption of water molecules initially adsorbed on the sample, a pellet of alumina outgassed at r.t., was exposed to isotopic exchanges with deuterated water by repeated cycles of adsorption/desorption of 20 mbar of D_2O vapour until the invariance of the IR spectra. After such a procedure, the complex absorption band due to stretching mode of O-

¹ The pKa of isostearic acid is 4.8 ± 0.5 ; the emulsion was prepared at $\text{pH}=12$, but it is possible to find also the carboxylic form of the acid, not completely deprotonated in the basic solution, due to the low solubility of ISOT and consequent difficulty in the formation of a stable emulsion.

H bond is shifted to lower frequency because of the isotopic exchange with an atom having a heavier mass ($2750\text{--}2000\text{ cm}^{-1}$) (Fig. 2.2.3).

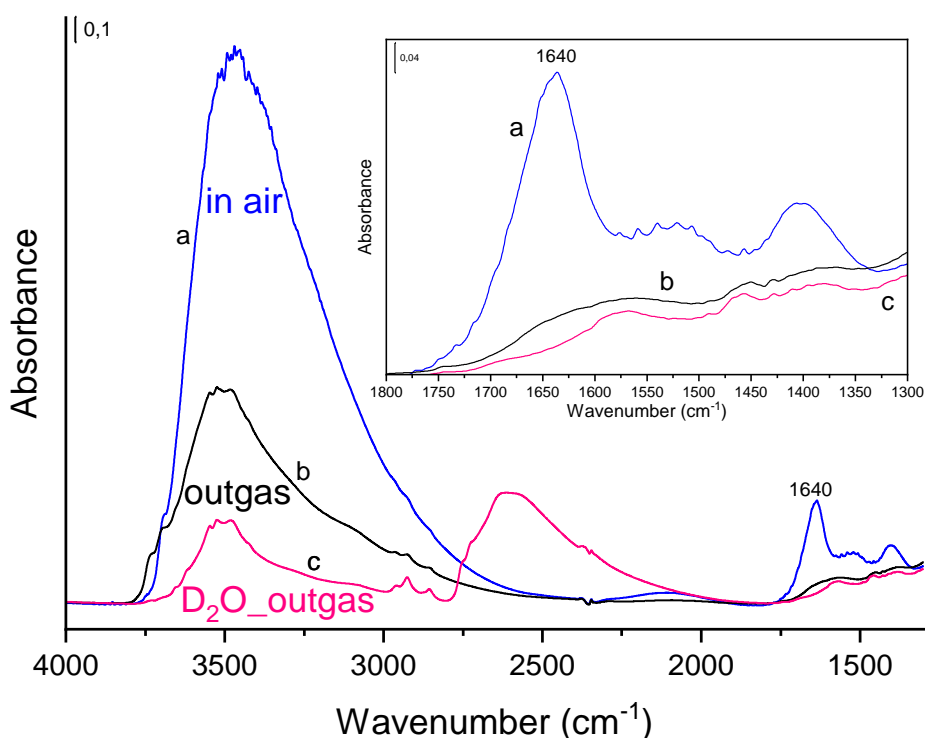


Figure 2.2.3. IR spectra of pristine alumina, AluC: a) spectrum in air; b) outgassed at beam temperature (ca. $50\text{ }^{\circ}\text{C}$); c) after H/D exchange and outgassing.

The zoomed inset between 1750 and 1530 cm^{-1} containing the bending mode of water is reported in the Fig. 2.2.3. For alumina, δHOH of adsorbed water molecules falls at 1640 cm^{-1} , clearly visible in spectrum a; after the H/D exchange (spectra b and c) and consequent outgassing a notable amount of the water band is removed, witnessing the presence of irreversibly adsorbed water on the surface.

After these considerations, the study of the interaction between AluC and ISOST was carried out. The detailed assignment of signals appearing in the spectra (Fig. 2.2.4) is reported in Table 2.2.2.

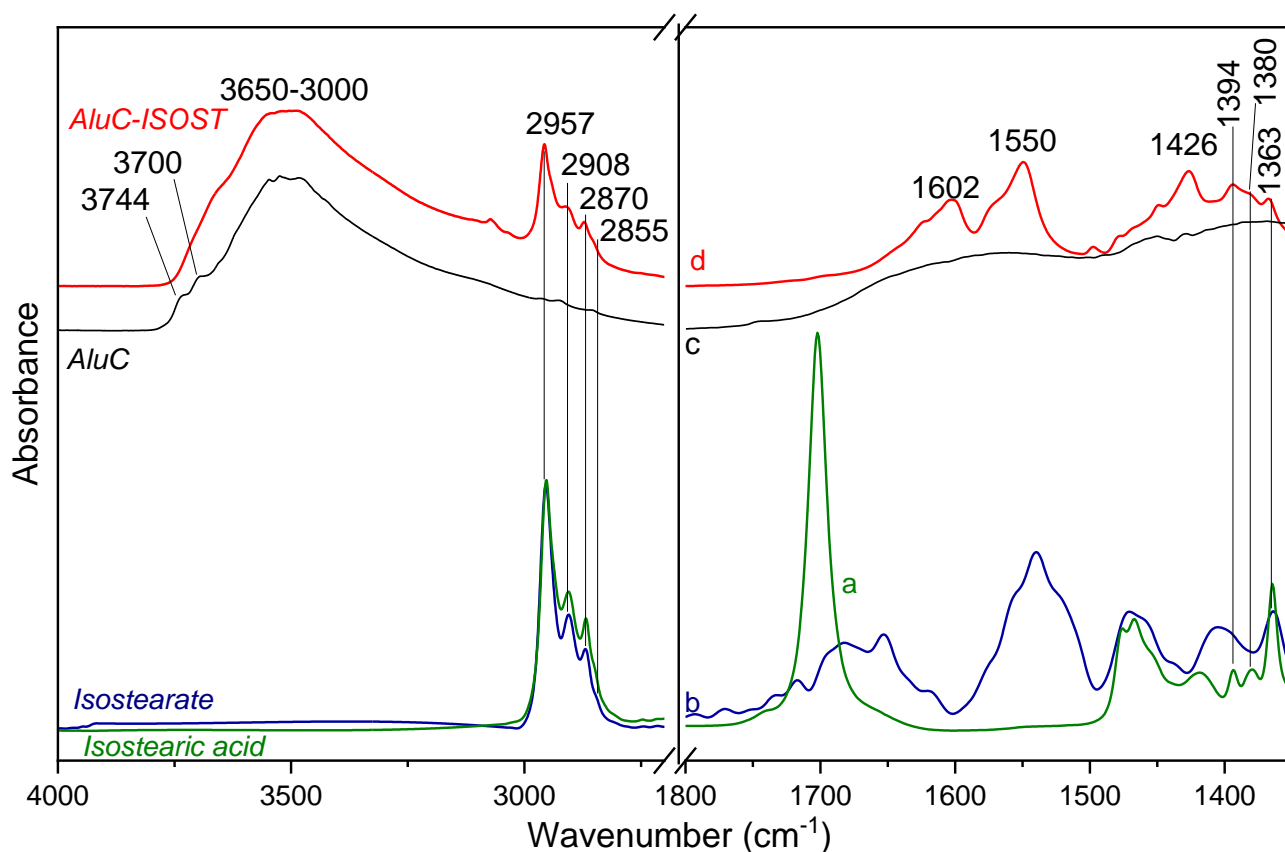


Figure 2.2.4. IR spectra of isostearic acid (green spectrum, a), isostearate (blue spectrum, b), Alu C (black spectrum, c) and AluC-ISOST (red spectrum, d), and in the 4000-1350 cm^{-1} range.

The only IR features related to surface species present in the spectrum of Al_2O_3 Alu C outgassed at b.t. (curve c) are a broad band spanning over the 3650-3000 cm^{-1} range, due to the O-H stretching mode (ν_{OH}) of H-bonded surface hydroxy groups, and definitely weaker components at ca. 3700 and 3737 cm^{-1} , due to the surface OH experiencing inter-groups interactions as weaker as higher the frequency is. After functionalization with ISOST (curve d), a depletion of the weak component at ca. 3737 cm^{-1} occurs, and a rich series of signals due to the organic molecules grafted on the surface appears. The set of signals in the 3000-2800 cm^{-1} range, due to $-\text{CH}_3$ and $-\text{CH}_2$ stretching modes, seems almost coincident with those in the spectra of ISOST in both acid and isostearate forms (spectra a and b), in agreement with the scarce sensitivity of these modes to the states of alkyl chains. At lower frequency, the δCH_x pattern is less defined, because of overlapping with a broad feature, with a better-defined component at 1426 cm^{-1} , assignable to the ν_{sym} mode of $-\text{COO}^-$ groups coordinated to surface Al^{3+} ions, with the ν_{asym} mode being responsible for the bimodal pattern in the 1650-1500 cm^{-1} range. Owing to the dependence of the $\nu_{\text{asym}}-\nu_{\text{sym}}$ splitting of $-\text{COO}^-$ groups on their coordinative structure,⁴ the multiplicity of both ν_{asym} and ν_{sym} $-\text{COO}^-$ components indicate the occurrence of a variety of grafting structures. Nevertheless, the better definition of the component at 1426 cm^{-1} seems to mirror that of those at 1550 and 1602 cm^{-1} . Depending on the pairing (1602 and 1426 cm^{-1} , or 1550 and 1426 cm^{-1} , disambiguation is not possible with the present data), the $\nu_{\text{asym}}-\nu_{\text{sym}}$ splitting can be 176 or 124 cm^{-1} . Both these values are close to 137 cm^{-1} obtained

for isostearate in aqueous solution, suggesting the presence of carboxylate groups forming bridging complexes with surface Al^{3+} ions (Fig. 2.2.5), in addition to other possible structures.

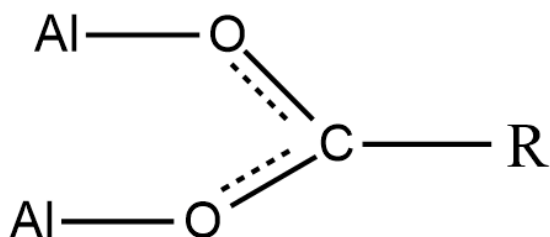


Figure 2.2.5. Scheme of bridging complex between alumina surface and isostearic acid.

Finally, the presence of $-\text{COO}^- \cdots \text{Al}^{3+}$ adducts implies the transfer to surface basic oxygen atoms of protons of pristine $-\text{COOH}$ groups. The resulting new surface OH groups should be responsible for the increase in intensity of the broad signal in the $3650\text{-}3000\text{ cm}^{-1}$ range, as well as for the depletion of the weak component at ca. 3737 cm^{-1} , because of their protonation (if basic), or by H-bonding with the newly formed surface hydroxyl groups.

Table 2.2.2 List of main IR signals and related assignment.

<i>Bands positions (cm⁻¹) in the IR spectra of</i>				<i>Band Assignment</i>
<i>AluC</i>	<i>AluC-ISOST</i>	<i>Isostearate</i>	<i>Isostearic acid</i>	
3737 and 3700				vOH (isolated) ⁵
3650-3000	3650-3000			vOH (H-bonded) ⁵
	2957	2957	2957	v _{asym} CH ₃ ⁶
	2908	2908	2908	v _{asym} CH ₂ ⁴
	2870	2870	2870	v _{sym} CH ₃ ⁴
	2855	2855	2855	v _{sym} CH ₂ ⁴
		1685-1675	1702	vC=O ⁴
		1620		δOH (water) ⁵
	1602			v _{asym} COO ⁻ (unidentate structure) ⁵
	1550	1540		v _{asym} COO ⁻ (bridging structure) ⁵
	1478		1478	δCH ₂ close to C-(CH ₃) ₃ ⁴
	1468	1468	1468	δ _{sym} CH ₃ in C-CH ₃ ⁴
	1450	1450	1450	δCH ₂ ⁴
	1426	1403		v _{sym} COO ⁻⁵
			1417	δCOH+δCH ⁴
	1394	1394	1394	δ _{sym} CH ₃ in C-(CH ₃) ₃ ⁴
	1380	1380	1380	δ _{sym} CH ₃ in C-CH ₃ ⁴
	1363	1363	1363	δ _{sym} CH ₃ in C-(CH ₃) ₃ ⁴

2.2.4 The grafting density through IR spectroscopy using a non-conventional mixture method and confirmation from TGA – evaluation of the hydrophobicity with contact angle measurements

Usually, the grafting density is calculated with a specific equation, taking into consideration the weight loss with TGA (see section 2.1.2.5). This method is applicable when the decomposition temperature of the molecules of interest is far from the other organic species present on the sample. In the AluC-ISOST sample, the TGA gives good results since the ISOST is the only organic compound at the surface. On the other hand, in the case of functionalized silica (see below, section 2.3.5), overlapping events related to different organic species on the samples are present and thus, it is not possible to evaluate properly the weight loss related to ISOST.

For the sake of comparative analysis with silica, a new way to estimate the extent of surface coverage using infrared spectroscopy was put forward. The strategy is based on a mixture of AluC nanoparticles with an amount of ISOST calculated as number of molecules per nm^2 , to obtain a sort of calibration curve to quantify the molecules present at the surface by infrared spectroscopy.

The alumina nanoparticles were placed in a solution of isostearic acid of known concentration and ethanol, in order to put together “mechanically” the surface and the molecules. The mixture was dried and then a self-supporting pellet was prepared for IR analysis.

The focus was on the stretching region of aliphatic chains ($3000\text{-}2800\text{ cm}^{-1}$) since these signals are related only to the alkyl chains of ISOST; moreover, this region is free from other vibrational modes. Different mixtures of alumina nanoparticles and isostearic acid at different molar ratios were prepared as a “calibration line”: 0.1, 0.6 and 1 ISOST/ nm^2 . In this way, it is possible to compare, in this region, the intensity of the AluC-ISOST signals.

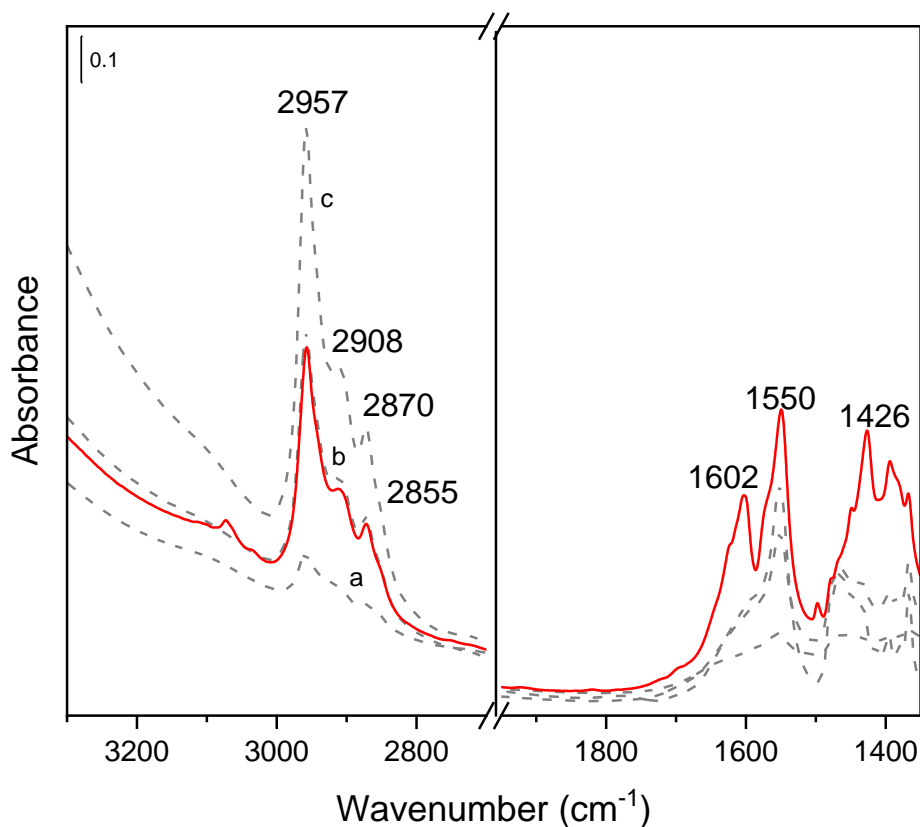


Figure 2.2.6 IR spectra of Alu C-ISOST (red spectrum) and the mixtures (grey spectra): 0.1/ mm^2 (spectrum a), 0.6/ mm^2 (spectrum b) and 1/ mm^2 (spectrum c).

The Fig. 2.2.6 shows the series of mixtures spectra (grey spectra: a, b and c), compared to the spectrum of AluC-ISOST after functionalization (red spectrum). The lower frequency region ($1950\text{--}1350\text{ cm}^{-1}$) witnesses the different interaction of the ISOST with alumina nanoparticles: the coordination modes already explained for AluC-ISOST are not present in the mixtures spectra, where the mechanical action does not produce any type of interaction between molecules and the surface. On the other side, the most interesting region falls between 3000 and 2750 cm^{-1} . The stretching modes of aliphatic chains of ISOST are proportional to the amount of isostearic acid on the surface. The spectrum of 0.6 ISOST/nm^2 (grey spectrum, b) is overlapped to the spectrum of AluC-ISOST. In order to see clearly this zone, the H/D exchange allows to obtain a better baseline, since it reduces the broad band of the stretching modes of OH groups ($3700\text{--}3100\text{ cm}^{-1}$) that can affect the slope of the $3000\text{--}2800\text{ cm}^{-1}$ region.

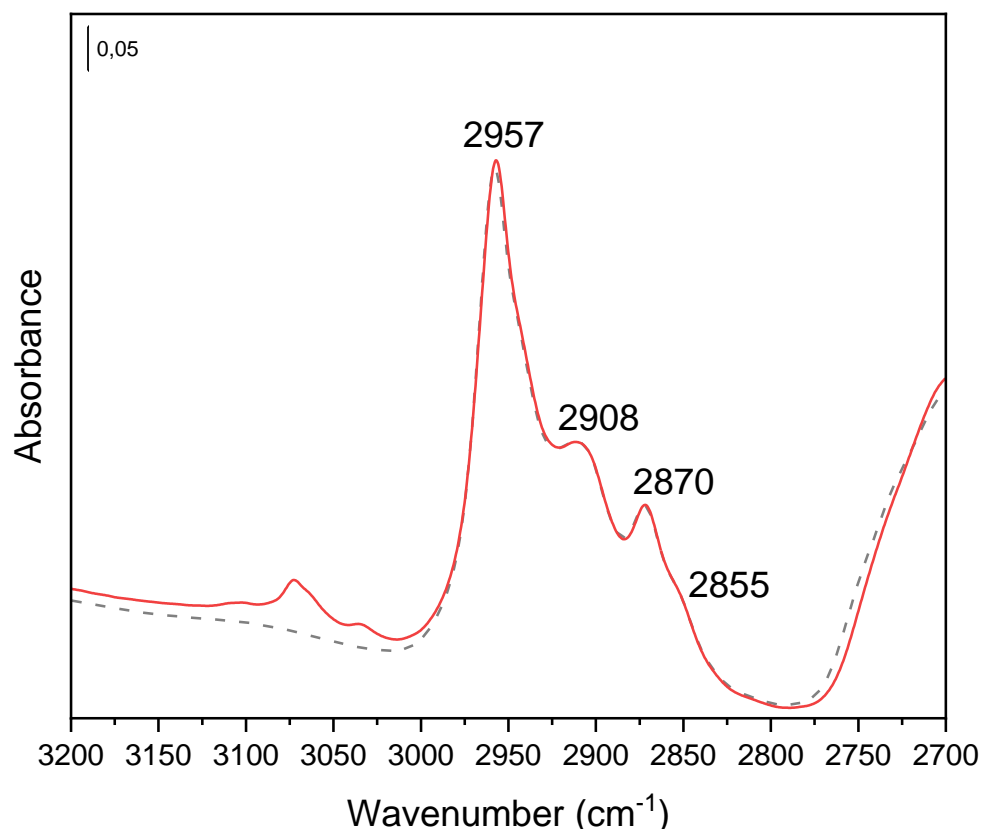


Figure 2.2.7 IR spectra of Alu C-ISOST (red spectrum) and the $0.6/\text{nm}^2$ (grey spectrum) after H/D exchange.

The good match between the two spectra (Fig. 2.2.7) allows to estimate the amount of ISOST in $0.6/\text{nm}^2$.

Moreover, this value was confirmed by thermogravimetric analysis. The TGA on dried samples was made to detect the presence and the amount of isostearic acid on the surface of alumina nanoparticles through weight loss obtained in a controlled atmosphere.

The analyses were carried out on all 5 batches referred to different tests in Tab. 2.2.1. The thermograms obtained gave in all cases a very similar result, and it was a further confirmation in the choice of the protocol that provided for a lower consumption of reagents and with a shorter reaction time (n. 5). Only the thermogram of the latter protocol for the estimation of the amount of ISOST is shown in Fig. 2.2.8.

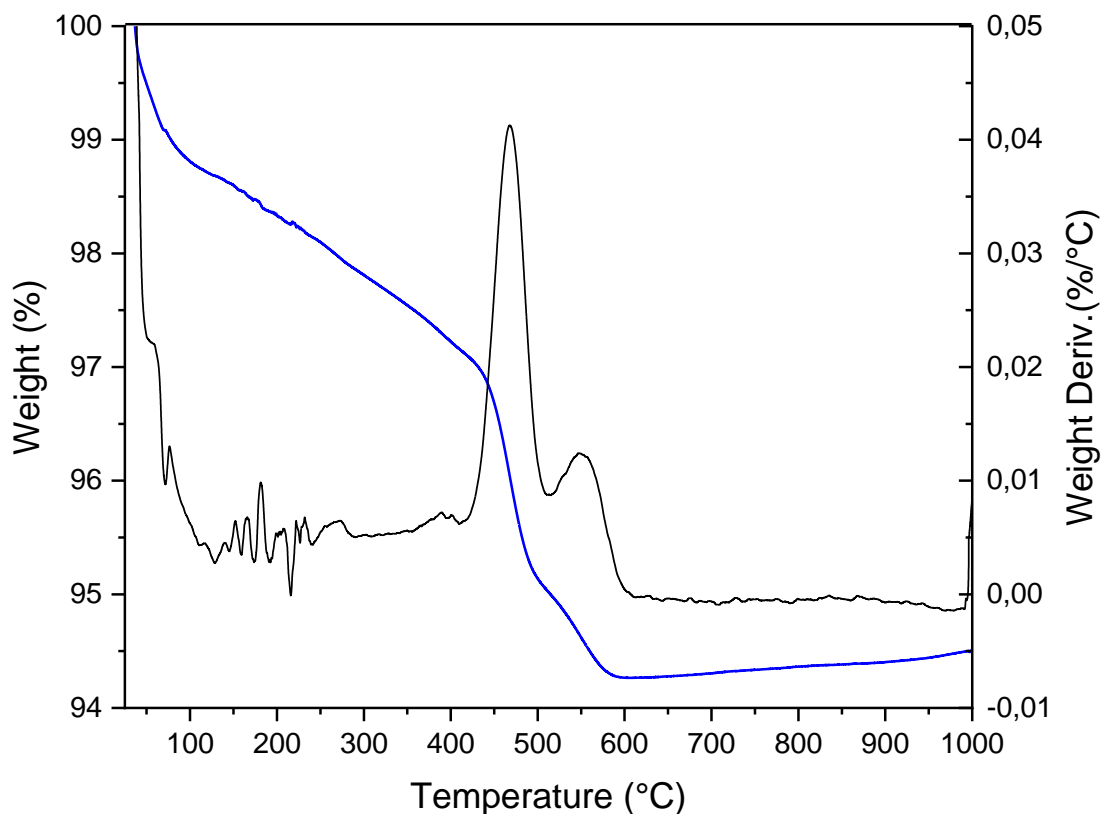


Figure 2.2.8 Thermogravimetric analysis (TGA) of AluC-ISOST. The thermogram and the corresponding derivative of the weight loss (%/°C) are reported.

The first weight loss is due to water (around 90-100°C); the second one is referred to ISOST. The grafting density is calculated from (1).

The weight loss *wt%*, not considering the water loss at the beginning of the measurement, is 2.9 %. *M_w* is the mass weight of the functionalized agents, 284,4772 g/mol and *SSA* is the specific surface area that corresponds to 91 m²/g. The grafting density results in 0.6/nm², confirming the value found in the IR analyses using mixture method.

After the characterization, at molecular level, of the functionalized alumina nanoparticles, the attention was drawn on the macroscopic aspect, evaluating the hydrophobicity of the sample. The contact angle measurements (CA) were carried out on thick self-supporting pellets with homogeneous surfaces, comparing the contact angle before and after functionalization with ISOST (Fig. 2.2.9).

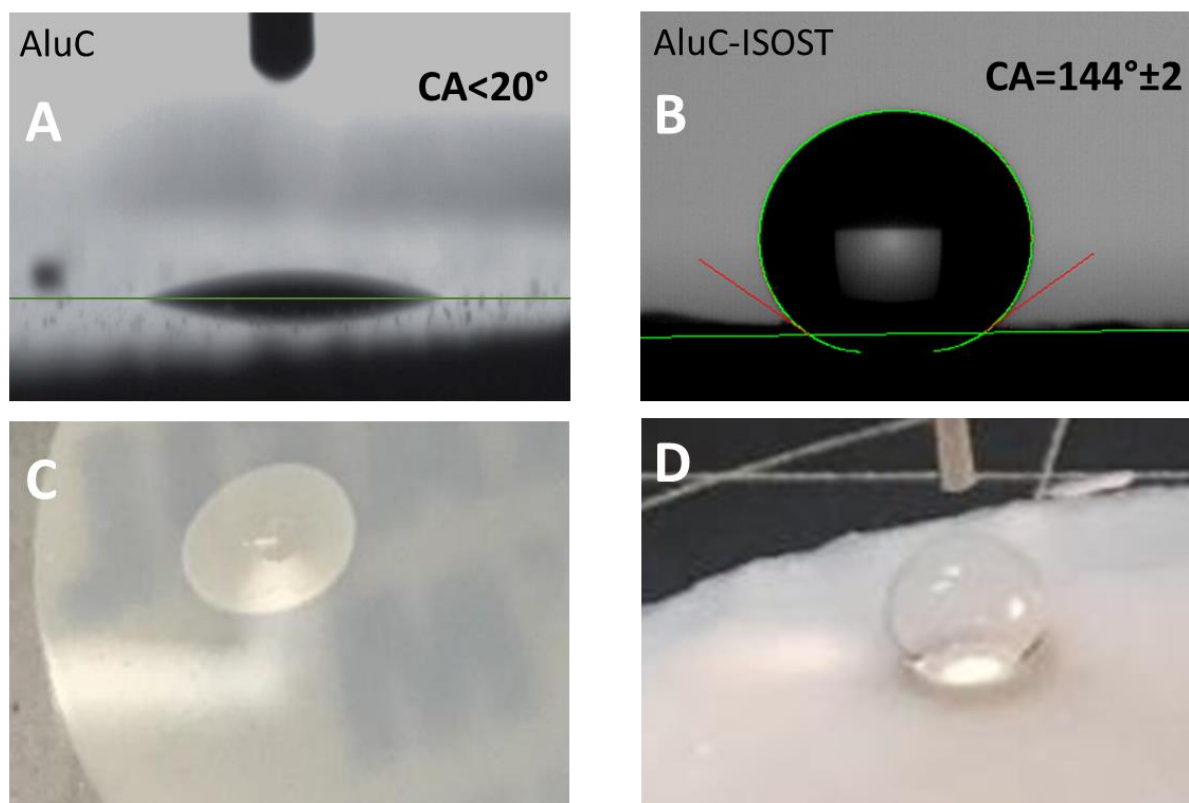


Figure 2.2.9. Contact angle measurements of AluC (panel A) and AluC-ISOST (panel B) with the real photos of the deposited droplets, respectively in panel C and D.

The angle between a water droplet and pristine alumina surface is barely detectable due to high hydrophilicity of the material ($\sim 20^\circ$) and the adsorption is immediate, as shown in Fig. 2.2.9, panel A and C. The functionalization with a hydrophobic molecule (ISOST) allows it to reach a high level of hydrophobicity (Fig. 2.2.9, panel B), passing to a contact angle of $\sim 144^\circ$. The water droplet remains on the surface without penetration, confirming the hydrophobicity of the surface after functionalization (panel D).

Bibliographic References

1. Alexander, S.; Eastoe, J.; Lord, A. M.; Guittard, F.; Barron, A. R., Branched Hydrocarbon Low Surface Energy Materials for Superhydrophobic Nanoparticle Derived Surfaces. *ACS Appl Mater Interfaces* **2016**, *8* (1), 660-6.
2. Horch, R. A.; Shahid, N.; Mistry, A. S.; Timmer, M. D.; Mikos, A. G.; Barron, A. R., Nanoreinforcement of Poly(propylene fumarate)-Based Networks with Surface Modified Alumoxane Nanoparticles for Bone Tissue Engineering. *Biomacromolecules* **2004**, *5* (5), 1990-1998.
3. Maguire-Boyle, S. J.; Liga, M. V.; Li, Q.; Barron, A. R., Alumoxane/ferroxane nanoparticles for the removal of viral pathogens: the importance of surface functionality to nanoparticle activity. *Nanoscale* **2012**, *4* (18), 5627-32.
4. Nakamoto, K., Infrared and Raman Spectra of Inorganic and Coordination Compounds. In *Handbook of Vibrational Spectroscopy* 6th ed.; Griffiths, J. M. C. a. P. R., Ed. **2006**; Vol. Vol.B.
5. Takeuchi, M.; Bertinetti, L.; Martra, G.; Coluccia, S.; Anpo, M., States of H₂O adsorbed on oxides: An investigation by near and mid infrared spectroscopy. *Applied Catalysis A: General* **2006**, *307* (1), 13-20.
6. Colthup, N.; Daly, L.; Wiberley, S., *Introduction to Infrared and Raman Spectroscopy*. 3rd ed.; Academic Press: **1990**.

2.3 SILICA INSTEAD OF ALUMINA: NEW PROCEDURES OF FUNCTIONALIZATION WITH ISOSTEARIC ACID

2.3.1 The surface of silica

Different issues led to the transition from alumina to silica nanoparticles:

- The possibility to modify the surface of silica already used in finishing process, in order to extend its functionality (also waterproof qualities) and to avoid adding a new material;
- The possibility to form a more stable covalent bond between isostearic acid and silica nanoparticles;
- The possibility to reach a higher level of hydrophobicity, until the achievement of a superhydrophobic surface.

The surface of silica is well-known for its potential conjugation with different molecules that can be easily adsorbed on surface; however, it is more useful to take advantage of its ability to form covalent bond, avoiding the desorption from the surface and controlling the number and the orientation of anchored moieties.¹

The surface of silica nanoparticles consists of an interconnection of siloxane bridges Si-O-Si, broken up by sites of silanol groups Si-OH that are formed by the incomplete condensation of silicic acid monomers during nanoparticle synthesis.² Silanols are the responsible for the hydrophilic/hydrophobic behaviour of silica,³ since they can interact with different molecules through hydrogen bonds.

The silanol types can be divided into four groups⁴ (Fig. 2.3.1):

- *Isolated* silanols (also called “free” silanols): they cannot interact through hydrogen bonding between them because the distance between closest silanols ($\sim 3.3 \text{ \AA}$) does not allow any interactions.
- *Geminal* silanols: the Si atom is linked to two hydroxyl groups but, despite their closeness, they cannot interact through H-bond for their orientation.
- *Vicinal* silanols: they share a common oxygen of the tetrahedra. The interactions depend on the distance between hydroxyl groups: they are usually separated by less than 3 \AA but not involved in H-bond; they can be considered as weakly H-bonded when the geometrical constraints bring closer the silanols.
- *H-bonded* silanols: they are silanols that do not belong to the same tetrahedra but the distance between the two oxygen atoms of OH groups is between 2.5 and 2.8 \AA , so they can interact through H-bond.

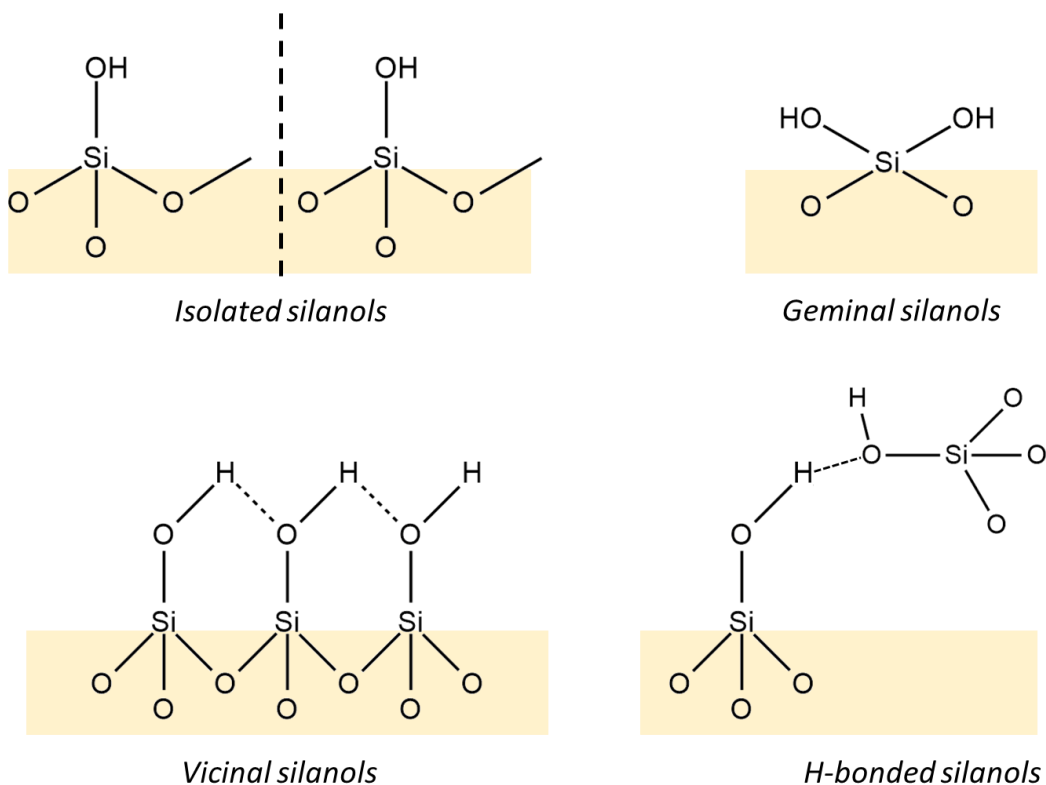


Figure 2.3.1. Classification of surface silanol groups.

Since silanol groups represent the main reactive sites on a silica surface, the study of their properties in terms of nature, concentration and distribution is a fundamental step. For this purpose, infrared spectroscopy allows to study the main characteristics of the silica surface.⁵

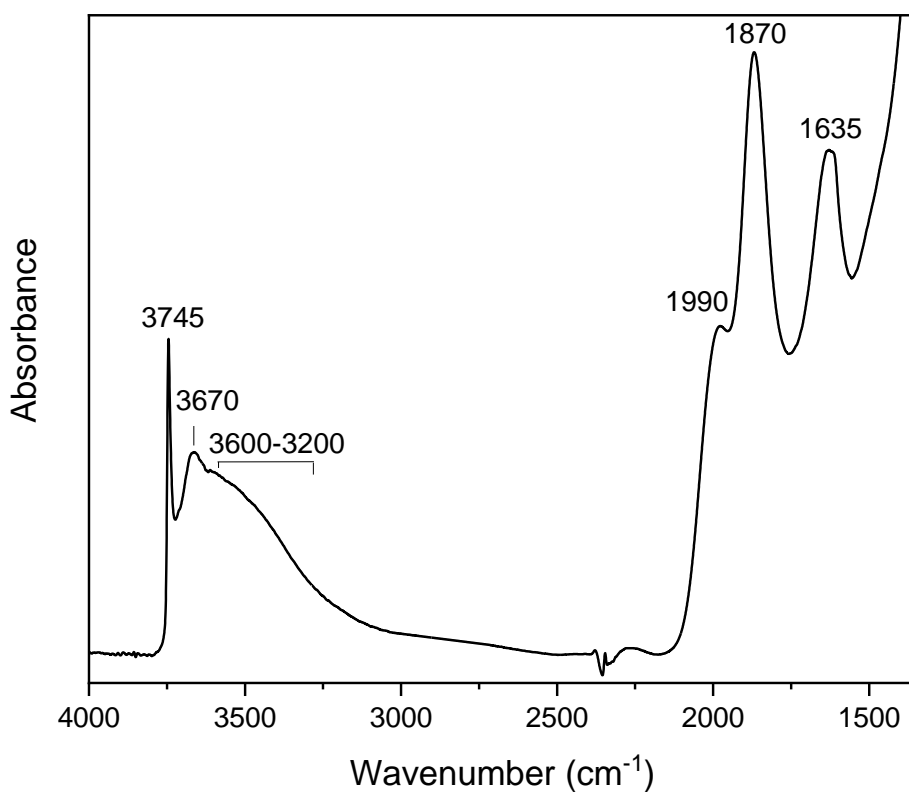


Figure 2.3.2 Infrared spectrum of silica (AOX50) in the 4000-1350 cm⁻¹ range outgassed at b.t. (~50°C).

Fig. 2.3.2 reports the spectrum of a widely-use commercial silica (AOX50), in order to explain the main signals of the material. Starting from the higher frequency region, different vibrational modes appear: 3745 cm^{-1} , 3670 cm^{-1} and a broad band between 3600 and 3200 cm^{-1} are assigned to isolated silanols, internal silanols and H-bonded silanols (weakly and strongly interacting), in the order. The relative intensity for each component is related to the amount of silanol groups present in the silica material.

Passing to the lower frequency region, the pattern in the $2000\text{-}1600\text{ cm}^{-1}$ is due to combination and overtones of inter- and intra-tetrahedra silica vibrational modes.⁵ This region, related to the modes of the silica bulk, is useful to normalize spectra of different samples, in order to make independent the intensities from the thickness of the pellets used for the analyses.

In this project, three types of silica nanoparticles were studied and tested for surface modification (the details on specific properties of nanoparticles are reported in chapter 2.1); two of them are commercial materials, Aerosil OX50 (AOX50) and Aerosil 300 (A300), while the third one is prepared at laboratory scale (m-SiO₂). The commercial nanoparticles (A300 and AOX50) differ for specific surface area values (300 and $50\text{ m}^2/\text{g}$, respectively), the primary particle size (40 and 7 nm , respectively) and for the surface silanol content (5.6 and $1.6\text{ SiOH}/\text{nm}^2$, respectively).

The choice of using lab-made silica nanoparticles resides in the possibility to employ nanoparticles with a controlled size and shape for the surface modification. The total amount of silanols, calculated from TGA, results in $30\text{ SiOH}/\text{nm}^2$, but this value is not related only to silanols exposed on the surface, including not accessible ones such as intraglobular silanols. In the work of Catalano et al.,⁶ the maximum amount of exposed silanols that can interact with molecules is measured, and the value is $7\text{ SiOH}/\text{nm}^2$.

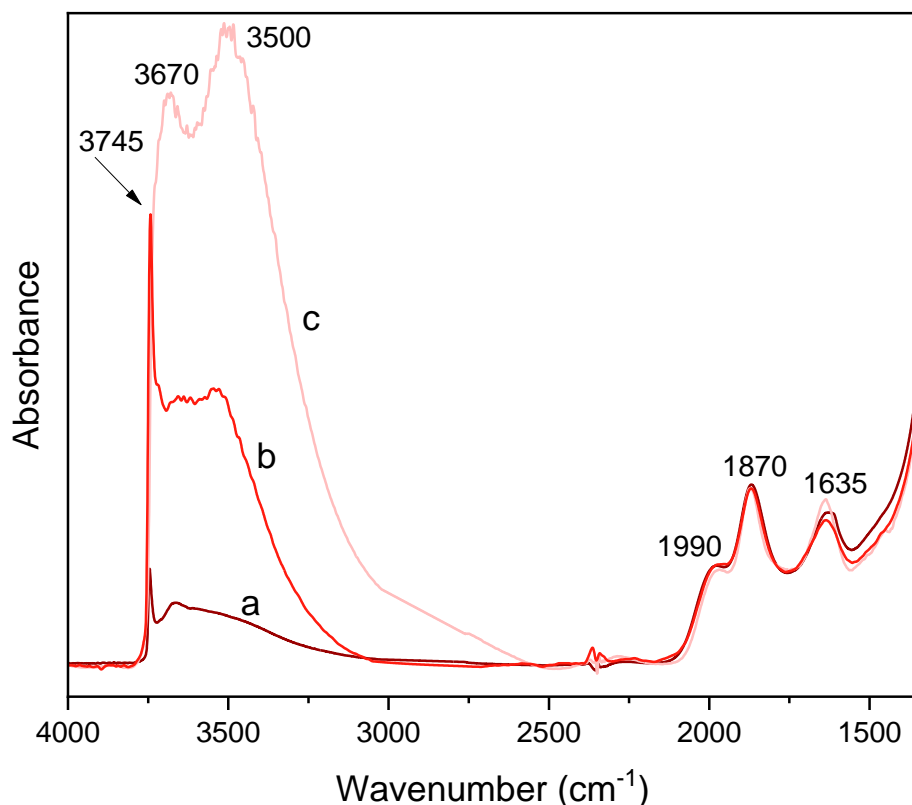


Figure 2.3.3. Infrared spectrum of different type of silica materials: AOX50 (dark-red, spectrum a), A300 (red, spectrum b) and m-SiO₂ (pink, spectrum c) in 4000-1350 cm⁻¹ range outgassed at b.t. (~50°C) in order to remove water signals from spectra.

The spectra of the three types of silica nanoparticles (Fig. 2.3.3) are normalized in the region referred to vibrational modes of silica bulk (2000-1850 cm⁻¹), in order to enhance differences in the relative intensities of signals of silanol groups (3800-3200 cm⁻¹).

The total amount of silanols for each sample, represented by the integrated area in the 3800-3200 cm⁻¹ zone, is proportional to the surface silanol densities reported above.

Furthermore, it is possible to notice the different distribution of silanol groups: the amount of isolated silanols changes in these three samples, and these are not present in the case of m-SiO₂.

The band at 3670 cm⁻¹ is related to weakly H-bonded bulk intraglobular silanols, more pronounced for m-SiO₂, due to the narrow pores exposing on their walls a big amount of silanols linked through H-bond.⁶

The infrared spectrum of the commercial hydrophobic sample AR812, a high thickening fumed silica surface treated with HMDS (hexamethyldisilazane) is reported and discussed (Fig. 2.3.4).

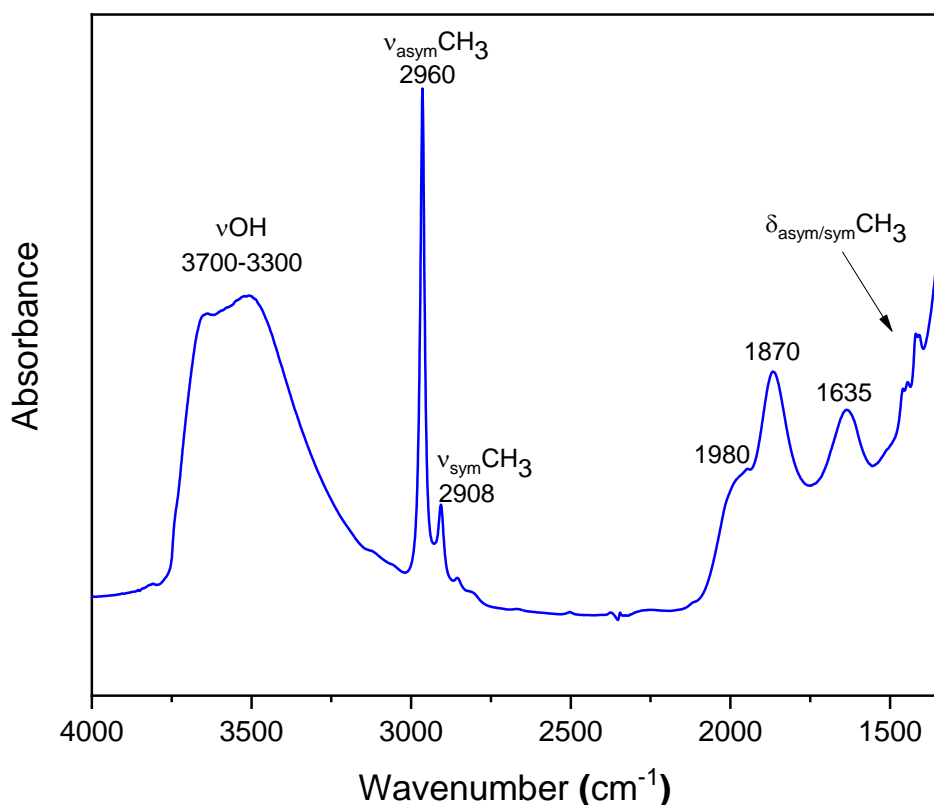


Figure 2.3.4. FT-IR spectrum of AR812 outgassed at b.t. (ca. 50°C), in the 4000-1350 cm^{-1} range.

The spectrum shows the presence of numerous alkyl chains on the surface, with a grafting density of ca. 3.5 molecules/ nm^2 (confirmed by TGA analysis). In the 3000-2800 cm^{-1} region, signals related only to $-\text{CH}_3$ groups (ν_{asym} and ν_{sym} CH_3 at 2960 and 2908 cm^{-1} , respectively) are visible. Apart from weak signals related to $\delta_{\text{sym/asym}}$ of $-\text{CH}_3$ groups, the lower frequency region presents only the combination and overtones modes of the silica surface (1980, 1870 and 1635 cm^{-1}). This is a remarkable difference with respect to the material functionalized with isostearic acid (see below, section 2.3.7). In the latter case the linkage is given by an amide bond between the amine groups exposed on the surface and isostearic acid previously transformed into its acyl chloride form. In the case of the commercial material, the absence of this bond is noted, thus leading to the idea of a condensation of HMDS with some surface silanols of the bare silica. The high grafting density with respect to what measured on the sample functionalized with ISOST (0.3 molecules/ nm^2 , see below) is in agreement with the smaller size of the molecule.

2.3.2 Procedure of functionalization with APTS

Since the final goal is the formation of a covalent bond between silica surface and molecules containing branched alkyl chains (carboxylic acids), the first step was to modify the silanol groups, that exhibit a limited reactivity towards carboxylic groups. The modification was carried out with a functionalizing agent that exposes amino groups (-NH₂).

An example of a widely used alkoxysilane for this purpose¹ is the APTS (3-aminopropyltriethoxysilane) that exposes primary amino groups on silica surface after functionalization (Fig. 2.3.5).

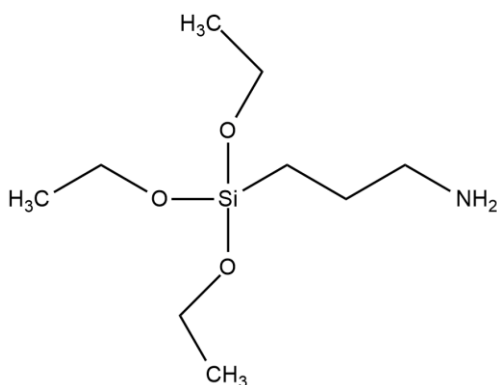


Figure 2.3.5. 3-aminopropyltriethoxysilane (APTS), (H₂N(CH₂)₃Si(OC₂H₅)₃): nucleophilic reagent necessary for surface functionalization of silica nanoparticles with amino groups (-NH₂).

APTS requires a partially aqueous environment since the ethoxy- groups are not reactive enough to react spontaneously with the OH groups present on the silica surface without first forming silanols by hydrolysis. Once deposited on the substrate, a covalent polymer is formed, exposing the primary amino groups available for the subsequent conjugation (Fig. 2.3.6).

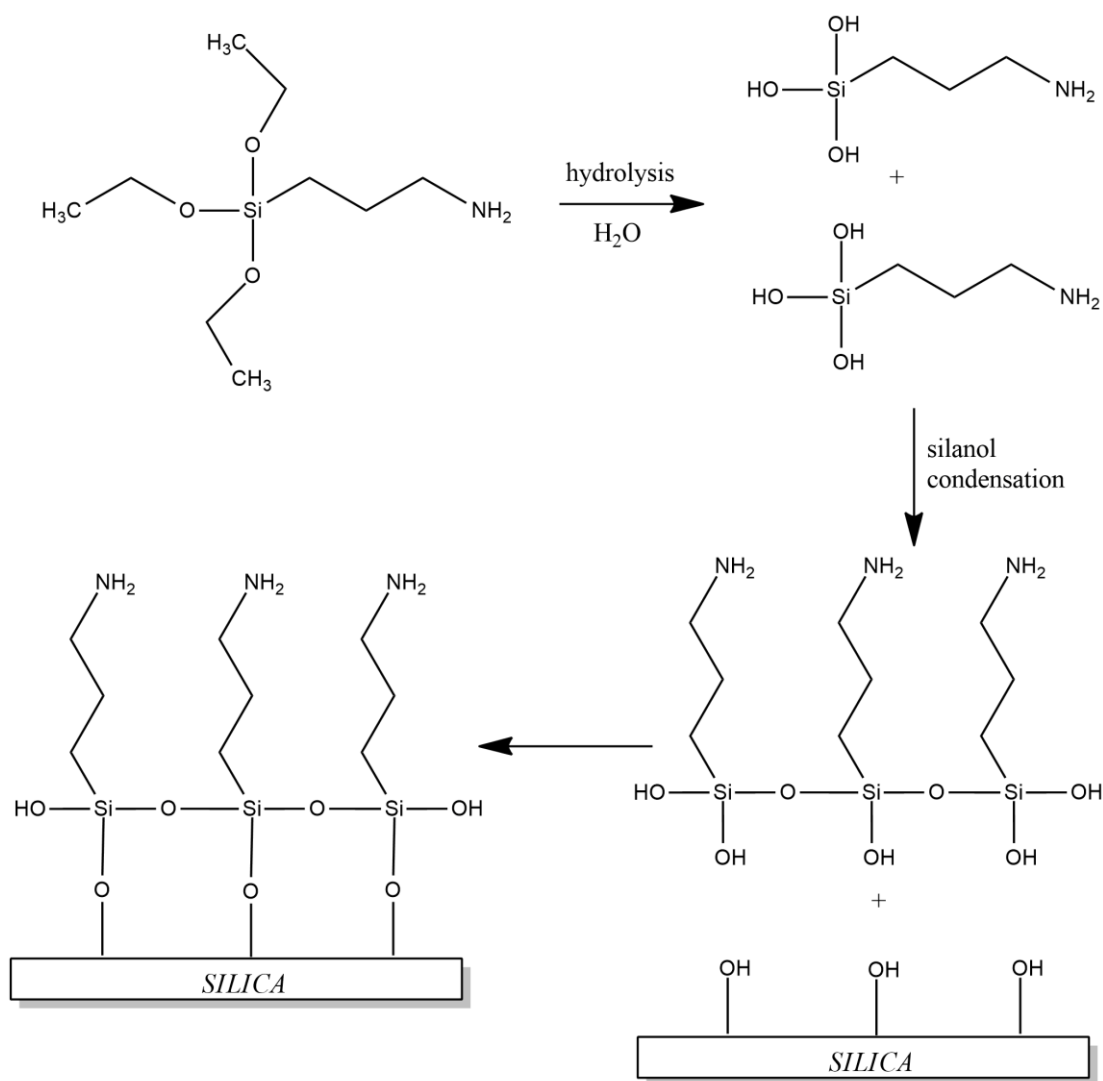


Figure 2.3.6. Mechanism of a hydrolysis and subsequent condensation with hydroxyl groups present at the silica surface. The scheme shows the ideal complete hydrolysis of the three ethoxy-groups, but it is possible that some groups remain unreacted.

The functionalization of the nanoparticles can be carried out by two methods:

- the "one-pot" method involves the addition of the functionalizing agent directly in the reaction mixture during the synthesis;⁷ this method can be used only for the m-SiO₂ nanoparticles.
- the "grafting" method, for the commercial silicas, involves the addition of APTS after the synthesis of silica nanoparticles.

Starting from the "one pot" method, 873 μ L (0.91 equiv) of APTS were added after 16 hours of nanoparticles synthesis (see chapter 2.1) and the mixture was left under magnetic stirring at room temperature for another 24 hours. Finally, the stability of the microemulsion was broken by the addition of ethanol and then the functionalized nanoparticles were washed in ethanol and water until the removal of non-reacted reagents. The nanoparticles were dried at 50°C, overnight.

The "grafting" method involves the addition of A300 or AOX50 nanoparticles and distilled water in a flask; then, under magnetic stirring, APTS was added. The reaction was carried out in an acidic

environment by the addition of HCl (0.01M). Finally, the reaction occurred at r.t. for 4 hours. Functionalized nanoparticles were washed with water, with re-suspension and centrifugation cycles, until the complete removal of the non-reacted APTS (3 cycles).

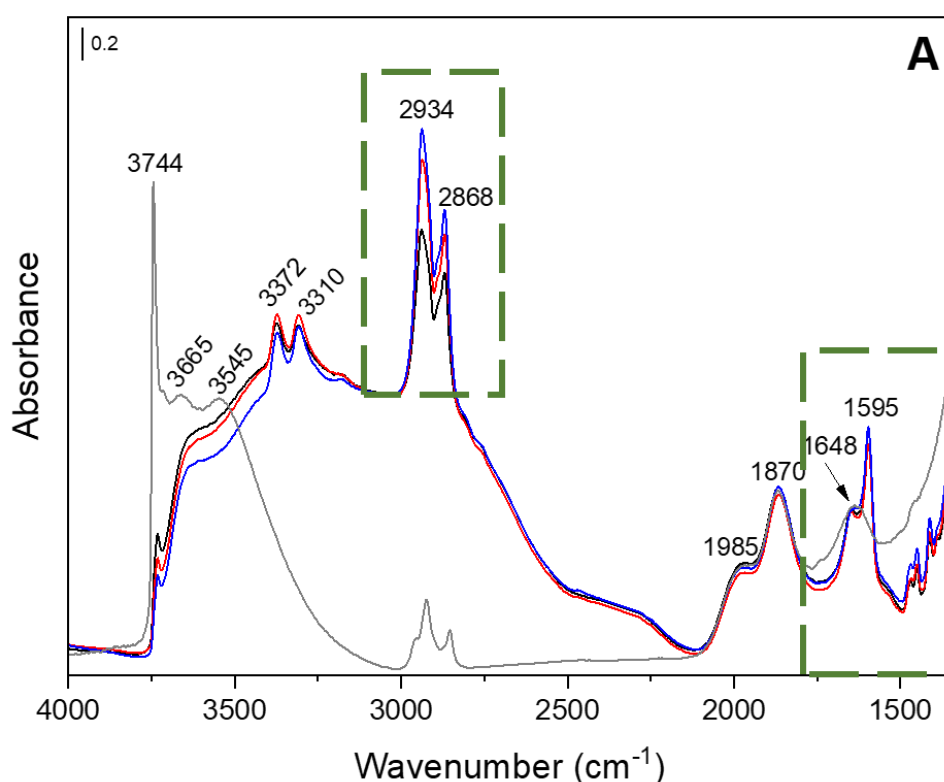
For both commercial silica (A0X50 and A300) three tests with different molar ratio between surface silanols and APTS were carried out (Tab. 2.3.1).

Table 2.3.1 Molar amounts of APTS are reported using a molar ratio of 5:1, 10:1 and 15:1 APTS:SiOH, considering 0.58×10^{-4} SiOH moles for AOX50 (1.6 SiOH/nm^2) and 0.12×10^{-2} SiOH moles for A300 (5.6 SiOH/nm^2).

Molar ratio APTS:SiOH	AOX50	A300
5:1	$0.29 \cdot 10^{-3}$	$0.6 \cdot 10^{-2}$
10:1	$0.58 \cdot 10^{-3}$	$1.2 \cdot 10^{-2}$
15:1	$0.87 \cdot 10^{-3}$	$1.8 \cdot 10^{-2}$

2.3.3 Evidence and quantification of amine groups on surface

The first material tested for the functionalization with APTS was Aerosil300, using the “grafting” method (Fig. 2.3.7).



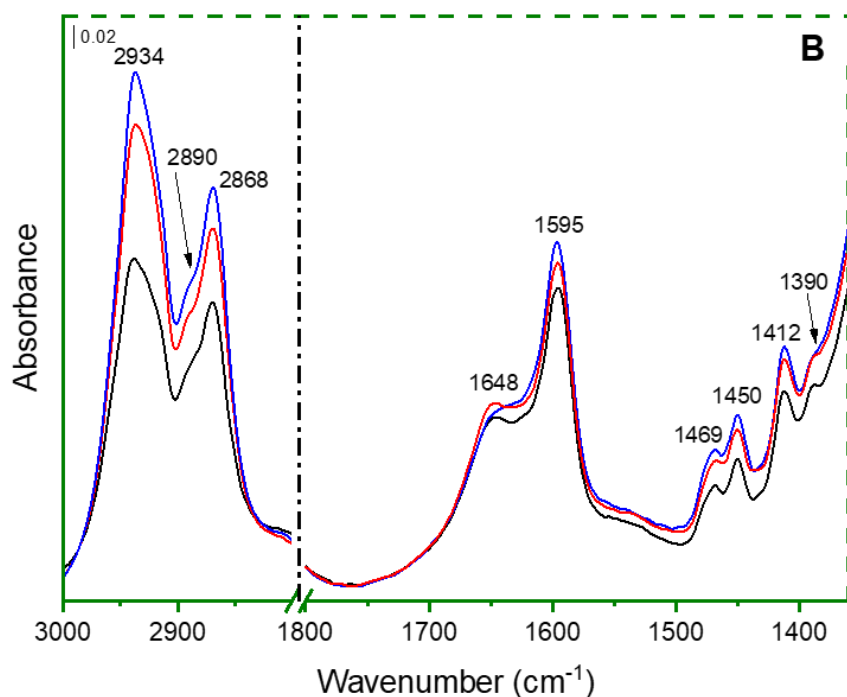


Figure 2.3.7. Panel A: Infrared spectra (IR) of pristine A300 (grey curve), A300 functionalized with APTS: molar ratio 5:1 (black curve), molar ratio 10:1 (red curve) and molar ratio 15:1 (blue curve). Panel B: the magnification shows the areas between 3000-2800 cm^{-1} and 1800-1350 cm^{-1} .

The IR spectrum of bare A300 (panel A, grey curve) shows a peak at 3744 cm^{-1} due to the isolated/weakly interacting silanols and a broad band in the 3700-3200 cm^{-1} range, produced by silanols experiencing a mutual interaction as stronger as lower the νOH frequency.⁸ The signals between 3000 and 2800 cm^{-1} are due to some impurities on the silica surface. The functionalization with APTS (colored curves), resulted in an almost complete depletion of the peak at 3744 cm^{-1} and in the increase in intensity and widening towards further lower wavenumbers of the band to interacting silanols.

Changes in the IR νOH pattern are accompanied by the appearance of a doublet at 3373 and 3306 cm^{-1} , due to ν_{asym} and ν_{sym} of $-\text{NH}_2$ groups,⁹ a pattern in the 3000-2800 cm^{-1} range typical of ν_{asym} and ν_{sym} of $-\text{CH}_2$ groups of the propyl chains and of $-\text{CH}_2$ and $-\text{CH}_3$ groups of ethoxy moieties still present in a part of anchored APTS, as revealed below by ^{13}C -CPMAS NMR spectroscopy (Fig. 2.3.8).

In particular, in panel B, it is possible to observe the signals referring to the antisymmetric and symmetric stretching of the $-\text{CH}_2$ groups (2935 and 2870 cm^{-1} , respectively) and the symmetric stretching mode, much less intense, of the CH_3 group (2885 cm^{-1}); the signal related to antisymmetric stretching of $-\text{CH}_3$ may be present weakly around 2960 cm^{-1} , but the intense signal of the $-\text{CH}_2$ group does not allow it to be clearly shown.¹⁰ This indicates, although in a minority amount, the presence of some ethoxy groups which have not been hydrolyzed during the reaction.

In the lower frequencies region, two signals are visible at 1985 cm^{-1} and 1870 cm^{-1} , assignable to overtones and combination modes of silica, which completely absorbs radiation below 1300 cm^{-1} . A third characteristic signal of the silica structure falls at 1648 cm^{-1} ,¹¹ which is partially overlapped, after functionalization with APTS, by the presence of the signal at 1595 cm^{-1} , characteristic of H-N-H bending mode.¹⁰

Finally, in this region (panel B) it is possible to detect different vibrational modes of the alkyl chains in the samples functionalized with APTS (black, red and blue spectra): the antisymmetric and symmetric bending modes of $-\text{CH}_2$ (1450 and 1412 cm^{-1}) and two signals assigned respectively to antisymmetric and symmetric bending modes of $-\text{CH}_3$ groups (1469 and 1390 cm^{-1}).¹⁰

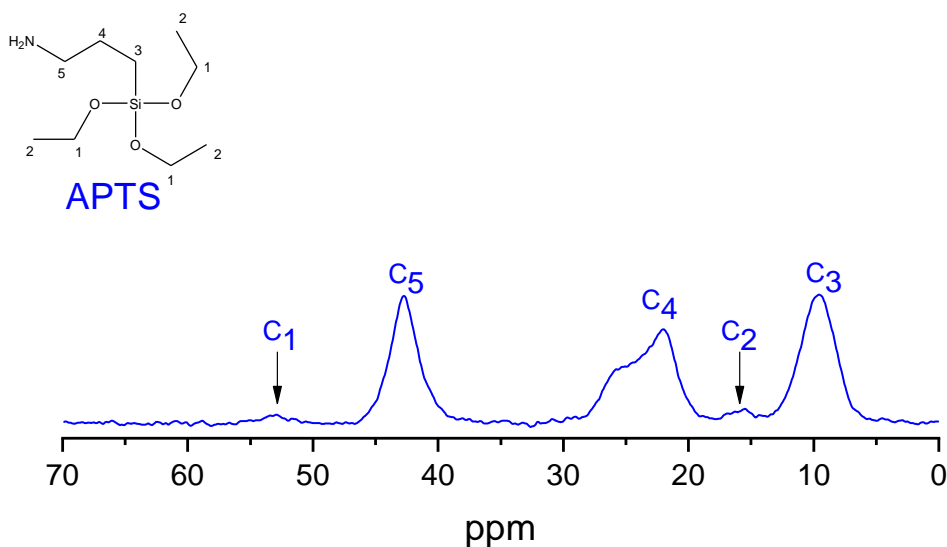


Figure 2.3.8. ^{13}C -CPMAS SSNMR spectra of A300-APTS.

The ^{13}C -CPMAS SSNMR spectrum of A300-APTS allows to identify signals of the propyl chains, in particular at 43 ppm, 22.3 ppm and 9.5 ppm, respectively assigned to C_5 , C_4 and C_3 atoms in the reported chemical structure of APTS. The signals of C_1 and C_2 , assigned to the ethoxy groups, witness the not complete hydrolysis during the functionalization with A300.

Although IR spectroscopy is not an absolute quantitative technique, it is possible to estimate the amount of APTS molecules per nm^2 present on the surface of the A300 from the different relative intensities of signals (Fig. 2.3.9).

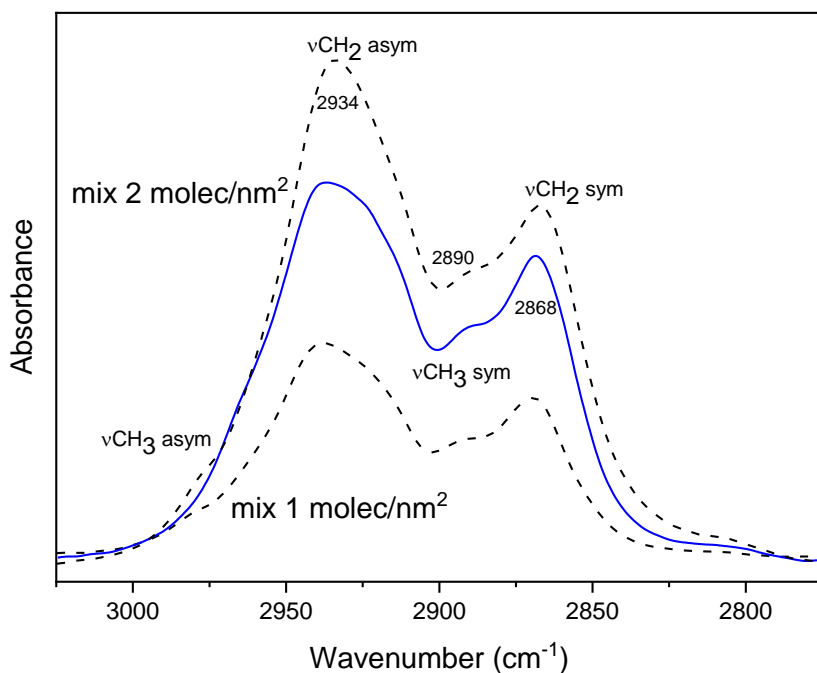


Figure 2.3.9. IR spectra in 3050-2750 cm^{-1} region of: A300-APTSx15 (blue curve), mixture 1 molec/nm^2 and mixture 2 molec/nm^2 (dashed black curves).

The quantification method (see section 2.2.4) involved the preparation of several mixtures of a known amount of APTS and A300, to be compared with the functionalized sample with the "grafting" method. In the case of mixtures, the surface and molecule are put into contact "mechanically" without, therefore, the formation of a covalent bond. The area of interest, free from bulk signals and referring only to the propylic chains of the APTS, is shown in Fig. 2.3.9. The ratio of the intensity of the signals referring to stretching CH_2 (e.g. 2934 cm^{-1}) between the mixture containing a known amount of APTS and the sample functionalized with a molar excess of 15, gives an indication of the amount of molecules present on the surface, which results in $\sim 1.2 \text{ APTS}/\text{nm}^2$. The use of a purely quantitative technique, the TGA, confirmed the value calculated by the FT-IR spectra (Fig. 2.3.10).

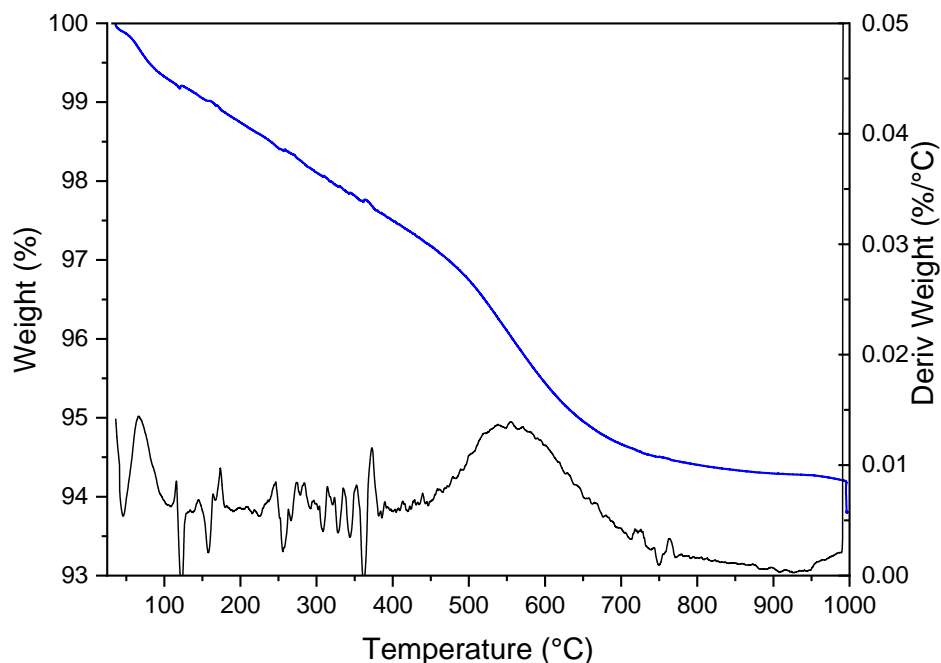


Figure 2.3.10. Thermogravimetric analysis (TGA) of A300-APTSx15. The blue curve represents the thermogram, or decomposition curve; the black curve is the derivative of weight loss (%/°C).

The grafting density is calculated by the formula (1), reported in section 2.1.2.5, and the weight loss of 4.86%, referred to APTS, results in 0.7-1.7/nm², calculated by considering respectively the presence of three ethoxy groups and their total hydrolysis. The average of these two values leads to 1.2 APTS/nm², which is the value additionally confirmed by IR spectroscopy.

Turning to the spectroscopic analysis of the AOX50 after functionalization with APTS, the situation is markedly different (Fig. 2.3.11):

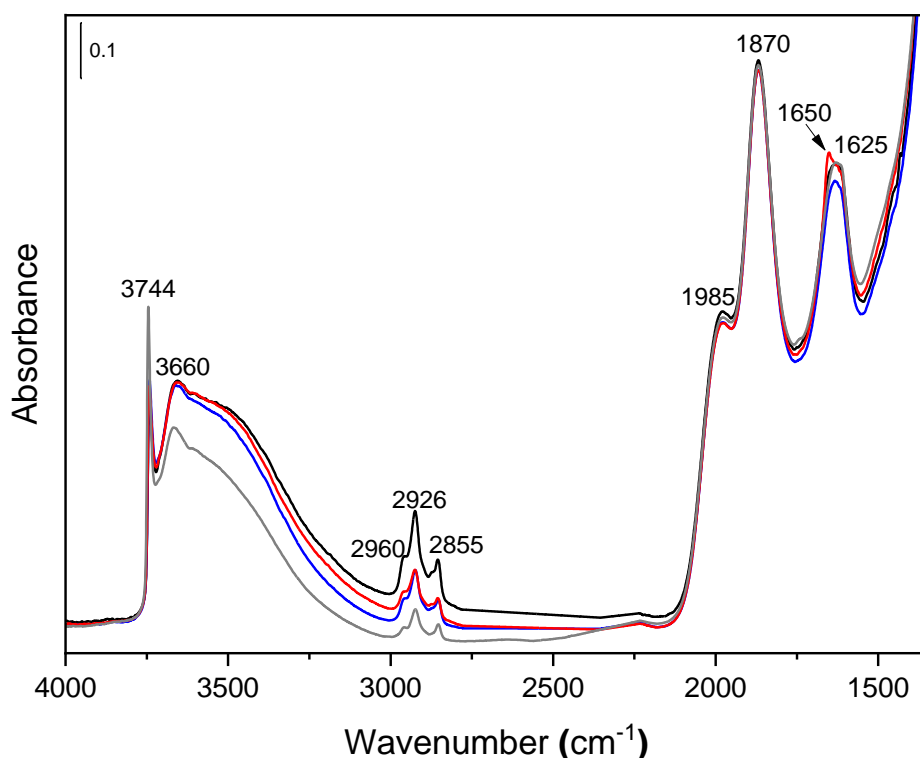


Figure 2.3.11. IR spectra of pristine AOX50 (grey curve), AOX50-APTSx5 (black curve), AOX50-APTSx10 (red curve) and AOX50-APTSx15 (blue curve).

The spectral profile of the AOX50 as such (grey spectrum), as expected for the smaller number of silanols present on the surface, turns out to be different between 3800 and 3000 cm^{-1} . The signal at 3744 cm^{-1} is clearly noticeable, referring to the stretching of isolated silanols, which shows a slight decrease after functionalization with APTS (black, red and blue spectra).⁸ In the zone referred to SiOH stretching modes (3700-3200 cm^{-1}), weakly and strongly interacting by hydrogen bond, is little perturbed after functionalization. This is a first indication that the amount of APTS that has been bound to the surface is much smaller than in the previous case (A300). In addition, the very low increase of signals assigned to stretching modes of aliphatic groups after functionalization (3000-2800 cm^{-1}), and also the absence of signals related to the $-\text{NH}_2$ groups (3372 and 3310 cm^{-1}), confirm the previous indication. The signal at 1650 cm^{-1} , present only in the AOX50-APTSx15 (blue spectrum), could be assigned to the formation of $\text{R-NH}_3^+-\text{OOC-R}$ salts, as a result of the reaction of CO_2 present in the air with two aminopropyl groups (PrNH_2) attached to the silica matrix.¹⁰ This may suggest a presence, even if minimal, of APTS on the surface, but irrelevant when compared to that present on the surface of the A300.

The lower amount of silanols on the AOX50 surface (1.6 SiOH/nm^2) may be the cause of the different behavior of the two materials towards the functionalization with APTS.

After the functionalization of the commercial silicas, obtaining good results only for A300, the lab-made m-SiO_2 were tested for the functionalization with APTS, following the “one pot” method (Fig. 2.3.12). The nanoparticles synthesized with the microemulsion method have a specific surface area

similar to AOX50 nanoparticles ($\sim 95 \text{ m}^2/\text{g}$), but a surface silanol densities closer to the A300 one ($\sim 7 \text{ SiOH}/\text{nm}^2$).

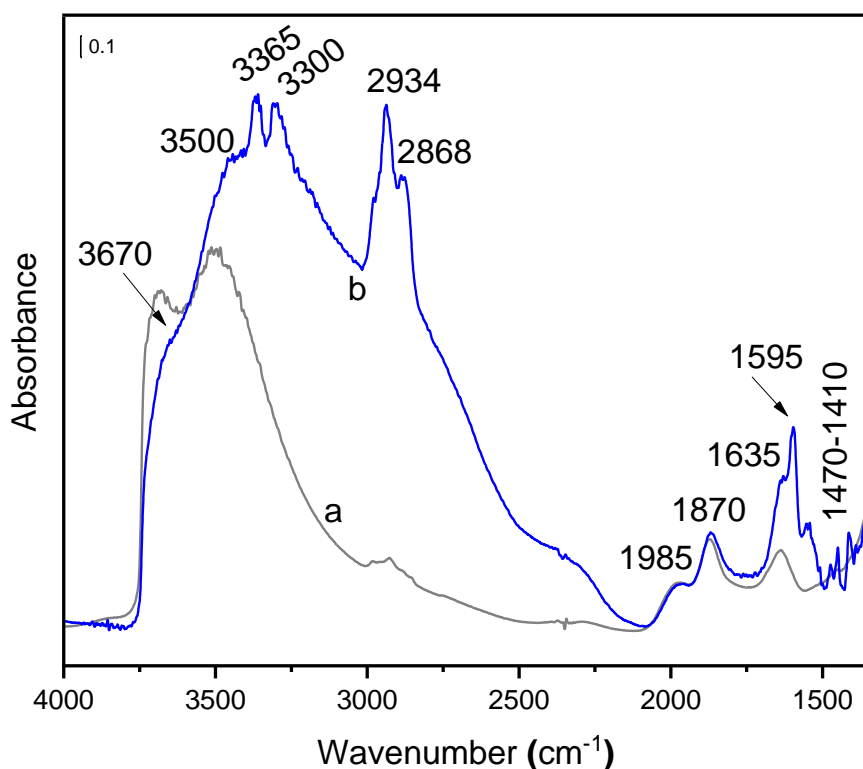


Figure 2.3.12. IR spectrum of m-SiO₂ as such (grey spectrum, a) and after functionalization with APTS through “one-pot” method (blue spectrum, b) in the 4000-1350 cm⁻¹ region.

For the sake of comparison, in Fig. 2.3.12 the spectrum of non-functionalized m-SiO₂ is reported (curve a). The functionalization with APTS (curve b), resulted in an almost complete depletion of peaks at $\sim 3700 \text{ cm}^{-1}$, referred to the isolated/weakly H-bonded silanols, and in the increase in intensity and broadening towards lower wavenumbers of the band to interacting silanols ($3500\text{-}3200 \text{ cm}^{-1}$).⁸

Two peaks at 3365 and 3300 cm⁻¹, are due to the vibrational modes of antisymmetric and symmetric stretching of -NH₂ groups, respectively;¹¹ in the aliphatic stretching region ($3000\text{-}2800 \text{ cm}^{-1}$) typical peaks of CH₃/CH₂ of aminopropyl chains are present and of -CH₂ and -CH₃ groups of ethoxy moieties still present in a part of anchored APTS. Also the region between 1800 and 1350 cm⁻¹ shows the typical signals referred to the “free” amine groups -NH₂ (1595 cm⁻¹), characteristic of the bending mode H-N-H, and several peaks due to the bending modes of CH₃/CH₂ between 1470 and 1400 cm⁻¹, previously described in detail for commercial silicas (see section 2.3.1).

Additionally, thanks to the “mixture method” for the quantification by FT-IR illustrated above for commercial silicas (see section 2.3.3), it was possible to quantify the amount of APTS anchored to the surface (Fig. 2.3.13).

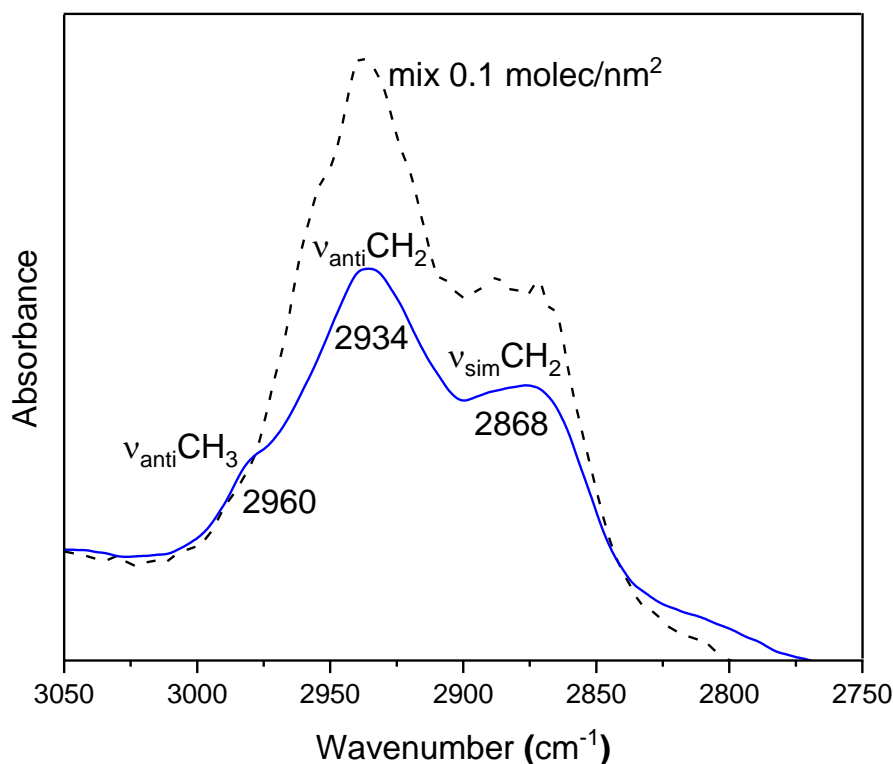


Figure 2.3.13. IR spectra in the region 3050-2750 cm⁻¹ of: m-SiO₂-APTS (blue curve), mixture 0.1 molec/nm² (dotted black curve).

Despite the presence of signals characteristic of the functionalizing agent, the amount of APTS molecules on m-SiO₂ surface turns out to be less than 0.1 molec/nm², definitely lower than the value found for A300 nanoparticles.

2.3.4 Procedure of functionalization with isostearic acid: first approach based on the activation of carboxylic groups in ester compounds

After confirming the possibility to expose amine groups on both lab-made silica nanoparticles (m-SiO₂) and the commercial one (A300), the second functionalization step with a hydrophobic molecule, isostearic acid (chemical structure reported in section 2.1.1), was carried out.

In order to bind covalently isostearic acid (ISOST) to the silica surface, it is necessary to increase the reactivity of the carboxylic groups towards amine moieties. For this purpose, the functional groups of isostearic acid were transformed in the active ester forms, in order to promote the formation of an amide bond with -NH₂ groups.

In literature there are different types of conjugation with linkers containing a carboxyl group, and it can be directly coupled with the amino-propyl group involving the use of carbodiimides (RN=C=NR').¹²

Carbodiimides are used to mediate the formation of the amide bond between carboxylates and amines and two types are widely used: soluble and insoluble in water.

The most common reaction involves the use of EDC (1-ethyl-3-(3-dimethylaminopropyl) carbodiimide), a water-soluble carbodiimide that acts as a crosslinker by activating carboxylic groups through a spontaneous reaction with primary amines. However, by using isostearic acid, the

reaction environment cannot be aqueous, and therefore we have opted for the use of water-insoluble carbodiimide. The reaction involves the esterification of isostearic acid with the use of two reagents: N-hydroxysuccinimide (NHS) and dicyclohexyl carbodiimide (DCC).¹³

The -NHS ester is a chemical activator for the formation of acylating compounds and can be formed by the reaction with a carboxylate in the presence of a carbodiimide. In order to prepare a stable ester derivative, the reaction must be conducted under anhydrous conditions and using insoluble carbodiimide or condensing agents, such as DCC (Fig. 2.3.14). DCC is often used in DMF (N,N-dimethylformamide) to prepare active esters compounds containing a carboxyl group using NHS.¹⁴

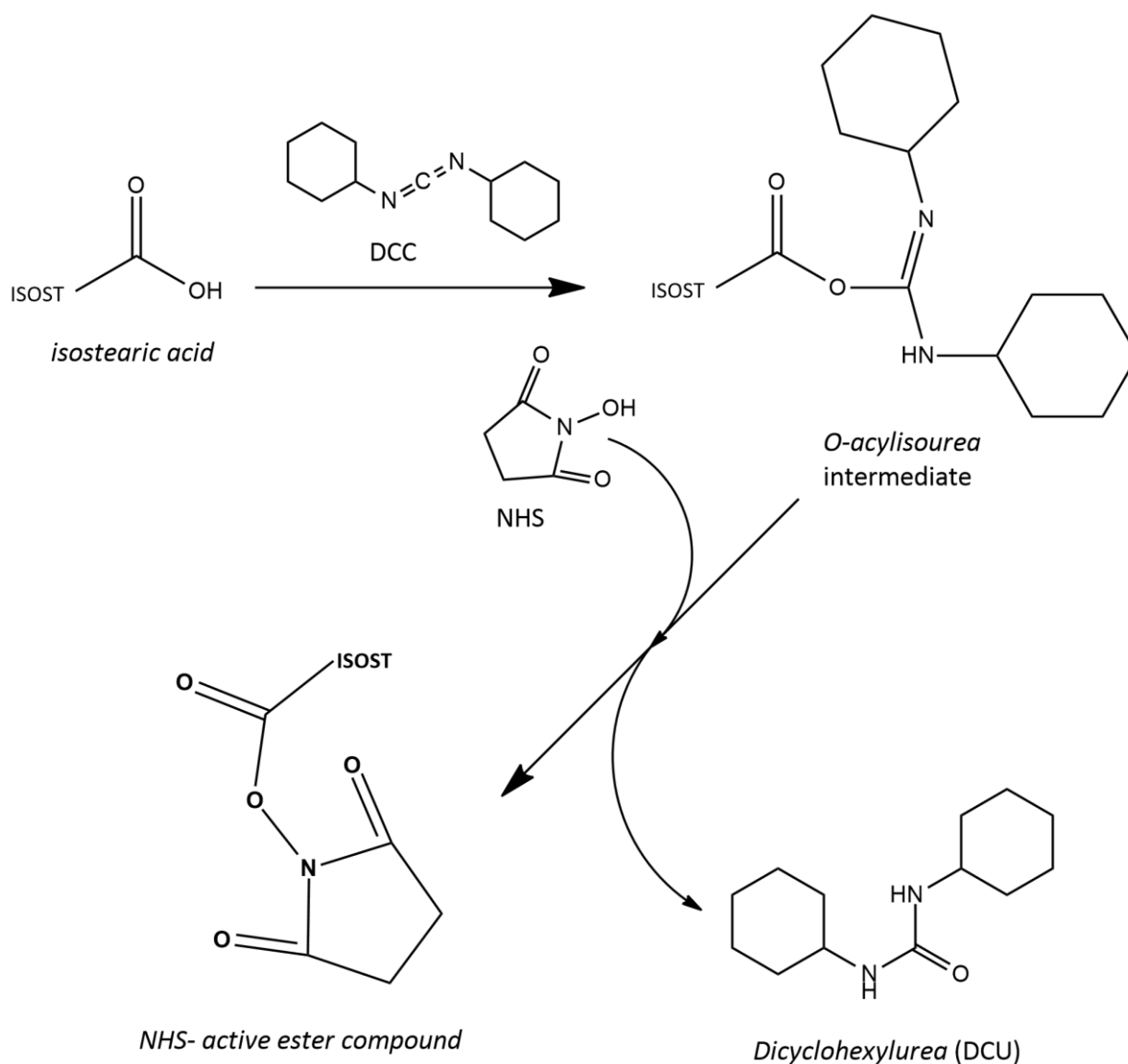


Figure 2.3.14. Use of DCC and NHS in the formation of NHS active ester compound starting from a molecule containing a carboxylic group (isostearic acid). The dicyclohexylurea is a side product of the reaction.

After the formation of NHS- active ester compound, silica nanoparticles functionalized with APTS were put in contact to form the amide bond (Fig. 2.3.15).

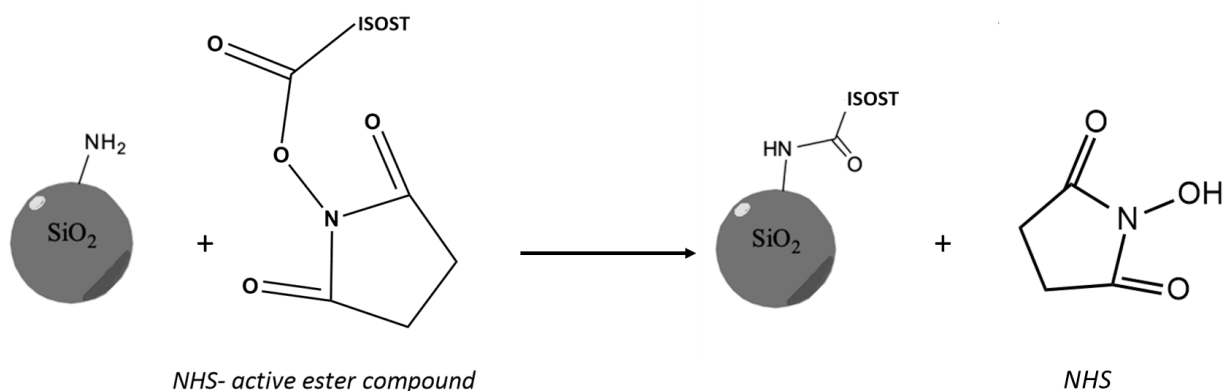


Figure 2.3.15. Formation of amide bond between silica nanoparticles functionalized with amine groups and the NHS-active ester compound. At the end of reaction NHS is re-formed.

For both silica nanoparticles (m-SiO₂ and A300) the following protocol was used:

-formation of active ester compound: working in anhydrous conditions, the NHS, DCC and ISOST are added simultaneously to the DMF, in a 4:1 (NHS, DCC: ISOST) molar ratio. The amount of ISOST to be added is calculated with a 10:1 molar ratio ISOST: SiOH groups. The temperature was set at 80°C for 4 hours, under magnetic stirring. Since it is important to work in an anhydrous environment, all the glassware used was kept in an anhydrous oven at T=120°C overnight before the reaction.

-after 4 hours of esterification, the temperature was decreased to T= 25°C and silica nanoparticles were added and kept under magnetic stirring for 20h at r.t.

-the functionalized nanoparticles were washed 2 times with ethanol, centrifuged at 10000 rpm for 20 min, in order to eliminate non-reacted ISOST, excess reagents and side products, and finally with 3 cycles of bidistilled water to eliminate any residues of reagents and more polar solvents. The product was dried at 50°C for 24 hours.

2.3.5 Evidence of the presence of isostearic acid on silica surface and evaluation of hydrophobicity: IR spectroscopy, SS-NMR and Contact Angle measurements

The first evidence of the effectiveness of functionalization was provided by infrared spectroscopy (FT-IR). Although the functionalization of m-SiO₂ and A300 was carried out in parallel, for sake of clarity the results concerning the lab-made silica nanoparticles are reported first (Fig. 2.3.16).

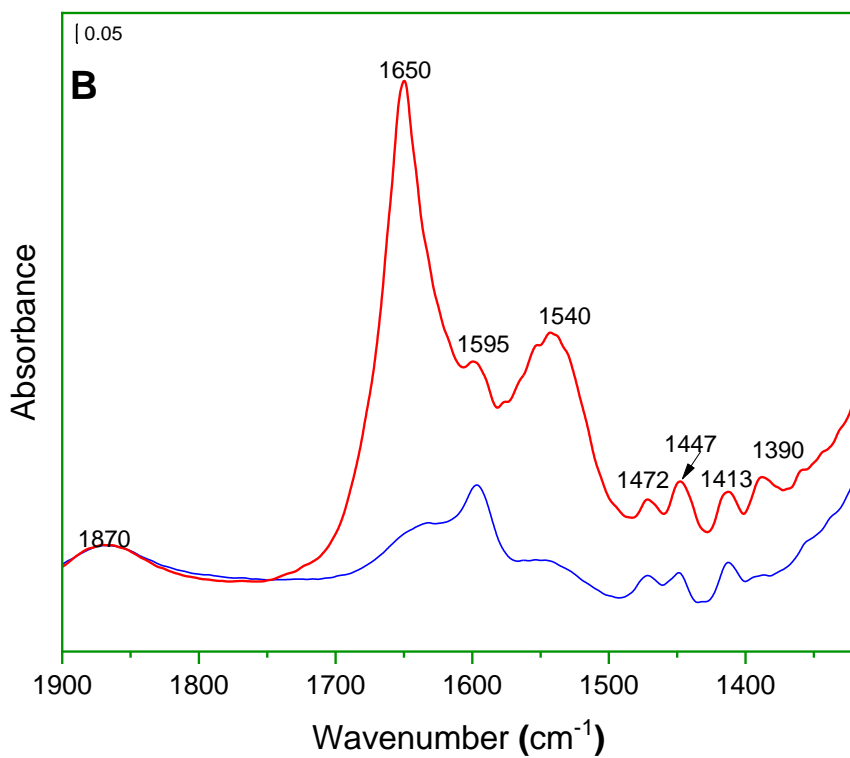
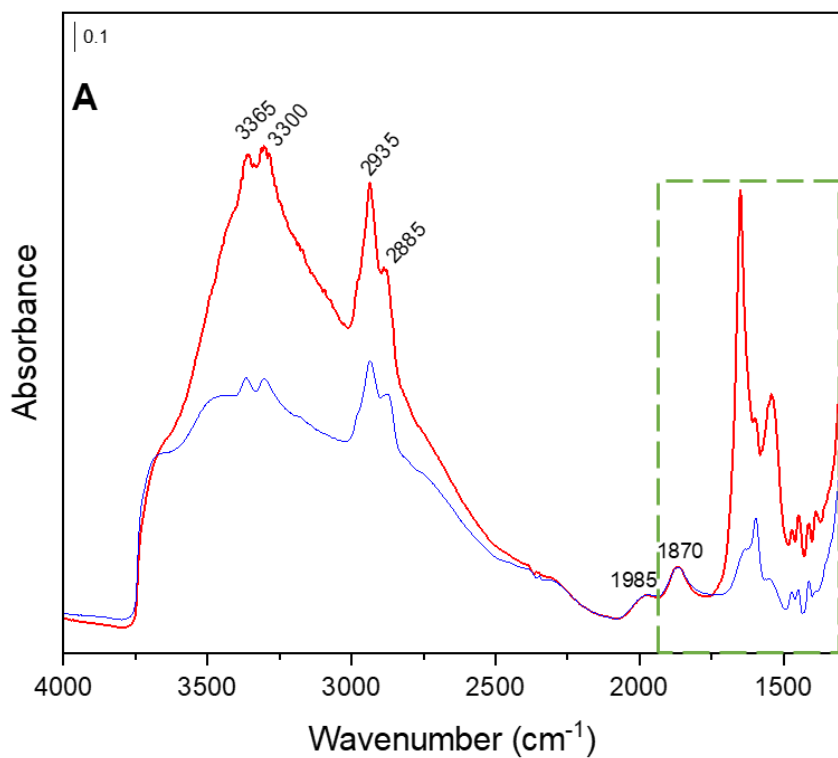


Figure 2.3.16. Panel A: FT-IR spectra of m-SiO₂-APTS (blue spectrum) and m-SiO₂-APTS-ISOST (red spectrum) in 4000-1350 cm⁻¹ region; Panel B: magnification in the 1900-1350 cm⁻¹ zone.

In Fig. 2.3.16, panel A, it is possible to observe spectra of the functionalized silica nanoparticles (m-SiO₂) with APTS (blue spectrum) and with the further functionalization with ISOST (red spectrum).

The pattern in 3800-3200 cm^{-1} region, referred to SiOH stretching modes, shows an increase in the broad band of the H-bond interactions, witnessing probably H-bond interactions involving the new functionalizing molecule (ISOST).⁸ Despite this, the two peaks of stretching modes of H-N-H (3365 and 3300 cm^{-1}) are still clearly visible, indicating the presence of $-\text{NH}_2$ groups that have not been involved in the amide bond formation.

The region referred to aliphatic stretching modes of CH_3/CH_2 moieties (3000-2800 cm^{-1}), already composed by signals of propylic chains of APTS (blue spectrum), shows an increase after the second functionalization (red spectrum) due to the presence of aliphatic chains (C18) of ISOST anchored to the surface.

The lowest frequency region, magnified in panel B (1900-1350 cm^{-1}), gives more detailed information on the reaction between the surface amino groups and the ISOST active ester. The two most intense signals at 1650 and 1540 cm^{-1} are assigned to the vibration modes typical of an amide bond: in particular, the first component corresponds to the stretching mode of the amide CO group (Amide I), while the second one is a combination of the C-N-H bending and N-H stretching modes (Amide II), confirming the success of the reaction. The signal at 1595 cm^{-1} (δNH_2) confirms the presence of "free" $-\text{NH}_2$ groups. Signals falling in 1480-1390 cm^{-1} region are assigned to the bending modes of aliphatic groups (δ_{asym} and δ_{sym} of CH_2 and CH_3).¹⁰

As described above, the IR mixture quantification method can give an indication of the number of ISOST molecules per nm^2 present on the surface (Fig. 2.3.17).

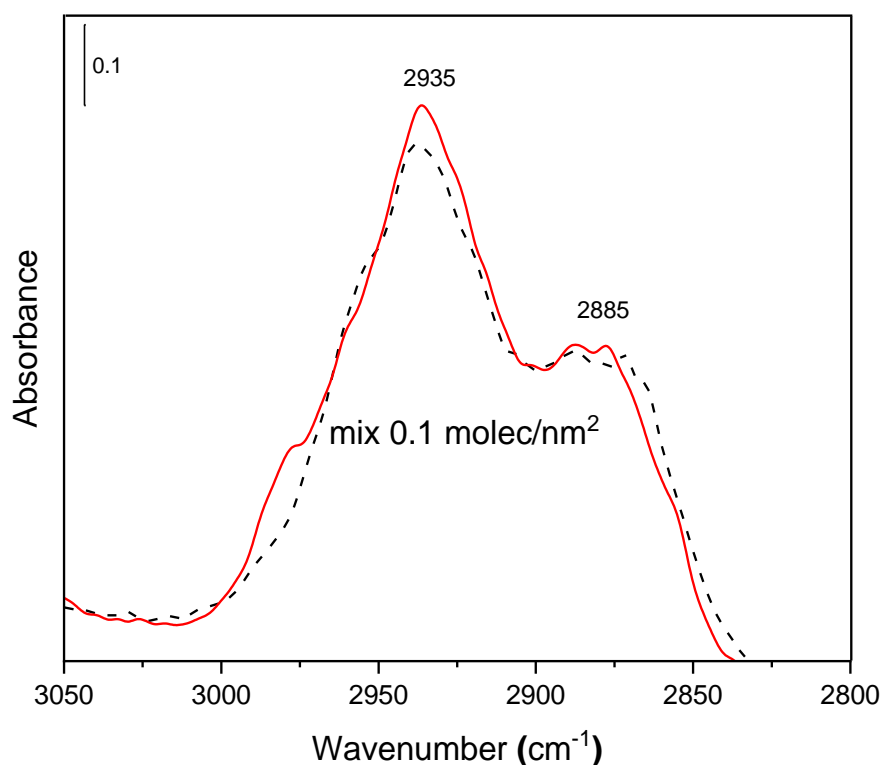


Figure 2.3.17. FT-IR spectra of m-SiO₂-APTS-ISOST (red curve) compared with the mixture of m-SiO₂-APTS with 0.1 ISOST/nm² (dashed black curve).

In this case the mixture was prepared by mixing the functionalized silica nanoparticles with APTS (the same batch used for functionalization with ISOST) with a known amount of ISOST. The value that can be extrapolated from Fig. 2.3.17 is about 0.1 molecules of ISOST/nm².

The next step involved the measurement of contact angle value, in order to assess the hydrophobicity of the material after functionalization with a branched hydrophobic molecule (Fig. 2.3.18).

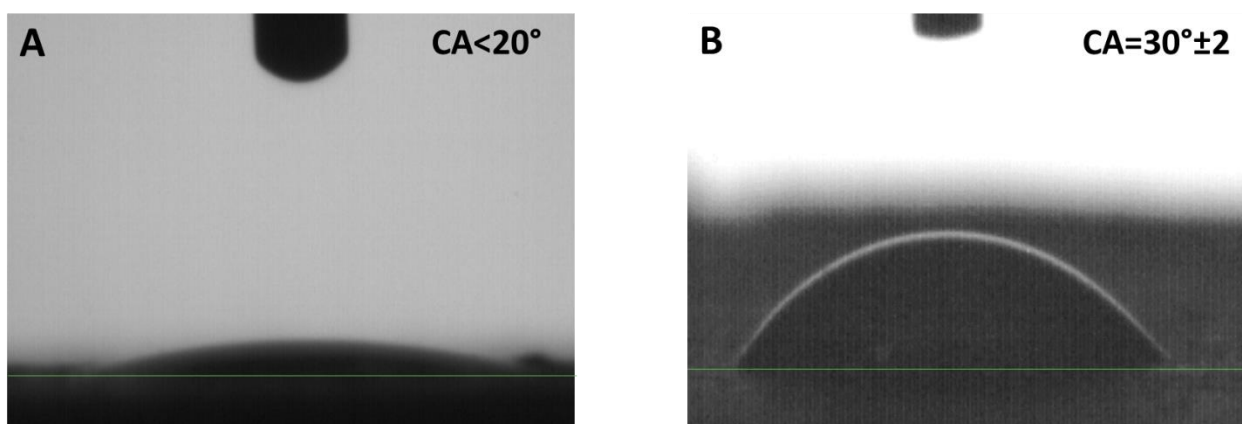


Figure 2.3.18. Contact angle measurements of pristine $m\text{-SiO}_2$ (panel A) and $m\text{-SiO}_2\text{-APTS-ISOST}$ (panel B). The contact angle values are recorded by DSA3 software are 20° for $m\text{-SiO}_2$ and $30^\circ \pm 2$ for $m\text{-SiO}_2\text{-APTS-ISOST}$.

The low increase of contact angle value after the functionalization with ISOST ($30^\circ \pm 2$) witnesses no significant improvement in hydrophobicity, despite the presence of isostearic acid on the surface witnessed by FT-IR measurements (Fig. 2.3.16).

To investigate in depth the type of interaction in the $m\text{-SiO}_2\text{-APTS-ISOST}$ system and to find a possible explanation to the low increase in contact angle value, the sample was also analyzed using the NMR technique. The acquisition of the ^{13}C CPMAS SSNMR spectrum (Fig. 2.3.19) has brought to light some aspects that cannot be investigated only by IR spectroscopy, thanks to the complementarity of the two techniques.

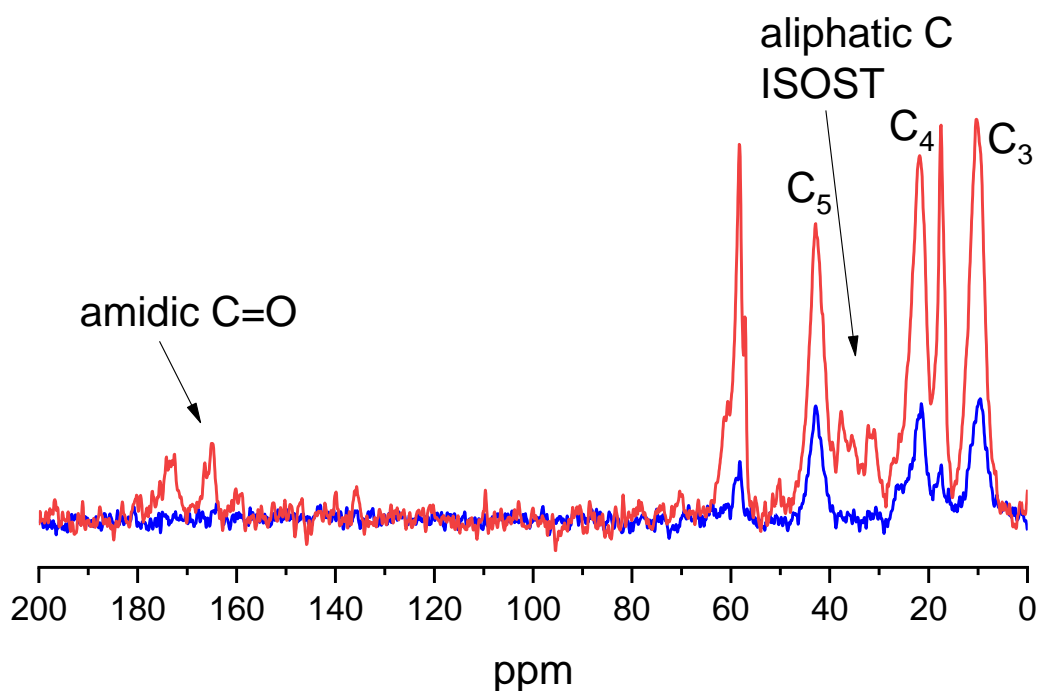


Figure 2.3.19. ^{13}C CPMAS SSNMR spectra: $m\text{-SiO}_2\text{-APTS}$ (blue spectrum) and $m\text{-SiO}_2\text{-APTS-ISOST}$ (red spectrum).

^{13}C CPMAS experiments confirm the presence of APTS and ISOST on silica indicated by IR spectra. In addition, at higher ppm, the presence of signals characteristic of the carboxyl/carbonyl groups of the acid is observed, around 165 and 173 ppm. While the first signal is assigned to an amide bond, the latter one is of difficult assignment, but it indicates the presence of another type of compound bonded to the silica surface. Peaks marked C_3 , C_4 , and C_5 are assigned to the propylic chains of the APTS.

In literature¹³ some undesirable compounds that can be potentially formed during the coupling reaction with DCC are reported; one of these is the spontaneous rearrangement of the *o*-acylisourea in an inactive *N*-acylisourea, and this rearrangement increases in an aprotic solvent such as DMF. In addition, an excess of DCC compared to molecules containing the carboxylate group without the presence of the amine target, leads activated carboxylate to react with another carboxylic acid, forming a symmetrical anhydride (Fig. 2.3.20).

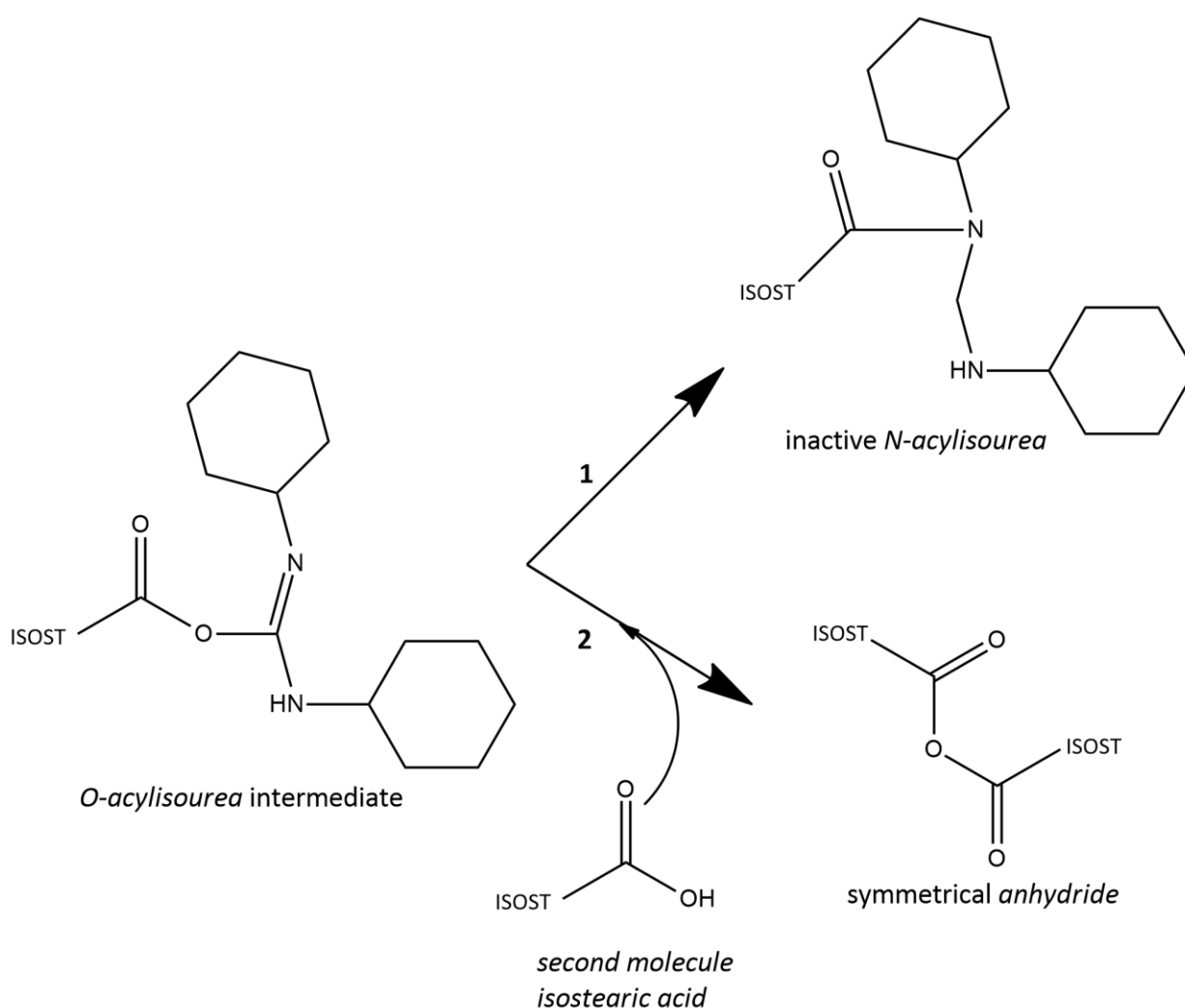


Figure 2.3.20. 1) Spontaneous rearrangement of the intermediate *O*-acylisourea in *N*-acylisourea during the esterification reaction; 2) an excess of carboxylate compounds can generate products such as symmetrical *anhydrides* in the absence of nucleophiles.

Since the functionalization of the m-SiO₂ and A300 were done in parallel, the A300 nanoparticles are functionalized using the same procedure, and in Fig. 2.3.21 it is possible to observe the new spectroscopic pattern:

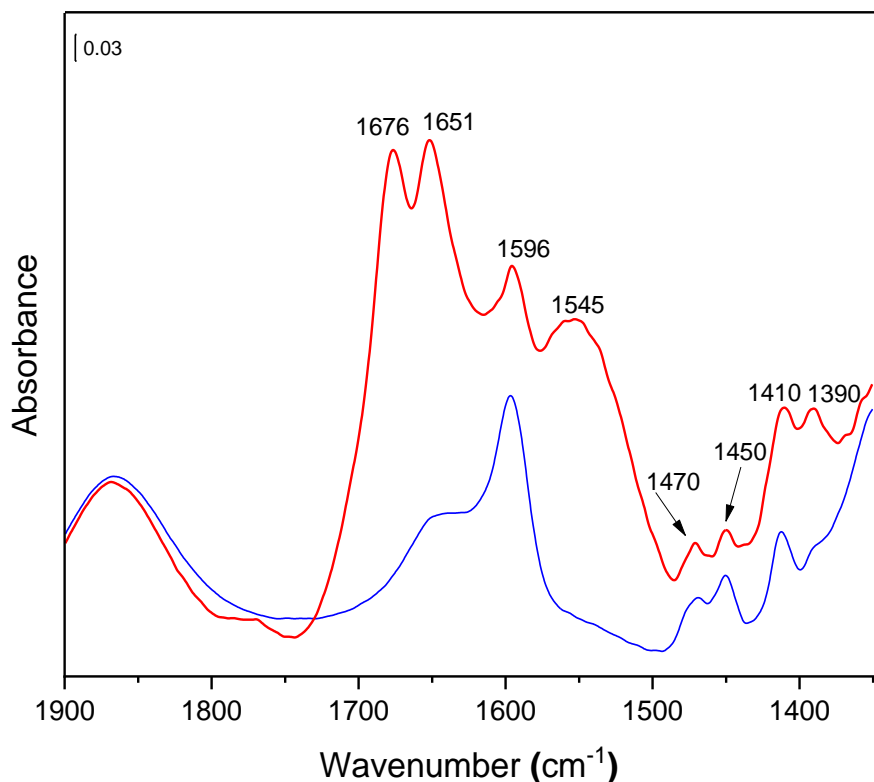


Figure 2.3.21. FT-IR spectra of A300-APTS (blue spectrum) and A300-APTS-ISOST (red spectrum) in 1900-1350 cm⁻¹ region.

In this case it is possible to observe the presence of an additional peak at 1676 cm⁻¹ and, together with the signals at 1650 and 1545 cm⁻¹, represent the typical pattern of an N-acylisourea.¹⁵ Since secondary reaction products were found in both samples of silica nanoparticles (m-SiO₂ and A300) without the increase of contact angle value (even for A300-APTS-ISOST), the next step involved the modification of the protocol.

2.3.6 Improvement of functionalization with isostearic acid: modification of isostearic acid into acyl chloride compound

Since the modification of carboxylic acid in its active ester compound is only one possible pathway to the formation of an amide bond with amine species, an alternative approach has been attempted, involving the transformation of isostearic acid into its corresponding acyl chloride compound (Fig. 2.3.22).

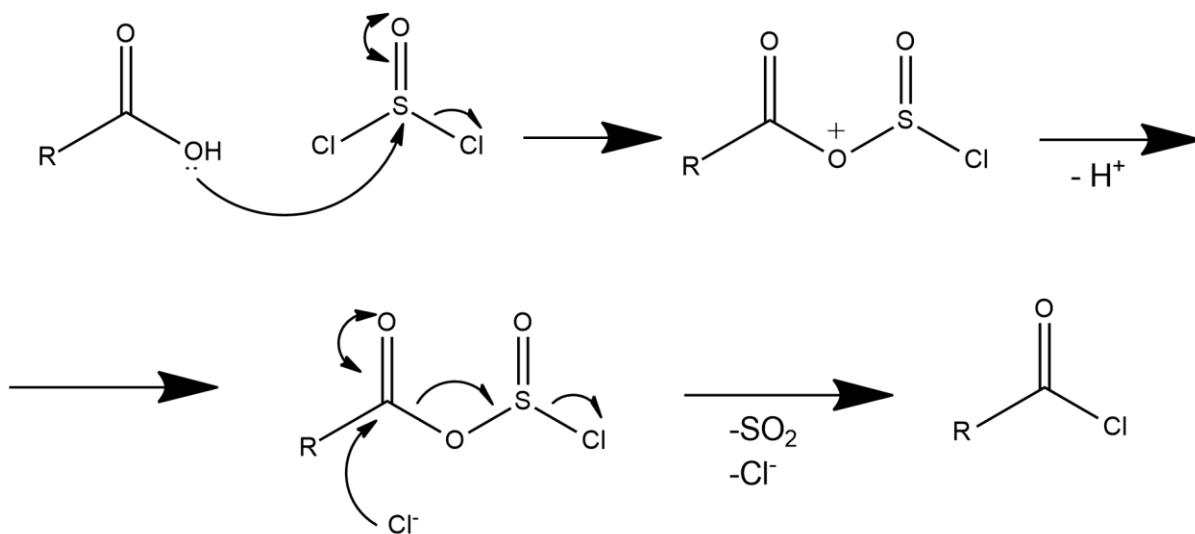


Figure 2.3.22. Synthesis scheme of isostearoyl chloride (2-(4,4-dimethylpentan-2-yl)-5,7,7-trimethyloethanol chloride).

The new reaction protocol has been tested only on commercial silica nanoparticles (A300), as they are the best alternative (for commercial availability and cost) at the industrial application level (Fig. 2.3.23).

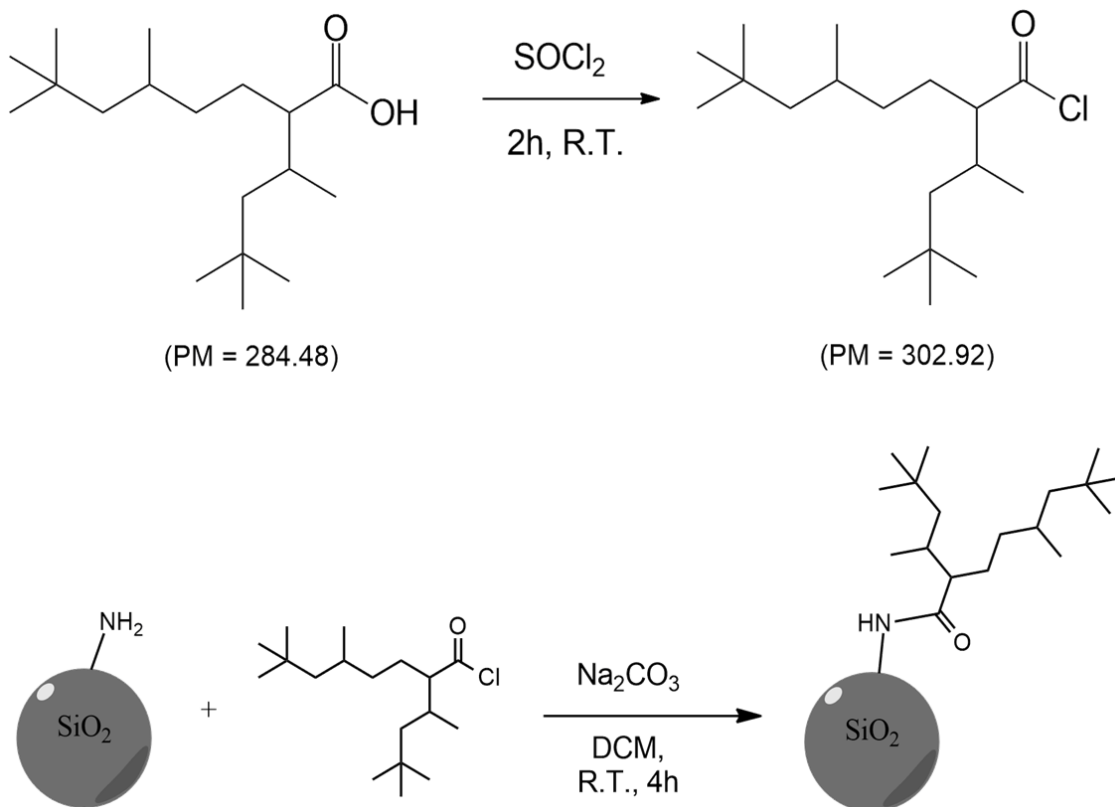


Figure 2.3.23. Functionalization scheme of silica nanoparticles with isostearoyl chloride.

In order to increase the reactivity towards amino groups on the surface of silica, the isostearic acid was preventively modified in isostearoyl chloride. 2.6 mmol of isostearic acid were solubilized in 4 mL of “fresh” thionyl chloride. The reaction occurred for three hours at r.t. under magnetic stirring. Then, the thionyl chloride was removed using a vacuum distillation; further distillations (3-4 times) were carried out adding 5 mL of dichloromethane each time, in order to completely remove the thionyl chloride.

The yield was 99,6 % and, after the distillations, the isostearoyl chloride in a light-yellow oil form was obtained.

After carrying out a series of tests on the best molar ratio between silica nanoparticles and isostearoyl chloride, the table shows the optimal result protocol for the functionalization (Tab. 2.3.2).

Table 2.3.2. Molar ratios of A300-APTS, isostearoyl chloride, Na₂CO₃ and DCM used in the functionalization protocol.

Reagents / solvents	PM (g/mol)	Mass (mg)	Moles (mmol)	Equivalents	Volume (mL)
A300-APTS	-	325	0.162	1	-
Isostearoyl chloride	302.92	148	0.486	3	-
Na ₂ CO ₃	105.99	104	0.972	6	-
DCM	-	-	-	-	10 mL

A300-APTS nanoparticles (1 equivalent), 3 equivalents of isostearoyl chloride and 6 equivalents of sodium bicarbonate (Na₂CO₃) were added together in 10 mL of dichloromethane. The reagents were magnetically stirred at r.t. for 4 hours. The functionalized nanoparticles, from now A300-APTS-ISOST, were then centrifuged and washed with dichloromethane (3x 10 mL, 5000 rpm, 5'), methanol (2x10 mL, 5000 rpm, 5') and water (2x10 mL, 5000 rpm, 5'). The washed material was dried in the oven at 323 K, overnight.

2.3.7 Evaluation of the effectiveness of functionalization and grafting density: IR spectroscopy, SS-NMR and contact angle measurements

As described in previous section, FT-IR analysis was carried out for the characterization of the material after functionalization (Fig. 2.3.24).

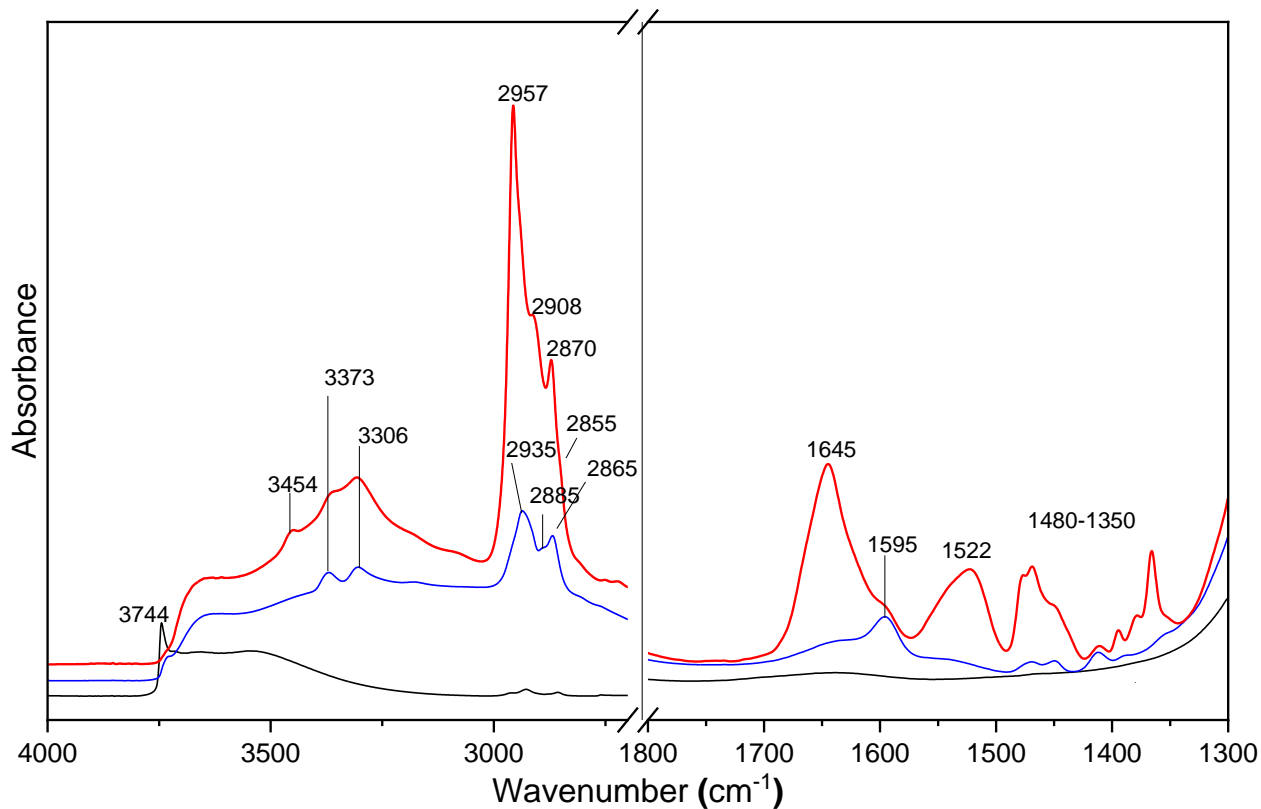


Figure 2.3.24. IR spectra of silica A300 materials in the pristine form (black spectrum) and after functionalization with APTS (blue spectrum) and further functionalization with ISOST (red spectrum) previously converted into isostearyl chloride compound.

Table 2.3.3. List of main IR signals in Fig. 2.3.24 and related assignment.

Bands positions (cm^{-1}) in the IR spectra of			Band Assignment
A300	A300-APTS	A300-APTS-ISOST	
3744			νOH (isolated) ⁸
3700-3200	3700-3200	3700-3200	νOH (H-interacting) ⁸
		3454	νNH (amide) ¹⁰
	3373		$\nu_{\text{asym}}\text{NH}_2$ ¹⁰
	3306		$\nu_{\text{sym}}\text{NH}_2$ ¹⁰
		2957	$\nu_{\text{asym}}\text{CH}_3$ ¹⁰
	2935	2908	$\nu_{\text{asym}}\text{CH}_2$ ¹⁰
	2885	2870	$\nu_{\text{sym}}\text{CH}_3$ ¹⁰
	2865	2855	$\nu_{\text{sym}}\text{CH}_2$ ¹⁰
		1645	νCO (Amide I) ¹⁰
	1596	1596	δNH_2 ¹⁰
		1522	$\nu\text{CN} + \delta\text{NH}$ (Amide II) ¹⁰
		1478	δCH_2 close to $\text{C}-(\text{CH}_3)_3$ ¹⁰
	1468	1468	$\delta_{\text{sym}}\text{CH}_3$ in $\text{C}-\text{CH}_3$ ¹⁰
	1450	1450	δCH_2 ¹⁰
	1412	1412	δCH_2 in CH_2-CH ¹⁰
		1394	$\delta_{\text{sym}}\text{CH}_3$ in $\text{C}-(\text{CH}_3)_3$ ¹⁰
		1380	$\delta_{\text{sym}}\text{CH}_3$ in $\text{C}-\text{CH}_3$ ¹⁰
		1363	$\delta_{\text{sym}}\text{CH}_3$ in $\text{C}-(\text{CH}_3)_3$ ¹⁰

The successful formation of amide bonds in the subsequent functionalization step with ISOST (red curve) is evidenced by the appearance of intense bands at 1645 and 1522 cm^{-1} , in the ranges typical for $\nu\text{C}=\text{O}$ and $\nu\text{CN} + \delta\text{NH}$ mode of amides, and the component at 3454 cm^{-1} , due to the νNH mode of isolated amides, while the alkyl chains of ISOST produced the pattern in the 3000-2800 and 1500-1350 cm^{-1} ranges, in analogy with the previous samples functionalized with the active ester compound of ISOST (Fig. 2.3.16).

The isolation of amide bonds results from the huge steric hindrance of the hyperbranched structure of ISOST. Consequently, the consumption of $-\text{NH}_2$ surface groups is quite limited, as indicated by the slight decrease in intensity of the δNH_2 band at 1596 cm^{-1} , and some fading of the NH_2 ν_{asym} and ν_{sym} doublet at 3373 and 3306 cm^{-1} . This latter appears overlapped to a slightly more intense broad band due to interacting silanols, resulting from the perturbation of these groups by the newly anchored molecules (also responsible for the complete depletion of the signal at 3744 cm^{-1}).

In this case, the SS-NMR analysis of the ^{13}C -CPMAS spectrum of A300-APTS-ISOST (Fig. 2.3.25) clearly reported the presence of only one peak at 178 ppm, typical of an amide $\text{C}=\text{O}$, without the presence of other peaks referred to side products.

^{13}C -CPMAS

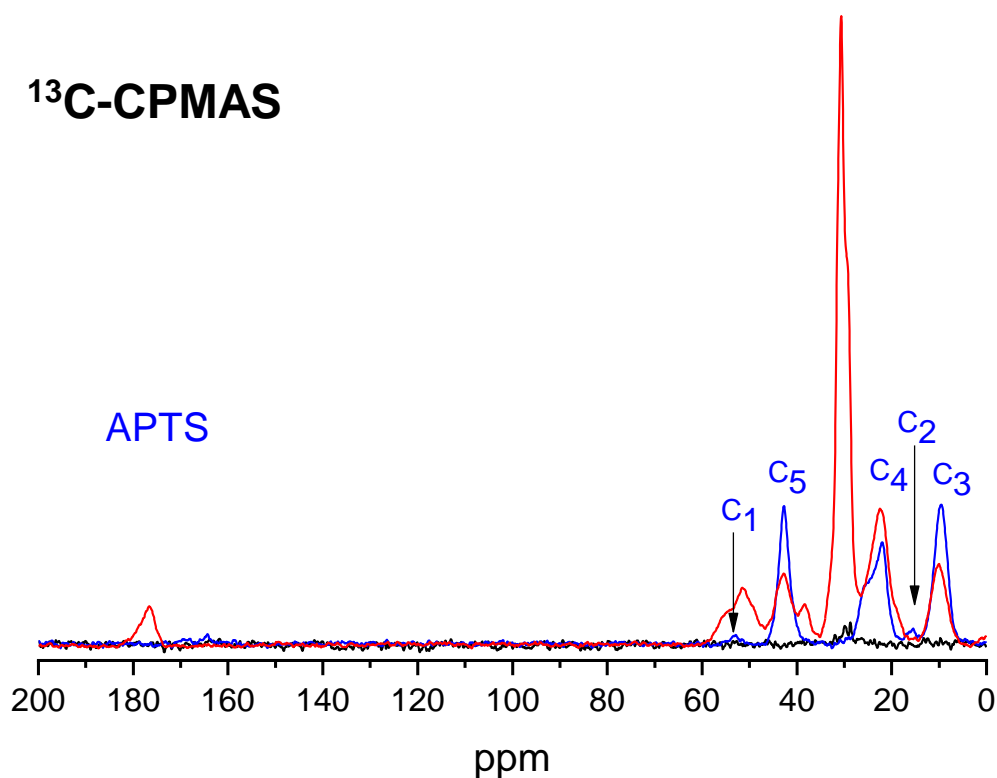


Figure 2.3.25. ^{13}C -CPMAS NMR spectra of A300 (black curve), A300-APTS (blue curve), and A300-APTS-ISOST (red curve).

The number of ISOST molecules on the A300 silica surface, calculated from the mixture method explained previously, results in ca. 0.3 molec/ nm^2 (Fig. 2.3.26). This roughly corresponds to a density of 1 grafted molecule every 10 nm^2 (square ca. 3.2x3.2 nm).

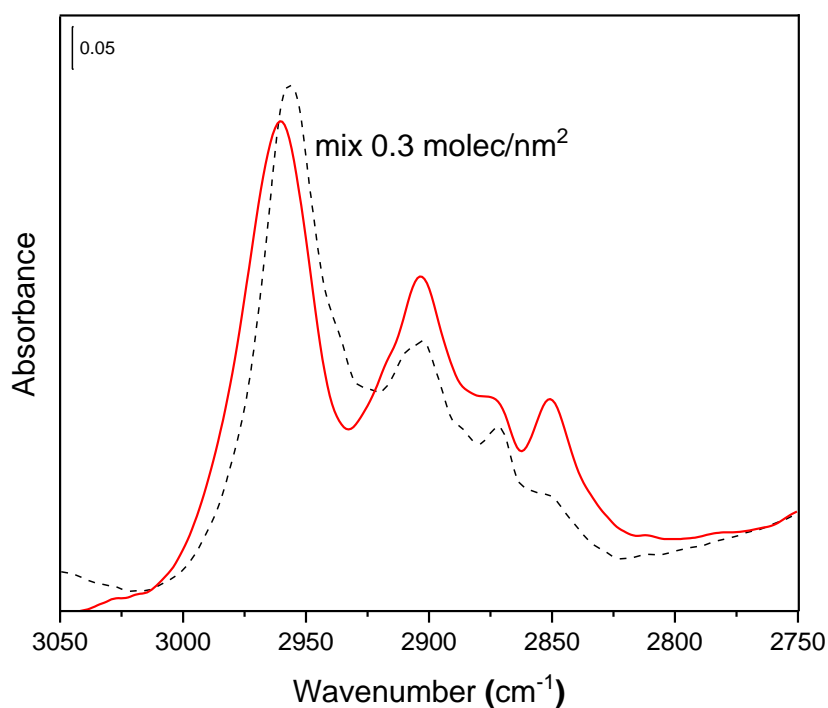


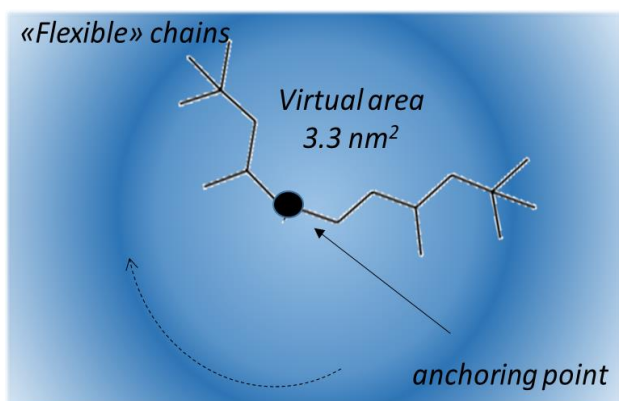
Figure 2.3.26. FT-IR spectra of A300-APTS-ISOST (red curve) and mixture with 0.3 molecules of ISOST/ nm^2 (dashed black curve).

In order to give a physical interpretation of the obtained values, the surface covered by one grafted molecule obtained by APTS+ISOST was calculated as follows:

- taking into account the structure of the acid that is used, which has a very branched structure, so there are more -CH₃ (8) than -CH₂ (4) and -CH (3) groups;
- bearing in mind the formula used to determine the critical length (*l_c*) of alkyl chains in micelles (*l_c*: maximum length of the chain before giving rise to repulsive interactions with diametrically opposite chains):

$$l_c \leq (0.154 + 0.1265 \times n) \text{ nm, where } n \text{ is the number of carbon atoms;}^{16}$$

- taking into account a free rotation around the C₅ atom of the main chain connecting it to the carboxylic group then transformed into an acyl chloride, then transformed into an amide group in the anchorage to the surface by reaction with the NH₂ groups; the portion of the circular-shaped surface that can be assumed to be "covered" by an anchored carboxylic acid that rotates around the anchoring point (C₅) is equal to ca. 3.3 nm², which corresponds to about 3 molecules per 10 nm² (0.3 molec/nm²). The surface density value obtained by the quantification method based on IR measurements is therefore far from negligible.



Moreover, contact angle measurements were performed to assess the achievement of surface hydrophobicity (Fig. 2.3.27).

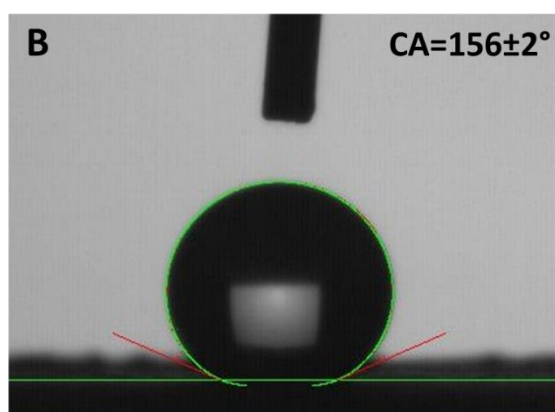
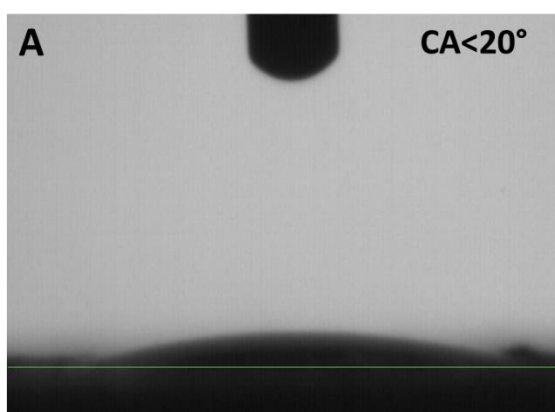


Figure 2.3.27. Contact angle measurements of pristine A300 (panel A) and A300-APTS-ISOST (panel B). The contact angle values recorded by DSA3 software are 20° for A300 and 156°±2 for A300-APTS-ISOST.

The measurements of static contact angle on the self-supporting pellets show for the A300-APTS-ISOST (Fig. 2.3.27, panel B) a value of contact angle of 156°; this value is greater than 150° (the limit value to consider a material as superhydrophobic), consequently the presence of the highly

branched carbon chains of the isostearic acid on the surface of silica nanoparticles allows to obtain a superhydrophobic surface, compared to the hydrophilic behaviour of the unmodified silica nanoparticles ($\theta < 20^\circ$, Fig. 2.3.27 panel A).

It can therefore be said that the sample of A300 functionalized with the acyl chloride compound of ISOST (isostearoyl chloride) is the one that gave the most satisfactory results in terms of increase of hydrophobicity.

Bibliographic References

1. Hermanson, G. T., Chapter 13 - Silane Coupling Agents. In *Bioconjugate Techniques (Third Edition)*, Hermanson, G. T., Ed. Academic Press: Boston, **2013**; pp 535-548.
2. Zhuravlev, L. T., The surface chemistry of amorphous silica. Zhuravlev model. *Colloids and Surfaces A: Physicochemical and Engineering Aspects* **2000**, *173* (1), 1-38.
3. Bolis, V.; Fubini, B.; Marchese, L.; Martra, G.; Costa, D., Hydrophilic and hydrophobic sites on dehydrated crystalline and amorphous silicas. *Journal of the Chemical Society, Faraday Transactions* **1991**, *87* (3), 497-505.
4. Rimola, A.; Costa, D.; Sodupe, M.; Lambert, J.-F.; Ugliengo, P., Silica Surface Features and Their Role in the Adsorption of Biomolecules: Computational Modeling and Experiments. *Chemical Reviews* **2013**, *113* (6), 4216-4313.
5. Gallas, J.-P.; Goupil, J.-M.; Vimont, A.; Lavalley, J.-C.; Gil, B.; Gilson, J.-P.; Miserque, O., Quantification of Water and Silanol Species on Various Silicas by Coupling IR Spectroscopy and in-Situ Thermogravimetry. *Langmuir* **2009**, *25* (10), 5825-5834.
6. Catalano, F.; Alberto, G.; Ivanchenko, P.; Dovbeshko, G.; Martra, G., Effect of Silica Surface Properties on the Formation of Multilayer or Submonolayer Protein Hard Corona: Albumin Adsorption on Pyrolytic and Colloidal SiO₂ Nanoparticles. *The Journal of Physical Chemistry C* **2015**, *119* (47), 26493-26505.
7. Alberto, G.; Caputo, G.; Viscardi, G.; Coluccia, S.; Martra, G., Molecular Engineering of Hybrid Dye-Silica Fluorescent Nanoparticles: Influence of the Dye Structure on the Distribution of Fluorophores and Consequent Photoemission Brightness. *Chemistry of Materials* **2012**, *24* (14), 2792-2801.
8. Takeuchi, M.; Bertinetti, L.; Martra, G.; Coluccia, S.; Anpo, M., States of H₂O adsorbed on oxides: An investigation by near and mid infrared spectroscopy. *Applied Catalysis A: General* **2006**, *307* (1), 13-20.
9. Liu, S.; Zhang, H.-L.; Liu, T.-C.; Liu, B.; Cao, Y.-C.; Huang, Z.-L.; Zhao, Y.-D.; Luo, Q.-M., Optimization of the methods for introduction of amine groups onto the silica nanoparticle surface. *Journal of Biomedical Materials Research Part A* **2007**, *80A* (3), 752-757.
10. Colthup, N.; Daly, L.; Wiberley, S., *Introduction to Infrared and Raman Spectroscopy*. 3rd ed.; Academic Press: **1990**.
11. Sartori, G.; Bigi, F.; Maggi, R.; Sartorio, R.; Macquarrie, D. J.; Lenarda, M.; Storaro, L.; Coluccia, S.; Martra, G., Catalytic activity of aminopropyl xerogels in the selective synthesis of (E)-nitrostyrenes from nitroalkanes and aromatic aldehydes. *Journal of Catalysis* **2004**, *222* (2), 410-418.
12. Nakajima, N.; Ikada, Y., Mechanism of Amide Formation by Carbodiimide for Bioconjugation in Aqueous Media. *Bioconjugate Chemistry* **1995**, *6* (1), 123-130.
13. Hermanson, G. T., Chapter 3 - The Reactions of Bioconjugation. In *Bioconjugate Techniques (Third Edition)*, Hermanson, G. T., Ed. Academic Press: Boston, **2013**; pp 229-258.
14. Staros, J. V., N-hydroxysulfosuccinimide active esters: bis(N-hydroxysulfosuccinimide) esters of two dicarboxylic acids are hydrophilic, membrane-impermeant, protein cross-linkers. *Biochemistry* **1982**, *21* (17), 3950-3955.
15. Ramazani, A. L. I.; Nasrabadi, F. Z.; Rezaei, A.; Rouhani, M.; Ahankar, H.; Asiabi, P. A.; Joo, S. W.; ŚLepokura, K.; Lis, T., Synthesis of N-acylurea derivatives from carboxylic acids and N,N'-dialkyl carbodiimides in water. *Journal of Chemical Sciences* **2015**, *127* (12), 2269-2282.
16. Becerra, N.; Toro, C.; Zanocco, A. L.; Lemp, E.; Günther, G., Characterization of micelles formed by sucrose 6-O-monoesters. *Colloids and Surfaces A: Physicochemical and Engineering Aspects* **2008**, *327* (1-3), 134-139.

2.4 A COMPARISON BETWEEN ALUMINA AND SILICA MATERIALS: BEHAVIOUR TOWARDS LIQUID WATER AND WATER VAPOURS

2.4.1 On the origin of superhydrophobic surfaces

Superhydrophobicity is an important required characteristic for materials that must show non-wetting properties. Many industrial fields (textile, leather, paper, electronics, etc) involve the use of this kind of materials as a barrier to water. The subsequent self-cleaning properties, derived from the high hydrophobicity, fulfill the required characteristics for solar energy panels, exterior glass and heat transfer surfaces in air conditioning equipment.¹

A primary indication of the hydrophilicity/hydrophobicity of a surface is the measurement of contact angle; as already mentioned, a superhydrophobic surface is characterized by a contact angle greater than 150°. ² Although the presence of non-polar molecules exposed on the surface (e.g. hydrocarbons) reflects the intrinsic hydrophobic chemistry of the material, another requirement, in order to enhance the water-repellency, is surface roughness, that allows to reach superhydrophobicity ($\theta > 150^\circ$).³

The specific construction of micro-nano-hierarchical structure on the surface combined with a low surface energy is inspired by nature; these characteristics are intrinsically present on several primary part of the plants⁴ and in particular in Lotus leaf, from which the “Lotus Effect” takes its name from.⁵ This kind of topography forms air gaps between microstructures that are totally repellent towards water.⁶

Several works on the preparation of superhydrophobic materials^{3, 7, 8} are based on the relation between superhydrophobicity and the presence of microstructure on the surface. The investigation of the hydrophobicity through contact angle analyses and SEM images are carried out on samples that are sprayed on a surface, as films or hydrophobic coatings. In this work, the contact angle measurements and the SEM analyses were performed in a different way, using self-supporting pellets of the non-functionalized and functionalized materials (see section 2.4.4).

Another aspect of a hydrophobic material is the low adsorption towards water vapors. Although several papers (mentioned above) on the preparation of superhydrophobic materials reported only the macroscopic behaviour towards water (contact angle measurements), in this work the attention was drawn also to molecular aspects. Microgravimetric analyses were performed in order to calculate the number of water molecules adsorbed per nm², while the Near-IR spectroscopy highlighted the states of adsorbed water on non-functionalized and functionalized materials.

Moreover, in the microcalorimetric studies of Fubini et al.,⁹ some aspects of water vapor reactivity on oxides were evidenced; in particular, it is possible to evaluate the hydrophilicity/hydrophobicity of the system through adsorption microcalorimetry. Based on the Brunauer classification,¹⁰ a water sorption isotherm of type III is typical of hydrophobic surfaces, while the type I and II correspond to hydrophilic materials. Furthermore, microcalorimetric analysis allows to evaluate the homogeneity/heterogeneity of the surface, in energetic terms, considering the heat of adsorption.

In order to clarify the different aspects, this chapter has been divided in three main parts:

- Study at the molecular level of the behaviour of the already mentioned materials (AluC, AluC-ISOST and A300, A300-APTS, A300-APTS-ISOST) towards water vapors, to assess the high/low adsorption capacity, compared to the reactivity towards water of the hydrophobic commercial materials (AluC805 and AR812) (section 2.4.2).
- Study of the morphological features through SEM analyses of the hydrophobic materials that showed high contact angle values (section 2.4.3).
- Interpretation of the unexpected results obtained in the previous sections based on the chemical structure of the hydrophobic agent used in the functionalization of alumina and silica materials (section 2.4.4).

2.4.2 Interaction of pristine and functionalized nanoparticles with water vapor: microgravimetric analysis, Near-IR spectroscopy, and microcalorimetric analysis

One of the main targets of this part of the work was the investigation of the effect of surface functionalization (both for alumina and silica nanoparticles) on the behaviour towards water vapor, by measuring amount, spectroscopic and energetic features of adsorbed H₂O molecules. As for the amount, microgravimetric water sorption isotherms were measured at 30 °C. For the sake of comparison, commercial hydrophobic alumina (AluC805) and silica (AR812) nanoparticles were also considered. The samples were pre-outgassed at 30°C for 8 hours (residual pressure > 1×10⁻³ mbar). Then water vapors adsorption-desorption cycles were repeated twice. The water uptake values reported in the Figures are referred to 100 m² for each sample.

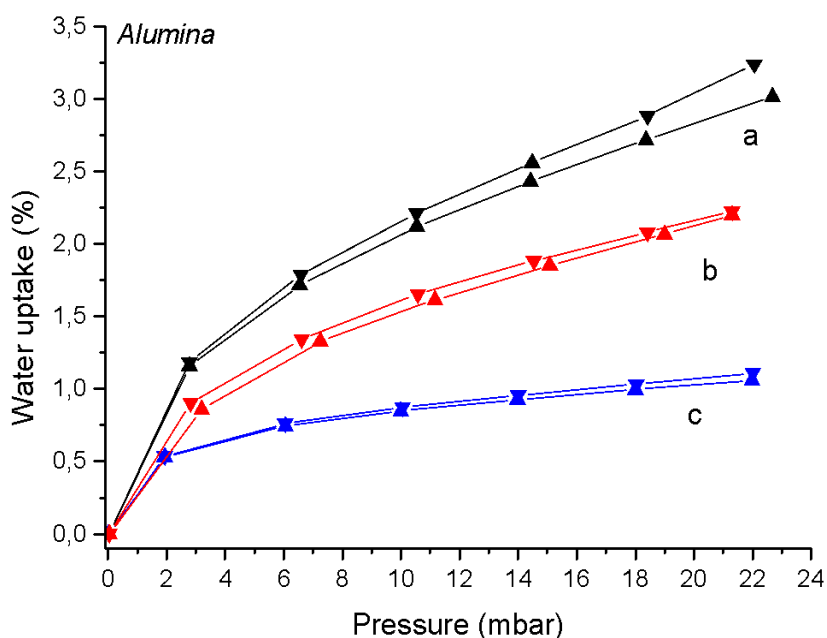


Figure 2.4.1. Microgravimetric measurements of water adsorption and desorption at 30°C. AluC (black isotherms, a), AluC-ISOST (red isotherms, b) and AluC805 (blue isotherms, c). Isotherms with “>” are adsorption isotherms; “<” are referred to desorption isotherms. Y-axis values are referred to 100 m² for each sample.

In Fig. 2.4.1 it is possible to notice that at lower vapor pressures (until 2 mbar) the amount of adsorbed water is very similar for the functionalized alumina (AluC-ISOST, red curve) and for the hydrophobic commercial one (AluC805, blue curve). At higher vapor pressures, AluC805 adsorbs a smaller amount of water, compared to AluC-ISOST. The pristine form of alumina (AluC, black curve) adsorbs the highest amount of water, even at lower water pressures.

For silica, the isotherms are collected following the same procedure as used for alumina and they are reported in Fig. 2.4.2.

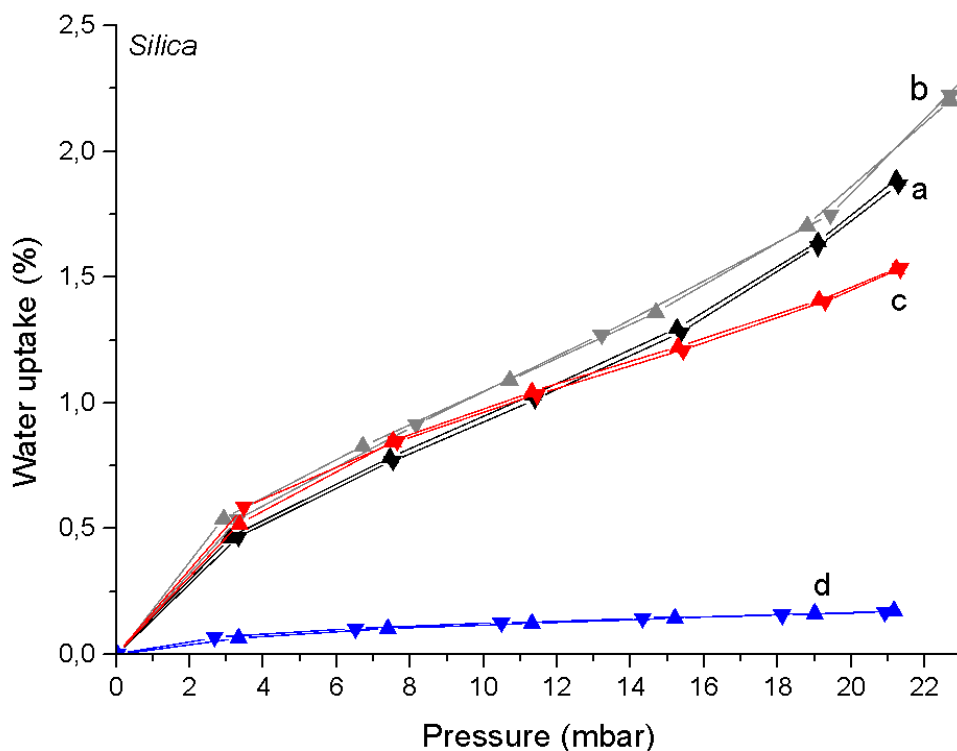


Figure 2.4.2. Microgravimetric measurements of water adsorption and desorption at 30°C. A300 (black isotherms, a), A300-APTS (grey isotherms, b), A300-APTS-ISOST (red isotherms, c) and AR812 (blue isotherms, d). Isotherms with “>” are adsorption isotherms; “<” are referred to desorption isotherms. Y-axis values are referred to 100 m² for each sample.

These data (normalized to the coefficient related to SSA) allow to observe a different behavior towards water of the A300 series, compared to the hydrophobic commercial material, even at lower vapor pressures. The amount of adsorbed water is very low for the AR812 (blue curve). The isotherms for A300 (functionalized and pristine) materials show a similar water adsorption for pressures below 10-12 mbar. After this point, the trend changes, and the A300-APTS-ISOST (red curve) results to be the material that adsorbs the lowest amount of water, compared to the A300 (black curve) and A300-APTS (grey curve). The surface-exposed amino groups of APTS contribute to increase of the water adsorption capacity of the A300, where only SiOH are effective in the interaction with H₂O molecules.

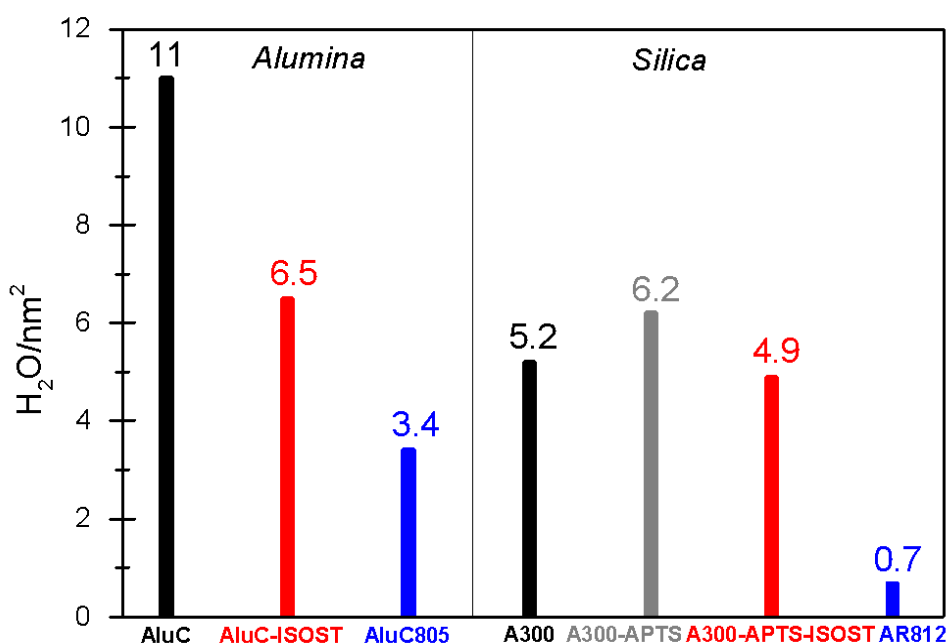


Figure 2.4.3. Specific water adsorption capability of alumina (AluC, AluC-ISOST, AluC805) and silica (A300, A300-APTS, A300-APTS-ISOST, AR812) materials. The number of water molecules adsorbed per nm² at 30 °C and 20 mbar is reported on top of the bars.

For a more comprehensive comparison, the number of adsorbed water molecules per nm² was calculated, combining microgravimetric data (water uptake per mg of sample, measured at 30 °C with water vapor at $p = 20$ mbar, i.e. the maximum pressure reached during microgravimetric measurements) with SSA_{BET} values, obtaining the specific capability to adsorb water of the materials (Fig. 2.4.3). Bare AluC shows the highest specific adsorption capability (11 H₂O/nm²), that is decreased by only ca. 40% by functionalization with ISOST (6.5 H₂O/nm²), being ca. two times higher of that showed by commercial AluC805 (3.4 H₂O/nm²).

Passing to silica, bare A300 seems able to adsorb less water molecules per surface unit (5.2 H₂O/nm²) than bare AluC, whilst the capability was slightly increased after functionalization with APTS (6.2 H₂O/nm²), likely because of the replacement of some isolated silanols (unable to adsorb water at r.t.)¹¹⁻¹³ with moieties terminated by the -NH₂ group, more effective in the interaction with H₂O molecules.¹⁴ The subsequent functionalization with ISOST resulted in a quite limited decrease (ca. 10%) of the specific capability to adsorb water (4.9 H₂O/nm²), definitely larger than the very poor capability shown by commercial AR812 (0.7 H₂O/nm²).

In order to assess possible effects of the presence of ISOST on the states of adsorbed water molecules, NIR spectra of pristine and functionalized nanoparticles in contact with water vapor at decreasing pressure were collected (Fig. 2.4.4). The focus was on the pattern due to the $\nu_{asym} + \delta$ combination mode of adsorbed molecules, falling in a range (5500-4600 cm⁻¹) free from contribution from surface hydroxy groups, unlike the ν_{OH} range in the mid-IR. The analysis of such pattern is highly effective for obtaining information on the state of water molecules; the number and strength of H-bonding donations experienced by water molecules influences the broadness and entity of shift to lower frequency of the resulting $\nu_{asym} + \delta$ band.¹⁴

Moreover, the state of adsorbed water molecules depends on the surface coverage. As reported in microgravimetric analyses, the maximum water coverage decreases when passing from AluC to

AluC-ISOST and from A300-APTS to A300-APTS-ISOST (\sim A300) (Fig. 2.4.3). Hence, for AluC and A300-APTS only spectra taken at surface coverages similar to those attained on the corresponding functionalized materials (and A300, for the silica-based set of nanoparticles) were considered for the comparison.

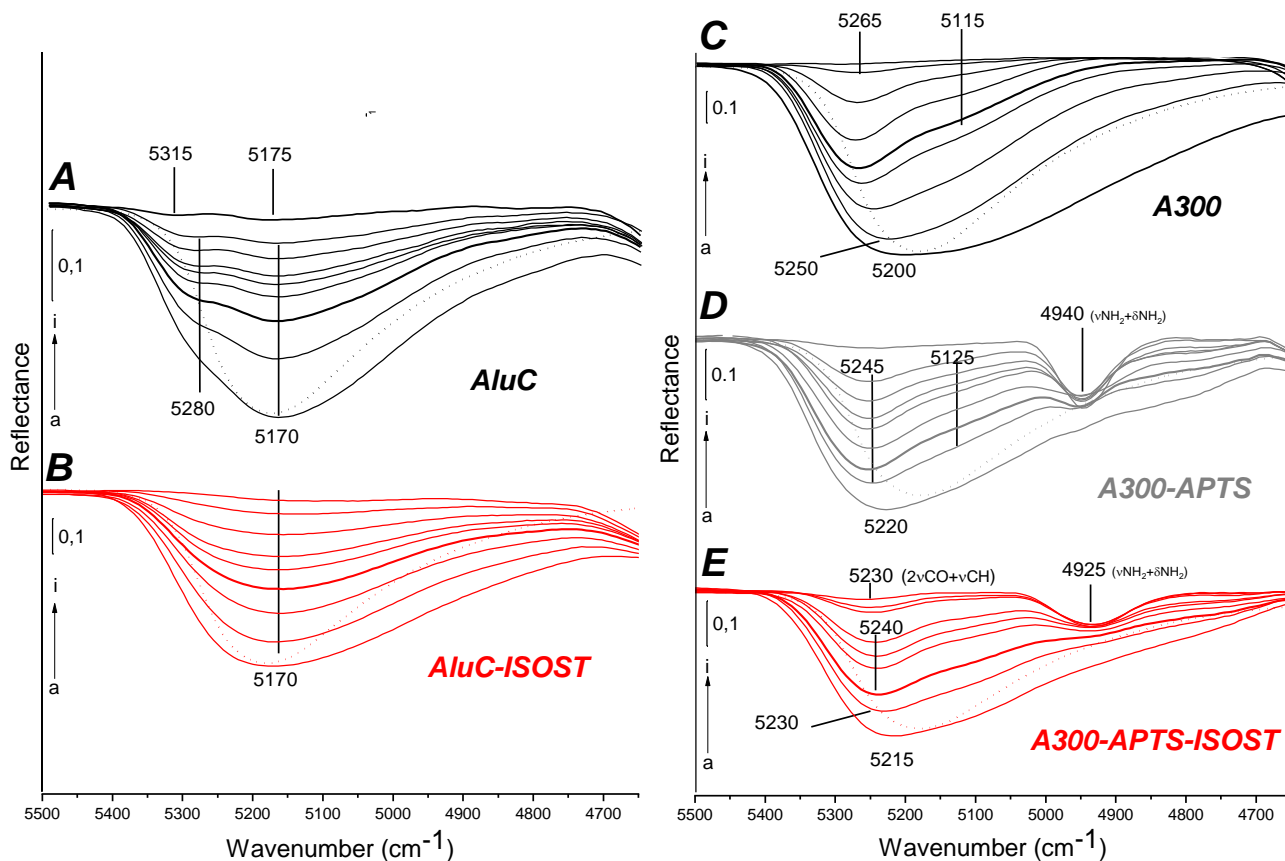


Figure 2.4.4 NIR spectra of water adsorbed over alumina (left) and silica (right) materials: AluC (panel A), AluC-ISOST (panel B), A300 (panel C), A300-APTS (panel D), A300-APTS-ISOST (panel E). The spectra are recorded in equilibrium with water vapor pressure (curves ‘a’) followed by stepwise outgassing (curves ‘b’-‘h’) until invariance of the spectra (curves ‘i’). The thickest curves in each panel represent the spectrum acquired in air.

The $\nu_{\text{asym}}+\delta$ patterns obtained for H_2O molecules adsorbed on AluC and AluC-ISOST are shown in panels A and B (Fig. 2.4.4). In both of them, the spectrum of bulk water is reported for comparison, also (dotted line). Starting with bare AluC (panel A), the spectrum at the maximum water coverage considered (curve ‘a’) shows a main component at 5170 cm^{-1} , accompanied by a shoulder at 5280 cm^{-1} . The main component appears located at lower frequency with respect to the $\nu_{\text{asym}}+\delta$ signal of bulk water (at 5180 cm^{-1}), and shows a wider asymmetric broadening towards the low frequency side. Both features indicated that most part of adsorbed water molecules are experiencing H-bonding interactions (as donors) slightly stronger than what is occurring among H_2O molecules in liquid water. Conversely, the shoulder at 5280 cm^{-1} is due to molecules at the actual interface between the adsorbed and the vapor phase, expected to point at least one -OH towards the exterior, also indicated as “dangling” -OH moieties.^{14, 15} This shoulder progressively gains in relative intensity by decreasing the water coverage, in agreement with an increase of the relative amount of interfacial water molecules with respect the total amount of adsorbed ones. After outgassing at r.t.

(curve 'i'), only very weak signals at 5315 cm^{-1} and 5175 cm^{-1} remain, due to water molecules coordinated to surface Al^{3+} sites with a high coordinative unsaturation level (see section 2.2.3). Apparently, these molecules are oriented with one OH pointing outward (signal at higher frequency) and the other interacting via H-bonding with a surface O atom (signal at lower frequency).

The presence of isostearic moieties has a not negligible impact on the states of water adsorbed on AluC-ISOST (panel B). The main component of the $\nu_{\text{asym}}+\delta$ signal of adsorbed H_2O still shows the same position, whilst it appears significantly broader on the lower frequency side than in the previous case, as inferred by the comparison with the signal of bulk water. This behaviour indicates the reinforcement of H-bonds involving some adsorbed H_2O molecules. Such behaviour might result from the interaction of these molecules with the oxygen atoms of the carboxylate groups anchoring ISOST molecules to the alumina surface.¹⁶ Interestingly, the shoulder at high frequency due to dangling $-\text{OH}$ pointing towards the exterior is almost absent. A similar behaviour was observed in the mid-IR for H_2O molecules at a liquid water/hexene interface, where the component to interfacial "dangling" OH appeared significantly less intense with respect the corresponding signal observed for liquid water/water vapour or CCl_4 interfaces.¹⁵ Thus, the significant decrease in the intensity of the high frequency shoulder can monitor the occurrence of an actual interaction between adsorbed water molecules and overlying alkyl branches of anchored ISOST molecules.

A second, expected effect, is the complete desorption of water molecules by outgassing at r.t., indicating that surface Al^{3+} sites with a higher coordinative unsaturation level are among those involved in the coordination of carboxylate groups allowing the anchoring of ISOST molecules to the surface.

Similar spectral feature and evolution by decreasing the water coverage were observed for commercial AluC805 (Fig. 2.4.5).

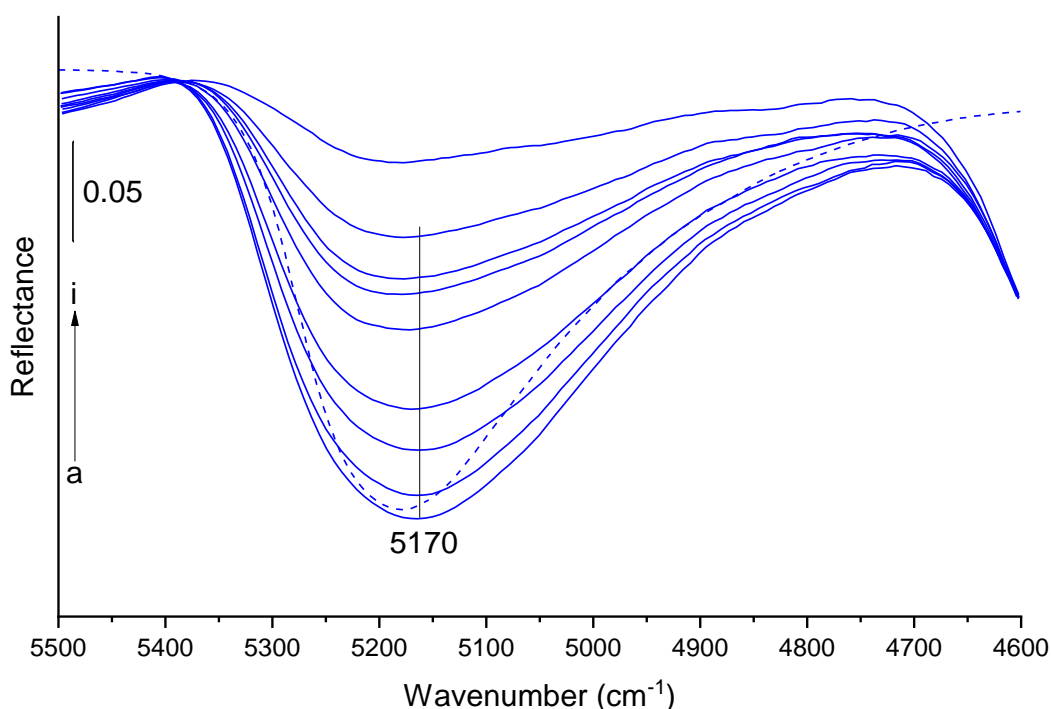


Figure 2.4.5. NIR spectra of AluC805 in the region $5500\text{-}4600\text{ cm}^{-1}$. The spectra are recorded in presence of water vapor pressure (curves 'a') and during outgassing steps (from 'b' to 'i').

The analysis of the set of spectra obtained for commercial AluC805 led to similar conclusions, compared to AluC: main part of the H-bonding network involving water molecules, adsorbed in a further lower amount ($3.4 \text{ H}_2\text{O}/\text{nm}^2$) with respect to the previous cases, is similar to that present for H_2O on AluC and AluC-ISOST at similar water coverage, and the high frequency component is absent, indicating that also in this case an interaction with alkyl chains (of a C8 type) should occur.

Passing to the silica-based set of nanoparticles (Fig. 2.4.4, panels C-E), the $\nu_{\text{asym}}+\delta$ signal of water adsorbed on A300 at maximum surface coverage shows a reflectance minimum at 5200 cm^{-1} (panel C). The spectral evolution at decreasing coverages indicates that such shape results from the overlapping of a broad component widely asymmetric on the low frequency side, progressively evolving in a shoulder at 5155 cm^{-1} and a narrower component progressively becoming the dominant one and shifting from 5250 to 5265 cm^{-1} . In comparison with the case of water on AluC (panel A), the relative intensity of these high and low frequency components appears reversed, indicating that a larger fraction of H_2O adsorbed on A300 should point towards the exterior one or both -OH moieties (responsible for the high frequency component). Moreover, the downshift of the low frequency component indicates that the remaining part of -OH moieties are involved in stronger H-bonds.

In the case of A300-APTS (panel D), the presence of grafted APTS increases the complexity of the interaction with water, because $-\text{NH}_2$ groups can act as adsorbing sites for H_2O molecules, and water adsorbed on remaining surface silanols can also interact with the apolar moieties of APTS, namely the propyl chain and the ethoxy groups that resisted hydrolysis, as already seen in SS-NMR measurements (see section 2.3.3). The role of $-\text{NH}_2$ groups as adsorbing sites is clearly indicated by the behaviour of the signal at 4940 cm^{-1} due to their $\nu_{\text{asym}}+\delta$ mode, progressively gaining in definition and intensity as the water coverage is decreased, clearly indicating that they are involved in the interaction with H_2O molecules.

Focusing on the spectral pattern due to adsorbed water, the low frequency component due to H-bonded -OH moieties appears even less pronounced and slightly upshifted with respect to the case of H_2O molecules on bare A300, indicating some weakening of H-bonds. The high frequency component due to -OH moieties pointing toward the exterior is conversely downshifted of ca. 20 cm^{-1} . On the basis of the downshift of ca. 30 cm^{-1} observed in the mid-IR for interfacial -OH of water when passing from the liquid/vapour interface to the liquid/ CCl_4 and liquid/hexane ones,¹⁵ such a change in position might result from the interaction with the apolar moieties of grafted APTS.

The additional presence of ISOST chains has a limited impact on the spectral profile of water adsorbed on A300-APTS-ISOST (panel E), likely because of the similarity of their interaction with underlying H_2O molecules with those of these latter with the apolar moieties of anchored APTS. Indeed, the main effect is a further 5 cm^{-1} downshift of the H_2O $\nu_{\text{asym}}+\delta$ component due to -OH moieties pointing toward the exterior, in agreement with the increase of the apolar character of the interface overlying adsorbed water molecules. Noteworthy, also $-\text{NH}_2$ groups of anchored APTS that were non consumed in the conjugation with ISOST molecules seem to experience an interaction with ISOST chains similar to that proposed for water, because the $-\text{NH}_2$ $\nu_{\text{asym}}+\delta$ appears now 10 cm^{-1} lower in frequency than in the case of A300-APTS.

Finally, the very signal at 5230 cm^{-1} remaining after water outgassing is probably due to the overtone/composition mode of $2\nu_{\text{CO}}+\nu_{\text{CH}}$ of the ISOST linked to the surface.

The situation was totally different for commercial hydrophobic silica (AR812) and the equivalent data are reported in Fig. 2.4.6.

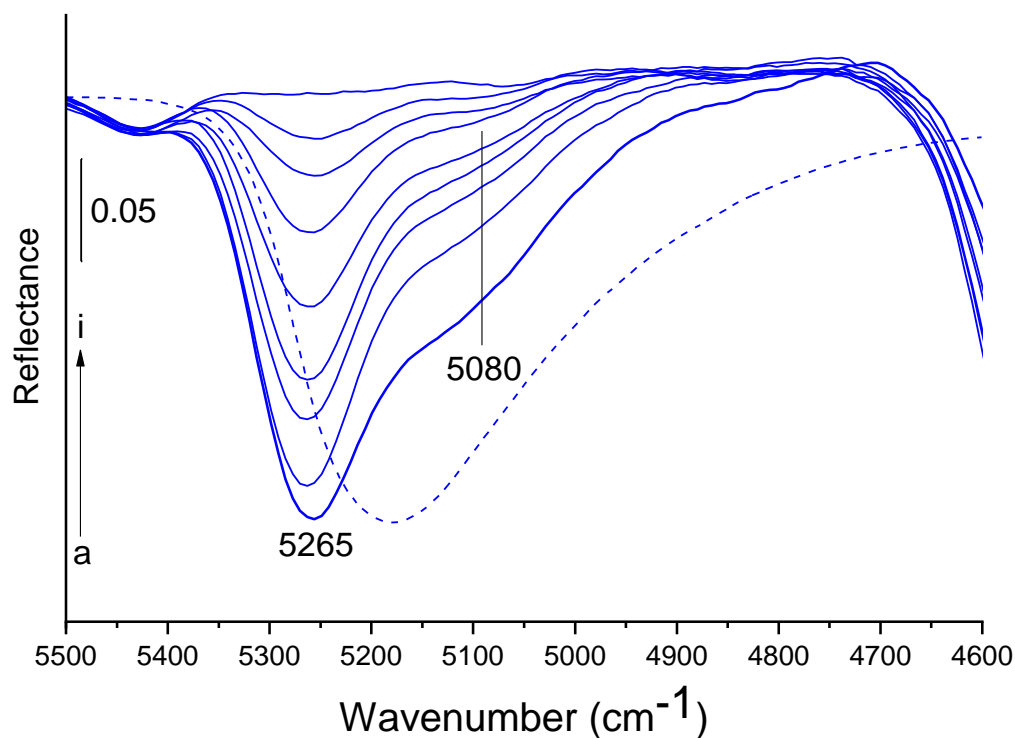


Figure 2.4.6. NIR spectra of water on AR812 in the 5500-4600 cm^{-1} range. The spectra are recorded in presence of water vapor pressure (curves 'a') and during outgassing steps (from 'b' to 'i').

The spectra of the few H_2O molecules adsorbed on commercial AR812 ($0.7 \text{ H}_2\text{O}/\text{nm}^2$ at maximum coverage, see microgravimetric analyses, Fig. 2.4.3) are dominated by the component due to "dangling" -OH moieties (5265 cm^{-1}). Noteworthy, the interaction of these moieties with the alkyl groups bound to the surface should be very weak, if any, because their spectral feature appears downshifted of only a few cm^{-1} with respect to the corresponding signal in the spectra of water on A300 and A300-APTS.

For the sake of completeness, the NIR spectra for alumina (Fig. 2.4.7) and silica (Fig. 2.4.8) materials in 8000-4000 cm^{-1} region are reported and commented, except for the part referred to the water interaction ($5500\text{-}4600 \text{ cm}^{-1}$) already explained.

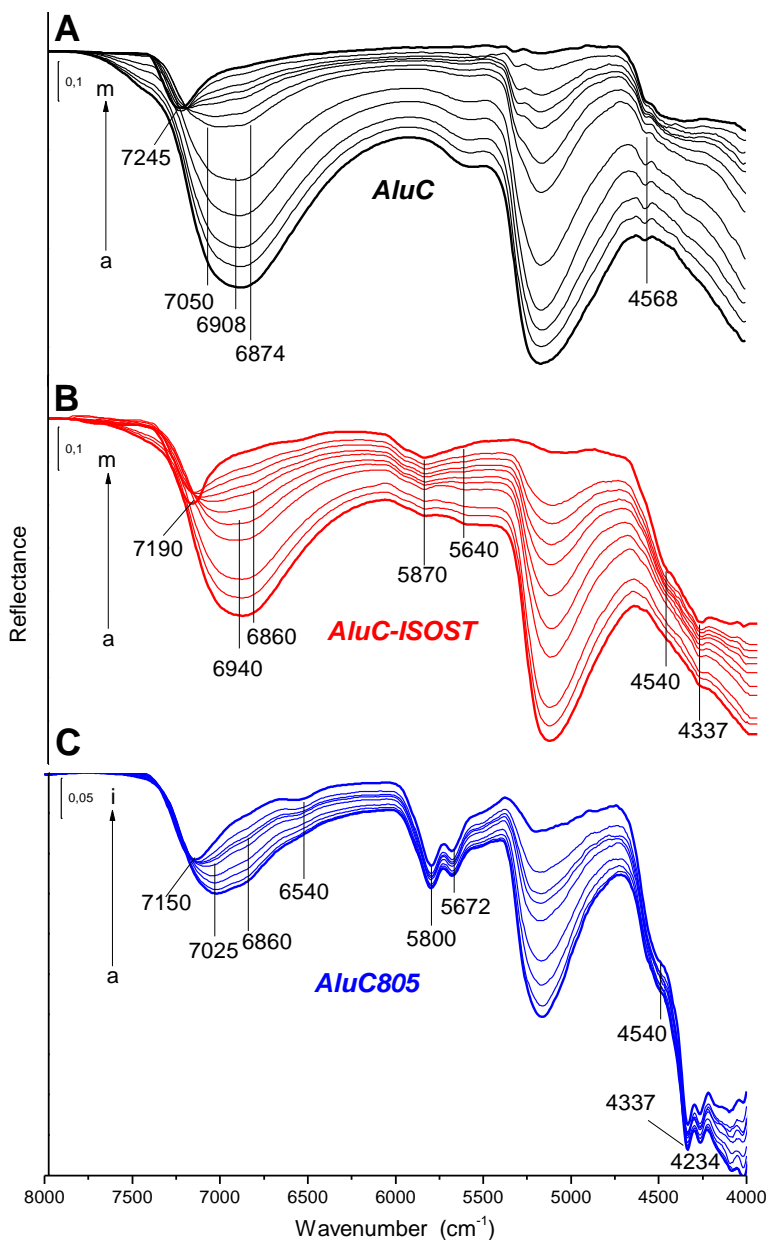


Figure 2.4.7. NIR spectra of water adsorbed on AluC (panel A), AluC-ISOST (panel B), AluC805 (panel C) in the 8000-4000 cm^{-1} range. The spectra are recorded in presence of water vapor pressure (curves 'a') and during outgassing steps (from 'b' to 'm' in the first two panels, from 'b' to 'i' in the third one).

The spectra of the bare alumina (panel A) exhibit a broad band centered at ca. 6908 cm^{-1} , referred to the $\nu_a\text{OH} + \delta_s\text{OH}$ of adsorbed water. Passing to the desorption sequence (from 'a' to 'm'), two different peaks referred to water only are visible, in particular, at 7050 and 6874 cm^{-1} . These bands are assigned, respectively, to transitions $\nu_1 + \nu_3$ and $2\nu_2 + \nu_3$ of water molecules removed from the alumina surface.¹⁷ From the study of Ruan et al.¹⁸ on alumina phases, the peak at 7245 cm^{-1} is referred to the hydroxyl groups on alumina surface ($2\nu\text{AlOH}$). The 4600-4400 cm^{-1} range corresponds to combinations whose principal character is $\nu\text{OH} + \delta\text{AlOH}$. The bending water mode could combine with a vibration localized in the bulk and, more precisely, H-bonding to water of a certain population of hydroxyl groups induces an absorbance at 4568 cm^{-1} .

The functionalization with ISOST (panel B) changes the wavenumber of the hydroxyl overtone region, shifting the peak of $2\nu\text{AlOH}$ mode to 7190 cm^{-1} , resulting in the change of the OH pattern. The following band, at 6940 cm^{-1} , is the broad band of the combination modes $\nu_a\text{OH} + \delta_s\text{OH}$ (bonded), while the peak at 6860 cm^{-1} is referred only to the $2\nu_2 + \nu_3$ of water.

It is possible to notice two signals at 5870 and 5640 cm^{-1} on the 'tail' of the water adsorption band ($5500\text{-}4600\text{ cm}^{-1}$); the first could be assigned to the $2\nu_s\text{CH}_3$ and the second one to the $2\nu_s\text{CH}_2$, due to the alkyl chains of the isostearic acid. It is impossible to appreciate the asymmetric modes for both signals, likely due to Darling-Dennisen resonance that causes a stronger intensity in the symmetric bands.¹⁹ Another region that involves aliphatic vibrational modes is at lower wavenumbers, and in the AluC-ISOST it is possible to notice a signal at 4337 cm^{-1} , due to the $\nu_a\text{CH}_2 + \delta\text{CH}_2$ of aliphatic chains of the carboxylic acid.

AluC805 (panel C) is functionalized with an unknown method using an organosilane (C8 type), in order to obtain a hydrophobic surface. A first evidence of the lower interaction with water is shown in the region at high wavenumbers: in addition to the 7150 cm^{-1} of the AlOH groups, the broad band of water bonded to the surface is not present, while the peaks referred to water (7025 and 6860 cm^{-1}) are two separate signals. As reported by Maeda et al.,²⁰ the width of this band is affected by the anharmonicity, so the molecules bonded to more adjacent molecules, having less anharmonicity, will be broader. Thus, the reduced width of the band witnesses the presence of water that weakly interacts with the surface. The peak at 6540 cm^{-1} is difficult to assign due to the unknown procedure of its functionalization. Immediately after the combination modes of $\nu\text{OH} + \delta\text{AlOH}$ (4540 cm^{-1}), other aliphatic bands are present: 4337 cm^{-1} peak is referred to the combination of $\nu_a\text{CH}_2 + \delta\text{CH}_2$ modes, while the signal at 4234 cm^{-1} may be assigned to $3\delta_s\text{CH}_3$.

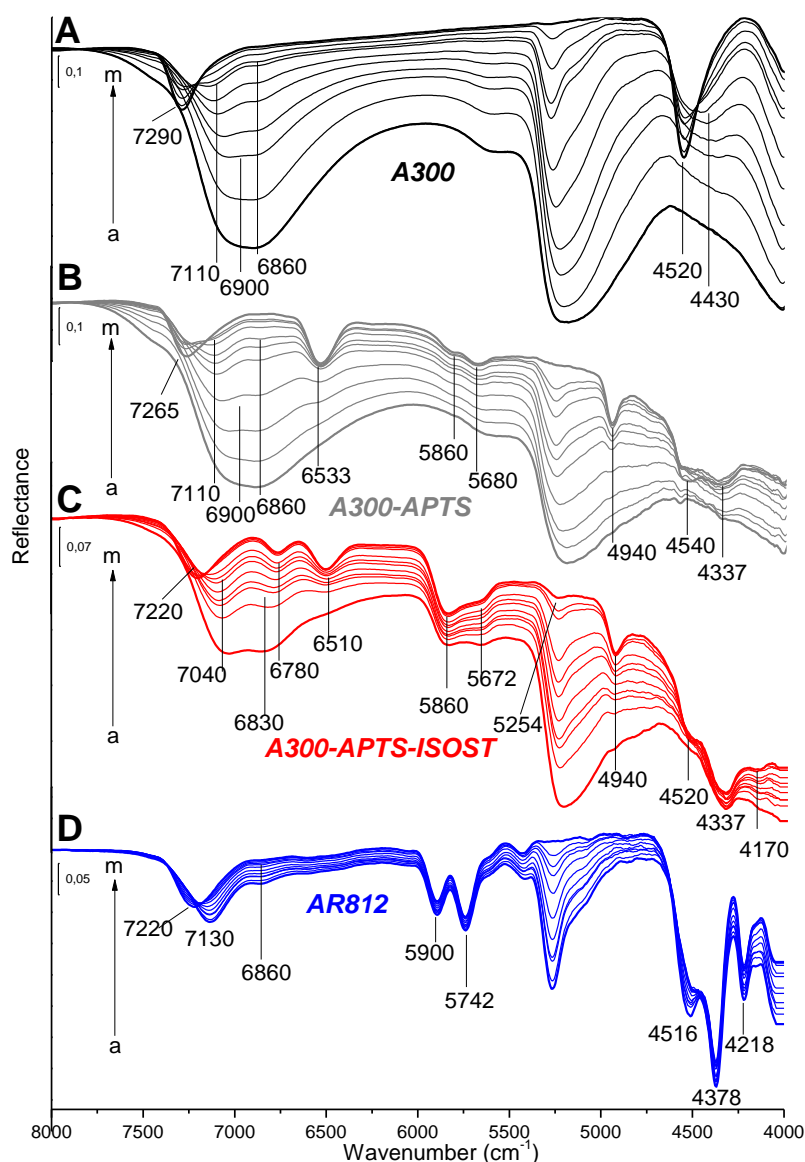


Figure 2.4.8. NIR spectra of A300 (panel A), A300-APTS (panel B), A300-APTS-ISOST (panel C), AR812 (panel D) in the region 8000-4000 cm^{-1} . The spectra are recorded in presence of water vapor pressure (curves 'a') and during outgassing steps (from 'b' to 'm') till the invariance of spectra.

Coming to silica materials (Fig. 2.4.8), the comment can be started from the higher frequency region of the most hydrated A300 (panel A, spectrum 'a'). As described for alumina, the broad band at 6900 cm^{-1} is referred to the $\nu_{\text{aOH}} + \delta_{\text{sOH}}$ of adsorbed (bonded) water. In the outgassed spectra ('b'-'h' spectra), two different peaks referred only to water are visible, in particular at 7100 and 6860 cm^{-1} . These wavenumbers are assigned, respectively, to transitions $\nu_1 + \nu_3$ and $2\nu_2 + \nu_3$ of water molecules that can be removed from silica surface by r.t. outgassing.¹⁷ In the last outgassed spectrum ('m'), the only peak that remains falls at 7290 cm^{-1} , assigned to $2\nu_{\text{OH}_i}$ of silanols of group I (isolated). After the water absorption region (5500-4600 cm^{-1}) already described, a signal at 4430 cm^{-1} ('b'-'f' spectra), that shifts towards 4520 cm^{-1} during the outgassing, appears in the last outgassed spectra ('g'-'m' spectra). In this case, H-bonding of a certain population of initially weakly perturbed silanols to water induces an absorbance decrease around 4520 cm^{-1} and a band at 4430 cm^{-1} appears when the amount of adsorbed water changes. Thus, it is possible that the peak around 4430 cm^{-1} corresponds to a distribution of H-bonded silanols on a quite dehydrated silica sample, that is

weakly affected by hydration. Similarly, the 4520 cm^{-1} component involves silanols uncomplexed with water, probably totally dehydrated isolated groups.²¹

In the A300-APTS spectrum (panel B), the bands referred to water in the region $7300\text{--}6000\text{ cm}^{-1}$ are the same as the A300 spectra, with a broad band at 6900 cm^{-1} of the water bonded ($\nu_a\text{OH} + \delta_s\text{OH}$) and the resulting two bands that appear during the outgassing (7110 and 6860 cm^{-1} respectively assigned to $\nu_1 + \nu_3$ and $2\nu_2 + \nu_3$ of water molecules, 'b'-'g' spectra); the band referred to $2\nu\text{OH}_i$ of silanols shifts at 7265 cm^{-1} in A300-APTS, for the different silanol patterns after functionalization.

The signal at 6533 cm^{-1} is referred to the $2\nu_s\text{NH}$ of amines, while the antisymmetric signal could appear at 6730 cm^{-1} , not visible in the spectrum, because the symmetric absorption is 6-7 times more intense than the asymmetric one.¹⁹ In the aliphatic region, it is possible to notice two signals at 5860 and 5680 cm^{-1} ; the first, less intense, could be assigned to the $2\nu_s\text{CH}_3$ and the second one to the $2\nu_s\text{CH}_2$, more intense for the presence of the propyl chains in the APTS. Also in this case, for the Darling-Dennisen resonance, the asymmetric bands are not visible.¹⁹

The band at 4940 cm^{-1} could be characterized as the combination of NH stretching and bending vibrational modes, only present in primary amines; the signals at 4540 cm^{-1} is due to $\nu\text{OH} + \delta\text{SiOH}$. In this particular case, it is more difficult to appreciate the band at lower frequencies region (4430 cm^{-1}) as in the A300 spectra, maybe for the presence of the aliphatic signal at 4337 cm^{-1} ($\nu_a\text{CH}_2 + \delta\text{CH}_2$) that is partially overlapped.

The A300-APTS-ISOST (panel C) exhibits a lot of signals in the entire spectrum ($8000\text{--}4000\text{ cm}^{-1}$), not present in the other two materials, due to the further functionalization with a carboxylic acid having a long alkyl chain. The peak referred to the $2\nu\text{OH}_{\text{int}}$ of silanols falls at 7220 cm^{-1} ; this family of internal silanols corresponds to species with high affinity for water: indeed, the signal immediately changes when the water arrives to the surface, and it turns to 7040 cm^{-1} at higher water coverage ('a'-'g' spectra). In this region the $2\nu_2 + \nu_3$ water mode at 6830 cm^{-1} is also present, but in this case no broad band of water bonded is formed: the two distinct signals remain separated, even at high water coverage.²⁰

In the following region, the signals referred to the amide bond and to the non-reacted amine groups are shown, respectively at 6786 cm^{-1} ($2\nu\text{NH}$, amides) and 6510 cm^{-1} ($2\nu_s\text{NH}$, amines). The aliphatic signals fall, as in the A300-APTS, at 5860 cm^{-1} ($2\nu_s\text{CH}_3$) and 5672 cm^{-1} ($2\nu_s\text{CH}_2$); conversely, it is possible to notice a difference, compared to the A300-APTS: in this case, the intensity of the combination modes of CH_3 are more intense than the CH_2 ones, witnessing the presence of the alkyl chain of isostearic acid.

The 4520 cm^{-1} band is referred to the $\nu\text{OH} + \delta\text{SiOH}$ modes; other aliphatic signals are present, in particular the 4337 cm^{-1} ($\nu_a\text{CH}_2 + \delta\text{CH}_2$) and 4179 cm^{-1} ($3\delta_s\text{CH}_3$).

Sample AR812 (panel D) exhibits the band of $2\nu\text{SiOH}_{\text{int}}$ at 7220 cm^{-1} ; in this region there is no evidence of a broad band referred to the combination stretching modes of water, but two peaks, one at 7130 cm^{-1} ($\nu_1 + \nu_3$) and the other, less intense, at 6860 cm^{-1} ($2\nu_2 + \nu_3$) are present. This kind of band is typical of hydrophobic material, confirming what was described in the $5500\text{--}4600\text{ cm}^{-1}$ region (Fig. 2.4.6). The hydrophobic commercial silica is commercially functionalized with HMDS (hexamethyldisilazane), a molecule that has only secondary amine and CH_3 groups in the structure.

The signal referred to the amine falls at 6494 cm^{-1} ; in the aliphatic region ($6000\text{--}5600\text{ cm}^{-1}$) it is possible to observe two intense peaks that fall at 5900 and 5742 cm^{-1} , assigned to the asymmetric and symmetric stretching modes of CH_3 groups ($2\nu_a\text{CH}_3$ and $2\nu_s\text{CH}_3$), respectively. It is noticed that the second signal is too weak and could be assigned to an antisymmetric mode of CH_2 (maybe for some grease contamination, since $-\text{CH}_2$ are not present in the HMDS molecule).

At lower wavenumbers, the signal at 4516 cm^{-1} is assigned to $\nu\text{OH} + \delta\text{SiOH}$ of isolated silanol. Moreover, it is possible to observe a peak at 4378 cm^{-1} , assigned to $\nu_s\text{CH}_3 + \delta\text{CH}_3$ modes, and a further peak at 4218 cm^{-1} , referred to the $3\delta_s\text{CH}_3$ modes.

The impact of the presence of long and branched alkyl chains on water adsorption from the vapour phase on alumina-based and silica-based nanoparticles was confirmed by microcalorimetric sorption experiments. The adsorption enthalpy ($-\Delta_{\text{ads}}H$) was measured by admitting H_2O vapour at increasing pressure at $30\text{ }^\circ\text{C}$ (Fig. 2.4.9, panels A and B, correspondingly). For reasons already explained in section 2.1.2.6, the maximum applied equilibrium pressure was 10 mbar, which is lower than what used in the microgravimetric experiments (20 mbar). Thus, in most cases the maximum amount of adsorbed water molecules was lower than what discussed above.

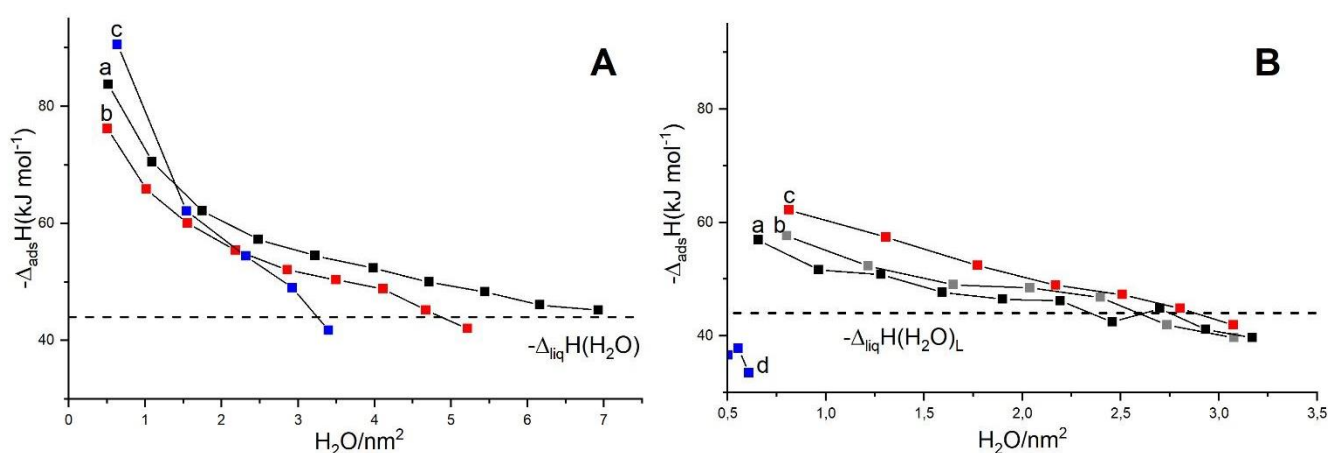


Figure 2.4.9 Adsorption enthalpy versus uptake of H_2O molecules on alumina-based (panel A) and silica-based (panel B) nanoparticles. Panel A a) AluC, b) AluC-ISOST, c) AluC805. Panel B: a) A300, b) A300-APTS, c) A300-APTS-ISOST, d) AR812. All materials were pre-outgassed at $30\text{ }^\circ\text{C}$. Dotted line: latent enthalpy of liquefaction of water. Measurements were carried out at $30\text{ }^\circ\text{C}$ in a pressure range 0.1-10 mbar.

When discussing the water adsorption enthalpy data it is useful to compare them with the latent enthalpy of liquefaction of water ($-\Delta_{\text{liq}}H(\text{H}_2\text{O}) = 44\text{ kJ}\cdot\text{mol}^{-1}$, dotted line in both panels). Water adsorption enthalpy values higher or lower than $-\Delta_{\text{liq}}H(\text{H}_2\text{O})$ are usually associated with a hydrophilic or hydrophobic character of adsorbing surfaces, respectively.⁹ On such a basis, it can be stated that, in the range of water surface coverage attained, the interaction of H_2O molecules with bare AluC (panel A, curve a) has always an hydrophilic character, progressively decreasing by increasing water coverage, because the first doses of H_2O molecules are preferentially adsorbed on stronger adsorbing sites.⁹ Basically, the same statement holds for water on AluC-ISOST and commercial alumina-based AluC805, although $-\Delta_{\text{ads}}H$ measured at the highest water uptake attained are slightly lower than $-\Delta_{\text{liq}}H(\text{H}_2\text{O})$ (panel A, curves 'b' and 'c', respectively). Noteworthy, the order of the

highest water uptake ($\text{H}_2\text{O}/\text{nm}^2$) for these three materials follows that found at high pressures in microgravimetric measurements (Fig. 2.4.3).

The energetics of water adsorption on silica A300-based nanoparticles (panel B) appears even less dependent on the surface features, with similar water adsorption enthalpy values for bare A300, A300-APTS and A300-APTS-ISOST (curves 'a'-'c', in the order). With respect to the alumina-based materials, the whole sets of values are lower, because surface silanols and $-\text{NH}_2$ groups are weaker adsorbing sites than surface Al^{3+} ions, and at the highest water uptake attained all three A300-based nanoparticles shown a slightly hydrophobic character. Moreover, water uptake by these three types of nanoparticles becomes progressively more similar as water coverage increases, in agreement with the limited difference in water uptake observed at 20 mbar in microgravimetric measurements (Fig. 2.4.3). Still in agreement with those data, water uptake by commercial silica-based AR812 appears definitely limited, resulting from adsorption enthalpy values definitely lower than $-\Delta_{\text{liq}}\text{H}(\text{H}_2\text{O})$ (curve 'd').

2.4.3 Interaction of pristine and functionalized nanoparticles with liquid water: evidence of superhydrophobicity

Despite the limited impact of ISOST functionalization on the capability to adsorb water vapour of both oxides, the contact angle measurements discussed above had shown high values (see chapter 2.2, section 2.2.4, and chapter 2.3, section 2.3.7). For sake of clarity, in Fig. 2.4.10 the contact angle measurements for all samples are summarized.

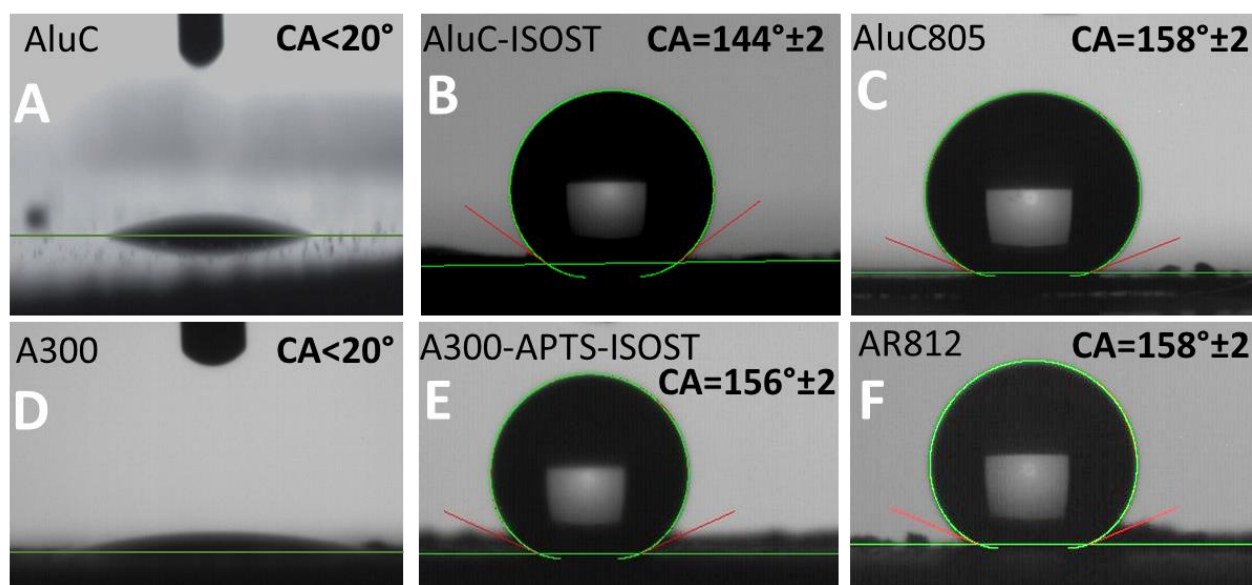


Figure 2.4.10. Contact angle measurements of AluC (panel A), AluC-ISOST (panel B), AluC805 (panel C), A300 (panel D), A300-APTS-ISOST (panel E) and AR812 (panel F).

In particular, for alumina nanoparticles functionalized with ISOST the contact angle results in $\sim 144^\circ$ (panel B), below the limit to consider a material as a superhydrophobic; conversely, the commercial alumina (AluC805, panel C) exhibits a superhydrophobic behaviour towards a water droplet. For A300-APTS-ISOST, the contact angle value is typical of superhydrophobic surfaces ($\text{CA} > 150^\circ$) and similar to that measured for the commercial hydrophobic silica (AR812, panel F).

The difference between contact angle values of AluC-ISOST and of A300-APTS-ISOST can be interpreted in terms of the different orientation of the hydrophobic molecules at the surface. The states of alkyl chains of ISOST molecules anchored on AluC and A300-APTS exposed to air were investigated by ^{13}C -CPMAS NMR spectroscopy (Fig. 2.4.11).

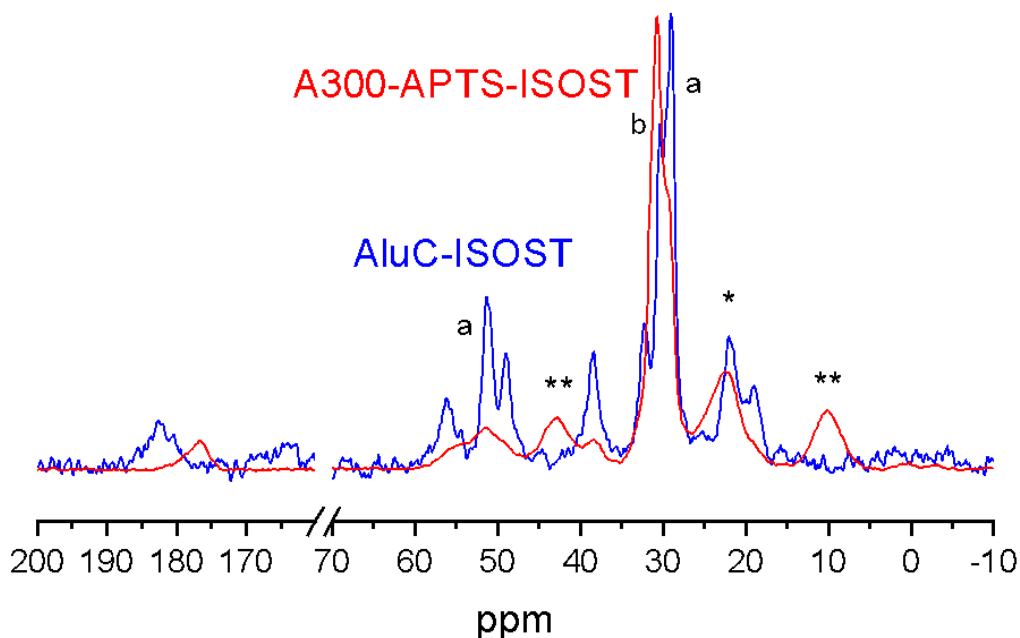


Figure 2.4.11 ^{13}C -CPMAS NMR spectra of a) AluC-ISOST and b) A300-APTS-ISOST exposed to air. Signals labelled with (**) and (*) in the spectrum of A300-APTS-ISOST are “affected” by the presence of the propyl chain of APTS, respectively. Spectra were normalized with respect to the intensity of the signals at ~ 30 ppm in order to appreciate differences in shape.

The highest frequency region witnesses the different interaction of ISOST with alumina and silica materials: the peak at 182 ppm in AluC-ISOST (a) is referred to a carboxylic form, and combining the information with IR measurements, it is possible to assign the peak to carboxylate species. The signal at 177 ppm, in A300-APTS-ISOST (b), is typical of an amide compound, in agreement with the presence of Amide I and Amide II bands in mid-IR spectra.

Both spectra contain typical peaks of a long aliphatic chain, in particular peaks that fall at lower chemical shifts (60-20 ppm) are assigned to the aliphatic chain of ISOST. Some peaks (43 ppm, 22.3 ppm and 9.5 ppm, labelled with ** and *) in A300-APTS-ISOST are “affected” by the presence of APTS; however, there are regions where only signals referred to the alkyl chains of ISOST fall (~ 50 and 30 ppm). The relative intensities and the shapes of these peaks in the two spectra changes, due to the different surface density (0.6 and 0.3 molec/ nm^2 for alumina and silica, respectively) and to the different orientation of the molecules on the surface.

As a conclusion, the alkyl chains exposed to air in the SS-NMR analyses interact differently with the chemical surrounding, witnessing a possible different alkyl chains exposure at the surface of the two functionalized materials. This could affect the effectiveness of the hydrophobic “barrier” at the surface towards water droplets.

As reported above, one of the requirements of a hydrophobic surface is the presence of micro- and nano- hierarchical structure on the surface.³ For this purpose, SEM images of the samples were acquired. The samples were analyzed as a self-supporting pellet, in which the powders of alumina/silica nanoparticles were pressed at ca. 1 ton (see chapter 2.1). This kind of procedure creates a flat and homogeneous surface, totally different from the texture of a sprayed coating. In Fig. 2.4.12, FESEM images of commercial alumina nanoparticles (AluC, panel A) and modified alumina nanoparticles with isostearic acid (AluC-ISOST, panel B) are reported.

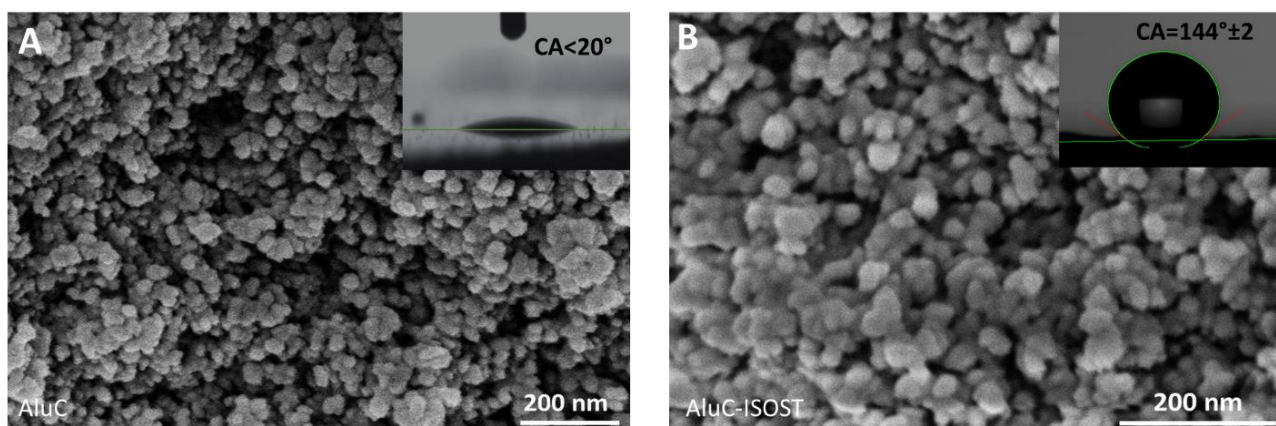


Figure 2.4.12. FESEM images of AluC (panel A) and AluC-ISOST (panel B). Inset reports the corresponding contact angles measured on the same pellet.

The surface morphology of the AluC-ISOST (panel B) does not show significant changes when compared to the unmodified alumina nanoparticles (panel A). In both cases typical aggregates of alumina are clearly visible, but no hierarchical microstructures that could entrap a thin air layer on the surface seem to appear. The same feature was observed for silica materials (A300 and A300-APTS-ISOST, see Fig. 2.4.13).

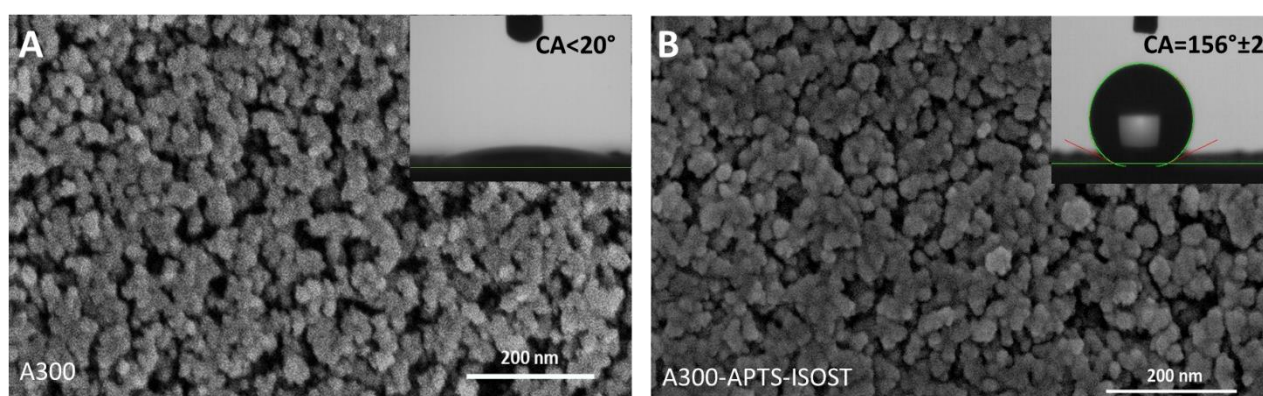


Figure 2.4.13. FESEM images of A300 (panel A) and A300-APTS-ISOST (panel B). Inset reports the corresponding contact angles.

The measurements of static contact angle were carried out on the same self-supporting pellets, that do not show hierarchical microstructures that may be considered responsible for the superhydrophobicity.³ In this case, therefore, the key of the hydrophobicity is in the chemical surface features of functionalized materials. The presence of the highly branched carbon chains of

the isostearic acid on the surface of alumina and silica nanoparticles allows to obtain high level of hydrophobicity (superhydrophobicity for silica), without the presence of microstructures at the surface.

Moreover, although the hydrophobic commercial materials present expected high contact angles (Fig. 2.4.14), they still show similar levels of micro-nano-hierarchical microstructure on the surface, as can be observed in Fig. 2.4.12 and 2.4.13.

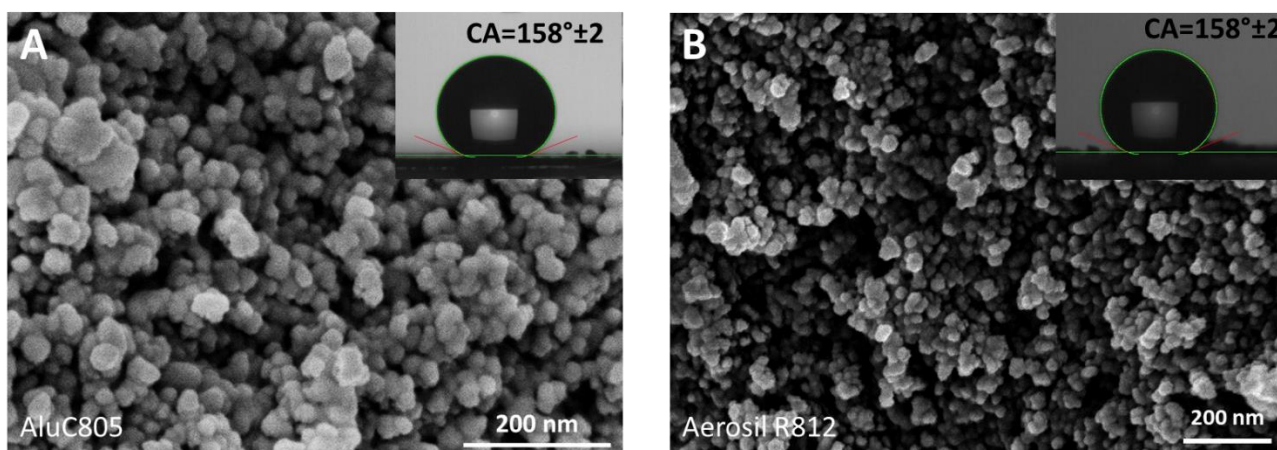


Figure 2.4.14. FESEM images and CA of commercial materials: AluC805 (panel A) and AR812 (panel B). Inset reports the corresponding contact angles.

2.4.4 A proposal of explanation: the study of the chemical structure of hydrophobic agents

Although the similar hydrophobic behaviour towards water droplets (without the presence of nano- and micro- hierarchical microstructures on the pellets) of the alumina and silica nanoparticles functionalized with ISOST (AluC-ISOST and A300-APTS-ISOST) and the hydrophobic commercial ones (AluC805 and AR812), these materials differ for the behaviour towards water vapor (see section 2.4.2).

As a whole, the surface functionalization with ISOST had a limited impact (very limited, in the case of silica) on the specific capability to adsorb water vapour, definitely lower than what resulting from the functionalization with non-highly branched alkyl moieties, as those present in commercial hydrophobic nanoparticles (AluC805 and AR812). Actually, ISOST molecules used in this work are made of two main sub-chains of 4 and 5 C atoms linked to the C atom in α position with respect to the carboxyl group exploited for linking to the surface. The conformational dynamics of such a structure can well leave room for water molecules in vapor phase to enter in contact with surface sites (Al^{3+} centres) not involved in the linking to the surface of ISOST molecules (Fig. 2.4.15).

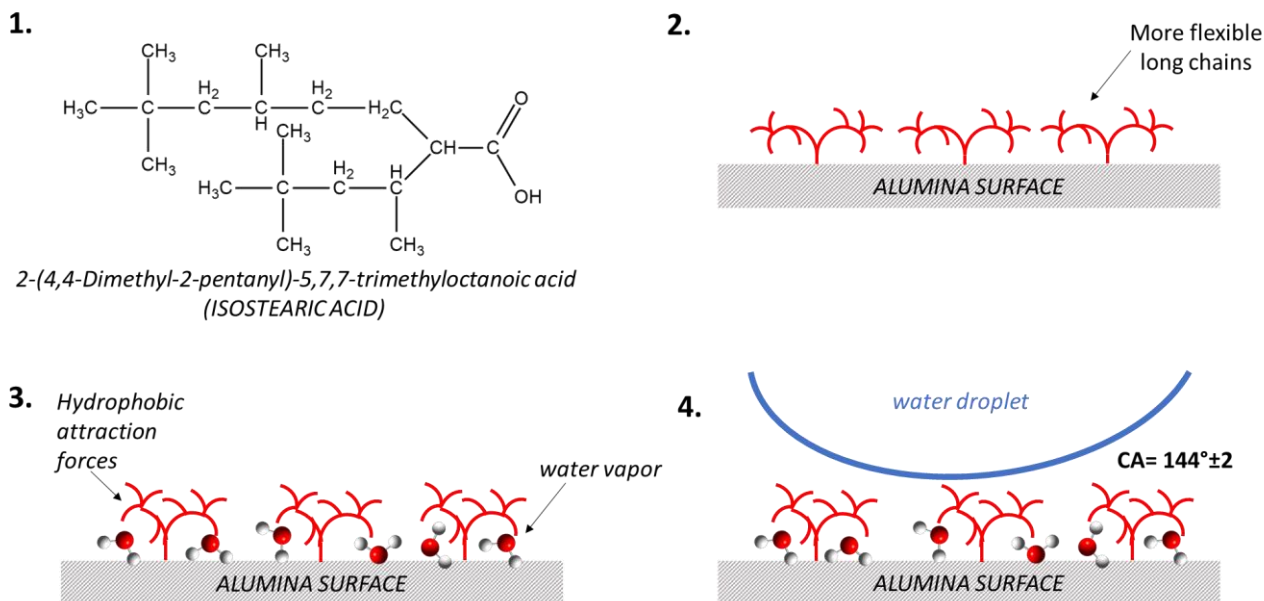


Figure 2.4.15 Scheme of the alumina surface functionalized with ISOST (1,2) and the different behaviour towards water vapor (3) and a water droplet (4). The long alkyl chains of ISOST have high flexibility; the water vapours arriving to the surface (3) could cause the aggregation of hydrophobic moieties thus resulting in a disclosure of a part of the surface and making it available for water adsorption. The static contact angle after deposition of water droplets (4) results in $144^{\circ}\pm 2$.

Moreover, in the case of silica (Fig. 2.4.16), moieties resulting from the grafting of APTS act also as a spacer between the surface of nanoparticles and covalently bound ISOST, and this can well explain the very limited decrease in specific capability to adsorb water observed by passing from A300-APTS to A300-APTS-ISOST. In summary, considering the dynamic behaviour of the chains at room temperature, ISOST molecules anchored to the surface through only one C atom, in an almost middle position of their main C atoms chains, should not represent an “impermeable” barrier preventing the adsorption of water molecules on the surface sites underneath the alkyl chains.

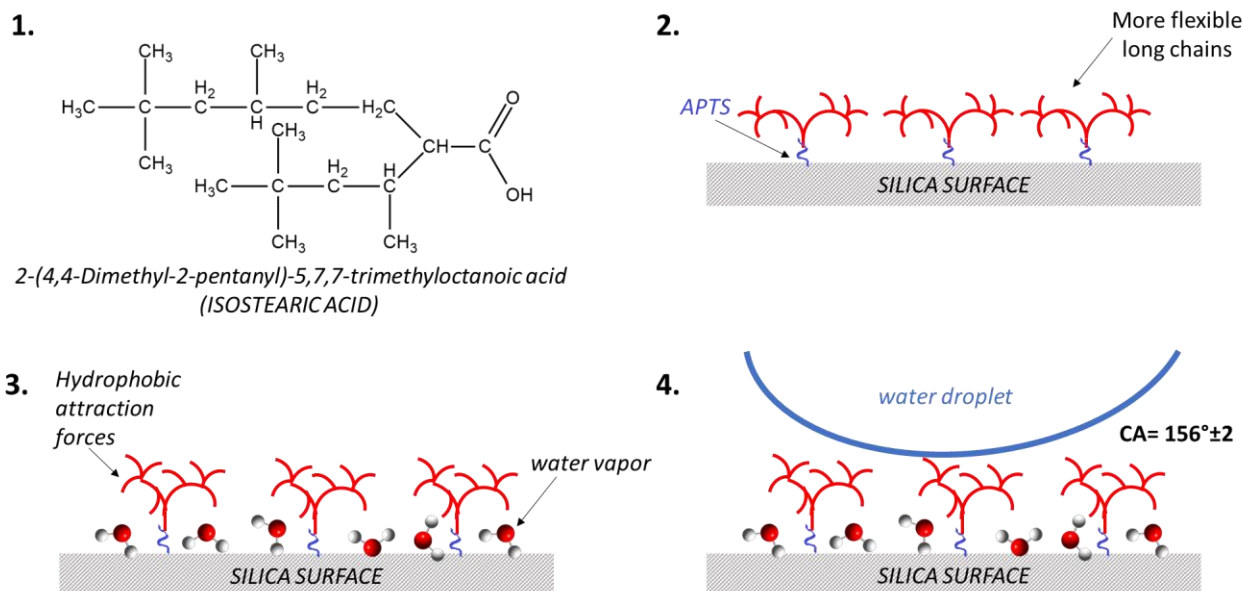


Figure 2.4.16 Scheme of the silica surface functionalized with ISOST (1,2) and the different behaviour towards water vapor (3) and a water droplet (4). The long alkyl chains of ISOST have high flexibility; the water vapours arriving to the surface (3) could cause the aggregation of hydrophobic moieties thus resulting in a disclosure of a part of the surface and making it available for water adsorption. The static contact angle after deposition of a water droplets (4) results in $156^{\circ} \pm 2$.

The definitely smaller molecular size of hexamethyldisilazane (HMDS) used for the surface functionalization of commercial silica-based AR812 (Fig. 2.4.17) allowed the attainment of a still higher surface density (3.5 units per nm^2) and exposes more rigid alkyl moieties, with a consequent larger consumption of surface silanols and a reduction of flexibility, and this might be the main reason of the poor capability of water adsorption shown by this material. Such a possibility appears be more limited in the case of commercial alumina-based AluC805 (Fig. 2.4.17), functionalized with quite long linear alkyl chains, but attaining a definitely higher surface density (2.5 units per nm^2 , see section 2.1.1).

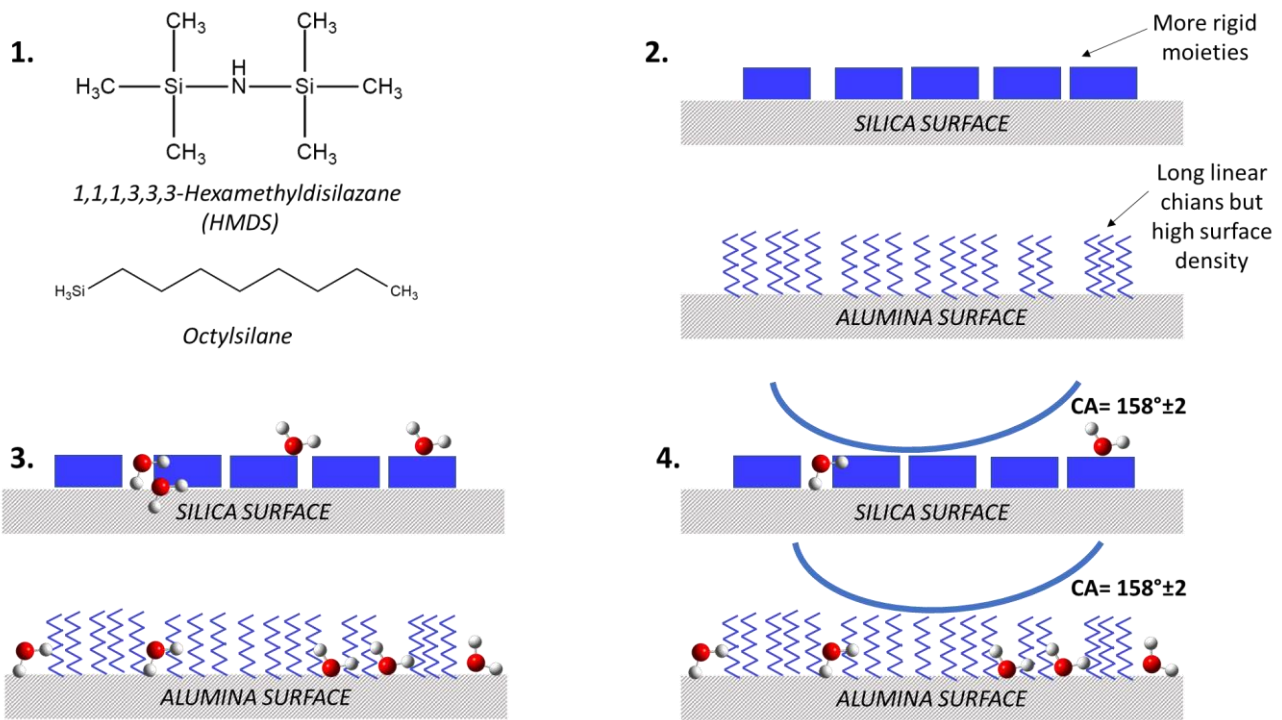


Figure 2.4.17 Scheme of the hydrophobic commercial silica and alumina surface functionalized with HMDS and octylsilane (1,2) and the different behaviour towards water vapor (3) and a water droplet (4). The functionalized silica surface exposes more rigid moieties, while the alumina surface is functionalized with quite long linear alkyl chains but with high grafting density (2). The decrease of flexibility and the higher surface densities allow to protect the surface from water vapors (3). The static contact angle after deposition of a water droplets (4) results in $158^\circ \pm 2$.

All the experimental results described in this chapter lead to the following conclusions:

- A superhydrophobic material does not necessarily expose micro- and nano-hierarchical structures; the FESEM images of self-supporting pellets of hydrophobic materials do not show any level of architectural features, thus the hydrophobic character of the chemical moieties can be enough to reach $CA > 150^\circ$. If these hierarchical structures can be formed when the particles are distributed/strayed randomly and we 'order' them by the pressure (1 ton), our system is in 'losing' position. Even without taking the advantage of these 'architectures', we get $CA = 156^\circ$. By being able to obtain a surface micro-nano hierarchical structure, we should thus improve the hydrophobicity by 'adding' the 'contribution' of the Lotus effect.
- A material with a $CA > 150^\circ$ can adsorb water vapors: the macroscopic behaviour towards water can be different from the molecular behaviour. The high adsorption capacity towards water vapors depends on the possibility of water molecules to reach uncovered parts of the surface by hydrophobic moieties (low grafting densities, flexibility of the alkyl chains) and it is independent from the capacity of the hydrophobic chemical surface features to protect surface from a macroscopic object such as water droplets.

Bibliographic References

1. Ma, M.; Hill, R. M., Superhydrophobic surfaces. *Current Opinion in Colloid & Interface Science* **2006**, *11* (4), 193-202.
2. Ahmad, D.; van den Boogaert, I.; Miller, J.; Presswell, R.; Jouhara, H., Hydrophilic and hydrophobic materials and their applications. *Energy Sources, Part A: Recovery, Utilization, and Environmental Effects* **2018**, *40* (22), 2686-2725.
3. Alexander, S.; Eastoe, J.; Lord, A. M.; Guittard, F.; Barron, A. R., Branched Hydrocarbon Low Surface Energy Materials for Superhydrophobic Nanoparticle Derived Surfaces. *ACS Appl Mater Interfaces* **2016**, *8* (1), 660-6.
4. Barthlott, W.; Neinhuis, C., Purity of the sacred lotus, or escape from contamination in biological surfaces. *Planta* **1997**, *202* (1), 1-8.
5. Marmur, A., The Lotus Effect: Superhydrophobicity and Metastability. *Langmuir* **2004**, *20* (9), 3517-3519.
6. Roach, P.; Shirtcliffe, N. J.; Newton, M. I., Progress in superhydrophobic surface development. *Soft Matter* **2008**, *4* (2), 224-240.
7. Wang, Z.; Yang, W.; Sun, F.; Zhang, P.; He, Y.; Wang, X.; Luo, D.; Ma, W.; Sergio, G.-C., Construction of a superhydrophobic coating using triethoxyvinylsilane-modified silica nanoparticles. *Surface Engineering* **2018**, *35* (5), 418-425.
8. Daoud, W. A.; Xin, J. H.; Tao, X., Synthesis and characterization of hydrophobic silica nanocomposites. *Applied Surface Science* **2006**, *252* (15), 5368-5371.
9. Fubini, B.; Bolis, V.; Bailes, M.; Stone, F. S., The reactivity of oxides with water vapor. *Solid State Ionics* **1989**, *32-33*, 258-272.
10. Brunauer, S.; Deming, L. S.; Deming, W. E.; Teller, E., On a Theory of the van der Waals Adsorption of Gases. *Journal of the American Chemical Society* **1940**, *62* (7), 1723-1732.
11. Morrow, B. A.; Cody, I. A.; Lee, L. S. M., Infrared studies of reactions on oxide surfaces. 7. Mechanism of the adsorption of water and ammonia on dehydroxylated silica. *The Journal of Physical Chemistry* **1976**, *80* (25), 2761-2767.
12. Ugliengo, P.; Saunders, V.; Garrone, E., Silanol as a model for the free hydroxyl of amorphous silica: ab-initio calculations of the interaction with water. *The Journal of Physical Chemistry* **1990**, *94* (6), 2260-2267.
13. Takeuchi, M.; Bertinetti, L.; Martra, G.; Coluccia, S.; Anpo, M., States of H₂O adsorbed on oxides: An investigation by near and mid infrared spectroscopy. *Applied Catalysis A: General* **2006**, *307* (1), 13-20.
14. Musso, G. E.; Bottinelli, E.; Celi, L.; Magnacca, G.; Berlier, G., Influence of surface functionalization on the hydrophilic character of mesoporous silica nanoparticles. *Physical Chemistry Chemical Physics* **2015**, *17* (21), 13882-13894.
15. Scatena, L. F., Water at Hydrophobic Surfaces: Weak Hydrogen Bonding and Strong Orientation Effects. *Science* **2001**, *292* (5518), 908-912.
16. Nakamoto, K., *Infrared and Raman spectra of inorganic and coordination compounds. Part B, Applications in coordination, organometallic, and bioinorganic chemistry*. 6th ed.. ed.; Hoboken, N.J. : Wiley: Hoboken, N.J., **2009**.
17. Burneau, A.; Corset, J., Etude comparée des spectres d'absorption dans le proche infrarouge des complexes 1-1 entre l'eau et les bases, en mélanges ternaires'. *Canadian Journal of Chemistry* **1974**, *52* (6), 915-923.
18. Ruan, H. D.; Frost, R. L.; Kloprogge, J. T., Application of Near-Infrared Spectroscopy to the Study of Alumina Phases. *Applied Spectroscopy* **2001**, *55* (2), 190-196.
19. Chalmers, J. M.; Griffiths, P., *Handbook of Vibrational Spectroscopy*. **2003**; Vol. 59.
20. Maeda, H.; Ozaki, Y.; Tanaka, M.; Hayashi, N.; Kojima, T., Near Infrared Spectroscopy and Chemometrics Studies of Temperature-Dependent Spectral Variations of Water: Relationship between Spectral Changes and Hydrogen Bonds. *J. Near Infrared Spectrosc.* **1995**, *3* (4), 191-201.
21. Burneau, A.; Gallas, J. P., Hydroxyl Groups on Silica Surfaces. In *The Surface Properties of Silicas*, Legrand, A. P., Ed. Wiley: **1998**; Vol. 3A.

2.5 A FURTHER IMPROVEMENT OF FUNCTIONALIZATION OF SILICA NANOPARTICLES: THE USE OF ACETIC ACID

2.5.1 Procedure of functionalization

The functionalization with ISOST allowed to reach a high level of hydrophobicity for silica (see section 2.3.7) but very low improvement in terms of water adsorption capacity, with a hydrophilic behavior towards water molecules (see section 2.4.2).

The surface of silica after functionalization with isostearic acid could present -NH_2 groups not reacted with the hydrophobic molecules, due to the steric hindrance of the bulky ISOST.

These moieties can interact very well with water, so the idea was to focus on the remaining amino groups. To this aim, a small hydrophobic molecule was used to cross the barrier of alkyl chains already exposed on the surface (ISOST) to reach and react with the -NH_2 groups.

For this purpose, acetic acid was employed to form an amide bond with -NH_2 groups, resulting in an exposure of -CH_3 moieties instead of hydrophilic amino groups. The size of this molecule fulfils the first request. Moreover, since acetic acid is a carboxylic acid, it was possible to use the same functionalization protocol used for isostearic acid. Thus, acetic acid was modified into acetyl chloride in order to increase its reactivity towards the exposed amine groups.

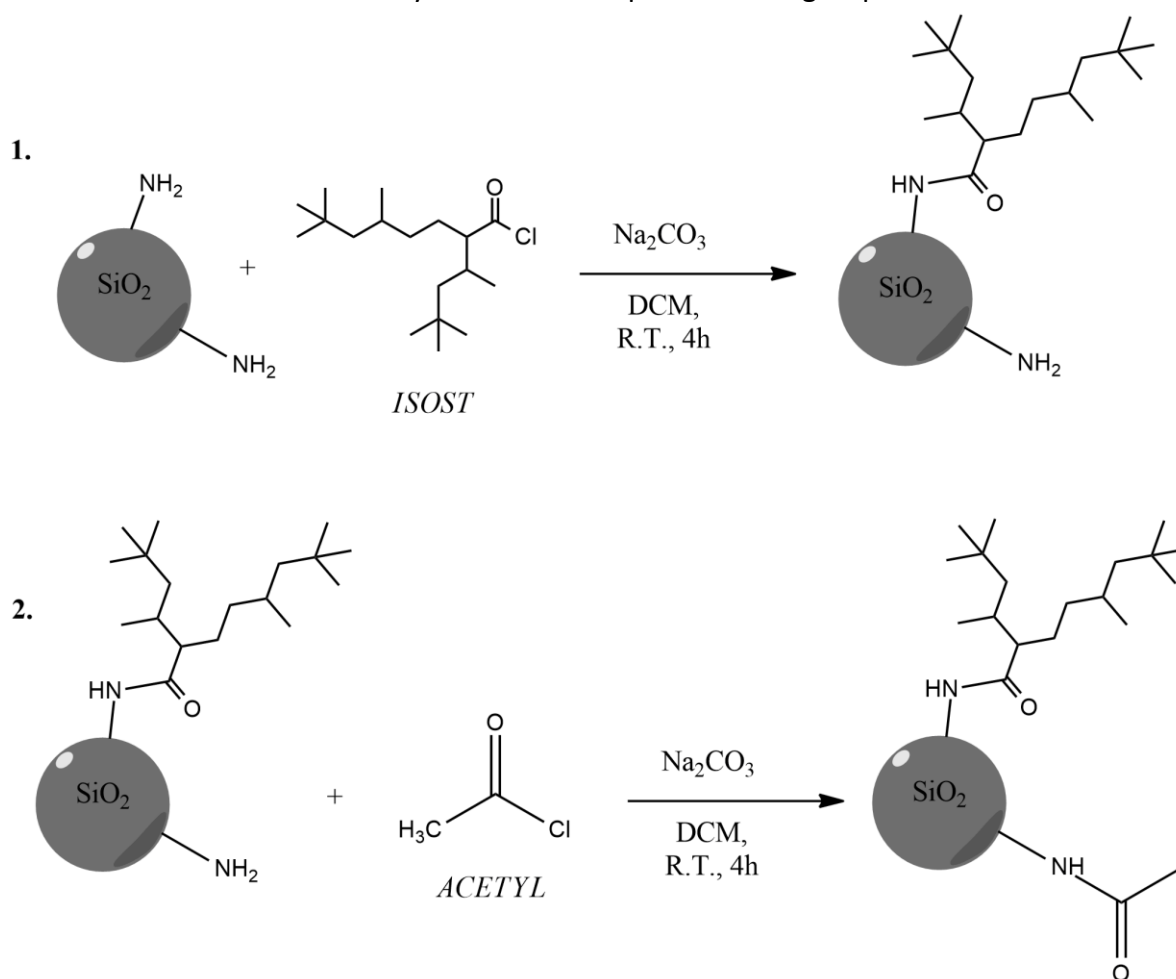


Figure 2.5.1. Functionalization scheme of silica nanoparticles with isostearoyl chloride (1) and further functionalization with acetyl chloride (2).

Different functionalization protocols have been followed: in the first two, acetyl chloride was added to the dried A300-APTS-ISOST nanoparticles in two different molar ratios (3:1 and 10:1, acetyl chloride: A300-APTS-ISOST), while the third one was the “one pot” method, and acetyl chloride was added after the first functionalization step with ISOST in the same reaction flask. Namely, after four hours of reaction at r.t. under magnetic stirring of ISOST, acetyl chloride was added, and the reaction occurred for another four hours.

The characterization of the obtained materials from these three reaction protocols showed the best results for the “10:1” functionalization protocol, and for sake of brevity and clarity the following data are only referred to this protocol. Table 2.5.1 shows the molar ratios of reagents and solvents used in the functionalization with acetyl chloride.

Table 2.5.1. Molar ratios of A300-APTS-ISOST, acetyl chloride, Na₂CO₃ and DCM used in the functionalization protocol.

Reagents / solvents	PM (g/mol)	Mass (mg)	Moles (mmol)	Equivalents	Volume (mL)
A300-APTS-ISOST	-	700	0.232	1	-
Acetyl chloride	78,49	182,1	2,32	10	-
Na ₂ CO ₃	105.99	491,7	4,64	20	-
DCM	-	-	-	-	10 mL

After the first functionalization with ISOST (see section 2.3.6), the nanoparticles were washed and dried and, subsequently, A300-APTS-ISOST nanoparticles (1 equivalent), 10 equivalents of acetyl chloride and 20 equivalents of sodium bicarbonate (Na₂CO₃) were mixed together in 10 mL of dichloromethane. The reagents were stirred magnetically at r.t. for 4 hours. The functionalized nanoparticles, from now A300-APTS-ISOST-ACETYL, were then centrifuged and washed with dichloromethane (3x 10 mL, 5000 rpm, 5'), methanol (2x10 mL, 5000 rpm, 5') and water (2x10 mL, 5000 rpm, 5'). The washed material was dried in the oven at 50°C, overnight.

2.5.2 Evidence of the effectiveness of functionalization: IR spectroscopy and Contact Angle measurements

The first evidence of the functionalization with acetyl chloride was provided by IR spectroscopy (Fig. 2.5.2).

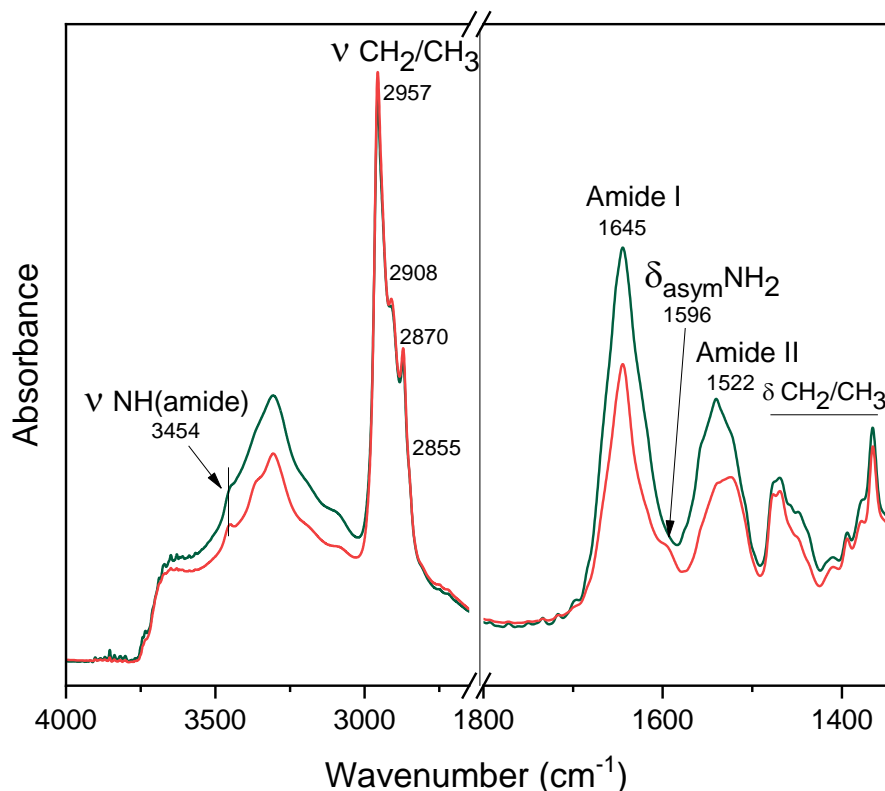


Figure 2.5.2. IR spectra of A300-APTS-ISOST (red spectrum) and of A300-APTS-ISOST-ACETYL (green spectrum) outgassed at b.t. (ca.50°C) in the 4000-1350 cm⁻¹ region.

The IR spectrum of the material after further functionalization with ACETYL (Fig. 2.5.2, green spectrum) is quite similar to the A300-APTS-ISOST spectrum (red spectrum) in the 4000-2700 cm⁻¹ region; the peak of ν NH of amide (3454 cm⁻¹)¹ is present, and the band of H- interacting silanols slightly changes due to the interaction with additional moieties on the material. The pattern of alkyl chains (3000-2800 cm⁻¹) is comparable between the two spectra, likely because only one -CH₃ is added, with respect to the more impactful C18 chains of ISOST.

In the 1800-1350 cm⁻¹ zone it is possible to observe an increase of the signals referred to the amide bond (Amide I and Amide II bands at 1645 and 1522 cm⁻¹, respectively)¹ and a similar pattern for the bending modes of alkyl chains, witnessing the lower impact of -CH₃ moieties of ACETYL.

To better appreciate the decrease of the signals referred to -NH₂ groups, it is necessary to focus on the parts of the spectrum due to ν NH₂ and δ NH₂ (Fig. 2.5.3).

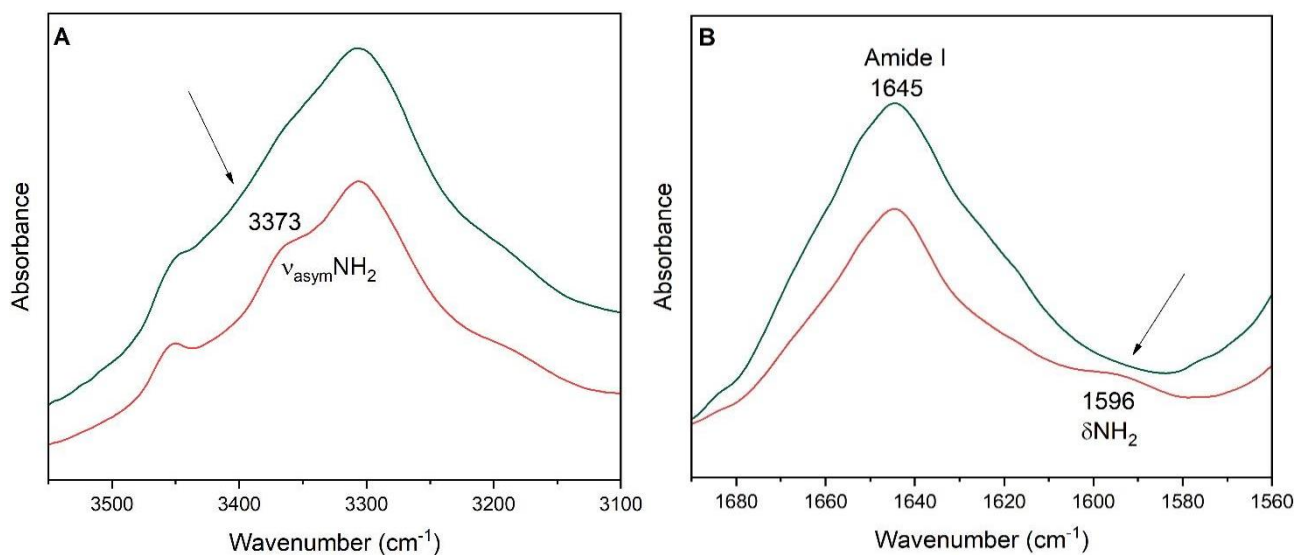


Figure 2.5.3. IR spectra of A300-APTS-ISOST (red spectrum) and of A300-APTS-ISOST-ACETYL (green spectrum) in: panel A (3600-3100 cm^{-1}) and panel B (1690-1560 cm^{-1}). The further functionalization with ACETYL leads to a decrease of the signals referred to $-\text{NH}_2$ groups (panel A, $\nu_{\text{asym}}\text{NH}_2$ and panel B, δNH_2).

The strong decrease (almost a complete disappearance) of the signals referred to the stretching and bending modes of $-\text{NH}_2$ groups (3373 and 1596 cm^{-1} , respectively)¹ after reaction with ACETYL, confirms the effectiveness of the functionalization. The next step was the study of the morphology of the new material through SEM analysis and the confirmation of the hydrophobic behavior by contact angle measurement (Fig. 2.5.4).

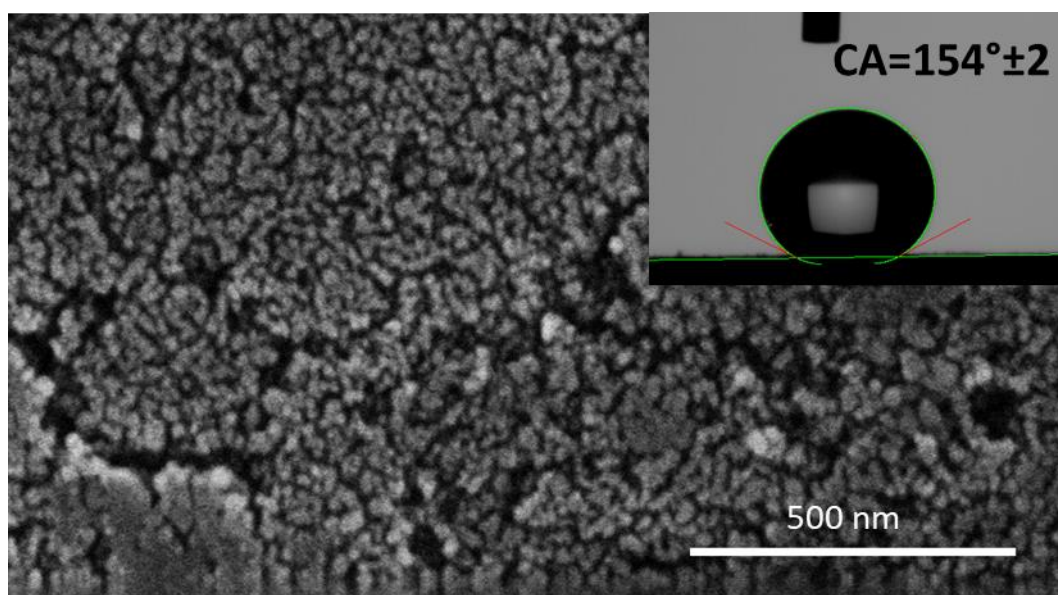


Figure 2.5.4. SEM image and corresponding CA measurement ($\theta=154^\circ\pm 2$) of a self-supporting pellet of A300-APTS-ISOST-ACETYL.

As expected, no hierarchical microstructures were present on the surface of silica functionalized with ISOST and ACETYL and the hydrophobicity was confirmed. As reported in 2.4.4 section, the role

of ISOST moieties is to “protect” surface from water droplets with the chemical hydrophobic strength of the alkyl chains, so the presence of ACETYL did not affect the hydrophobicity at macroscopic level and the change in the morphology of the silica surface.

2.5.3 Microgravimetric analysis: study of the adsorption capacity towards water vapours

The scope of the functionalization with ACETYL was to decrease the adsorption capacity towards water vapors. With the aim of evaluating quantitatively the number of H₂O molecules/nm² by samples in contact at 25 °C with water vapor at p =20 mbar (the maximum pressure reached during microgravimetric measurements), in Fig. 2.5.5 the results of microgravimetric analyses are reported.

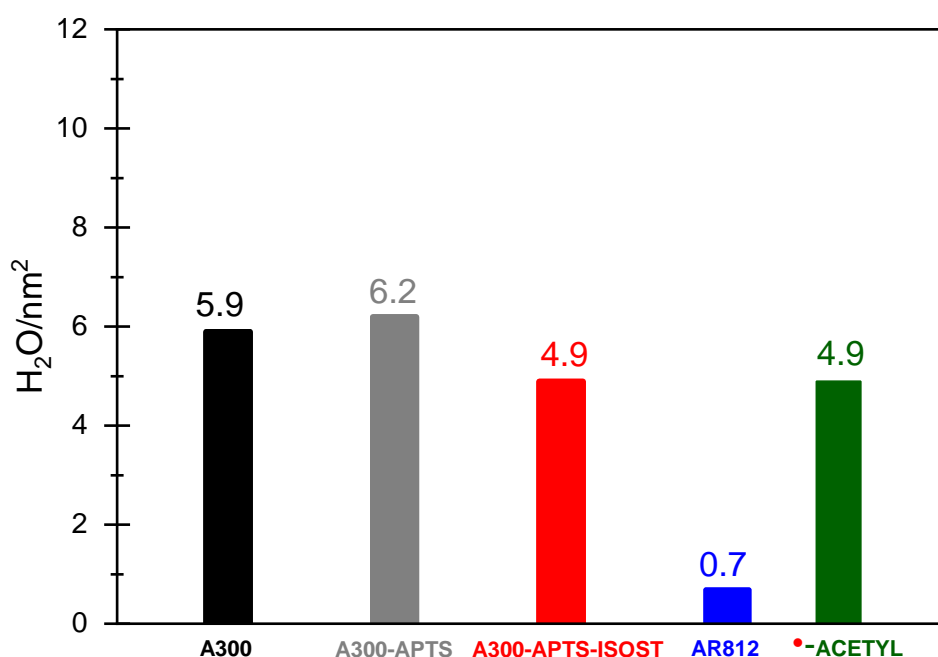


Figure 2.5.5. Microgravimetry analysis on A300 (black bar), A300-APTS (grey bar), A300-APTS-ISOST (red bar), AR812 (blue bar) and A300-APTS-ISOST-ACETYL (green bar) at p=20mbar. The number of water molecules adsorbed per nm² is reported on top of the bars.

As already explained (see section 2.4.2), the A300-APTS material shows the higher adsorption capacity (6.2 H₂O/nm²), greater than the one of bare A300 (5.9 H₂O/nm²), likely because of the replacement of some isolated silanols (unable to adsorb water at r.t.)²⁻⁴ with moieties terminated by the -NH₂ group, more effective in the interaction with H₂O molecules.⁵ The subsequent functionalization with ISOST resulted in a quite limited decrease (ca. 10%) of the specific capability to adsorb water vapors (4.9 H₂O/nm²) and, unexpectedly, the same capability was observed for A300-APTS-ISOST-ACETYL. The strategy to “cover” -NH₂ groups with alkyl groups (-CH₃) of acetic acid has not proved effective enough to decrease the number of water molecules adsorbed per nm².

2.5.4. A possible explanation of the high water adsorption capacity after functionalization: SS-NMR studies

With the intention of explaining the constancy of water adsorption capacity after the further functionalization with ACETYL, it was necessary to take a step back and to consider also the presence of the free non-reacted silanols as another protagonist in water adsorption (Fig. 2.5.6). Even if they are less effective compared to the $-NH_2$ groups,⁵ they could play an important role when water arrives on the silica surface.



Figure 2.5.6. Schematic representation of the different moieties that can interact with water vapors: the blue one is representative of the APTS, the black dots of the non-reacted silanols, while the ISOST is represented by the red structures.

As far as quantitative aspects are concerned, ^{29}Si -MAS SSNMR studies allowed to investigate the silanol pattern after the functionalization with APTS and, consequently, to quantify the number of free silanols that can react with water (Fig. 2.5.7).

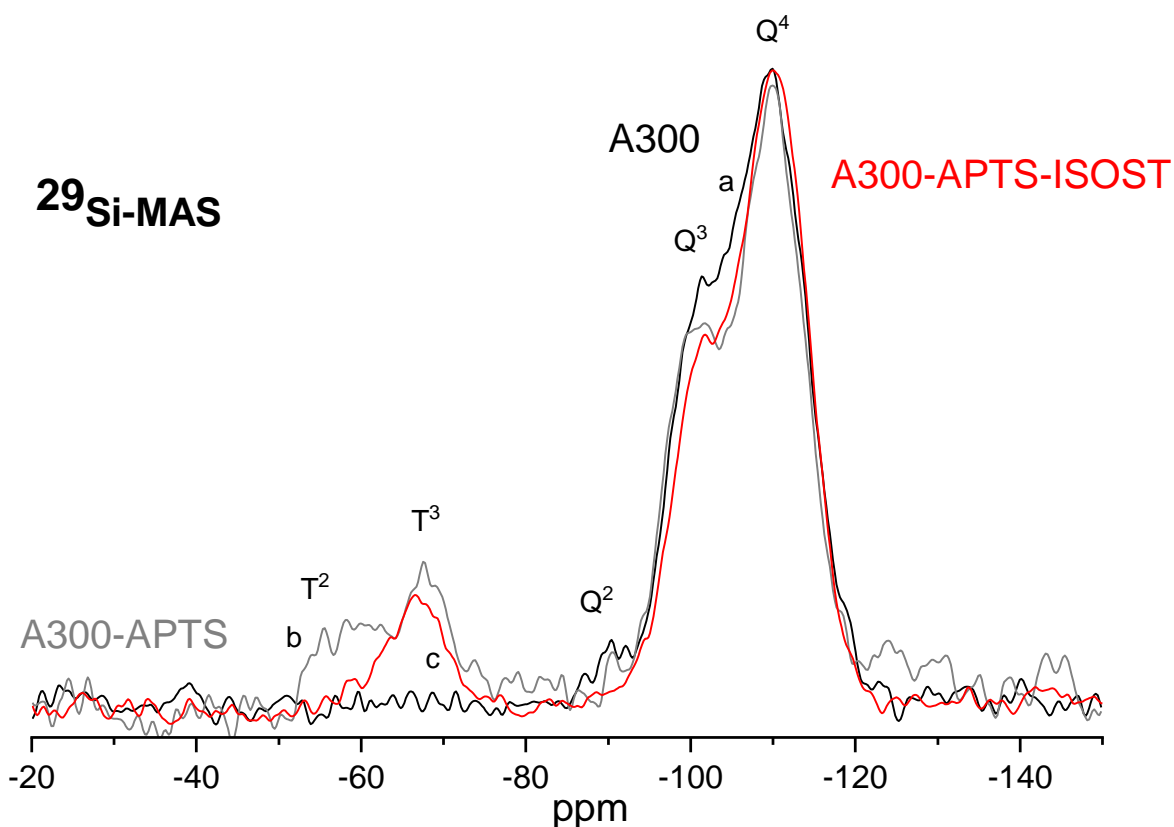


Figure 2.5.7. ^{29}Si -MAS SSNMR spectra of A300 (black spectrum, a), A300-APTS (grey spectrum, b) and A300-APTS-ISOST (red spectrum, c). The spectra are normalized for Q^4 .

The ^{29}Si MAS (Magic Angle Spinning) experiments allow to evaluate the change in the distribution of ^{29}Si atoms after the functionalization with APTS and ISOST. This technique is considered as intrinsically quantitative; this means that it is possible to evaluate the amount of silanol remaining after functionalization.

The signals are referred to silicon atoms involved in siloxane bridges $(\text{SiO})_4\text{Si}$ (called Q^4 , resonance at -110 ppm with respect to TMS), single silanols $(\text{SiO})_3\text{SiOH}$ ($\text{Q}^3 = -100$ ppm) and geminal silanols $(\text{SiO})_2\text{Si}(\text{OH})_2$ ($\text{Q}^2 = -90$ ppm).⁶ In the reported spectra, normalized for Q^4 (that are nuclei that are very weakly affected by the functionalization), the signals referred to Q^3 and Q^2 decrease after the functionalization with APTS, and T^3 and T^2 signals start to appear. The T^3 species $(\text{SiO})_3\text{SiR}$ fall at -66 ppm, while the T^2 forms, referred to $(\text{SiO})_2\text{SiR}(\text{OX})$, $\text{X} = \text{H}$ or Et , at -58 ppm,⁷ indicating the presence of APTS on the surface. Since the APTS is responsible for the modification in the silanol pattern, the spectra do not significantly change after functionalization with ISOST (red spectrum).

To focus the attention on the signals referred only to silanols, Fig. 2.5.8 reported the signals related to Q^4 , Q^3 and Q^2 before and after functionalization.

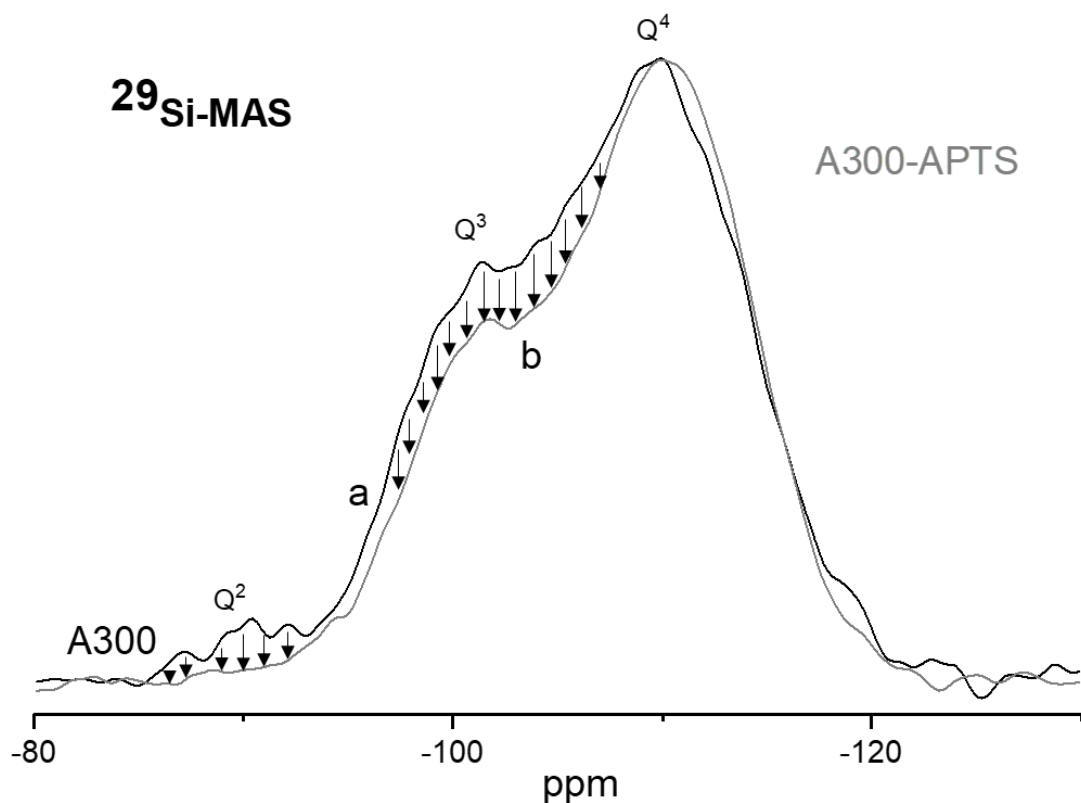


Figure 2.5.8. ^{29}Si -MAS SSNMR spectra of A300 (black spectrum) and A300-APTS (grey spectrum, b). The spectra are normalized for Q^4 .

From the integrated area of each peak, the calculated amount of free silanols after functionalization with APTS is still high: the decrease of the integrated area of the Q^3 is ca. 7%, that corresponds to ca. 4.2 SiOH/nm^2 that can interact with water in vapour forms, in agreement with the high level of adsorbed water found in microgravimetric analysis (Fig. 2.5.5).

So, the focus has been shifted to non-reacted silanols responsible for the high water adsorption capacity. The goal was to find a new way of functionalization with APTS. In literature there are a number of works based on the functionalization of materials with alkoxysilane,⁸⁻¹¹ that report the possibility to vary parameters such as reaction temperature, amount of APTS, pH, time, etc. in order to increase the grafting density. It was necessary to find the best combination, taking into account the further functionalization with ISOST but, unfortunately, the global pandemic interrupted the work in the laboratory for several months, and so this could be a starting point for further investigation on this topic.

Bibliographic References

1. Colthup, N.; Daly, L.; Wiberley, S., *Introduction to Infrared and Raman Spectroscopy*. 3rd ed.; Academic Press: **1990**.
2. Morrow, B. A.; Cody, I. A.; Lee, L. S. M., Infrared studies of reactions on oxide surfaces. 7. Mechanism of the adsorption of water and ammonia on dehydroxylated silica. *The Journal of Physical Chemistry* **1976**, *80* (25), 2761-2767.
3. Ugliengo, P.; Saunders, V.; Garrone, E., Silanol as a model for the free hydroxyl of amorphous silica: ab-initio calculations of the interaction with water. *The Journal of Physical Chemistry* **1990**, *94* (6), 2260-2267.
4. Takeuchi, M.; Bertinetti, L.; Martra, G.; Coluccia, S.; Anpo, M., States of H₂O adsorbed on oxides: An investigation by near and mid infrared spectroscopy. *Applied Catalysis A: General* **2006**, *307* (1), 13-20.
5. Musso, G. E.; Bottinelli, E.; Celi, L.; Magnacca, G.; Berlier, G., Influence of surface functionalization on the hydrophilic character of mesoporous silica nanoparticles. *Physical Chemistry Chemical Physics* **2015**, *17* (21), 13882-13894.
6. Luhmer, M.; d'Espinose, J. B.; Hommel, H.; Legrand, A. P., High-resolution ²⁹Si solid-state NMR study of silicon functionality distribution on the surface of silicas. *Magnetic Resonance Imaging* **1996**, *14* (7), 911-913.
7. Lelli, M.; Gajan, D.; Lesage, A.; Caporini, M. A.; Vitzthum, V.; Miéville, P.; Héroguel, F.; Rascón, F.; Roussey, A.; Thieuleux, C.; Boualleg, M.; Veyre, L.; Bodenhausen, G.; Coperet, C.; Emsley, L., Fast Characterization of Functionalized Silica Materials by Silicon-29 Surface-Enhanced NMR Spectroscopy Using Dynamic Nuclear Polarization. *Journal of the American Chemical Society* **2011**, *133* (7), 2104-2107.
8. Xu, Z.; Liu, Q.; Finch, J. A., Silanation and stability of 3-aminopropyl triethoxy silane on nanosized superparamagnetic particles: I. Direct silanation. *Applied Surface Science* **1997**, *120* (3-4), 269-278.
9. Liu, S.; Zhang, H.-L.; Liu, T.-C.; Liu, B.; Cao, Y.-C.; Huang, Z.-L.; Zhao, Y.-D.; Luo, Q.-M., Optimization of the methods for introduction of amine groups onto the silica nanoparticle surface. *Journal of Biomedical Materials Research Part A* **2007**, *80A* (3), 752-757.
10. Čampelj, S.; Makovec, D.; Drogenik, M., Functionalization of magnetic nanoparticles with 3-aminopropyl silane. *Journal of Magnetism and Magnetic Materials* **2009**, *321* (10), 1346-1350.
11. Kralj, S.; Drogenik, M.; Makovec, D., Controlled surface functionalization of silica-coated magnetic nanoparticles with terminal amino and carboxyl groups. *Journal of Nanoparticle Research* **2010**, *13* (7), 2829-2841.

2.6 APPLICATION OF HYDROPHOBIC MATERIALS ON LEATHER SAMPLES

2.6.1 Deposition of alumina nanoparticles using the spray technology – characterization of treated leather samples with SEM-EDS analyses

The satisfactory results in terms of hydrophobicity, and the possibility to produce a consistent amount of AluC-ISOST (10-20 gr) at laboratory scale, allowed to pass to applicative tests on leather samples at Kemia Tau. The following protocol is reported in the literature¹ and involves the application of an emulsion of polyacrylate and functionalized nanoparticles by a spray gun (Fig. 2.6.1).

In the described protocol, compressed air generated by a compressor in a tank passes through a pressure regulator and a filter, that eliminates traces of oil or water, and finally arrives at the gun, connected through the air inlet. The suspension containing the nanoparticles is sent under pressure into the gun and is sprayed onto the leather in the form of finely atomized droplets, mixing air and material in a controlled manner.² The leather is lying on a net. Excess spraying is removed by a suction system, placed behind the frame. Thanks to the structure of the gun head, it is possible to adjust the size of the micro drops applied to the leather. The suspension should be evenly distributed over the entire surface of the leather before drying.

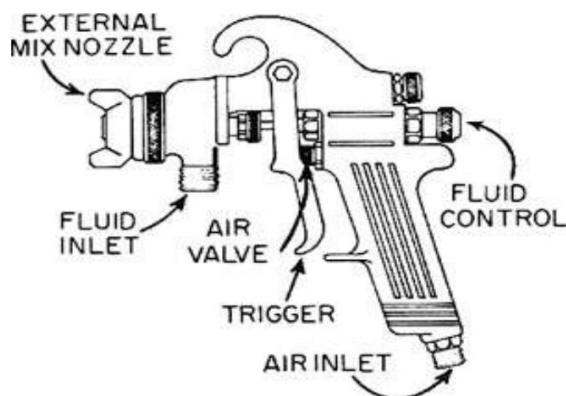


Figure 2.6.1. Scheme of a spray gun used in the deposition of the NPs over the leather samples.²

To apply this protocol some tests have been carried out to select the type of reticulating polymer and the characteristics of the used leather. For the tests an acrylic resin already employed in the processing of Kemia Tau was used, on a sample of finished leather (chrome tanning, retanning with synthetic acrylic tannin, fattening with synthetic and natural greasers, and dyeing with azo dyes). Some critical issues have been identified, concerning:

- the use of ethanol for the suspension of nanoparticles, in relation to safety concerns (ethanol use is strictly controlled in companies);
- variations of some surface properties of the leather;
- a control on the stability of the dispersion, that tends to separate, giving inhomogeneity of spray and risk of clinging the nozzles of guns.

In fact, despite all the precautions adopted, the homogeneity of the suspension of nanoparticles was very low: the particles could not be well suspended and, accumulating in the lower part of the gun tank, determined a non-homogeneous distribution on the leather. This is important, since a

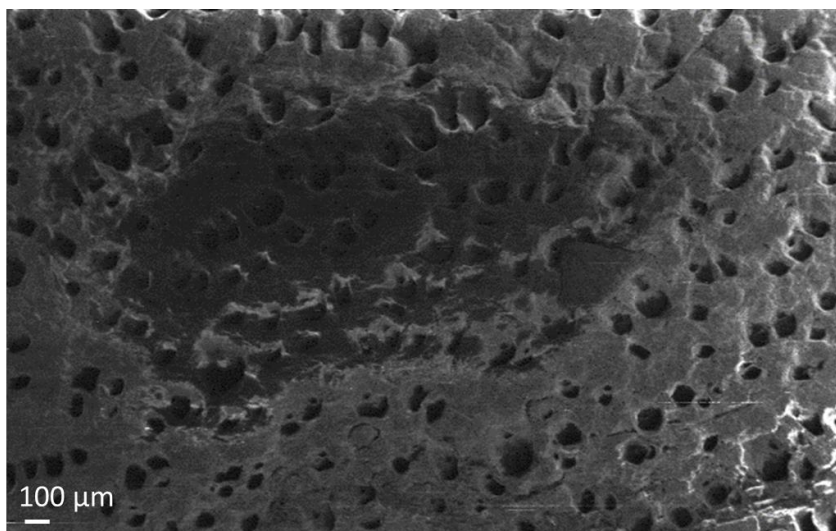
heterogeneous distribution of the spraying liquid can cause a number of drawbacks, such as poor anchorage, low resistance to rubbing and uneven film (“orange peel” effect).

Indeed, the water drop deposition tests showed poor hydrophobicity of the surface of the leather treated with AluC-ISOST (Fig. 2.6.2, sample 4). For comparison also the leather sample treated with the acrylic resin is considered.



Figure 2.6.2 Deposition and water drop tests (t=0 sec in the center, t=32 sec on the right) on leather samples: 1) non-treated leather 2) leather treated with perfluorinated waterproofing agents, 3) leather treated with acrylic polymer and 4) leather treated with acrylic polymer + AluC-ISOST.

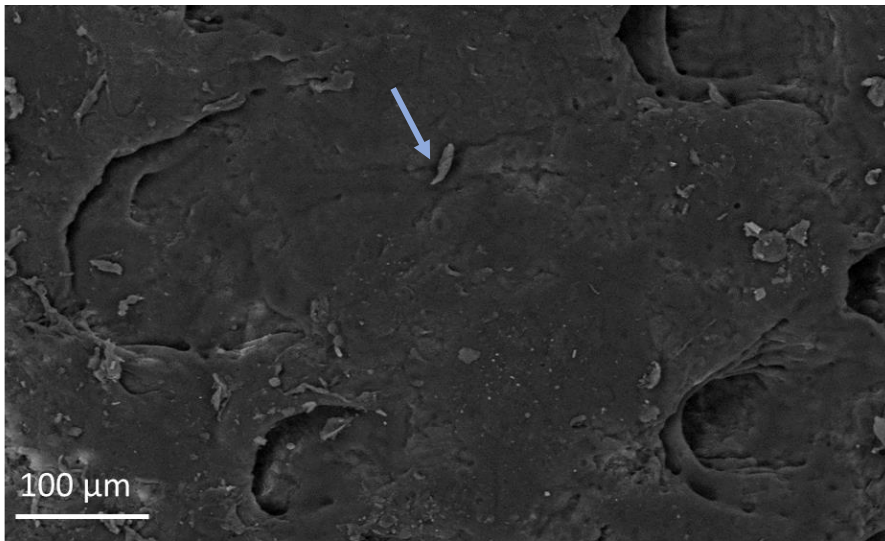
Scanning electron microscopy (SEM) and EDS spectroscopy analyses were carried out to observe the morphology and composition of leather samples, and to investigate the homogeneity of deposition. Just for comparison, Fig. 2.6.3 shows the image and composition analysis of the untreated leather sample (1), in which the pores of the skin can be observed, and EDS shows the presence of only carbon and oxygen elements.



Element	Weight %
C	66,27
O	33,73

Figure 2.6.3. SEM (left) and EDS (right) analyses of the non-treated leather (1). Mag=100X, EHT=15.00 kV, WD=8.5mm, Signal=SE1.

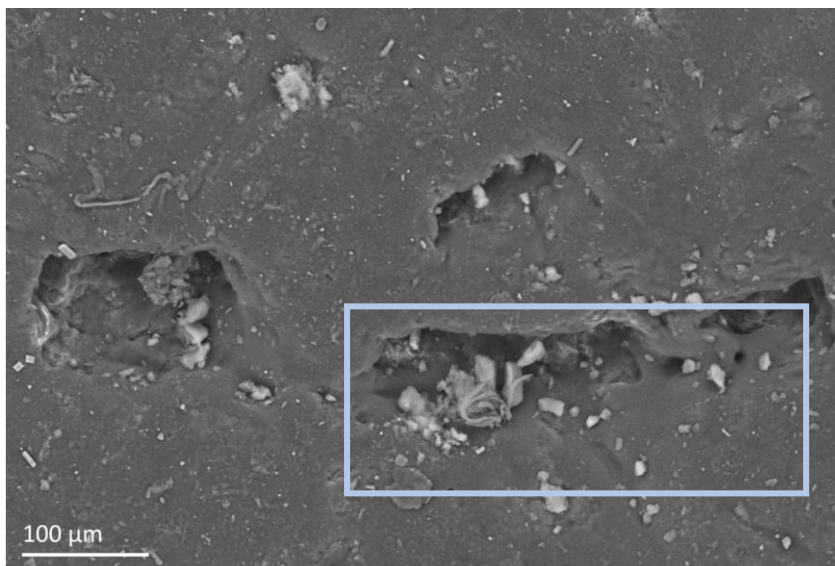
In the sample of leather treated with acrylic resin only (3), the pores of the skin are still visible but, in this case, the presence of agglomerates is noted. EDS carried out on these lighter areas reveals the presence of several elements, compatible with the composition of an acrylic resin (Fig. 2.6.4).



Element	Weight %
C	58.19
O	32.52
Na	0.99
Si	0.42
S	1.26
Cl	1.02
K	0.68
Ca	1.04
Cr	2.84
Ti	1.05

Figure 2.6.4. SEM (left) and EDS (right) analyses of the treated leather with acrylic resin (3). Mag=500X, EHT=20.00 kV, WD=8.5mm, Signal=QBSD. The blue arrow indicates agglomerates of acrylic resin.

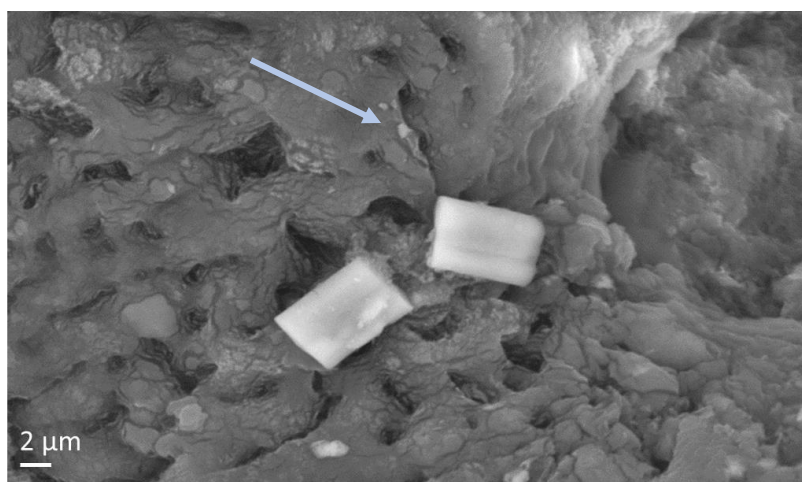
The SEM image of the sample treated with alumina nanoparticles functionalized with ISOST presents different agglomerates, and EDS analysis in the highlighted area shows the presence of Al. From the images, it is clear that the functionalized nanoparticles are not well distributed on the sample (Fig. 2.6.5).



Element	Weight %
C	54.68
O	38.40
Al	4.61
Na	0.47
S	0.81

Figure 2.6.5. SEM (left) and EDS (right) analyses of the treated leather with acrylic resin and AluC-ISOST (4). Mag=500 X, EHT=20.00 kV, WD=8.5mm, Signal=QBSD.

By analysis of higher magnification images, the presence of micrometer sized crystal-like structures is observed, together with smaller agglomerates (Fig. 2.6.6). EDS analysis of the smaller particles (highlighted by the blue arrow) shows a significant presence of aluminum, suggesting that these could be related to the functionalized nanoparticles. The large white crystals, on the other hand, contain high amount of K (about 40% by weight), and may derive from some salt used during the leather processing step.



Element	Weight %
O	67.55
Al	13.59
S	6.27
Cr	7.18
Zn	5.41

Figure 2.6.6. SEM (left) and EDS (right) analyses of the treated leather with acrylic resin and AluC-ISOST (4). Mag=6.00 kX, EHT=20.00 kV, WD=8.5mm, Signal=QBSD.

In conclusion, the presence of agglomerates of alumina nanoparticles is highlighted, but the dispersion is not homogeneous, and the overall EDS analysis on the treated leather shows a small amount of aluminum, thus confirming the critical issues already observed during the deposition process in Kemia Tau. Another deposition protocol, using a different technology, was thus tested to improve the homogeneity of the dispersion.

2.6.2 Deposition of commercial hydrophobic silica using a new technology: Roll Coater – characterization of treated leather samples with SEM-EDS analyses

The aim of the work was to test another technology to improve the deposition of hydrophobic nanoparticles on leather samples. This was carried out using commercial hydrophobic silica nanoparticles (AR812). The functionalized A300 silica nanoparticles described in this work could not be tested for two reasons. First, the amount obtained at lab-scale was too low for the deposition tests. Secondly, the synthetic procedure could not be easily upscaled in Kemia Tau due to the use of dichloromethane as solvent and the necessity of a distillation apparatus to purify the isostearyl chloride. The application of AR812, despite the fact that it is a commercial material, represents an innovation in terms of employment of a material that does not contain fluorinated molecules for leather waterproofing.

As already mentioned, the AR812 nanoparticles showed the lower water adsorption capacity (see section 2.4.2) and contact angle measurements (see section 2.4.3) demonstrated superhydrophobicity at macroscopic level, with a value very similar to that found for laboratory-functionalized silica nanoparticles: $158^{\circ}\pm 2$ for AR812 versus $156^{\circ}\pm 2$ for A300-APTS-ISOST. These features make the commercial hydrophobic silica nanoparticles suitable candidates for the deposition tests on leather samples.

In the following, the attention is focused on the selection of the technology to increase the homogeneity of the dispersion.

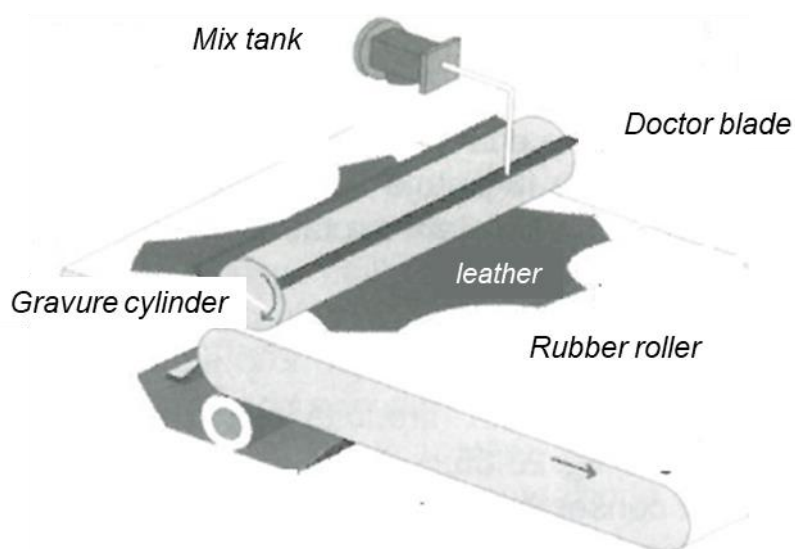


Figure 2.6.7. Representation scheme of the *Roll Coater* (image provided by Kemia Tau).

The roller finishing machine or *Roll Coater* consists of an endless rubber roller that brings the leather into contact with a metal cylinder engraved to a certain texture: the finishing liquid is stretched and smeared by pressure on the leather through direct contact with the cylinder, called "gravure cylinder" (Fig. 2.6.7). The cylinder is wetted with the finishing solution contained in the mix tank and, after scraping the excess liquid, compresses the leather by depositing the finishing layer on it. The engraving of the cylinder consists of several alveoli that contain the finishing liquid and the amount deposited on the leather depends on the size, number of alveoli per unit surface and the

rate of rotation of the gravure cylinder. This allows a uniform distribution over the entire surface of the leather and avoids waste of a finishing solution that remains deposited on the gravure and recovered cylinder. A rubber transport cylinder (support roller) ensures the perfect contact between the leather and the cylinder. In this specific case the "Reverse" application technique in which the gravure cylinder rotates in the opposite direction to that of the leather rubber belt was used (Fig. 2.6.8).

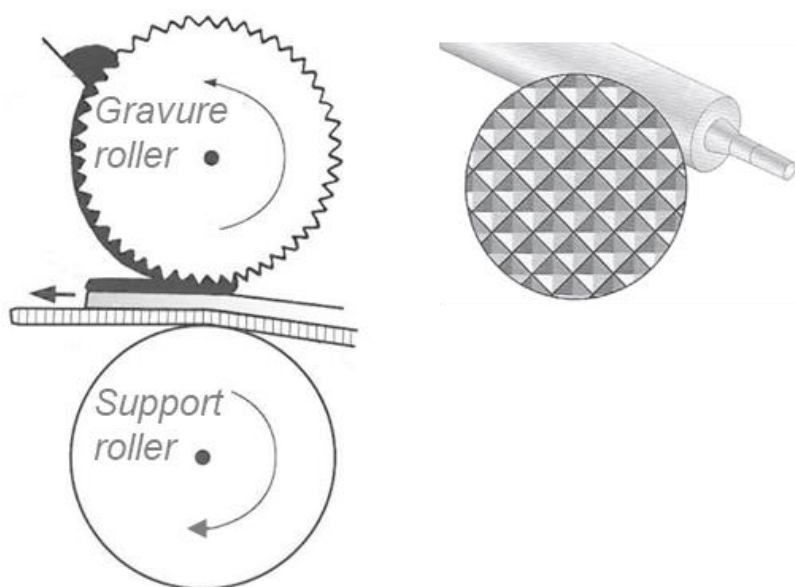


Figure 2.6.8. On the left: scheme of the rotation of the gravure roller and the support roller in the “reverse” application. On the right it is possible to observe the frame of the gravure cylinder used for the deposition of AR812 on leather (images provided by Kemia Tau).

The cover mixture to be distributed on the leather can be dosed continuously and in quantities ranging from 3 to 30 g/ft², with a saving of 30-40% of the products compared to the spray guns.

Leather samples treated in Kemia Tau with AR812 with this technology, were analyzed by SEM-EDS, to obtain information on the degree of homogeneity of nanoparticles dispersion on the sample and on the amount of deposited material. The leather samples were placed on conductive and adhesive supports used for electron microscopy analysis, and several parts were analyzed for the same sample of treated leather.

For sake of brevity, only the most representative images for each sample are reported. EDS analysis allowed to evaluate the amount of deposited material; the homogeneity of the dispersion was assessed by measuring EDS maps of Si element.

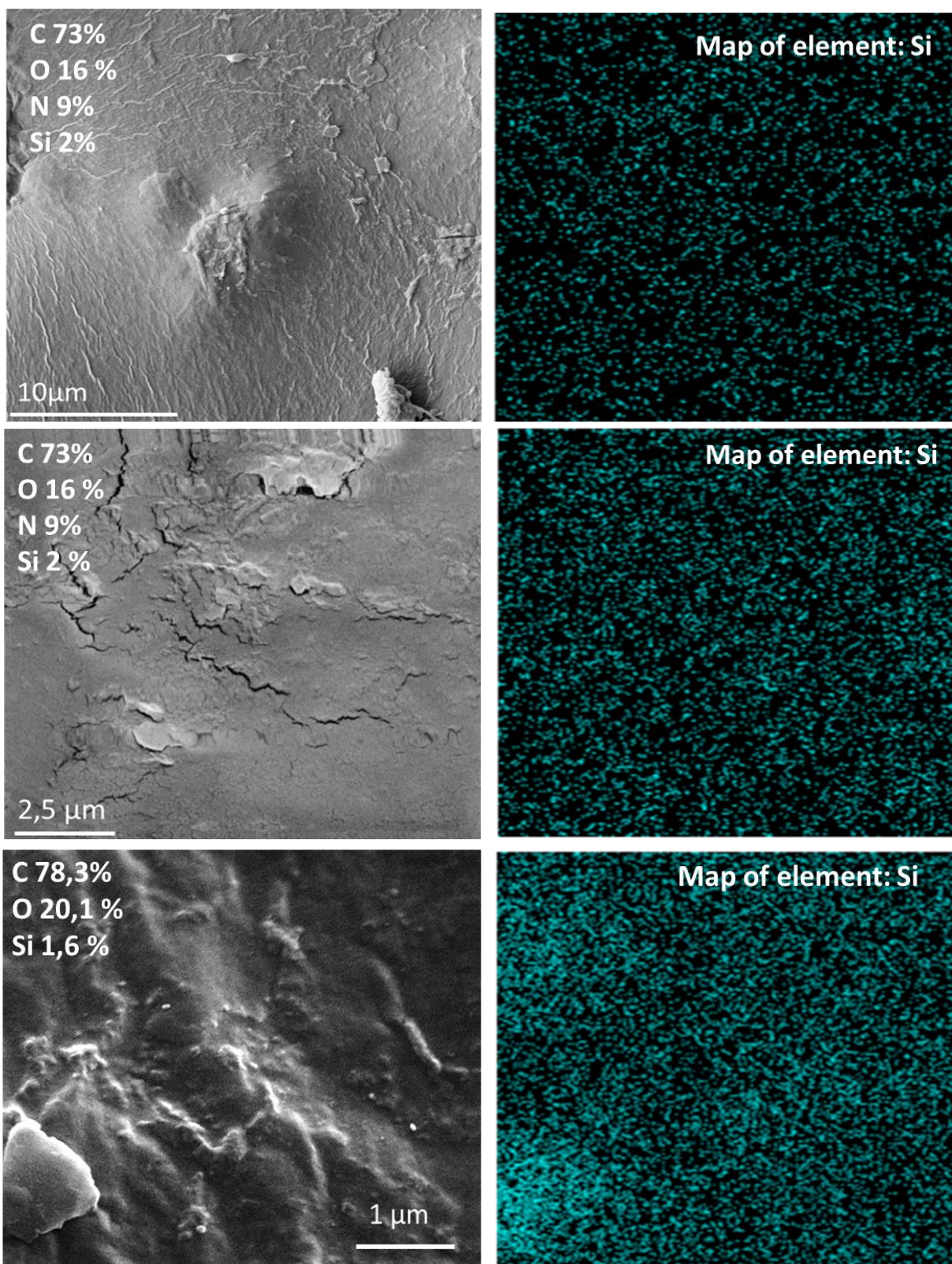


Figure 2.6.9. SEM-EDS analysis of different leather samples treated with AR812 at different magnifications. On the right, for each leather sample analyzed, the silicon atom map is shown.

As can be seen from the images of Fig. 2.6.9, the dispersion of AR812 results to be quite homogeneous; the map of the silicon atom, shown on the right, allows to visualize, through a blue coloration, where the silicon is physically located, giving an indication on the dispersion of

nanoparticles on the surface of the leather. The Roll Coater technology used for deposition improved the homogeneity of deposition as compared with the spray technology described above. Quantification was provided by EDS analysis and, in addition to the presence of carbon, oxygen and in some cases nitrogen (main components of the leather), the presence of the silicon atom is recorded. However, the amount is limited (about 1.6-2%), thus witnessing an improvement in dispersion but not in the amount of deposited material.

This may depend both on the amount used in the process, and on the type of interactions occurring in the cover mixture, which may have retained most of the nanoparticles in the cylinder.

Notwithstanding the limited amount of hydrophobic nanoparticles on leather samples, dynamic water resistance tests (Maeser Water Penetration tester) were performed. In this test, the treated leather sample is put on V-shaped clamps to flex the sample at a certain angle and speed. The sample is immersed in water and steel balls connected to an electrical circuit are located in the internal part of the leather, the flesh side. This allows to measure a potential difference, so that a signal is emitted when the balls are wet.



Figure 2.6.10. Maeser Water Penetration Tester. On the right the situation at the beginning and at the end of the test of a leather sample can be observed.

This is a dynamic test, where the leather sample is subjected to continuous traction, to stretch and shrink the fibers and increase the penetration of the water between them. The results obtained on the leather samples treated with the commercial AR812 samples were satisfactory, with room of improvement with the increase of deposited material on leather samples.

Bibliographic References

1. Ma, J.; Zhang, X.; Bao, Y.; Liu, J., A facile spraying method for fabricating superhydrophobic leather coating. *Colloids and Surfaces A: Physicochemical and Engineering Aspects* **2015**, *472*, 21-25.
2. Ponsubbiah, S.; Gupta, S., Role of Machineries for Film Forming in Leather Finishing,. *International Journal of Latest Technology in Engineering, Management & Applied Science (IJLTEMAS)*, **2018**, *VII* (IV), 8.

3. FIREPROOFING ASPECTS

3.1 MATERIALS AND METHODS

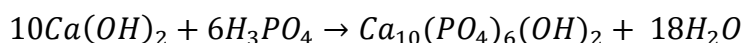
3.1.1 Materials

Different types of commercial and lab-made materials were employed in treatment of leather samples in this part of the project, with the aim to improve leather fire resistance.

- *Nano-TiO₂*, a commercial pure titanium dioxide (80% anatase, 20% rutile, SSA = 50 m²/g), purchased from Evonik (Aeroxide TiO₂ P25).
- *Nano-SiO₂*, a commercial silica purchased from Evonik (Acematt TS 100). Its transparency makes it suitable for coating.

• *Nano-HA* was prepared at laboratory scale following a classic preparation methodology reported in literature.¹ Commercially available reagents and solvents were used: calcium hydroxide (Ca(OH)₂, Sigma-Aldrich, 96%), phosphoric acid (H₃PO₄, Sigma-Aldrich, 85%), ammonium hydroxide solution (NH₄OH, Sigma Aldrich) and distilled water.

The reagents were combined in a 10:6 molar ratio, giving a typical stoichiometric neutralization reaction:



In particular, 0.1 mol of calcium hydroxide (Ca(OH)₂) was stirred for 20 min in 200ml of distilled water, 0.06 mol of phosphoric acid (H₃PO₄) diluted in 200ml of distilled water was added dropwise to the suspension over 45 min. The pH was maintained above 10.5 by addition of ammonium hydroxide solution. After completing the phosphoric acid addition, the suspension was left under stirring for 2 hours. After this period, stirring was stopped and the suspension was left overnight in the mother solution.

The synthesized particles were then centrifuged (4000 rpm, 5 min), separated from supernatant, re-dispersed in water, and then centrifuged again in order to remove unreacted reagents (3 times, 4000 rpm, 5 min); finally, particles were oven-dried at 50°C overnight; the reaction yield is 99.6%.

The prepared nano-HA at laboratory scale was used as a re-tanning agent in leather treatment for fireproofing.

• *Oxidized sodium alginate (OSA)* was prepared in the Leather and Footwear Research Institute (ICPI) of the National Research and Development Institute for Textiles and Lather (INCDTP), Bucharest, Romania, using the selective oxidation of sodium alginate (SA) with potassium periodate following a protocol described by Ding et al.^{2,3}

Sodium alginate (analytical grade) was purchased by Merck. The sodium alginate (SA) is a linear polysaccharide derivative of alginic acid composed of 1,4-β-d-mannuronic (M) and α-l-guluronic (G) acids with a high ability for crosslinking. Ethylene glycol (C₂H₆O₂, >99%) and sodium periodate

(NaIO_4 , >99%), as oxidizing agent, were also purchased by Merck. Sodium chloride, sodium bicarbonate and water were used at industrial grade.

During the oxidation, the $\text{C}_2\text{-C}_3$ bond between two neighboring hydroxyl groups in the glucuronic or mannuronic units is broken down and the 1,2-diol group is converted into dialdehyde.

For the preparation of OSA as a tanning agent for un-pickled pelt, 20 g of sodium alginate were dispersed in 1000 mL of distilled water and sodium periodate was added. The dispersion was stirred for 6 hours and left overnight. The reaction was stopped after 24 hours by addition of ethylene glycol in the same mol ratio as sodium periodate, under stirring for 30 min. The resultant solution was filtered to collect the final product.

- *Leather samples* were made available by the Leather and Footwear Research Institute (ICPI) of the National Research and Development Institute for Textiles and Lather (INCDTP), Bucharest.

3.1.2 Methods

The following techniques were used to characterize the nanomaterials used for leather treatments.

3.1.2.1 XRD analysis

XRD analysis was carried out in order to obtain information on the structure of the lab-made nano-HA. XRD patterns of the powders were acquired with an Analytical X'Pert Pro equipped with an X'Celerator detector powder diffractometer using $\text{Cu K}\alpha$ radiation generated at 45 kV and 40 mA. The instrument was configured with $1/2^\circ$ divergence and receiving slits and a quartz sample holder was used.

3.1.2.2 TEM measurements

In order to study the morphology of the nano-HA, HR-TEM images were obtained with a TEM JEOL JEM 3010-UHR instrument operated at 300 kV. The resolution was set at 0.17 nm using a LaB_6 source. The sample, in powder form, was dispersed on a 3 mm copper grid coated with a lacey carbon film.

The following sections describe the leather treatments with OSA and nanomaterials and the techniques used to study the interaction between nanomaterials and leather at the ICPI-INCDTP.

3.1.2.3 Leather treatments - tanning with OSA and re-tanning with nano-HA

Leather tanning with OSA – laboratory experiments

The pelt sample and Oxidized Sodium Alginate (OSA) solution were stirred at 35°C for 24 hours. In order to ensure the swelling of the collagen fibers and the penetration of the tanning agent, NaCl was added to the OSA solution up to 12% and 24%, respectively. The mass ratio between pelt and OSA was established according to the standard tanning procedure with glutaraldehyde, namely 1: 0.4. Basification of the sample was carried out by adding sodium bicarbonate (NaHCO_3), until pH reached value 8. The samples were left to rest on float for 18 hours and filtered and dried afterwards.

The effect of OSA oxidation degree was studied. For this purpose, two SA: KIO₄ ratios were used for OSA preparation, i.e. 1: 0.2 and 1: 0.8, respectively. The influence of NaCl concentration was also investigated (12 or 24%).

A classic wet-white tanning process was performed in parallel using a commercial aldehyde tanning agent and the tanned hide was used for tanning performance comparison.

Retanning method using nano-HA at laboratory scale

Nano-HA was prepared as described above and used as a retanning agent in solid state. 5 g of leather tanned with OSA were added to 50 mL of water solutions of nano-HA at 0.5, 1, 1.5 and 3%, which were stirred for 2 hours at 25 °C. Final pH value of the solution was around 9.3. The re-tanned leathers were dried at r.t.

3.1.2.4 Shrinkage temperature

One parameter to the degree and type of tanning is the shrinkage temperature (Ts).⁴ Collagen shrinking is the intrinsic property of reducing its fibers length up to a quarter of the original one when heated in an aqueous environment. The shrinkage temperature of pelt and tanned hides was measured in accordance with the standard method SR EN ISO 3380-2003.13.

3.1.2.5 Micro-DSC analysis

The hydrothermal stability of pelt and tanned hides was measured with a high-sensitivity micro-DSC III Setaram microcalorimeter equipped with Haake DC10 circulator for stabilizing the heating/cooling temperature. Samples were hydrated in 0.5 M acetate buffer solution with pH 5.0 for 30 min directly in the calorimetric cells and then heated in the temperature range (25 to 95°C) at 0.5 K/min heating rate. Experimental DSC data acquired with the SETARAM SetSoft2000 software were analysed using PeakFit 4.1 (Jandel Scientific) software. Denaturation temperature, T_{max}, was determined as the temperature attained at peak maximum. Temperature span of the transition was reported as peak width at half height, ΔT_{1/2}, and specific denaturation enthalpy, ΔH was calculated as the area under the peak by integrating (T) curve across the denaturation temperature range.

3.1.2.6 NMR-MOUSE (Nuclear Magnetic Resonance – MOBILE Universal Surface Explorer)

NMR-MOUSE is a non-invasive technique, based on a portable instrument suitable for on-site measurements. Single-sided ¹H NMR measurements were performed at room temperature using an NMR MOUSE PM2 (Magritek GmbH) controlled by a Kea 2 spectrometer (Magritek GmbH) operating at 27 MHz ¹H resonance frequency. This system can measure proton relaxation times. Effective ¹H spin-spin relaxation T_{2eff} measurements have been measured using the Carr-Purcell-Meiboom-Gill (CPMG) pulse sequence with an echo-time (TE) of about 25 μs. The experimental CPMG curves were analyzed by a combination of double exponential functions. The proton spin-lattice relaxation times T₁ were measured with a saturation-recovery pulse sequence using a Hahn-echo with an echo time of about 25 μs for detection. The analysis of the saturation recovery data was performed with the help of a single exponential function.

3.1.2.7 SEM measurements

SEM images of the treated leather samples were acquired using a SEM ZEISS (EVO50 XVP) instrument. The accelerating voltage (EHT) was set between 10 and 15 kV, with a resolution of 10 nm and a LaB₆ source. The leather samples were preventively cut in pieces of 1x1 cm and deposited on stubs with a double-sided carbon tape, in order to promote conductivity. For the same reason the samples were subsequently subjected to metallization by deposition of a thin layer of gold, using a specific metallizator.

Bibliographic references

1. Aina, V.; Lusvardi, G.; Annaz, B.; Gibson, I. R.; Imrie, F. E.; Malavasi, G.; Menabue, L.; Cerrato, G.; Martra, G., Magnesium- and strontium-co-substituted hydroxyapatite: the effects of doped-ions on the structure and chemico-physical properties. *J Mater Sci Mater Med* **2012**, *23* (12), 2867-79.
2. Ding, W.; Yi, Y.; Wang, Y. n.; Zhou, J.; Shi, B., Preparation of a Highly Effective Organic Tanning Agent with Wide Molecular Weight Distribution from Bio-Renewable Sodium Alginate. *ChemistrySelect* **2018**, *3* (43), 12330-12335.
3. Ding, W.; Wang, Y.-N.; Zhou, J.; Shi, B., Effect of structure features of polysaccharides on properties of dialdehyde polysaccharide tanning agent. *Carbohydr Polym* **2018**, *201*, 549-556.
4. Badea, E.; Carșote, C.; Hadîmbu, E.; Șendrea, C.; Lupaș, M.-C., The effect of halloysite nanotubes dispersions on vegetable-tanned leather thermal stability. *Heritage Science* **2019**, *7* (1).

3.2 THE PRODUCTION OF NANO-HYDROXYAPATITE (nano-HA) AS FLAME RETARDANT AGENT

3.2.1 Characterization of the prepared nano-HA

The minimal required amount of nano-HA for the application to one leather sample (ca. 30x40cm) is ca. 15-20 g.; each synthesis allows to produce ca. 8.5 g, so that four batches have been prepared. These have been fully characterized about their physico-chemical properties (IR, HR-TEM, SSA_{BET} , XPRD), to assess the reproducibility of the procedure.

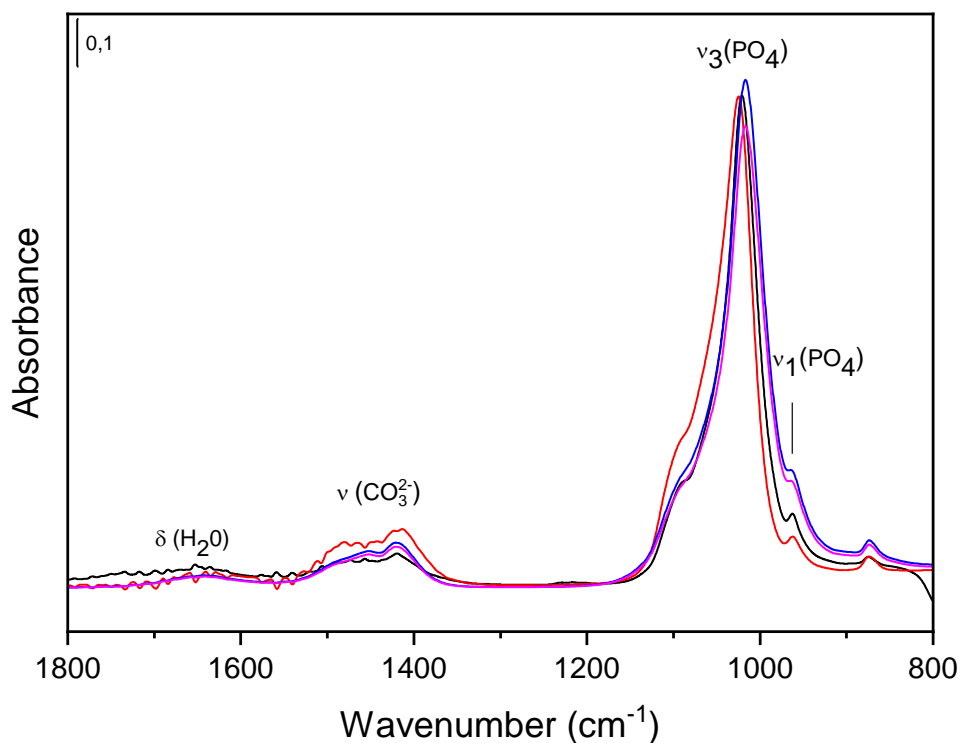


Figure 3.2.1 IR spectra acquired in ATR mode of HA_1 (magenta spectrum), HA_2 (black spectrum), HA_3 (red spectrum), and HA_4 (blue spectrum) in the 1800-800 cm^{-1} region.

IR measurements in ATR modes were carried out on the four prepared batches. In Fig. 3.2.1 the spectra of HA_1, HA_2, HA_3, and HA_4 are reported. The most intense bands, in all cases, fall between 1090 and 1000 cm^{-1} , due to the triply degenerate antisymmetric vibration modes of P-O bonds ($\nu_3(\text{PO}_4)$).¹ The shoulder at ca. 960 cm^{-1} is assigned to non-degenerate symmetric vibration modes of P-O bonds ($\nu_1(\text{PO}_4)$). Since the spectra are recorded in ATR mode (in presence of air), the bending mode of water ($\delta\text{H}_2\text{O}$) is present in all cases. The bands between 1480 and 1410 cm^{-1} are related to the antisymmetric stretching mode of carbonates ($\nu(\text{CO}_3^{2-})$), which are formed during the synthesis by CO_2 dissolution in the water solvent. The average content of carbonates in HA samples prepared by this method is ca. 1%.²

The spectra of the four samples are very similar and show the typical peaks of HA, giving a first indication of the reproducibility of the synthesis.

Morphological features of the four prepared batches were investigated by TEM measurements (Fig. 3.2.2).

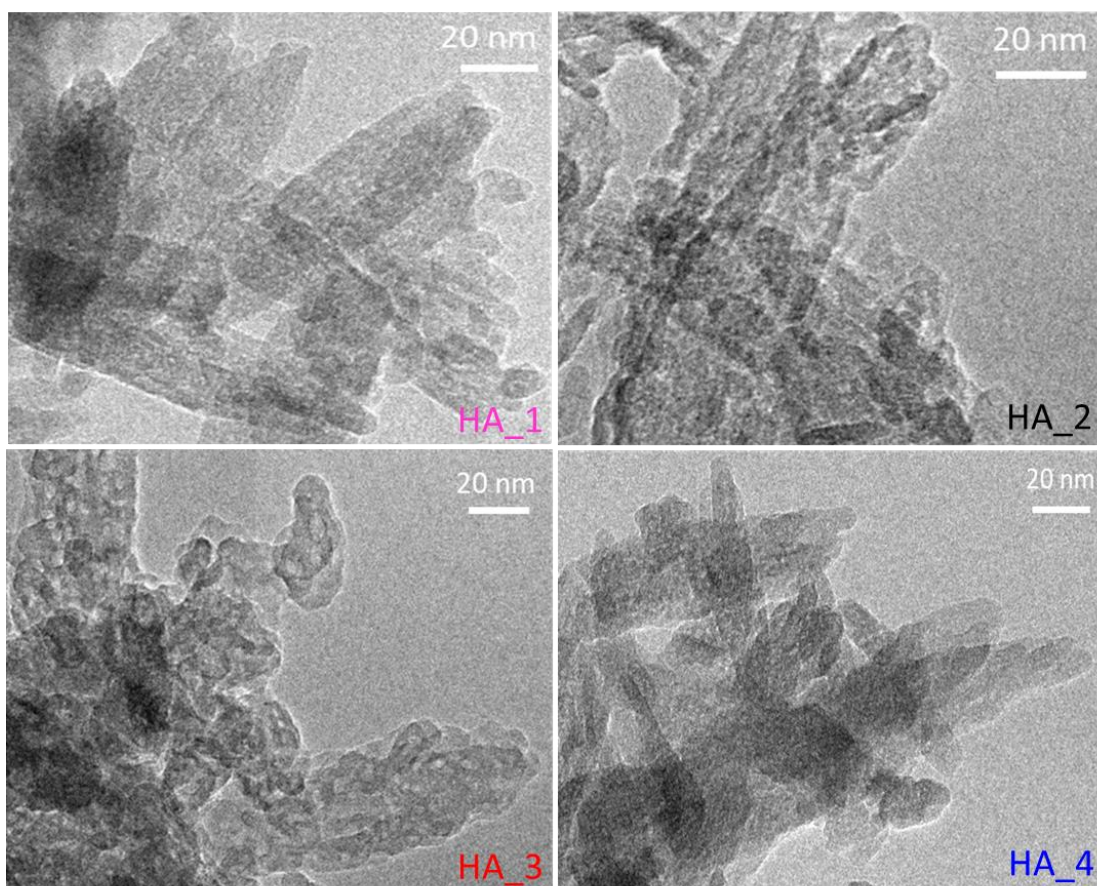


Figure 3.2.2. HR-TEM images of different batches of nano-HA (HA_1, HA_2, HA_3, HA_4). Original magnification: 100kx.

In Fig. 3.2.2 it is possible to notice a tight agglomeration of the nanoparticles, and for a significant portion of the particles a needle-like shape can be appreciated, with size (length \times width \times thickness) of ca. 150-100 nm \times 40-20 nm \times 5-10 nm. The morphology of the nanoparticles is similar among different batches, confirming the reproducibility of the preparation.

The nanometric size of HA observed by TEM was confirmed by specific surface area (SSA) values (between 110 and 115 m²/g) reported in Tab. 3.2.1.

Table 3.2.1. Specific surface area values of nano-HA of different batches (HA_1, HA_2, HA_3, HA_4).

nano-HA batch n°	SSA _{BET} (m ² ·g ⁻¹)
1	110
2	111
3	115
4	112

Structural insights were obtained by XRD patterns reported in Fig. 3.2.3.

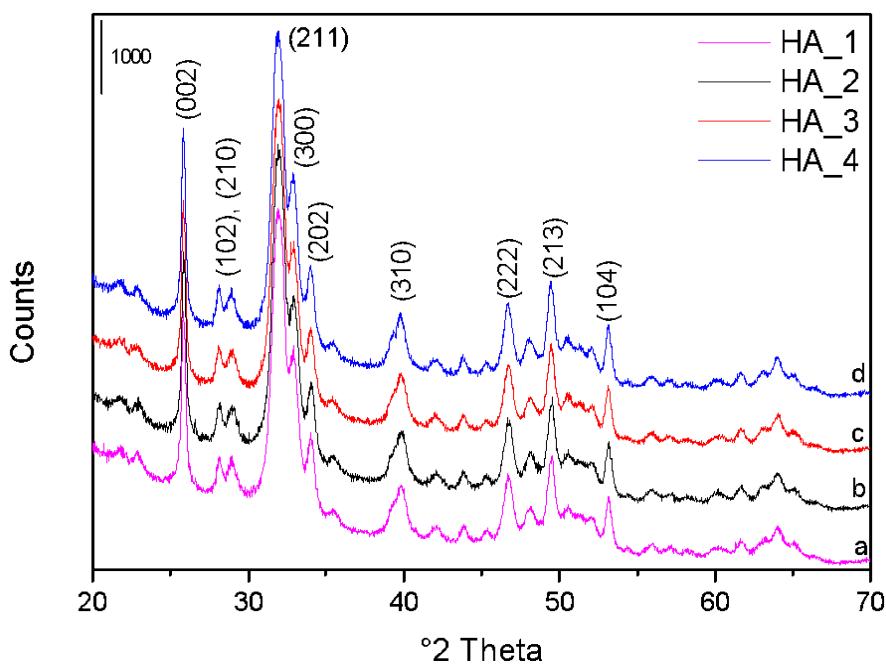


Figure 3.2.3. XRD patterns of different batches of nano-HA (HA_1 (a), HA_2 (b), HA_3 (c), HA_4 (d)).

Analysis of the XRD patterns allow to identify the structure and crystallinity of the materials. Peaks at 2θ characteristic of the HA structure (JCPDS 9-432)³ are present in all samples, with no significant differences in absolute/relative intensity and peak width. No peaks related to extra phases can be seen, indicating the purity of the HA material.

3.2.2 Life Cycle Assessment (LCA) at lab-scale: assessment of the sustainability of nano-HA production

As reported in the Introduction, the primary aspect of this project is the contribution to the increase of sustainability in chemical and leather-product manufacturing that represent two of the most pollution-intensive industrial activities. The preparation of nano-HA as a sustainable alternative to brominated flame-retardant agents is one of the possible ways to contribute to environmental issues in this field.

The study of Ingrao et al.⁴ in collaboration with our Chemistry department reported the investigation of the environmental impacts and damages of the production of nano-HA at laboratory scale through Life Cycle Assessment. LCA is a useful tool to evaluate the environmental impact in terms of quality and quantity associated with the cycles of life of a product. LCA was applied in this study according to the International Standards 14040 and 14044 (ISO, 2006) and was thus articulated in the following steps: *Goal and Scope Definition*; *Life Cycle Inventory (LCI)*; *Life Cycle Impact Assessment (LCIA)*; and *Life Cycle Interpretation*. These phases are interlinked, with all of them playing key roles for the consistency of the study and for the reliability of the results obtained. In the first phase (*Goal and Scope Definition*), the system boundaries and the Functional Unit (FU) were defined. The FU was chosen considering the system service, that is, producing 10 g nano-HA for finishing a given surface of leather sample (ca. 30 x 40cm). The system boundaries were set at the lab exit-gate and included: the preparation of both input materials, auxiliaries and electricity

from resource extraction; their transformation into the finished product (10 g nano-HA) through a set of steps including magnetic stirring, centrifugation, and drying (Fig. 3.2.4).

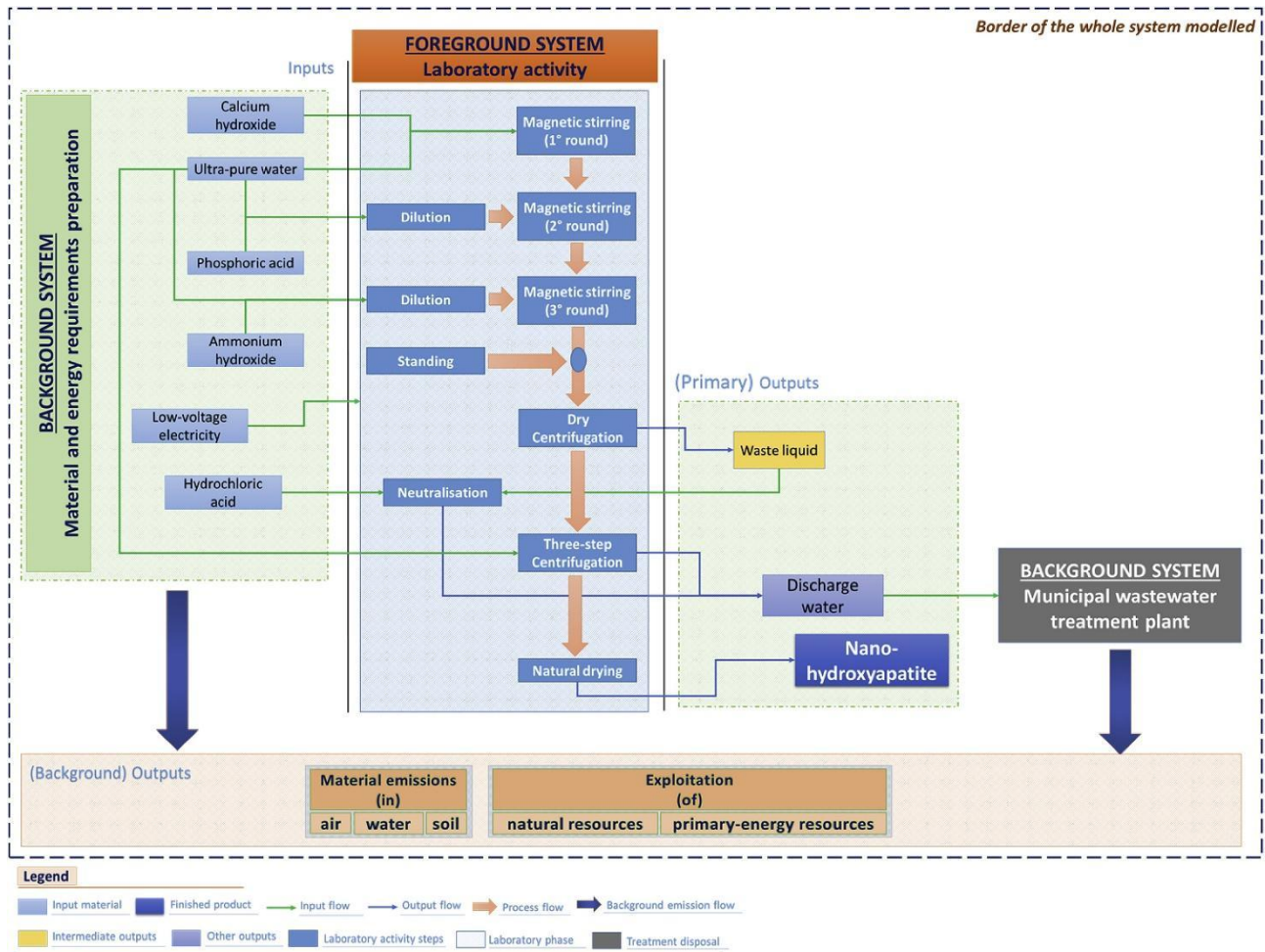
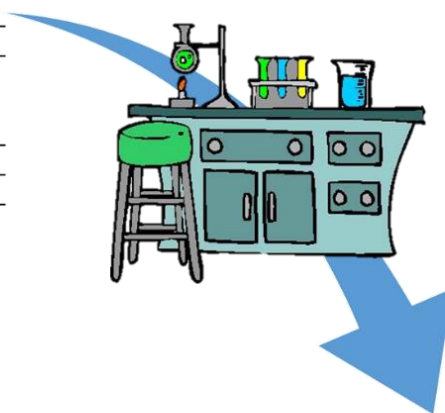


Figure 3.2.4. System boundaries assessed in this study.

Thereafter, the elaboration comes to the *Life Cycle Inventory*. It is based upon the compilation and quantification of all incoming and outgoing flows which pertain to the given production system or supply chain. The delicacy and importance of this phase comes from the essential need to create a dataset related to a model of the system to be as close as possible to the real one. The inputs are represented by the materials and energy sources that are utilized in the system investigated, whilst the outputs are the material emissions in air, water and soil, as well as the exploitation of natural and primary-energy resources. For the LCA development, primary data were recorded in collaboration with the lab technicians and regarded both inputs and outputs as associated with the synthesis process.

ITEM	QUANTITY	UNIT
INPUTS		
<i>Raw materials</i>		
Calcium hydroxide		
+	14.33	g
Phosphoric acid (85%)		
Ultra-pure water	424	g
<i>Auxilairies</i>		
Liquid ammonia	1.05	g
Ultra-pure water	600	g
Hydrochloric acid	2.85	g
<i>Energy</i>		
Low-voltage electricity	127.61	Wh



ITEM	QUANTITY	UNIT
OUTPUTS		
<i>Finished product (FU of the study)</i>		
Nano-hydroxyapatite	10	g
<i>Waste streams</i>		
Discharge water	1027.9	g

Figure 3.2.5 Inventory dataset used for the environmental impact assessment.

Fig 3.2.5 shows the data that have been inventoried for the study development. The amounts reported for NH_4OH (1.05 g) and HCl (2.85 g) correspond to 6 and 2.4 ml, respectively. This is the reason why the amount of discharge water is equal to 1032.4 ml, namely almost 1028 g. Additionally, the amount of discharge water contains an almost negligible quantity of chemical waste, which is represented by a 3.32 mg ensemble of unreacted substances ($\text{Ca}(\text{OH})_2$ and H_3PO_4). As shown in Fig. 3.2.4, to make the whole water dischargeable and safe for human health, those substances were treated through a neutralization process involving use of HCl .

Transports for raw material supply were also accounted for: the transport flow was calculated and resulted to be equal to a total of 13.65 kg/km. In addition to this, no transport of ultra-pure water was accounted for, because the water is produced locally through a distillation plant serving all laboratories working within the Department of Chemistry.

For the study development, secondary data were used to model the production of those material and energy inputs. This was done by extrapolating them from a database of acknowledged scientific relevance and value, as is Ecoinvent. In this study, those data were represented by the production of the raw materials and of the related transports and were modelled by accessing the Ecoinvent database: the modules are reported in Tab. 3.2.1.

Table 3.2.1 The main Ecoinvent modules used for the modelling of the system were listed along with the related descriptions.

Input item	Ecoinvent module	
	Modelled as	Dataset description
Calcium hydroxide	Lime, hydrated, packed (RoW) C ⁵ production Alloc Def, S	The dataset includes processes like milling, sieving, filtering, packing, and storing
Phosphoric acid	Phosphoric acid, industrial grade, without water, in 85% solution state (RER) purification of wet-process phosphoric acid to	This module refers to concentration of acid after purification to 85% H ₃ PO ₄ content. The dataset includes raw materials, processing chemicals and processing energy, direct emissions to water from process, disposal of solid process waste to landfill and of spent solvent to incineration, estimations on of raw materials transport to the plant.
Ultra-pure water	Water, ultrapure (RoW) production Alloc Def, S	The module refers to production of ultrapure water including materials, energy uses, infrastructure and emissions.
Ammonium hydroxide	Ammonia, liquid (RoW) ammonia production, steam reforming, liquid Alloc Def, S	The dataset considers the manufacturing process starting with natural gas, air and electricity, plus auxiliaries, energy, transportation, infrastructure and land use, as well as wastes and emissions into air and water. Transport of the raw materials, auxiliaries and wastes is included, whilst the delivery phase of the finished product is not incorporated in the module, mainly because it was considered as pertaining to the downstream utilisation.
Hydrochloric acid	Hydrochloric acid, without water, in 30% solution state (RER) benzene chlorination Alloc Def, S	The module provides production of hydrochloric acid, in 30% solution state, from benzene chlorination; the dataset includes materials, energy uses, infrastructure and emissions.
Electricity	Electricity, low vantage transformation from medium to low voltage Alloc Def, S	This dataset describes the transformation from medium to low voltage as well as the distribution of electricity at low voltage. Included are the electricity production in Italy and from imports, the transmission network as well as direct SF ₆ -emissions to air. Electricity losses during low-voltage transmission and transformation from medium-voltage are accounted for.
Transport mean	Transport, freight, lorry 3.5-7.5 metric ton, EURO 5 (RER) transport, freight, lorry 3.5-7.5 metric ton, EURO 5 Alloc Def, S	Inventory refers to the entire transport life cycle. For road infrastructure, expenditures and environmental interventions due to construction, renewal and disposal of roads have been allocated based on the Gross tonne kilometre performance. Expenditures due to operation of the road infrastructure, as well as land use have been allocated based on the yearly vehicle kilometre performance. For the attribution of vehicle share to the transport performance a vehicle life-time performance of 540000 vkm/vehicle has been assumed. Included processes are the followings: operation of vehicle; production, maintenance and disposal of vehicles; construction and maintenance and disposal of road.

As shown in Table 3.2.1, NH₄OH was modelled as liquid ammonia (NH₃) through the related module contained in Ecoinvent: a different amount was used, however, for the assessment. It was calculated considering that, based upon information provided by the lab technicians, the NH₃ content in NH₄OH

is 28%. In the light of this, a consumption value of 0.294 g was calculated and assigned to the ammonia production module.

The third phase (*Life Cycle Impact Assessment*) is aimed at assessing the environmental impacts of the identified substances and the resulting effects (damages) to a set of duly identified environmental categories. The emitted substances and consumed resources already quantified in the LCI phase were organized in a limited set of 'midpoint categories', also known as Impact Categories (ICs) and organized in Damage Categories (DCs), in order to assess the quality changes that the life cycle of the product causes to the environment.^{5,6}

A generalized version of the assessment framework is depicted in Fig. 3.2.6.

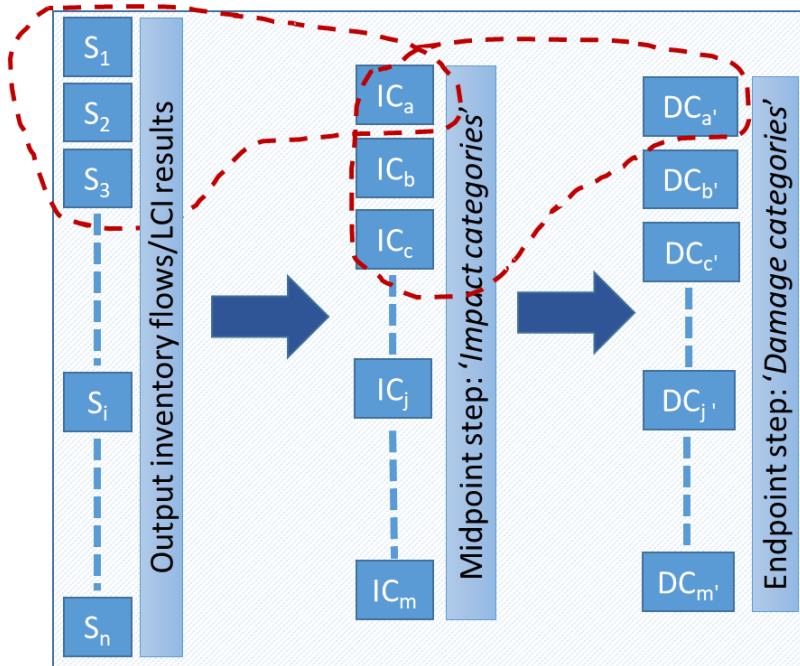


Figure 3.2.6 A generalized version of the LCIA framework, that was elaborated by the authors using the relevant information pack contained in Jolliet's et al.⁴ Aside from the LCI, CI and DI acronyms that have already been given in the text, 'S' refers to the given substance emitted, or resource consumed.

Equivalent indicators were used to quantify LCIA results in the form of specific characterization values; these were expressed as: kgCO_2 eq for 'Global Warming'; MJ primary for 'Non-renewable Energy'; and $\text{kgPM}_{2.5}$ eq for 'Respiratory Inorganics'. As a standardized practice in LCA, end-weighting was based upon estimation of results from the study, through equivalent numerical parameters that are known as 'weighing points' or 'damage points' or 'eco-points' or, more simply, 'points'. The endpoint analysis was then narrowed to the damage point associated with each and every background material and energy commodity utilized, and with both the emission of pollutants and the exploitation of primary-energy resources. This made it possible to highlight the most environmentally burdening ones, as the base to find room for improvement, in line with the objectives of this study. Finally, the end-weighting results were reported also in reference to both ICs and DCs, making it possible to identify the most important ones on a unique point scale and, hence, the most representative of the system investigated.

Finally, the interpretation phase and therefore the evaluation of the results was achieved (*Life Cycle Interpretation*). The endpoint LCIA showed the environmental damage associated with the system investigated to be quantified in 37.18 μpt , with the highest contributions staying in the production and consumption of electricity (23.345 μpt) and in the production of H_3PO_4 (9.304 μpt), as both demanded for the process, and in the transport mix for acquisition of all chemical substances utilized (2.564 μpt): these three items contributed together 94.71% of the total environmental damage. With regard to production of the chemicals utilized, H_3PO_4 is the most environmentally harmful one, whilst far lesser contributions were found in the production of $\text{Ca}(\text{OH})_2$, HCl , and NH_3 , equal to a total of 1.276 μpt , which is just 3.43% of the total damage. On average, such damage should be attributed mainly to the combined effect of the little amounts in stake of those substances and to the environmental impact associated with the specific production processes on equal amounts of substance produced. Results in terms of damages-assessment values are plotted in Fig. 3.2.7 as weighing points.

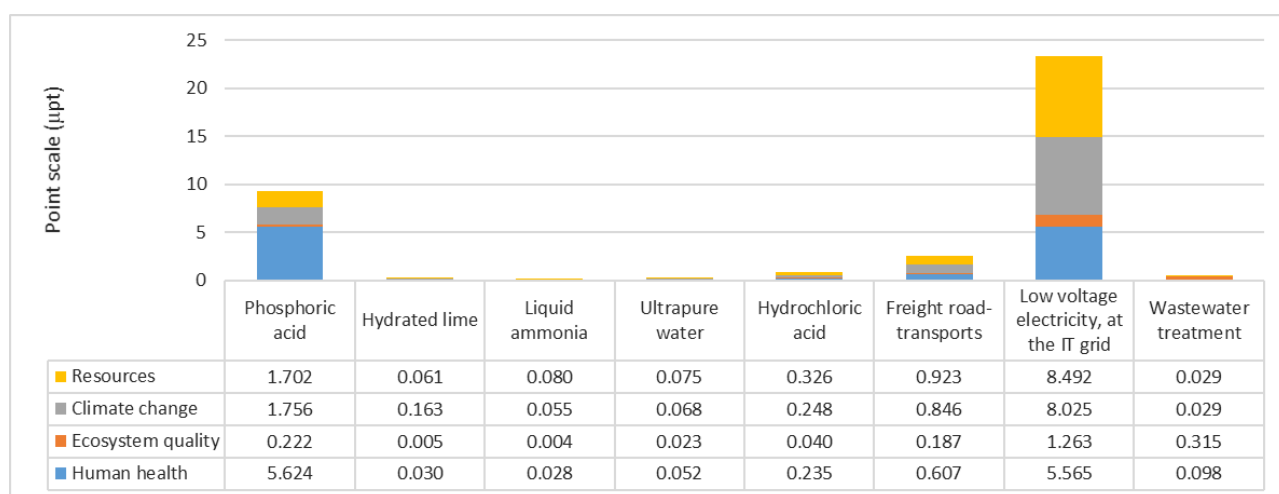


Figure 3.2.7 Weighing results per damage category reported on a μpt scale.

From Fig. 3.2.7, it is confirmed that, along with H_3PO_4 production, the major environmental impacts stay in the electricity consumption, and in the road transports for the acquisition of all the chemical substances utilized in the process. So, there is evidence that, in the light of their environmental relevancy, these two items cannot be neglected for creation of reliable models of lab-scale processes. However, their accounting could tend to divert the focus of the analysis from the process core-substances, mainly because of the little amounts at stake as a classic of synthesis processes. Just think that, the damage caused by electricity consumption is nearly two times and a half bigger already than the production of the most impactful substance, namely phosphoric acid. Furthermore, from Fig. 3.2.7 it can be concluded that the most affected damage categories are, in line with the inventory dataset, 'Human health' (HH), 'Resources' (R), and 'Climate change' (CC), with damage values equal to a total of 12.39, 11.688, and 11.19 μpt . 'Ecosystem Quality' (EQ) is the DC suffering the lowest damage, as the latter resulted in a value of 2.059 μpt .

More detailed information on the values extrapolated from LCIA, in order to assess the most environmentally relevant ICs, are reported in the article.⁴

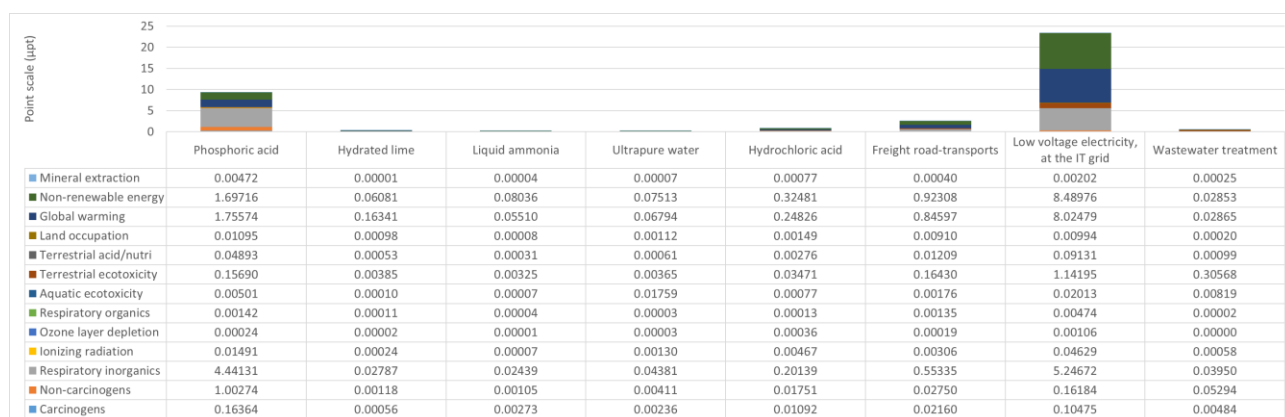


Figure 3.2.8 Weighing results per impact category were reported on a µpt scale.

Fig. 3.2.8 was elaborated to show the association between the impact categories contemplated by the method and the material and energy items composing the synthesis process investigated. These data could serve as a starting base to identify environmental impact indicators that can be used for potential development.

Based upon findings from the study, electricity consumption, H_3PO_4 production, as well as the transports for acquisition of the chemicals utilized in the processes, are the three most environmentally damaging items. From laboratory to industrial scale, electricity consumption and transport may have a not-fully proportional impact compared with the increase in the quantity of chemicals. This awareness based upon LCIA results may lead to foster more attention on H_3PO_4 supply chain rather than upon electricity consumption, in terms of making strategies oriented to process optimization and innovation.

Bibliographic references

1. Aina, V.; Lusvardi, G.; Annaz, B.; Gibson, I. R.; Imrie, F. E.; Malavasi, G.; Menabue, L.; Cerrato, G.; Martra, G., Magnesium- and strontium-co-substituted hydroxyapatite: the effects of doped-ions on the structure and chemico-physical properties. *J Mater Sci Mater Med* **2012**, *23* (12), 2867-79.
2. Ivanchenko, P.; Delgado-López, J. M.; Iafisco, M.; Gómez-Morales, J.; Tampieri, A.; Martra, G.; Sakhno, Y., On the surface effects of citrates on nano-apatites: evidence of a decreased hydrophilicity. *Scientific Reports* **2017**, *7* (1).
3. Sakhno, Y.; Ivanchenko, P.; Iafisco, M.; Tampieri, A.; Martra, G., A Step toward Control of the Surface Structure of Biomimetic Hydroxyapatite Nanoparticles: Effect of Carboxylates on the {010} P-Rich/Ca-Rich Facets Ratio. *The Journal of Physical Chemistry C* **2015**, *119* (11), 5928-5937.
4. Ingraio, C.; Vesce, E.; Evola, R. S.; Rebba, E.; Arcidiacono, C.; Martra, G.; Beltramo, R., Chemistry behind leather: Life Cycle Assessment of nano-hydroxyapatite preparation on the lab-scale for fireproofing applications. *Journal of Cleaner Production* **2021**, 279.
5. Ingraio, C.; Selvaggi, R.; Valenti, F.; Matarazzo, A.; Pecorino, B.; Arcidiacono, C., Life cycle assessment of expanded clay granulate production using different fuels. *Resources, Conservation and Recycling* **2019**, *141*, 398-409.
6. Jolliet, O.; Margni, M.; Charles, R.; Humbert, S.; Payet, J.; Rebitzer, G.; Rosenbaum, R., IMPACT 2002+: A new life cycle impact assessment methodology. *The International Journal of Life Cycle Assessment* **2003**, *8* (6), 324-330.

3.3 A SUSTAINABLE ALTERNATIVE IN THE TANNING PROCESS AND APPLICATION OF NANOMATERIALS ON LEATHER

3.3.1 Oxidized sodium alginate (OSA) as a sustainable tanning agent

The chemical nature of collagen allows it to interact with a variety of mineral and vegetal agents, resulting in the hide conversion to leather. As already described in the 'Introduction', the potential risk of the Cr(III) tanning¹ is prompting different countries to find safer alternatives.

In the tanning process using aldehydes, the effect of crosslinking occurs when the first step of formation of alpha-hydroxy amines (between aldehyde and collagen amino group) leads to the condensation with side amino groups of collagen.² However, the highlighted hazard to human health in the release of formaldehyde during leather treatment has led to the imposition of restrictions in its use.³

The analysis of the literature revealed that the development of alginate oxidation approaches has expanded the potential of alginate applications, including its tanning ability.⁴ Thanks to the abundance of this polysaccharide, that mainly occurs in marine brown algae and in soil bacteria, its industrial production is considered inexpensive.⁵

Moreover, the biocompatibility of alginic acid and its sodium salts has been demonstrated,⁶ and its role in the increase of thermal stability when used as a dehydrating agent for collagen films shown.⁷ It was also reported that through partial oxidation, sodium alginate decreases its molecular weight while the number of aldehyde groups are increasing;⁸ oxidized alginate has thus shown the ability to link to amino groups of collagens and behave as a tanning agent,⁹ prompting the National Research & Development Institute for Textiles and Leather (INCDTP) to find an experimental procedure for obtaining sustainable leather.

The tanning properties of oxidized sodium alginate (OSA) described in section 3.1, at both laboratory and micro-pilot levels were firstly studied by shrinkage temperature method, the industrially approved tanning test.

Table 3.3.1. Shrinkage temperature determined by standard method: a) leather tanned with synthetic aldehyde, b) leather tanned with pure OSA at laboratory level, c) leather tanned with industrial OSA at micro-pilot level, d) leather tanned with industrial OSA at laboratory level, e) calf crust leather.

	Sample	T _{shrinkage} (°C)
a)	L_SA	77
b)	L_OSA _{pure_lab}	86
c)	L_OSA _{ind_milot}	86
d)	L_OSA _{ind_lab}	83
e)	Crust_L_OSA	84

The parameters associated with the shrinking activity of samples tanned with OSA are reported in Tab. 3.3.1 (b, c, d, e), in comparison with parameters associated with shrinkage activity of leather tanned with synthetic aldehyde (L_SA) (a). Distinct shrinkage behavior is dependent on tannin type and molecular size, therefore different models of activity can be observed in case of leather tanned with synthetic aldehyde with molar mass below 150 g/mol. In case of crust leather, the sample completed the entire tanning process which provides better and uniform interaction between collagen and OSA (e).

Micro-differential scanning calorimetry (micro-DSC) was used to reveal the deterioration patterns of collagen fibers in pure or industrial OSA-tanned leather and in comparison, with synthetic aldehyde tanned leather. One of the most important changes induced by the tanning process in general is the increased hydrothermal stability due to collagen matrix stabilization through crosslinking with the tanning agent.

The position, width, height, and symmetry of the thermogram peak provide information about the thermal denaturation of collagen-based samples over the 20-95°C temperature range. Fig. 3.3.1 shows the micro-DSC denaturation curves for calf leather tanned with synthetic aldehyde (a), pure OSA at laboratory level (b) and leather tanned with industrial OSA at micro-pilot level (c).

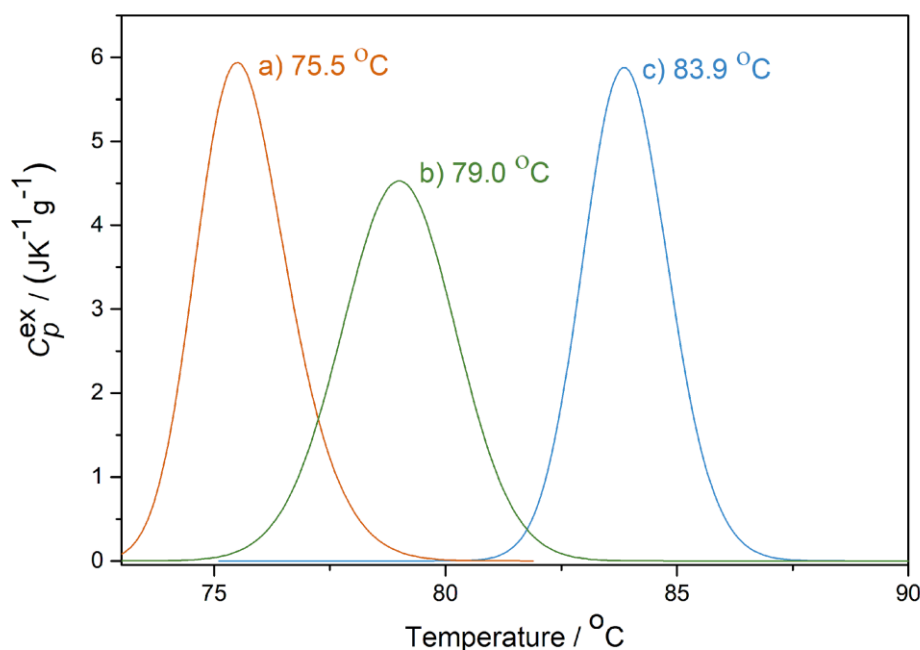


Figure 3.3.1. Micro-DSC thermograms: a) calf leather tanned with synthetic aldehyde, b) calf leather tanned with pure OSA at laboratory level, c) calf leather tanned with industrial OSA at micro-pilot level. The maximum thermal denaturation temperatures (T_{dmax}) are reported for each curve.

According to Fig. 3.3.1, the tanning ability of OSA, both pure and industrial, is superior to commercial synthetic aldehydes and it is correlated with the hydrothermal stability. Thermal stability of crosslinked collagen fibers, characterized by thermal denaturation temperature (T_d), is in direct connection with the bonds created in the crosslinking. The degraded sodium alginate presents

multiple aldehydic groups and thus the higher probability to form multiple crosslinking with the amino groups from the collagen fiber providing higher T_d of samples tanned with OSA, as expected. An increase in the T_d is usually an indication of an increase in the stability of tanned leather being a measure of the hydrothermal stability.

Once confirmed the good tanning ability of OSA, the attention was directed to the best oxidation degree (different SA:KIO₄ ratios) (Table 3.3.2) and to the influence of NaCl concentration in the tanning process (Fig. 3.3.2).

Table 3.3.2 Hydrothermal stability parameters of pelt and tanned hides: shrinkage temperature (T_s), denaturation enthalpy (ΔH), and denaturation temperature (T_{dmax}).

	Sample	T_s(°C)	ΔH (J/g)	T_{dmax} (°C)
a)	P	51	47.06	53.5
b)	L_SA	77	17.30	77.7
c)	L-OSA-0.2-24	82	15.42	83.0
d)	L-OSA-0.8-24	86	13.56	85.2
e)	L-OSA-0.8-12	86	15.76	83.7

The variation of the SA:KIO₄ molar ratio (comparing c and d) did not produce a significant change in the value of the denaturation enthalpy (ΔH); however, the value of shrinkage temperature (T_s) further increased by 4 °C in case of the higher SA:KIO₄ molar ratio (d).

This thermal stabilization can be explained by the fact that the oxidation of the polysaccharide takes place more vigorously in the case of the molar ratio 1: 0.8, resulting in polyaldehyde molecules with smaller molecular sizes, formed by breaking the polyaldehyde O-glycosidic bonds. These polyaldehyde molecules can more easily penetrate the pores of the leather and interact with free amino groups in the collagen chain, forming several covalent bonds.

A high concentration of salt is useful for ensuring the swelling of the three-dimensional fibrous network of the leather, but, on the other hand, it creates difficulties in purifying the liquor. For this reason, the tanning operation was first carried out with the standard NaCl concentration of 24%, followed by a process where the amount of salt was halved to 12% NaCl.

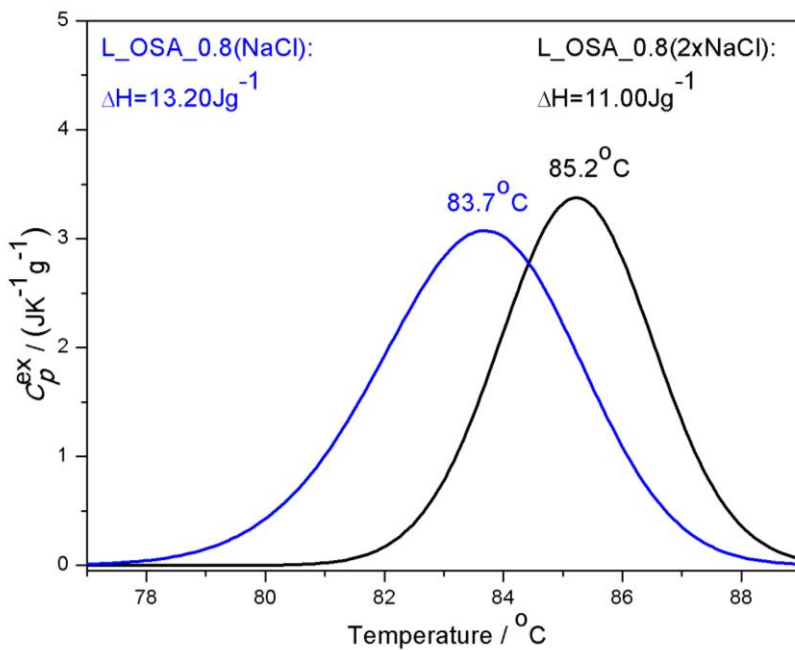


Figure 3.3.2. Micro-DSC thermograms of leather samples tanned with a molar ratio of 1: 0.8, but different amounts of salt: 12% (blue curve) and 24% (black curve).

Fig. 3.3.2 shows a decrease of approximately 2°C in the denaturation temperature in the case of sample L-OSA-0.8-NaCl (black curve), with 12% salt in the fleet, an undesirable effect, due to insufficient swelling of the collagen matrix. This indicates a more efficient and homogeneous tanning process when using a larger amount of NaCl (blue curve).

The relaxometric characterization of the sample was carried out through NMR-MOUSE. ^1H spin-spin relaxation times provide complex information about the dynamics of molecules; in fact, they are sensitive to movement which in turn is influenced by restrictions imposed by the environment. More in detail, longitudinal relaxation time T_1 quantifies the time it takes for nuclear spin to return to thermal equilibrium after a perturbation. The transverse relaxation time T_2 is a measure of the degree of mobility of polypeptide chains.¹⁰ For collagen materials two components are measured: a short relaxation time $T_{2\text{short}}$ in the range (0.1-2.1) ms and a long relaxation time $T_{2\text{long}}$ in the range (10-90) ms. $T_{2\text{long}}$ is a characteristic parameter of amorphous collagen matrix, while $T_{2\text{short}}$ characterizes the behavior of the rigid (crystalline) area. Moreover, T_1 and $T_{2\text{short}}$ values are influenced by the tanning type.¹¹

Tab.3.3.3. NMR-MOUSE analysis on leather tanned with SA (a), with OSA-0.2-2xNaCl (b), OSA-0.8-2xNaCl (c), and OSA-0.8-NaCl (d).

	Sample	T ₁ (ms)	T _{2long} (ms)	T _{2short} (ms)
a)	L-SA	43.84	0.29	0.06
b)	L-OSA-0.2-2xNaCl	48.17	4.44	0.22
c)	L-OSA-0.8-2xNaCl	22.17	0.56	0.08
d)	L-OSA-0.8-NaCl	27.00	0.44	0.08

Table 3.3.3. resumes the three parameters T₁, T_{2long} and T_{2short} measured by NMR-MOUSE on the leather samples tanned with OSA and with synthetic aldehyde. The value of the longitudinal relaxation time T₁ for the leather tanned with OSA is lower than that of the one tanned with synthetic aldehyde L_SA, indicating a stronger interaction between collagen and OSA. On the other hand, both the T_{2eff_long} and T_{2eff_short} components of the transverse relaxation time measured for OSA tanned leather have higher values than those measured for SA tanned leather. This could suggest greater fibril mobility in the collagen-OSA matrix.

3.3.2 Application of nano-TiO₂, nano-SiO₂ and nano-HA on leather tanned with OSA: SEM-EDS analysis

The leather tanned with OSA was further treated with nano-titania, nano-silica, and nano-HA. The leather samples were analysed by SEM-EDS in different parts, namely, grain that is the exposed surface, flesh, the back surface, and the section representing the internal part of the sample. SEM images reveal the complex morphology and composition of leather samples, presenting pores and fibrous structures, typical of the skin, and salts agglomerates produced during the tanning process.

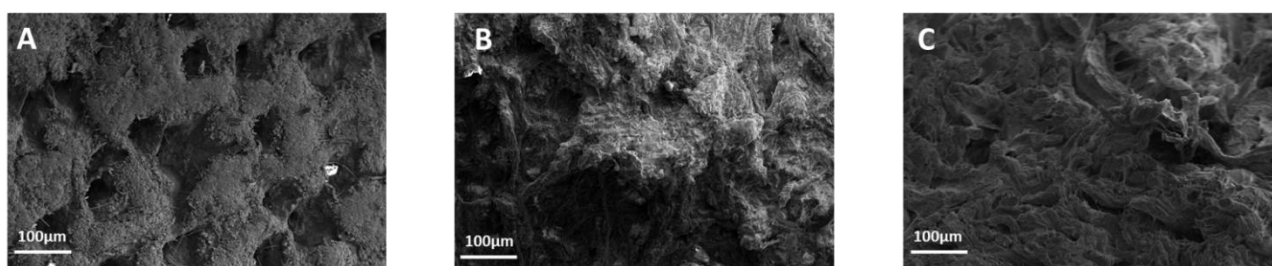


Figure 3.3.3. SEM images of leather sample tanned with OSA: A) flesh, B) grain, C) section.

For this reason, it was difficult to visually observe differences between the treated and not treated samples with nanomaterials. In this respect, it was decided to take advantage of EDS analysis. In case of nano-SiO₂ (Fig. 3.3.4, panels A, B, and C), nanoparticles were distributed across all the leather thickness; however, in case of nano-TiO₂ (Fig. 3.3.4, panels D, E, and F), there were no evidence of nanoparticles presence in the section of the sample.

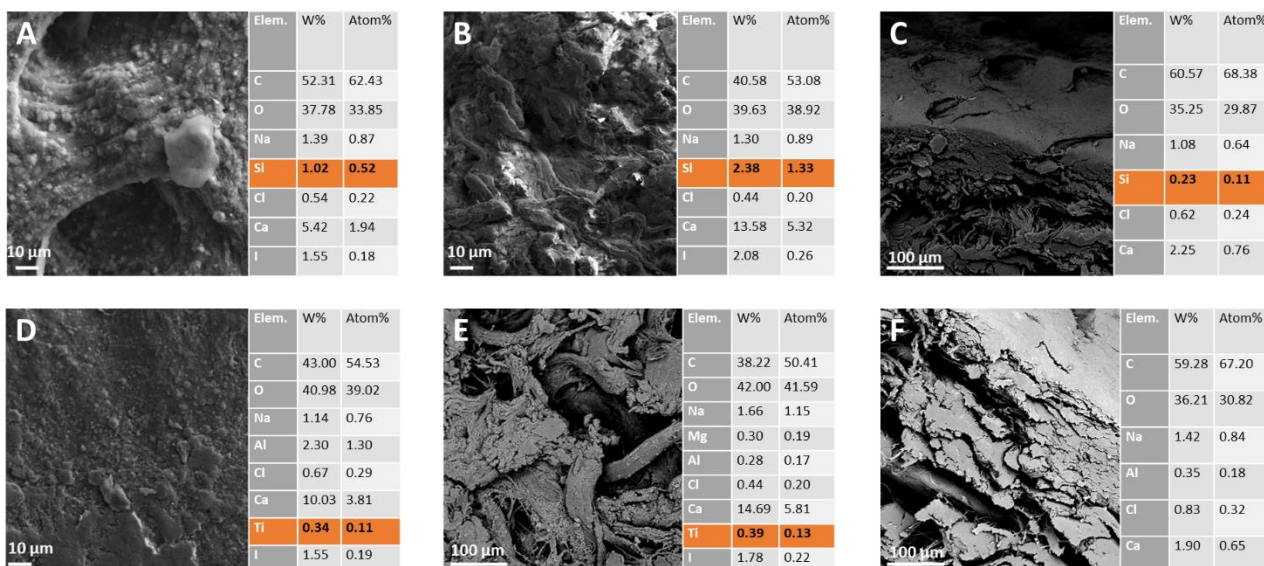


Figure 3.3.4. SEM images of treated leather sample with: A) nano-SiO₂, flesh, B) nano-SiO₂, grain, C) nano-SiO₂, section, D) nano-TiO₂, flesh, E) nano-TiO₂, grain, F) nano-TiO₂, section. For each image the EDS analysis is reported in tables.

The retanning with nano-HA produced a different situation: SEM images reveal some agglomerates in the three parts of the analysed sample (Fig. 3.3.5).

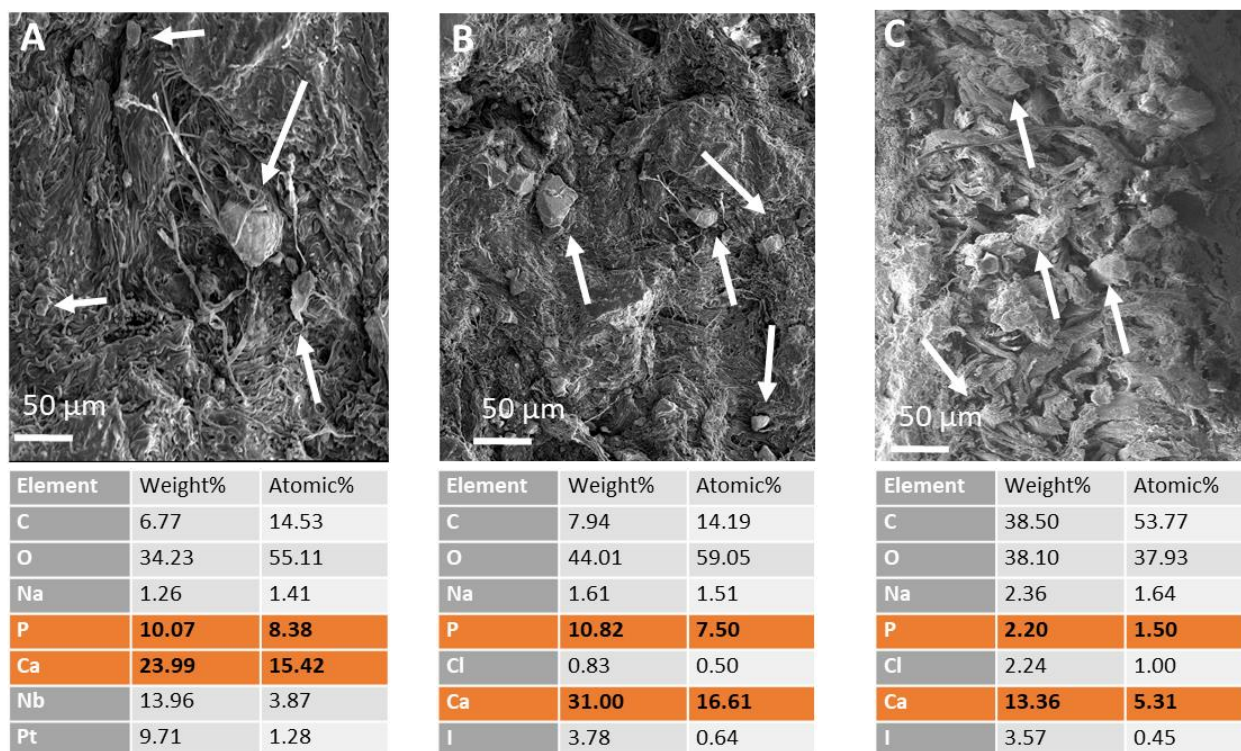


Figure 3.3.5. SEM images of treated leather sample with nano-HA: A) flesh, B) grain, C) section. For each image the EDS analysis is reported in tables.

The EDS analyses were performed in the entire region, not only on the agglomerates, in order to assess the distribution of nano-HA. The amount of P and Ca element, the main constituent of nano-HA, is higher than the Si and Ti elements found in the previous samples (Fig. 3.3.4). Moreover, the

homogeneity of nano-HA dispersion in leather samples was analysed by EDS element distribution mapping. This allows a qualitative estimation of the nanoparticle distribution, thanks to representation by colours of the different elements (Fig. 3.3.6).

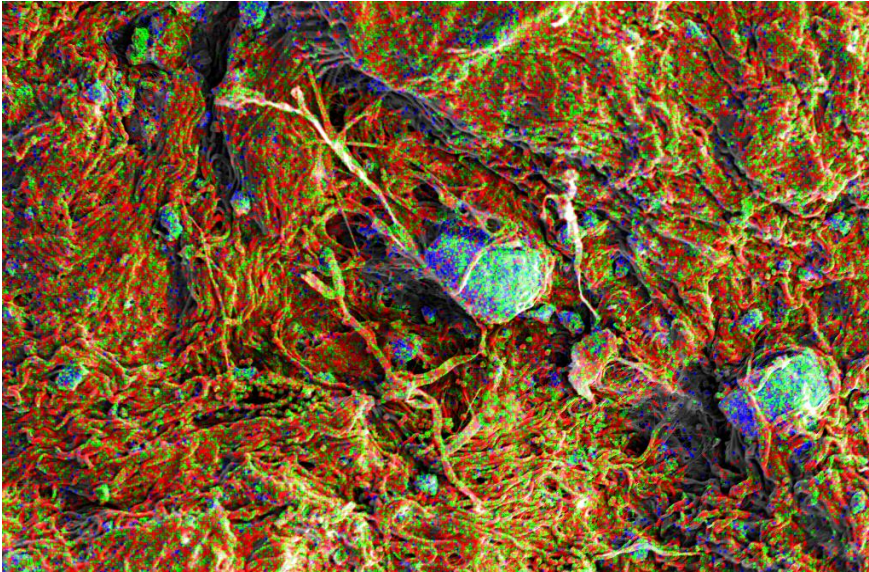


Figure 3.3.6. Map of element on SEM image of leather sample retanned with nano-HA. Color code: red-phosphorous, black-calcium, green-carbon, blue-oxygen.

From Fig. 3.3.6. it is possible to observe a good homogeneity in the dispersion of nano-HA in a leather sample, since the P and Ca elements (highlighted in red and black, respectively) are distributed in the entire selected area, and not only on agglomerates.

3.3.3 Assessment of thermal capacity of treated leather samples: micro-DSC analysis

The best results in terms of penetration and distribution of nanoparticles were obtained in the case of nano-HA. So, the assessment of the hydrothermal stability of the leather retanned with different percentages of nano-HA were performed by micro-DSC analysis. In Table 3.3.4 the denaturation parameters of leather samples tanned with OSA (compared to the leather tanned with a synthetic aldehyde L_SA) are reported.

Table 3.3.4. Denaturation parameters (T_{dmax} and ΔH) of leather samples tanned with SA and OSA and retanned with different percentages of nano-HA (0.5, 1, 1.5, 3 %) analysed by microDSC.

Sample	$T_d(^{\circ}C)$	$\Delta H (J/g)$
L_SA	75.5	14.80
L_OSA _{pure-mpilot}	81.0	10.16
L_OSA _{pure-lab}	79.0	14.08
L_OSA _{ind-mpilot}	83.9	13.68
L_OSA _{pure+nHA (0.5%)}	78.1	16.89
L_OSA _{pure+nHA (1%)}	77.4	19.40
L_OSA _{pure+nHA (1.5%)}	78.0	18.24
L_OSA _{pure+nHA (3%)}	79.3	17.57
Crust_L_OSA	81.2	17.01

The retanning effect of nano-HA was analysed by micro-DSC, reported in Fig. 3.3.7 and summarized in Table 3.3.4. The data show a slight decrease of denaturation temperature T_d after treatment with nano-HA, while the enthalpy of denaturation increases by 2-3 J/g. This is a clear indication of the occurrence of an interaction between the nanoparticles and the collagen matrix, which results in stabilization. An effect of nano-HA content on both parameters is observed, with a minimum in the value of T_d and a maximum in the enthalpy of denaturation for the sample with 1% nano-HA.

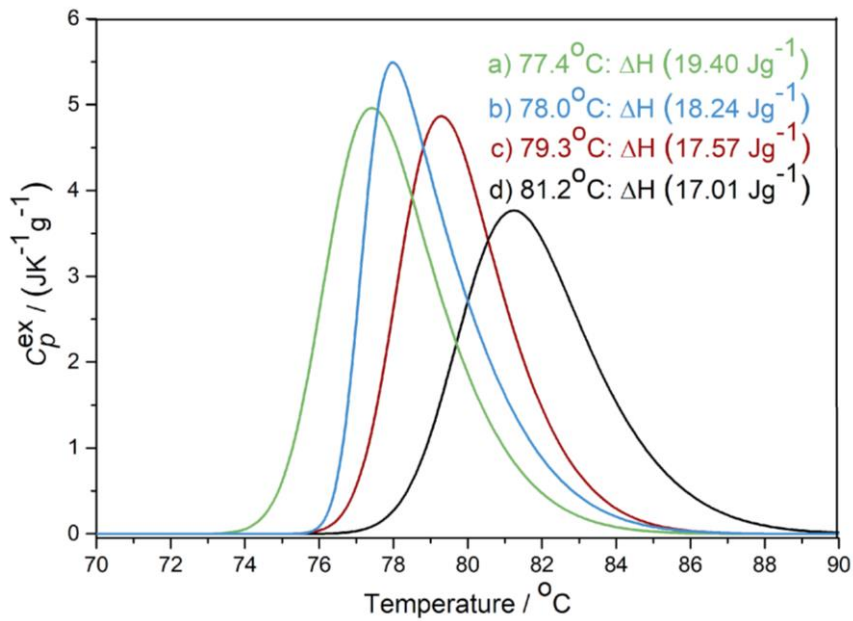


Figure 3.3.7. Micro-DSC thermograms of: a) leather tanned with pure OSA and retanned with nHAp 1% b) leather tanned with pure OSA and retanned with nHAp 1.5% c) leather tanned with pure OSA and retanned with nHAp 3% d) Crust leather.

With the increase of the concentration of nano-HA (from curve a to c), the almost linear increase of the denaturation temperature is observed. The enthalpy of denaturation also increases with respect to the reference (L-OSA_pure_lab, $\Delta H=14.08$ J/g).

3.3.4 Study of the interaction between nano-HA and leather: ATR and NMR-MOUSE analyses

As reported above (section 3.3.1), relaxation times calculated by NMR-MOUSE analysis provide information on the mobility of collagen fibers, and thus on the degree of crosslinking. In Tab. 3.3.5 the longitudinal and transverse relaxation times of leather treated with different percentages of nano-HA are reported.

Table 3.3.5 Longitudinal and transverse relaxation times (T_1 , $T_{2\text{long}}$ and $T_{2\text{short}}$) of leather tanned with SA, OSA and treated with different percentages of nano-HA (0.5, 1, 1.5, 3 %).

Sample	T_1 (ms)	$T_{2\text{long}}$ (ms)	$T_{2\text{short}}$ (ms)
L_SA	43.84	0.29	0.06
L_OSA _{pure-lab}	28.29/29.84	0.66	0.1
L_OSA _{pure+nHA (0.5%)}	34.62	1.2	0.13
L_OSA _{pure+nHA (1%)}	47.71/42.26	0.7	0.1
L_OSA _{pure+nHA (1.5%)}	31.01	1.02	0.13
L_OSA _{pure+nHA (3%)}	26.25/28.41	0.42	0.07
Crust_L_OSA	27.00	0.44	0.08

Following treatment with nano-HA, the values of the T_1 longitudinal relaxation time increase and reach the measured value for leather tanned with SA, suggesting an interference of the nanoparticles in the structure of the collagen-aldehyde matrix. The decrease in the values of the $T_{2\text{eff_long}}$ and $T_{2\text{eff_short}}$ components of the transverse relaxation time also indicate an interaction of collagen with the nanoparticles in both the amorphous and crystalline phases. This could be interpreted by an increase in the degree of crosslinking, the effect being that of a reduction in the mobility of collagen fibrils in the matrix treated with nanoparticles.

The secondary structure of collagen and its change due to the interaction with tanning agent and nanomaterials were also investigated through FTIR-ATR analysis.¹²

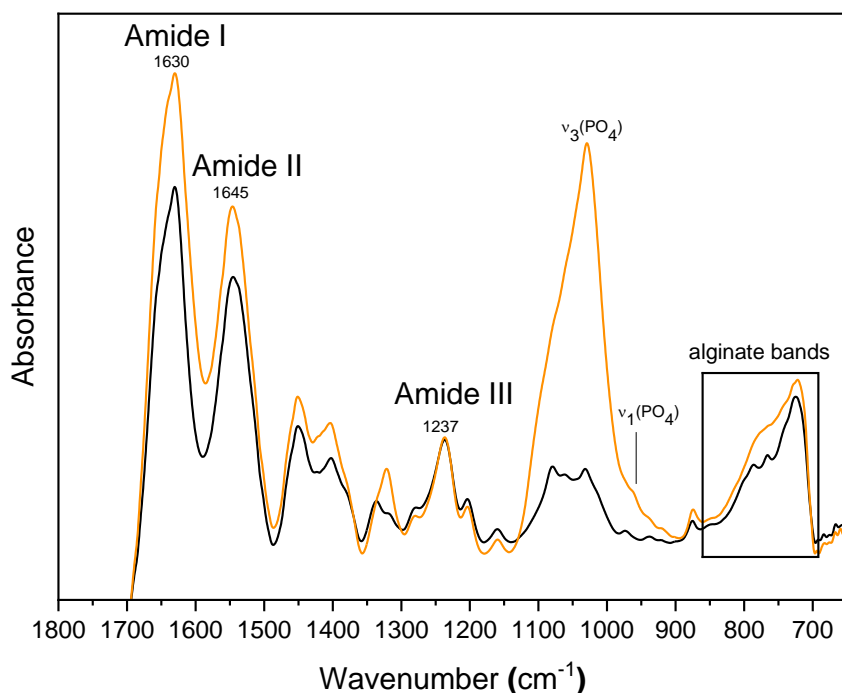


Fig. 3.3.8. FTIR-ATR spectra of L_OSA_{pure_lab} (black spectrum) and L_OSA_{pure}+nano-HA (1%) (orange spectrum) in the 1800-650 cm⁻¹ region.

Fig. 3.3.8 shows IR spectra of the leather samples tanned with OSA (black spectrum) and retanned with nano-HA (orange spectrum). The most intense bands in the black spectrum are referred to Amide I and Amide II bands; the first one (1630 cm⁻¹) is due to the νC=O vibration mode and related to the backbone conformation, while the second one (1545 cm⁻¹), conformationally sensitive, is the combination of δNH and νCN vibration modes. The Amide III band (1237 cm⁻¹) is complex in that it depends on the hydrogen bonding pattern but also on the nature of side chains of collagen. Carbonate bands due to the presence of carbonate salts in leather samples are visible in the 1500-1400 cm⁻¹ range; the set of signals between 850 and 700 cm⁻¹ are referred to the alginate monomeric unit bands. After the retanning treatment with nano-HA (orange spectrum), it is possible to observe typical signals of nano-HA (1090-960 cm⁻¹), related to phosphate groups (see section 3.2.1 for the detailed assignment). The ratio between Amide I and Amide II relative intensities (A_I/A_{II}) is related to the hydrolysis degree of the polypeptide chains, and in particular, reflects the peptide bond breakdown that occurs in the leather sample.¹³ This value was calculated in leather samples tanned with OSA, before and after the retanning with nano-HA. Since the Amide I is affected by a huge contribution of water bending, the values were calculated after a deconvolution of this band. The A_I/A_{II} ratio was constant (ca.1) both in black and orange spectra, witnessing no interference of nano-HA in the stability of collagen.

Furthermore, at lower frequencies region (850-700 cm⁻¹), a modification in alginate monomeric unit bands appears after the retanning with nano-HA. This may suggest an interaction between nano-HA and collagen-OSA matrix, also witnessed by relaxometric measurements (Table 3.3.5).

Bibliographic References

1. Moretto, A., Hexavalent and trivalent chromium in leather: What should be done? *Regulatory Toxicology and Pharmacology* **2015**, *73* (2), 681-686.
2. Harlan, J. W.; Fearheller, S. H., Chemistry of the crosslinking of collagen during tanning. *Advances in experimental medicine and biology* **1977**, *86a*, 425-40.
3. Marsal, A.; Cuadros, S.; Ollé, L.; Bacardit, A.; Manich, A. M.; Font, J., Formaldehyde scavengers for cleaner production: A case study focused on the leather industry. *Journal of Cleaner Production* **2018**, *186*, 45-56.
4. Ding, W.; Yi, Y.; Wang, Y. n.; Zhou, J.; Shi, B., Preparation of a Highly Effective Organic Tanning Agent with Wide Molecular Weight Distribution from Bio-Renewable Sodium Alginate. *ChemistrySelect* **2018**, *3* (43), 12330-12335.
5. Hecht, H.; Srebnik, S., Structural Characterization of Sodium Alginate and Calcium Alginate. *Biomacromolecules* **2016**, *17* (6), 2160-2167.
6. Kim, W. S.; Mooney, D. J.; Arany, P. R.; Lee, K.; Huebsch, N.; Kim, J., Adipose tissue engineering using injectable, oxidized alginate hydrogels. *Tissue engineering. Part A* **2012**, *18* (7-8), 737-43.
7. Wang, L.-F.; Rhim, J.-W., Preparation and application of agar/alginate/collagen ternary blend functional food packaging films. *International Journal of Biological Macromolecules* **2015**, *80*, 460-468.
8. Sarker, B.; Papageorgiou, D. G.; Silva, R.; Zehnder, T.; Gul-E-Noor, F.; Bertmer, M.; Kaschta, J.; Chrissafis, K.; Detsch, R.; Boccaccini, A. R., Fabrication of alginate–gelatin crosslinked hydrogel microcapsules and evaluation of the microstructure and physico-chemical properties. *Journal of Materials Chemistry B* **2014**, *2* (11), 1470.
9. Ding, W.; Zhou, J.; Zeng, Y.; Wang, Y.-N.; Shi, B., Preparation of oxidized sodium alginate with different molecular weights and its application for crosslinking collagen fiber. *Carbohydrate Polymers* **2017**, *157*, 1650-1656.
10. Fathima, N. N.; Baias, M.; Blumich, B.; Ramasami, T., Structure and dynamics of water in native and tanned collagen fibers: Effect of crosslinking. *International Journal of Biological Macromolecules* **2010**, *47* (5), 590-596.
11. Sendrea, C.; Badea, E.; Sunculescu, I.; Miu, L.; Iovu, H. In Dose-Dependent Effects of Gamma Irradiation on Collagen in Vegetable Tanned Leather by Mobile NMR Spectroscopy, *Leather and Footwear Journal* **2015**, *15*(3), 139-150.
2015.
12. Badea, E.; Miu, L.; Budruga, P.; Giurginca, M.; Mašić, A.; Badea, N.; Della Gatta, G., Study of deterioration of historical parchments by various thermal analysis techniques complemented by SEM, FTIR, UV-Vis-NIR and unilateral NMR investigations. *Journal of Thermal Analysis and Calorimetry* **2008**, *91* (1), 17-27.
13. Sendrea, C.; Carsote, C.; Badea, E.; Adams, A. R.; Niculescu, M.; Iovu, H., Non-invasive characterisation of collagen-based materials by nmr-mouse and atr-ftir. *Scientific bulletin / B* **2016**, *78* (3), 27-38.

3.4 INDUSTRIAL SCALE-UP OF NANO-HA PRODUCTION

3.4.1 Preparation and characterization of nano-HA at industrial scale

The preparation method of nano-HA at lab level (section 3.1.1) was scaled up stepwisely in Kemia Tau. Batches of 5 kg and 100 kg were prepared sequentially. The first step was the selection of the suitable reagents for industrial manufacturing. Since the use of ultrapure/pure reagents is possible only at laboratory scale, industrial alternatives were selected from Kemia Tau (Table 3.4.1).

Table 3.4.1. Reagents used for the preparation of nano-HA at lab scale and at industrial scale (5 kg and 100 kg).

Lab procedure 0.5 kg	Scale up 5kg/100kg
Calcium hydroxide, 96% Ca(OH) ₂	Hydrated lime
Phosphoric acid, 85% (H ₃ PO ₄)	Phosphoric acid, 85%
Ammonium hydroxide, 5N (NH ₄ OH)	NH ₃ solution 33%
Distilled water	Mains water

For the 5 kg nano-HA production, a big beaker and a propeller stirrer was used, in order to reproduce as close as possible the factory process (Fig. 3.4.1, panel A). For the scale up of 100 kg, the production was moved to the processing department, and cylindrical tanks equipped with propeller stirrers were employed. The final yield was more than 99%, with only a 0,73% of non-reacted hydrated lime (Fig. 3.4.1, panel B).

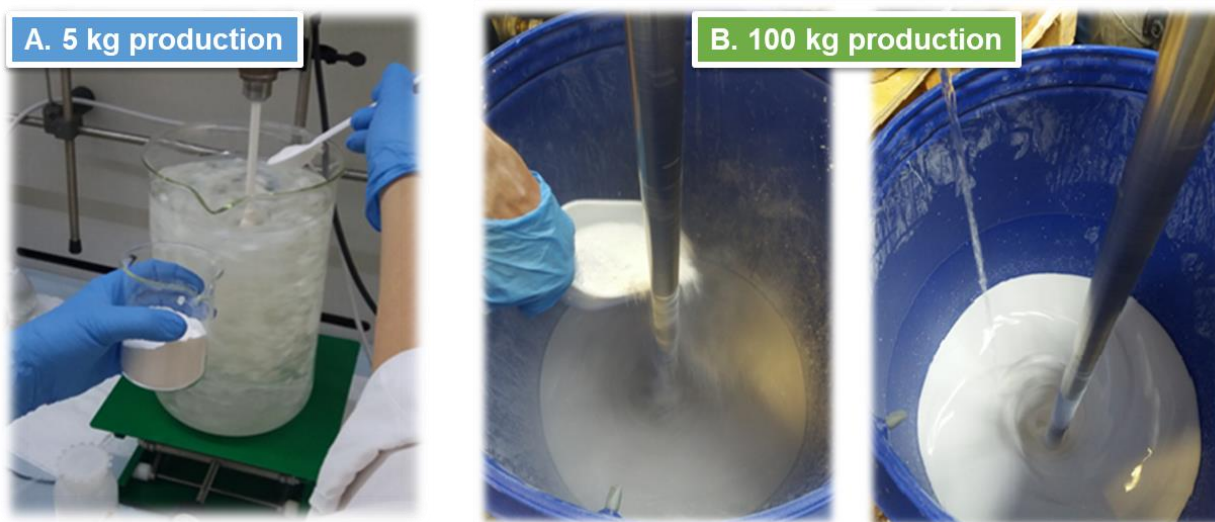


Figure 3.4.1. Nano-HA production; panel A: 5 kg of nano-HA were produced using a big beaker and a propeller stirrer. Panel B: 100 kg of nano-HA were produced in the factory, using a cylindrical tank and a propeller stirrer.

Both batches (5kg and 100kg) were analysed with the same characterization techniques used for the lab-scale samples (see section 3.2), in order to assess the formation of HA and its nano-dimensional size.

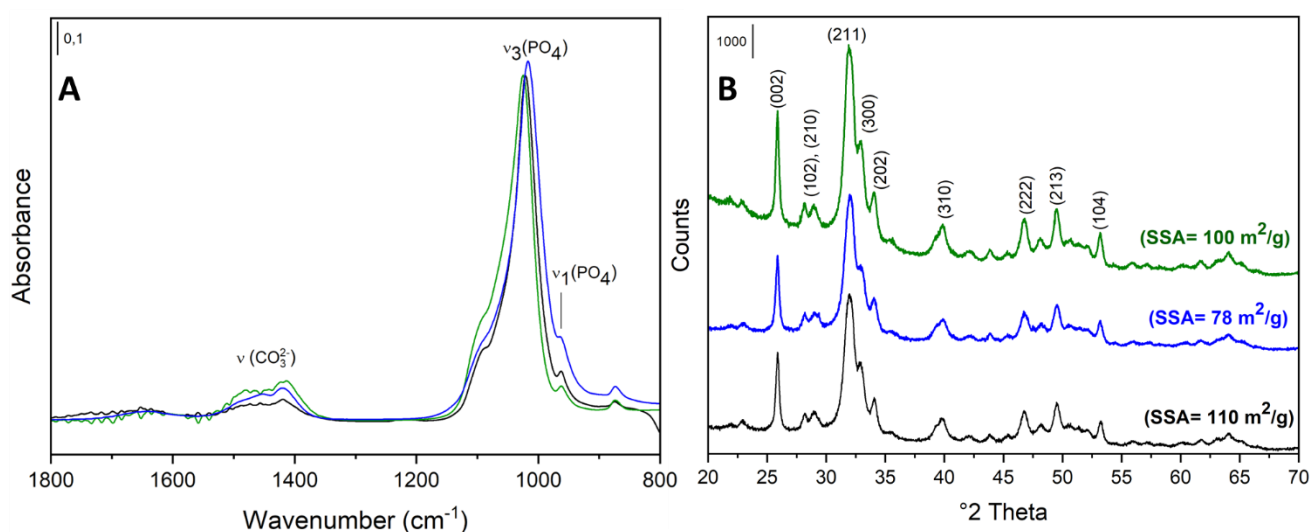


Figure 3.4.2. Panel A: FTIR-ATR spectra of nano-HA at lab scale (black curve), nano-HA scale up 5 kg (blue curve), and nano-HA scale up 100 kg (green curve). Panel B: XRD patterns of nano-HA at lab scale (black curve), nano-HA scale up 5kg (blue curve), and nano-HA scale up 100 kg (green curve). The specific surface area (SSA) values are reported above each curve.

In Fig. 3.4.2, panel A, FTIR-ATR spectra of the produced nano-HA in Kemia Tau are shown (blue and green spectra), compared to the spectrum of produced nano-HA at lab scale (black spectrum). In all cases typical signals of carbonates ($1500\text{-}1400\text{ cm}^{-1}$) and bulk phosphate groups are present ($1090\text{-}960\text{ cm}^{-1}$), showing only slight differences in the bands relative intensities (see section 3.2.1 for the detailed assignments).

Moreover, in panel B, XRD patterns of the same samples are reported, showing the typical peaks of HA single phase in all cases. The high specific surface area (SSA) values confirm the nano-

dimensional size of HA produced even at industrial scale (see section 3.2.1 for the detailed assignments).

Another important parameter to be evaluated before putting a product on sale is the shelf life. The market requires shelf life ≥ 12 M, and for this reason different storage tests were performed. The nano-HA produced at industrial scale were stored in suspension and, after a few days, precipitation of nanoparticles was observed. This could be a problem for the potential formation of agglomerates and, most of all, for the applicative step. The use in leather processes of a not well-dispersed product requires a preliminary complex mixing phase that could affect the entire leather treatment.

In order to avoid the precipitation of nano-HA particles, the viscosity of the suspension was increased adding different types of thickening agents (polymeric and/or inorganic agents). In order to find the best type and amount of thickening agents, a number of stability tests were performed. The products were subjected to accelerated aging tests, thermal stresses, and sunlight exposure tests.

The selected thickening agents (Fig. 3.4.3) gave a thixotropic effect to the formulation: under stationary conditions, the product has a viscosity such as to avoid separation; in dynamic conditions, the viscosity decreases making it easier to use.



ROHAGIT SD 15: water based acrylic ester copolymer-methacrylic acid dispersion
ACRY SOL TT -615: water based polyacrylate dispersion – thixotropic effect
THICKENER PUL: water based polyurethane dispersion
RHEOLATE 278: water/diethylene glycol based polyurethane dispersion – thixotropic effect

Figure 3.4.3. The selected thickening agents (ROHAGIT SD 15, ACRY SOL TT -615, THICKENER PUL, and RHEOLATE 278) added to the formulation.

Finally, the best results in accelerated aging tests in order to evaluate the shelf life, was achieved with ACRY SOL TT -615 as thickening agent (12.4%), with a shelf life > 12 M.

3.4.2 Application of nano-HA at industrial scale on leather samples and preliminary fire-resistance tests

The application of nano-HA on leather samples takes place in the retanning step; the nano-HA was added as a final product in this wet phase, in order to increase the possibility of penetration into leather fibers. The first tests were carried out using the nano-HA produced at lab-scale, in powder form, but first critical aspects occurred (Fig. 3.4.4).

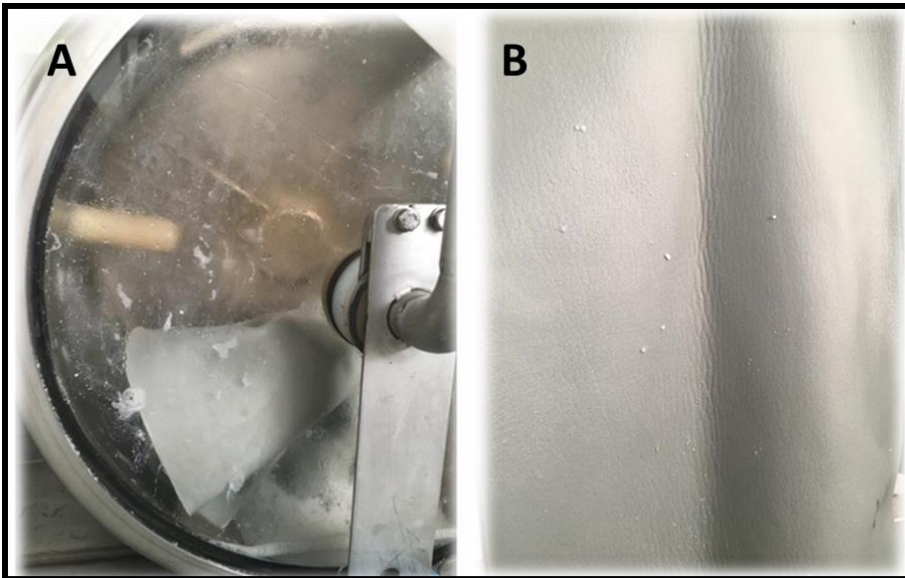


Fig. 3.4.4. Panel A: nano-HA in powder form added to the wet phase during the retanning process; panel B: the final retanned leather; in this photo it is possible to observe some agglomerates of nano-HA on the grain side.

Firstly, a consistent amount of nano-HA cannot penetrate into leather during the retanning process (Fig. 3.4.4, panel A), leading to the loss of almost all nanomaterial; secondly, the final retanned leather exhibited some agglomerates on the grain side of the leather that could scratch it. These problems have been solved using the nano-HA in suspension: so, the final step of the production of nano-HA at lab scale was the washing and not the drying (see section 3.1).

The satisfactory results obtained for retanned leather with nano-HA in suspension, allowed to pass to a preliminary fire resistance test. The employed method was the fire testing according to FAR/JAR 25.853 (vertical) regulated by the Federal Aviation Administration (FAA); this method measures afterflame time and damaged length of materials in passenger and crew compartments in aircrafts (Fig. 3.4.5).

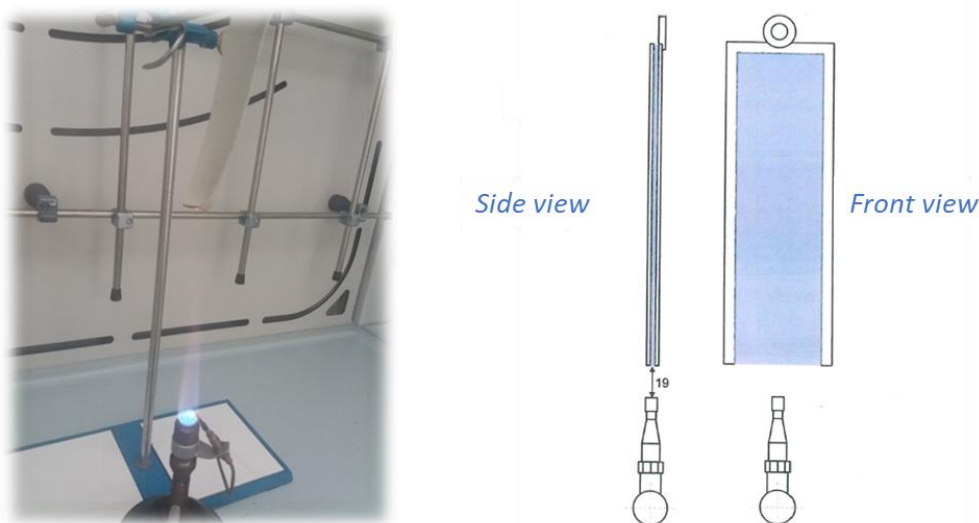


Figure 3.4.5. FAR/JAR 25.853 (vertical) test; leather sample was placed vertically on a gas flame.

The leather samples were placed on a flame for 12-60 seconds and then, during the test, the burning length and flaming time of drippings from the material were recorded. In Fig. 3.4.6. photographs of the leather samples (treated and non-treated with nano-HA) after the FAR/JAR 25.853 test are reported.

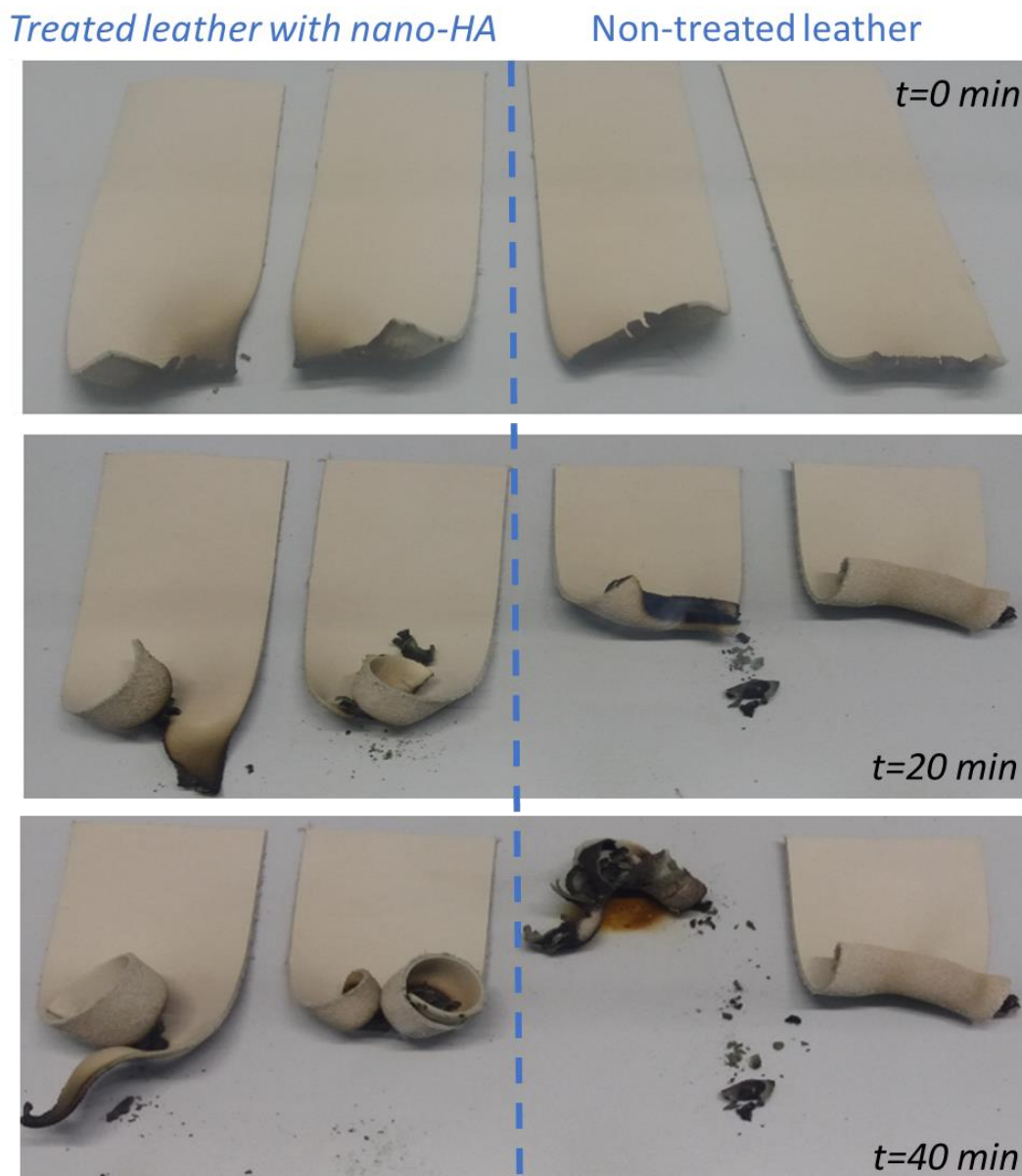


Figure 3.4.6. Treated leather samples with nano-HA (on the left side) and non-treated leather samples (on the right side) subjected to FAR/JAR 25.853 (vertical) test. The photographs reported the situation a $t=0$ min (after 60 seconds of contact with gas flame), $t=20$ min, and $t=40$ min.

The leather consumption after the exposure to a gas flame was recorded at different times ($t=0$, 20, 40 min). It is possible to notice a good resistance in case of leather treated with nano-HA (Fig. 3.4.6, left side) even after 40 min; the combustion was partial and the flame was extinguished in a shorter time, witnessing the increase of fire resistance due to the presence of nano-HA.

Bibliographic References

1. https://www.faa.gov/regulations_policies/advisory_circulars/index.cfm/go/document.information/documentID/22673

General conclusions

The main purpose of the research work carried out in this PhD thesis was the development of new sustainable processes and non-toxic nanomaterials for waterproofing and fireproofing purposes in leather treatments.

Based on the pushing need of improvement of the sustainability of the leather processing, and reduction of the environmental impact of the tanning industry, and thanks to the fruitful collaboration with a number of institutions with different areas of expertise, good results were achieved during these three years.

Here, the key achievements of this research work are:

- The use of nanomaterials as *waterproofing agents* for the substitution of the conventionally applied perfluoroalkyl substances (PFAS) in hydrophobic coatings for leather was thoroughly studied; the innovative aspect is related to the possibility to functionalized silica nanoparticles with a fluorine-free molecule containing highly branched alkyl chains (isostearic acid) that positively affect the hydrophobicity of the surface. The experimental research work on the preparation of the functionalized material led to the development of a superhydrophobic surface ($CA > 150^\circ$); the study of the main characteristics of the augmented functionality of nanomaterial using different techniques allowed to highlight some aspects: a material does not necessarily expose micro- and nano-hierarchical structures to reach high level of hydrophobicity (also known as 'lotus effect') and, moreover, material with a $CA > 150^\circ$ can adsorb water vapors. The water adsorption capacity depends on the possibility of water molecules to reach the parts of the surface non-covered by hydrophobic moieties and it seems to be independent from the capacity of the hydrophobic chemical surface features to protect the surface from a macroscopic object such as water droplets. This represents an innovation in this field, given that no relevant studies of the similar effect have been found up to now.
- The application of nanocomposites based on nano-hydroxyapatite (nano-HA), nano-SiO₂ and nano-TiO₂ as the main constituents instead of brominated organic flame retardants (PBB, PBDE, HBCD) to impart *flame resistance* properties to the leather was exploited. The results obtained in terms of interaction between nanomaterial and leather (SEM-EDS, NMR-MOUSE and ATR measurements) and the increase of thermal resistance of treated leather samples with nanomaterials (micro-DSC) have evidenced the best practical effectiveness of nano-HA in the flame propagation retardancy. Moreover, the preparation of nano-HA at lab scale using a low-cost method and the availability along with low cost of the main reagents allowed to scale up the production at industrial level in Kemia Tau, obtaining good reproducibility of the synthesis of 100 kg batches of nano-HA. The precise knowledge of all the material and energetic inputs of the synthesis carried out at laboratory level has permitted to evaluate environmental impacts of nano-HA life cycle through Life Cycle Assessment, in collaboration with the Management Department of University of Torino. On the basis of LCA results, electricity infrastructure, H₃PO₄ utilization, and the transports for delivery of the reagents needed for the synthesis, are the three most environmentally

impactful factors. However, when passing from laboratory to industrial scale, the effect of the electricity consumption and transport may have a not-fully proportional character due to the wider flexibility of the options for the optimization of logistics, compared with the increase in the quantity of chemicals. These concerns based on LCA results suggest that more attention should be paid to H₃PO₄ supply chain rather than to the electricity consumption, in terms of making strategies oriented towards process optimization and innovation. These results were the basis for the article published during this project (Ingrao, C.; Vesce, E.; Evola, R. S.; Rebba, E.; Arcidiacono, C.; Martra, G.; Beltramo, R., *Journal of Cleaner Production* 2021, 279.).

- The possibility to use oxidized sodium alginate (OSA) as an eco-friendly alternative to synthetic aldehydes as *tanning agent* was exploited. The part of the work related to the development of new knowledge-based organic tanning agents from alginate was carried out in collaboration with the Institute for Textiles and Leather of Bucharest. Good results were obtained concerning thermal stability (micro-DSC) and resistance to shrinkage (T_s) on leather tanned with OSA, allowing to employ OSA at micro-pilot level. Moreover, the application of nano-HA in the retanning step as fireproof agent allows to decrease the amount of synthetic tannins used in the tanning/retanning process, typically employing phenol-formaldehyde-based resins and, at the same time, to increase the thermal stability of collagen-OSA matrix.

As a final remark, this work has contributed to explore and develop strategies to reduce the environmental impact of leather production. This project is an example of how two different realities, the industrial and the research one, can cooperate and exploit the capability of individual groups to reach the set targets.

Publications and congress & conference participation

Publications

- *Erica Rebba*, Pavlo Ivanchenko, Michele Remo Chierotti, Simone Bordignon, Alessandro Barge, Mirko Sacco, Gloria Berlier, Gianmario Martra, Study of water interaction with silica surface modified with branched hydrocarbons: molecular and macroscopic levels (manuscript in progress).
- Elena Peira, Giulia Chindamo, Daniela Chirio, Simona Sapino, Simonetta Oliaro-Bosso, *Erica Rebba*, Pavlo Ivanchenko, Marina Gallarate, Assessment of In-Situ Gelling Microemulsion Systems Upon Temperature and Dilution Condition for Corneal Delivery of Bevacizumab, *Pharmaceutics* (2021), 13, 258.
- Carlo Ingraio, Enrica Vesce, Rosalia S. Evola, *Erica Rebba*, Claudia Arcidiacono, Gianmario Martra, Riccardo Beltramo, Chemistry behind leather: Life Cycle Assessment of nano-hydroxyapatite preparation on the lab-scale for fireproofing applications, *Journal of Cleaner Production* (2021), 279, 123837.
- Federico Catalano, Pavlo Ivanchenko, *Erica Rebba*, Yuriy Sakhno, Gabriele Alberto, Galyna Dovbeshko, Gianmario Martra, Towards the control of the biological identity of nanobiomaterials: Impact of the structure of {0110} surface terminations of nanohydroxyapatite on the conformation of adsorbed proteins, *Colloids and Surfaces B: Biointerfaces* (2020) 188, 1107802.
- Gabriele Alberto, Nadia Barbero, Carla Divieto, *Erica Rebba*, Maria Paola Sassi, Guido Viscardi, Gianmario Martra, Solid silica nanoparticles as carriers of fluorescent squaraine dyes in aqueous media: Toward a molecular engineering approach, *Colloids and Surfaces A* (2019) 568, 123–130.
- Marco Fabbiani, *Erica Rebba*, Marco Pazzi, Marco Vincenti, Ettore Fois, Gianmario Martra, Solvent-free synthesis of Ser–His dipeptide from nonactivated amino acids and its potential function as organocatalyst, *Res. Chem. Intermed.* (2018) 44, 1797–1810.

Congress & conference participation

- Merck Young Chemists Symposium (MYCS 2019), Rimini (RN) 25-27 November 2019 – Oral contribution: “Sustainable leather treatment: a promise of nanomaterials as fireproofing auxiliaries”
- International Conference on Functional Nanomaterials and Nanodevices (NANOMAT2019), Prague, Czech Republic 11-13 September 2019 – Oral contribution: “Preparation of silica-based hydrophobic nanomaterials for leather waterproofing purpose”
- The 16th International Conference on Nanosciences and Nanotechnologies (NN19), Thessaloniki, Greece, 2-5 July 2019– Oral contribution: “Nanomaterials for sustainable leather products”
- Merck – Elsevier Young Chemist Symposium 2018 (MEYCS 2018), Rimini (RN) 19-21 November 2018_Award for the best flash communication “Hydrophobization of nanomaterials for application in leather finishing”

- The 7th International Conference on Advanced Materials and Systems (ICAMS 2018), Bucharest, Romania 18-20 October 2018 – Poster contribution: “Nanomaterials for eco-sustainable waterproofing leather finishing”
- Workshop “High resolution separation of nanoparticles and macromolecules-Field Flow Fractionation”, DSTF, Torino (TO) 13-14 September 2018
- Sesto Workshop del Gruppo Interdivisionale di Green Chemistry - Chimica Sostenibile (CG-CS 2018), Milano (MI) 15 June 2018 – Oral contribution: “Nanomateriali per la produzione eco-sostenibile di manufatti in pelle impermeabilizzati nell’industria conciaria”
- Giornate Italo-Francesi di Chimica (GIFC 2018), Genova (GE) 16-18 April 2018 – Poster contribution: “Applicative aspect of bionanomaterials: leather coatings for fire and water resistance”
- Workshop on Patent and Intellectual Property, Torino (TO) 26 February 2018
- Merck Young Chemists Symposium (MYCS 2017), Milano Marittima (RA) 13-15 November 2017 – Poster contribution with flash communication: “Green synthesis of peptides from non-activated amino acids: production of Ser-His dipeptides with potential capability as organocatalyst”

PhD courses

- “Environmental pollution and health” (4CFU) Prof. Bono
- “Drug Design” (4CFU) Prof.ssa Lazzarato, Prof. Bertinaria, Prof.ssa Caron, Prof.ssa Spyraakis
- “Advances in Nanotechnology” (4CFU) Prof. Martra
- “Food-omics: integrated analytical strategies for in-depth chemical characterization of food” (4CFU) Prof.ssa Cordero
- “Engineering viral genomes: viral vectors for delivering genes” (4CFU) Prof. Ghibaudo
- “Advances in Pharmacology” (4CFU) Prof. Collino, Prof.ssa Serpe e Prof. Miglio
- “Interactive laboratory to stimulate an attitude to outreach activities on basic physico-chemical phenomena” (3CFU), Prof.ssa Berlier e Prof.ssa Magnacca, with final presentation “The light experience”.

Acknowledgement

Ringrazio dal profondo del mio cuore tutte le persone che hanno contribuito alla realizzazione di questo lavoro di ricerca. La Dott.ssa Rita Porcaro, della Kemia Tau, per la possibilità che ci ha dato di interfacciarci con una meravigliosa azienda, e che la sinergia tra il mondo aziendale e quello della ricerca può portare a risultati eccellenti.

Ringrazio dal profondo del cuore il Prof. Michele Remo Chierotti e Simone Bordignon, che oltre al supporto per le misure NMR sono stati dei preziosi compagni di viaggio in questi tre anni.

Un grazie al team di Management, Prof.ssa Enrica Vesce, Rosalia Stella Evola e Carlo Ingrao, per le nostre intense giornate di lavoro ma in compagnia di persone speciali.

La Prof.ssa Elena Badea e Maria Cristina Micu, dell'ICPI di Bucarest, con cui siamo riusciti a interfacciarci sempre nel migliore dei modi, riuscendo anche a passare qualche giorno insieme nella vostra splendida città.

Abbiamo creato un team pazzesco!

Un ringraziamento speciale va a tutti i miei colleghi, che negli anni sono diventati la mia seconda famiglia. Rosangela, la persona senza la quale sarei letteralmente persa, che si è subito tutte le crisi di panico prima di ogni presentazione orale senza batter ciglio. Il sostegno che mi hai dato ogni giorno, lavorativo e personale, ha contribuito a far nascere un'amicizia speciale. Tu sei e sarai sempre la mia ancora di salvezza. Pavlo, amico e collega prezioso, che oltre ad aiutarmi in questi tre anni con tutte le misure sperimentali si è dovuto leggere la tesi, facendosi anche qualche risata per qualche mia frase senza senso. Ora inizia la tua nuova avventura a Bruxelles ma rimarrai sempre il mio amico del cuore. Fabbiani, il mio punto fermo in tesi magistrale e il mio assistente informatico nel periodo di dottorato; senza di te sarei ancora qui a cercare di inserire la bibliografia con EndNote. Nonostante la lontananza degli ultimi mesi so che ci sei sempre per me, qualsiasi cosa accada.

Guille, che porta il sorriso anche nei giorni più bui, che non accetta di vederti triste o abbattuto. Sei il drama king del gruppo, ma anche la persona più allegra che io conosca.

Nannuz, la piccola tesista, ormai dottoranda, che si è perfettamente inserita nel gruppo. Instancabile lavoratrice che non si rende conto del suo potenziale; la bassa autostima ci accomuna, sarà per quello che ci capiamo con un solo sguardo.

Ola, a cui il mio ringraziamento lo dedico in italiano perché ormai lo parla perfettamente. Sei arrivata nel nostro gruppo un anno fa, ma da subito ho capito che ne saresti diventata parte integrante. La tua intelligenza e capacità di recepire i pochi insegnamenti che ti ho dato mi hanno lasciata senza parole, sei grande. Hai spronato (e obbligato) me e Ros a parlare inglese, con la tua dolcezza infinita e il tuo sorriso contagioso hai sicuramente migliorato le nostre eterne giornate di esperimenti.

Un ringraziamento a tutti i tesisti che hanno lavorato con noi in questi anni, Luca, Peppe, Gabriele, Tiziano; avete aumentato di gran lunga la soglia della mia pazienza (e mi avete fatto fare anche tante risate!).

Voglio ringraziare tutte le persone che in questi anni mi sono state vicine, chi per una chiacchierata, chi per una pausa caffè, chi per un supporto scientifico: Giuly, Pinuccia, Alessia, Dodo, Lorenzo, Elisa, Sara, Chiara N., Martini, Geppo, Gabriele Ricchiardi, Silvia Bordiga, Valentina Crocellà.

Gabriele Alberto, che mi ha insegnato tutto quello che so sulla sintesi di nanoparticelle di silice, e con una pazienza infinita è stato il mio punto di riferimento del primo anno.

Francesca Bonino, una professoressa e donna eccezionale, sempre sincera. Grazie agli estenuanti laboratori studenti abbiamo creato un ottimo rapporto, e so che su di te posso sempre contare (anche se dici che sono io la tua badante!).

Un ringraziamento enorme va a Mayita, che oltre ad avermi trasmesso la sua passione per la microscopia elettronica è una delle persone più belle e solari che io conosca. Venire da te a fare le analisi è una gioia per la mente e per il cuore!

Alla mia super-supervisor Gloria Berlier, che in un periodo difficile per tutti noi mi ha preso sotto la sua ala, scientificamente e umanamente, e mi ha spronata nella scrittura della tesi nonostante sembrasse uno scoglio insormontabile. Grazie per tutto il tempo che mi hai dedicato, e per la tua comprensione, sempre.

Un ringraziamento gigante alla mia famiglia, ai miei genitori e a mia sorella Ilaria che mi sostengono da sempre. Ognuno, a suo modo, contribuisce alla mia felicità; non potrei desiderare una famiglia migliore.

Jacopo, colui che si è subito più di tutti i miei successi e i miei fallimenti; la tua pazienza è infinita, ora ne sono certa! Grazie per l'amore che mi doni ogni giorno, senza di te non saprei come fare.

Un ringraziamento alla mia amica del cuore Chiara (e al mio nipote peloso Chablis), che ormai mi supporta e sopporta da anni: tutti i nostri momenti insieme, tra passeggiate (tante) e vita sociale (poca), hanno contribuito alla mia sanità mentale. Sei la migliore amica che si possa desiderare.

Grazie Marti, la mia compagna di magistrale e di dottorato, la mia romana preferita; ne abbiamo passate davvero tante insieme, e sei sempre nel mio cuore e nei miei pensieri, anche ora che sei tornata nella tua città.

Grazie a Serine, la mia "piccola" cagnolona, la mia anima gemella. Sei entrata nella mia vita proprio quando ho iniziato il dottorato, e senza di te sarebbe stato tutto molto più difficile. L'amore che proviamo l'una per l'altra è indescrivibile, e riempi le mie giornate di gioia, sempre. Hai cambiato le mie abitudini, le mie passioni, mi hai incasinata con la tua gestione nei momenti più pieni a lavoro (santa Zia Chiara), ma non tornerei mai indietro, per nessun motivo al mondo.

E l'ultimo ringraziamento, il più grande e il più sofferto, va a te, Gianmario. Non trovo le parole giuste per scrivere quello che penso, e quello che vorrei dirti. Posso però ringraziarti perché tutto quello che ho scritto in questa tesi (e non solo) me lo hai insegnato tu. Sei sempre stato il mio punto di riferimento, scientifico e non, per questi tre anni di dottorato. Non potrò mai dimenticare i momenti passati a lavorare insieme, ai congressi in giro per il mondo e alle cene tutti insieme. Mi sembra impossibile che tu non abbia letto la mia tesi, che non ci sia stato in questo periodo di scrittura. Nella mia testa, immaginandomi questo periodo, mai avrei pensato di non condividerlo con te. Spero che tu possa essere fiero, da lassù, del mio lavoro. So che avresti cambiato il 70% delle cose che ho scritto, che avresti presentato le figure in altro modo e cambiato la disposizione dei capitoli, ma spero che tutto il sapere che mi hai trasmesso sia servito a renderti orgoglioso e felice lo stesso di questa tesi. Mi manchi.

Article

Assessment of In-Situ Gelling Microemulsion Systems Upon Temperature and Dilution Condition for Corneal Delivery of Bevacizumab

Elena Peira ^{1,*}, Giulia Chindamo ¹, Daniela Chirio ^{1,*}, Simona Sapino ¹, Simonetta Oliaro-Bosso ¹, Erica Rebba ², Pavlo Ivanchenko ² and Marina Gallarate ¹

¹ Department of Drug Science and Technology, University of Turin, 10125 Turin, Italy; giulia.chindamo@unito.it (G.C.); simona.sapino@unito.it (S.S.); simona.oliaro@unito.it (S.O.-B.); marina.gallarate@unito.it (M.G.)

² Department of Chemistry and Interdepartmental Nanostructured Interfaces and Surfaces (NIS) Centre, University of Turin, 10125 Turin, Italy; erica.rebba@unito.it (E.R.), pavlo.ivanchenko@unito.it (P.I.)

* Correspondence: elena.peira@unito.it (E.P.); daniela.chirio@unito.it (D.C.); Tel.: +39-011-670-7143 (E.P.); +39-011-670-7167 (D.C.)

Abstract: Bevacizumab (BVZ), a recombinant humanized monoclonal antibody, has recently been proposed as a topical application in the treatment of anterior segment neovascularization; however, as there are some disadvantages in the administration of common eye-drops, ophthalmic topical drug delivery systems are under study to improve the precorneal residence time, reducing the frequency of administration. In this work, oil-in-water and water-in-oil BVZ-loaded microemulsions are developed, able to increase their viscosity, either by the formation of a liquid-crystalline structure upon aqueous dilution, thanks to the presence of Epikuron[®] 200 and polysorbate 80, or by body-temperature-induced jellification for the presence of Pluronic[®] F127 aqueous solution as an external phase. In oil-in-water microemulsion, hydrophobic ion pairs of BVZ were also prepared, and their incorporation was determined by release studies. Microemulsions were characterized for rheological behavior, corneal opacity, in vitro corneal permeation, and adhesion properties. The studied microemulsions were able to incorporate BVZ (from 1.25 to 1.6 mg/mL), which maintained dose-dependent activity on retinal pigment epithelial ARPE-19 cell lines. BVZ loaded in microemulsions permeated the excised cornea easier (0.76–1.56% BVZ diffused, 4–20% BVZ accumulated) than BVZ commercial solution (0.4% BVZ diffused, 5% accumulated) and only a mild irritation effect on the excised cornea was observed. The good adhesion properties as well the increased viscosity after application, under conditions that mimic the corneal environment (from 1×10^3 to more than 100×10^3 mPa-s), might prolong precorneal residence time, proving these systems could be excellent topical BVZ release systems.

Citation: Peira, E.; Chindamo, G.; Chirio, D.; Sapino, S.; Oliaro-Bosso, S.; Rebba, E.; Ivanchenko, P.; Gallarate, M. Assessment of in-situ Gelling Microemulsion Systems Upon Temperature and Dilution Condition for Corneal Delivery of Bevacizumab. *Pharmaceutics* **2021**, *13*, 258. <https://doi.org/10.3390/pharmaceutics13020258>

Academic Editor: Carlotta Marianecci
Received: 7 January 2021
Accepted: 10 February 2021
Published: 13 February 2021

Publisher's Note: MDPI stays neutral with regard to jurisdictional claims in published maps and institutional affiliations.

Keywords: microemulsions; in situ gelling systems; corneal delivery; intraocular neovascularization



Copyright: © 2021 by the authors. Licensee MDPI, Basel, Switzerland. This article is an open access article distributed under the terms and conditions of the Creative Commons Attribution (CC BY) license (<http://creativecommons.org/licenses/by/4.0/>).

1. Introduction

Bevacizumab (BVZ) is a recombinant humanized monoclonal antibody, available in the EU as Avastin[®] since 2005, directed against vascular endothelial growth factor (VEGF), which is responsible for the proliferation and migration of vascular endothelial cells causing tumor angiogenesis in vivo [1], which plays a central role in tumor growth, invasion and metastasis, also acting as a survival factor for endothelial cells via the inhibition of apoptosis.

BVZ is approved in the EU for the treatment of metastatic colorectal cancer, for the first-line treatments of metastatic breast cancer, advanced non-squamous non-small cell

lung cancer, advanced renal cell carcinoma, advanced epithelial ovarian, fallopian tube and primary peritoneal cancer [2].

VEGF is also considered as the major angiogenic stimulus for intraocular neovascularization (NV), which is a severe complication of different inflammatory and ischemic ocular diseases [3] involving the anterior and posterior segment of the eye. Recently, the efficacy and safety of anti-VEGF agents (BVZ, ranibizumab, and aflibercept) in the diabetic macular edema treatment were assessed. Although other VEGF inhibitors are approved for the treatment of ophthalmological conditions, BVZ is currently used in ophthalmology and clinical practice all around the world [4].

BVZ was initially introduced as intravenous therapy for age-related macular degeneration (AMD); however, major disadvantages associated with systemic BVZ administration, such as the possibility of life-threatening adverse events [5], induced to use it off-label as intravitreal injection [6,7]. Clinicians worldwide continue to treat AMD with off-label BVZ, whose cost is a small fraction of that of ranibizumab (Lucentis®), and whose effectiveness appears to be analogous.

In recent years, many studies refer to the use of BVZ in the treatment of anterior segment NV, such as in corneal NV occurring because of inflammatory, traumatic, and metabolic diseases of the cornea itself and leading to a marked reduction in vision due to angiogenesis of abnormal vessels that block light [8]. Current therapies, based on the use of non-steroidal anti-inflammatory drugs (NSAID), steroids [9], prolactin, thalidomide, cyclosporine [10], angiostatin [11] and methotrexate [12] are not always completely successful. Although the results of recent experimental and clinical studies on the use of BVZ in both human and animal eye models suggest that it may be effective in the treatment of corneal and iris NV [13], the number of literature data, even if increasing, is still relatively small. Anyway, some studies [14,15] demonstrated the capability of topically administered BVZ to penetrate the neovascularized cornea without altering corneal transparency or exerting specific toxicity on both epithelium and endothelium.

Recent clinical studies [16] report on the safety and efficacy of topical applied BVZ in the treatment of corneal NV secondary to a variety of corneal diseases, such as glaucoma [17,18] and pterygium [19,20].

Although topical BVZ was well tolerated with no adverse events and no toxicity to the epithelium, keratocytes or endothelium was reported [14], in a clinical study conducted on seven patients [21], the duration and the dose of topical delivered BVZ seemed to be related with an increased risk of adverse reactions, as, by the second month of application, loss of epithelium integrity and stromal thinning were noted in 10 eyes.

That being said, the topical application of BVZ seems to be a non-invasive and practical procedure to treat several anterior segment diseases; however, there are some disadvantages that cannot be underestimated when common eye-drops are administered, such as the poor ocular bioavailability, due to high tear-fluid turnover rate and high nasolacrimal drainage. Novel ocular drug delivery approaches, including nanomicelles, nanoparticles [22], drug-eluting contact lenses, ocular inserts, ocular iontophoresis and ocular devices that prolong precorneal residence and enhance the bioavailability of the therapeutic agent are under study [23–25]. The primary goal of any ophthalmic topical drug delivery system is to improve the precorneal residence time, maintain a therapeutic drug concentration level at the target site, reduce the frequency of administration and overcome the various ocular barriers. Among the different nanosystems described in the literature, microemulsions (MEs), which are transparent colloidal oil-in-water (O/W) or water-in-oil (W/O) nanodispersions, that present sizes between 5 and 200 nm with significant thermodynamic stability and low surface tension [26], seem to be adequate to be administered topically as ophthalmic delivery systems owing to their ease of preparation and sterilization, and to their supersolvent properties allowing to deliver both hydrophilic and lipophilic drugs. Several studies on this topic are reported in the literature [27–31]. Recently, a comprehensive review paper was published underlying that MEs could

significantly play a major role in ocular disease treatments as they are easily handled and cost-effective, but, up to today, applications found in the literature are still limited [32].

In recent years, increasing interest has grown to exploit systems able to thicken under external stimuli [33], such as temperature and/or pH changes or dilution-induced transformation from isotropic systems to liquid crystals. In situ-forming thermosensitive hydrogels are aqueous solutions, which jellify after a temperature change, owing to a temperature-induced phase transition governed by the balance of hydrophilic and hydrophobic moieties [34]. These systems, exhibiting low viscosity at 18 °C and forming gels at 32 °C, are generally based on natural polymers such as polysaccharides (cellulose and chitosan) or synthetic polymers (including PEG, poly-*N*-isopropylacrylamide, Pluronic® F127) crosslinked by a variety of mechanisms [35,36].

Ideally, they can be easily administered topically as eye-drops, whose viscosity increases at body temperature, prolonging the retention time on the eye surface to provide and maintain an adequate drug concentration in the precorneal area.

The aim of the present paper is the development of BVZ-loaded MEs, able to prolong the residence time of BVZ on the corneal surface compared with conventional BVZ aqueous solutions and to promote BVZ corneal penetration.

To achieve this goal, several BVZ-loaded MEs are developed, using non-toxic and biocompatible ingredients, able to increase their viscosity, either by the formation of a liquid-crystalline structure upon dilution or by temperature-induced jellification of a thermosensitive polymer present in the continuous aqueous phase. Both MEs and the derived nanocomposite systems are characterized for physicochemical properties, corneal opacity, and in vitro corneal permeation. Moreover, in vitro cell viability assays on human retinal pigment epithelial ARPE-19 cells are performed to evaluate the effect of BVZ, after releasing from these systems, on cellular growth.

2. Materials and Methods

Avastin® Roche (Basilea, Switzerland) was kindly purchased by Molinette Central Hospital (Turin, Italy). Deionized water was obtained by a Milli-Q system (Millipore, Bedford, MO, USA). Tween® 20 (polysorbate 20), Tween® 80 (polysorbate 80), hydroxyethyl cellulose, sodium phosphate monobasic and sodium phosphate dibasic were purchased from ACEF (Fiorenzuola d'Arda, Italy); trehalose dihydrate, cefuroxime, decyl polyglucoside, ethyl oleate, Pluronic® F127, dioctyl sodium sulfosuccinate (AOT) from Merck (Darmstadt, Germany); Epikuron® 200 (phosphatidylcholine 92%) from Cargill (Minneapolis, MN, USA); hyaluronic acid, sodium sulfate and sodium chloride from Alfa-Aesar (Ward Hill, MA, USA); Labrasol® from Gattefossè (Saint-Priest, France). Sulforhodamine B (SRB), dimethyl sulfoxide (DMSO), trichloroacetic acid, fetal calf serum and antibiotics for cell cultures were all purchase from Sigma-Aldrich (St. Louis, MO, USA). The retinal pigment epithelial ARPE-19 cell line (ATCC-CRL-2302) and the DMEM:F12 medium was purchase from ATCC® (Manassas, VA, USA).

2.1. Corneas

Corneas were explanted from rabbits sourced from the slaughterhouse: eye-balls were excised within 2 h of the animal's death, according to a protocol currently used for human cornea transplantation. They were transported to the laboratory chilled in normal saline (4 °C). A sclera ring of nearly 4 mm was maintained around the explanted corneas, which were kept in sterile Steinhardt medium for less than 1 week [37]. Before corneal opacity and permeation tests, corneas were assayed for their opacity by using the holder described below in the text, and corneas whose opacity exceeded 0.1 units of absorbance ($\lambda = 570$ nm) were discarded [38].

2.2. SEC-HPLC Analysis

The SEC-HPLC analysis method for BVZ quantification was performed as follows: BVZ solution from a freshly opened Avastin® vial was diluted with normal saline (0.9% *w/w* NaCl) or with a solution, hereafter named “vehicle”, at the same composition of the commercial product (trehalose dihydrate, monobasic sodium phosphate, dibasic sodium phosphate, polysorbate 20). BVZ solution samples at increasing concentrations (from 5 to 50 µg/mL) were injected onto an SEC column, TSK-GEL G3000S Wx1 5 µm (300 mm × 7.8 mm, Merck KGaA, Darmstadt, Germany) for separation using a system comprised of a UV detector (Shimadzu SPD-10A at 280 nm, Shimadzu Corporation, Kyoto, Japan) and HPLC pump (Shimadzu LC-10 AD, Shimadzu Corporation, Kyoto, Japan) interfaced with a computer with Class VP Chromatography Manager Software (Shimadzu Corporation, Kyoto, Japan). The mobile phase consisted of 0.01 M pH 7.4 PBS added 0.1 mM Na₂SO₄. Linear regressions ($R^2 = 0.9995$ and $R^2 = 0.9998$) were obtained from the calibration curves determined using normal saline or vehicle solution, respectively, as dilution media. In release studies and permeation tests, SEC-HPLC analysis was conducted in triplicate for each sample for both batches.

2.3. AF4 Analysis

The analysis of the monomeric form of BVZ was performed using an AF2000 asymmetric flow field-flow fractionation (AF4) instrument (Postnova Analytics, Landsberg, Germany), combined with a UV-vis spectrophotometer operating at a wavelength of 280 nm. The channel was 350 µm thick, and regenerated cellulose membranes with 10 kDa cutoff were used. The flow rate of the outlet channel was set to 0.2 mL/min. The focusing step was performed for 4 min with a focusing flow rate of 2.3 mL/min. For the separation step, an initial constant crossflow rate of 4.0 mL/min for 35 min was set and then lowered to 0.00 mL/min in 10 min using a linear gradient. The mobile phase was: 9 mM phosphate buffer (pH 7.2) added with 137 mM NaCl (filtered through 0.1 µm Durapore membrane). The software NovaFFF AF2000 Control (Postnova Analytics, Landsberg, Germany) was used to set and control the flow rate values. Detection parameters and signal acquisition were controlled by NovaFFF Analysis.

2.4. Ion Pairs Preparation and Apparent Ethyl Oleate/Aqueous Solution Partition Coefficient Calculation

The ability of some counter ions to form hydrophobic ion pairs with BVZ increasing its lipophilicity, was studied. Bis(2-ethylhexyl) sulfosuccinate sodium salt (AOT) and cefuroxime (CEF) were chosen as counter ions. The ionic interactions were established between the residues of the basic amino acids of BVZ (ionizable amino groups) and the sulfonate group of AOT or the carboxylic group of CEF at pH 5.5. BVZ–AOT and BVZ–CEF ion pairs were prepared by mixing 80 µL of Avastin® (containing 2 mg BVZ) and 2 mL of AOT or CEF solution (0.45 mg/mL) to obtain 1:150 molar ratio BVZ:counter ion. In the case of the BVZ–AOT, the 1:75 molar ratio was also studied. The obtained suspensions were centrifuged at 20,800 g (Eppendorf centrifuge, Hamburg, Germany). The supernatant was analyzed with SEC-HPLC and AF4, and the precipitated solid ion-pairs were dried under N₂ flux. Apparent oil–water partition coefficient (P_{app}) was determined using the shake-flask method. Each ion pair was dissolved in ethyl oleate and shaken at 22 ± 3 °C with an equal volume (1 mL) of 20% Pluronic® F127 aqueous solution. The oil and the aqueous phase were then left to rest for 24 h until separation took place. Three replicates of each determination were carried out to assess reproducibility. BVZ molar concentration [BVZ_{aq}] was then determined in the aqueous phase by SEC-HPLC, and BVZ molar concentration in ethyl oleate [BVZ_{oil}] was obtained by the difference between the initial oil molar concentration [BVZ_{in}] and [BVZ_{aq}]. From these data, Log P_{app} of BVZ ion pairs in ethyl oleate/polymer aqueous solution at pH 5.5 were determined, using the equation (1):

$$\text{Log } P_{\text{app}} = \text{Log} \frac{[BVZ_{\text{in}}] - [BVZ_{\text{aq}}]}{[BVZ_{\text{aq}}]} \quad (1)$$

Log P_{app} of the BVZ–AOT ion pairs (1:75 and 1:150 molar ratio) and of BVZ–CEF (1:150 molar ratio) were compared to Log P_{app} of free BVZ to confirm the formation of BVZ lipophilic ion pairs.

2.5. BVZ Stability

BVZ solutions (1.25 and 5 mg/mL) were prepared by diluting freshly opened Avastin® with normal saline or with a vehicle. In order to detect any possible degradation or aggregation of the antibody in aqueous media, each BVZ solution, stored at 4 °C, was analyzed for monomeric BVZ content by SEC-HPLC over a 30 day period and compared with an identical BVZ solution obtained from freshly in the day opened Avastin® vials to obtain decrease percentage ($\Delta C\%$) over time of monomeric BVZ, with the equation (2):

$$\Delta C\% = \left[\frac{\text{concentration of BVZ monomeric form in solution stored over time} - \text{concentration of BVZ monomeric form in freshly diluted Avastin®}}{\text{concentration of BVZ monomeric form in freshly diluted Avastin®}} \right] \times 100 \quad (2)$$

A 1.25 mg/mL BVZ solution in normal saline or in a vehicle, stored at 4 °C, and successively 1:10 *v/v* diluted in the mobile phase was also analyzed by AF4 to confirm the presence of monomeric peak over a 30 day period.

The secondary structural stability of Avastin® diluted in normal saline, in a vehicle, in pH 7.2 phosphate buffer and in pH 10.5 carbonate buffer (0.1 M) were analyzed by circular dichroism (CD) spectroscopy. The analyses were performed with a circular dichroism spectropolarimeter (JASCO J-815, Jasco, Tokyo, Japan), equipped with a Xe arc lamp, to record data in the far-UV spectral range. CD spectra resulted from the average of 4 scans recorded for each sample at 100 nm/sec scanning rate, and they were acquired at 20 °C. The measurements were carried out using a quartz cuvette with a path length of 0.1 mm in the 190–240 nm wavelength range. All spectra recorded were corrected using the correspondent solvent medium as the baseline. Since the saturation signal (UV absorbance greater than 1.0) impairs the linearity of the response of the instrument in the CD signal, the measures required preliminary steps of dilution necessary to calibrate the concentration of BVZ in each sample. Data were analyzed by Spectra Analysis software, purchased by JASCO. The secondary structure content of BVZ in different aqueous solutions was predicted from UV-CD spectra by using K2D software. The stability of the BVZ–AOT (1:150) ion pair solubilized in 0.1 M carbonate buffer at pH 10.5 was also analyzed by the same technique to confirm the structural maintenance of BVZ once the ion pair breaks.

2.6. Formulative Studies of Microemulsion

In this study, ME-based phase transition systems at different viscosities were developed to propose them as ocular delivery systems for BVZ by topical instillation. The phase transition upon water dilution of a water-in-oil ME (W/O ME) system was studied. ME contained a mixture of Epikuron® 200 and polysorbate 80 (1:1.1 *w/w*), as a surfactant, and Avastin®, diluted to 8.33 mg/mL of BVZ in a vehicle as aqueous phase, was prepared, and ethyl oleate was selected as oil phases, due to a fair solubilizing capacity of the resulting ME systems. The final BVZ concentration in the W/O ME formulation was 1.25 mg/mL. The phase transition of an oil-in-water ME (O/W ME) system upon temperature increase, from 18 ± 3 °C to 32 ± 3 °C, which is close to the internal temperature of the eye, was also studied. These systems comprised a mixture of Labrasol® and polysorbate 80 (1:10 *w/w*) as a surfactant, ethyl oleate as oil phase, and Avastin® diluted in the polymeric solution as the aqueous phase. The polymeric solution was composed of 20% Pluronic® F127 in a vehicle. From approximately 32 °C upwards, an aqueous Pluronic® F127 solution

at high concentration (20% *w/w*) undergoes sol–gel transition. Therefore, the formulation is liquid at low-temperature, facilitating its application on the corneal surfaces and reverts to a viscous form at the temperature of 32 ± 3 °C. The final BVZ concentration in O/W ME was 1.6 mg/mL. BVZ was added in O/W ME free and as a hydrophobic ion pair to allow the incorporation of BVZ in the dispersed oil phase. In this case, the O/W ME was prepared to add all components to the ion pair previously precipitated. The presence of monomeric BVZ in MEs was confirmed by AF4 analysis.

2.7. Pseudo-Ternary Phase Diagram Construction

Pseudo-ternary phase diagrams were constructed using Origin software (Origin 8.0, OriginLab Corporation, Northampton, MA, USA). The pseudo-ternary phase diagrams of oil, surfactant mixture and aqueous phase were constructed at 25 °C using the water titration method to obtain the components and their concentration ranges that can result in a large existing area of the W/O ME. Surfactants were blended in fixed weight ratios (1:1.1). Aliquots of a surfactant mixture (TA) were then mixed with oil at room temperature. The oil:TA ratio varied from 5:95 to 95:5. Water or diluted Avastin® in a vehicle was added dropwise to each mixture (oil:TA) under gentle magnetic stirring at room temperature. The resulting systems were then vortex mixed for 5 min and left to equilibrate overnight at room temperature. Following each addition of an aliquot of the aqueous phase, the mixtures were assessed visually. They were then characterized and classified based on their visual appearance (transparency) and behavior using polarized light to distinguish the liquid crystal region (LC) from the ME region. No heating was done during the preparation. The samples were marked as points in the phase diagram. The regions of existence of the ME and LC were demarcated. Amounts of all three phases were taken in *w/w* percentage. Based on this diagram, selected oil, surfactant, and co-surfactant were used for the preparation of the W/O ME that converts in the LC system by water dilution.

2.8. Rheological and Viscosity Measurements

Viscosity and rheological behavior of the W/O ME and LC were measured at 25 °C; O/W ME viscosity was measured at 18 and 32 °C using a Brookfield digital viscometer (DV-III+, Brookfield, Milwaukee, WI, USA) with SC4-25 spindle coupled to a temperature-controlling unit. The samples were thermostated at the required temperature with a circulating bath connected to the viscometer. Viscosity was recorded at a shear rate of 0.08 s^{-1} . The rheological behavior was estimated by submitting the samples to increasing and then to progressively decreasing shear rates in an appropriate range (0.001 to 6 s^{-1}) for each system. Rheograms were constructed by plotting shear stress as a function of shear rate.

2.9. Sol–Gel Transition Time of O/W ME

20% *w/w* Pluronic® F127 aqueous solution shows interesting thermoreversible gelation behavior. This renders Pluronic® F127 attractive in designing thermoreversible gels for many topical, injectable and controlled drug delivery. The sol–gel transition of the polymeric solution and of O/W ME was determined by a test tube inverting method [39] with temperature increments of 2 °C per step. Each sample was prepared in a 1 mL vial. After equilibration at 4 °C for 24 h, sample-containing vials were immersed in a water bath at a constant designated temperature for 15 min. The gelation temperature was characterized by the formation of a firm gel that remained intact when the tube was inverted by 180°.

2.10. DSC Measurements

DSC measurements were performed with a PerkinElmer (DSC7, PerkinElmer, Norwalk, CT, USA), equipped with an instrument controller Tac 7/DX (PerkinElmer) with elaboration software data Pyris Version 3.71, by heating the samples at 10 °C/min from 10 °C to 40 °C. Signals were recorded and used to localize the micellization phenomenon of

Pluronic® F127 in the external aqueous phase of O/W ME with and without BVZ compared with Pluronic® F127 solution.

2.11. Release Studies of BVZ from O/W ME

To study the release of BVZ, free and as hydrophobic ion pair, from O/W ME, test tubes were filled with 1 mL ME, gently covered with 1 mL of pH 7.2 phosphate buffer (0.1 M) as receiving phase and placed in an incubator at $32\text{ °C} \pm 0.5\text{ °C}$ [36]. The release of BVZ as an ion pair from O/W ME was also investigated at $18\text{ °C} \pm 0.5\text{ °C}$. At fixed times, the total volume of the receiving phase was withdrawn and analyzed by SEC–HPLC for BVZ determination. In the SEC–HPLC analysis of BVZ ion pairs, the receiving phases were diluted with 0.1 M carbonate buffer to break the ion pairs and to detect monomeric BVZ.

2.12. Corneal Opacity Tests

A corneal opacity test was performed adapting the Bovine Cornea Opacity/Permeability (BCOP) method, as reported by Casterton et al. [38], to evaluate the corneal toxicity of the systems. The opacity test was performed by clamping the cornea, through its scleral ring, in the appropriate holder and filling both the compartments with glutathione bicarbonate Ringer (GBR) buffer prepared according to the literature [40] as a control. Then, in the donor compartment, GBR buffer was substituted by the W/O and O/W ME formulations for 1 or 10 min. After withdrawing and washing for 15 min, the opacity was measured by determining the absorbance of the cornea ($\lambda = 570\text{ nm}$) clamped in the holder. The results were expressed as an increase of cornea absorbance (ΔAU), before and after incubation with the formulations under study. The holder was housed in a spectrophotometer (Lambda 2 UV-vis PerkinElmer, Norwalk, CT, USA) at $\lambda = 570\text{ nm}$ for opacity readings with the help of suitable support so that the beam precisely crossed the donor, the receptor compartment and the cornea clamped in the holder.

2.13. Diffusion and Accumulation Studies in Rabbit Cornea

Muchtar et al. studied the diffusion of drugs through a rabbit cornea used as a membrane between two compartments [41]. In the present work, the experiments were carried out by using modified all-Plexiglas Franz diffusion cell on the W/O ME and LC containing free BVZ or O/W ME containing free BVZ compared to BVZ commercial solution. The holder used consisted of a Plexiglas structure, with a donor and a receiving compartment, respectively, on the epithelial and on the endothelial side of the cornea, which must be placed in the orifice, which divides the two compartments as reported by Gallarate et al. [30]. To minimize the irritation caused to the cornea by the holder itself, according to the literature [42], the Plexiglas structure O-ring clamped the scleral ring all around the corneal circumference; moreover, the holder structure allowed maintaining the natural cornea curvature. The area available for diffusion was 0.63 cm^2 . The receptor compartment was filled with 3 mL freshly prepared normal saline solution, constantly stirred at 150 rpm with a Teflon-coated magnetic stir bead and all air bubbles were expelled from the compartment. One mL of the formulated ME was placed on the excised cornea. The diffusion cell was kept in an incubator at $32\text{ °C} \pm 0.5\text{ °C}$. The permeation study was carried out for 24 h and samples were withdrawn from the receptor at the end of the experiments. The withdrawn samples were analyzed for drug content by SEC–HPLC. At the end of the 24 h experiment, the cornea was removed from the diffusion cell and washed three times with normal saline for 15 s. The cornea was cut into small pieces and extracted in 2 mL of normal saline for 4 h at 37 °C . The extract was analyzed by the SEC–HPLC method.

2.14. Adhesion Studies

To study the influence of ME on corneal adhesion, an empirical method was developed following the procedure described by Gallarate et al. [30]. A gel with the same

surface tension of tear fluid (28 mN/m) was prepared; its composition was: 1% hydroxyethyl cellulose, 3% decyl polyglucoside, 5% hyaluronic acid, q.b. 100% water. The gel was spread on a 24 × 32 cm glass support and kept resting until hardening was reached. 0.1 mL of each sample was placed onto the shorter side of the hardened gel, and the support was sloped of 18°. The time needed to flow over a 10 cm-distance was evaluated for each preparation. The flow rate was calculated as distance/time (cm/s).

2.15. Cell Growth Assay

The BVZ activity after release from O/W ME was evaluated in retinal pigment epithelial ARPE-19 cells by using a sulforhodamine B colorimetric cell growth assay (SRB assay) modified by Vichai and Kirtikara [43]. ARPE-19 were routinely grown in DMEM:F12 medium, with the addition of 10% (*v/v*) fetal bovine serum, 1% (*v/v*) penicillin–streptomycin, and were maintained in standard conditions (37 °C, 5% CO₂ and 95% humidity). For growth assay, BVZ released in phosphate buffer solution at a different time from O/W system was used. Briefly, ten thousand cells were seeded into 96-well plates. After 24 h of growth, cells were incubated for 48 h, in triplicate wells, with the samples properly diluted in the culture medium. Then, the cells are fixed on plates with 10% (*w/v*) trichloroacetic acid, washed and stained with an SRB solution (0.057% *w/v* in 1% *v/v* acetic acid) for 30 min. After washing with 1% (*v/v*) acetic acid and drying, the bound dye is solubilized with Tris-buffer (10 mM, pH 10.5), and the optical density (OD) was quantified photometrically (492 nm). The cell growth was expressed as a percentage (mean OD of treated cells/mean OD of control cells × 100). The experiment was replicated three times for all the incubation times.

2.16. Data Analysis

Data are shown as mean ± SD (standard deviation/number of replicate).

3. Results

3.1. BVZ Stability in Aqueous Solution

In Table 1, the concentration decrease percentage ($\Delta C\%$) over time of monomeric BVZ as Avastin® diluted in normal saline and in a vehicle is reported, compared to freshly diluted Avastin®. Samples were analyzed by the SEC-HPLC method described in Materials and Methods.

Table 1. Decrease percentage of monomeric bevacizumab (BVZ) concentration ($\Delta C\%$) in normal saline and in a vehicle (an aqueous solution with the same composition of the commercial product).

Initial Concentration	1.25 mg/mL	5 mg/mL	1.25 mg/mL	5 mg/mL
Time (days)	$\Delta C\%$ in normal saline		$\Delta C\%$ in a vehicle	
1	-24	-10	0	0
4	-30	-12	0	0
30	-33	-14	-1.8	-1.2

As can be noted, the SEC-HPLC analysis showed that BVZ was more stable in a vehicle than in normal saline at both investigated concentrations.

The same results were confirmed by analyzing 1.25 mg/mL BVZ aqueous solutions (in normal saline and in a vehicle) by AF4 analysis, as shown in Figure 1. These analyses were performed with the crossflow at 4 mL/min that allows a sharper peak of BVZ compared to that obtained with lower cross flows (2.0 and 0.5 mL/min).

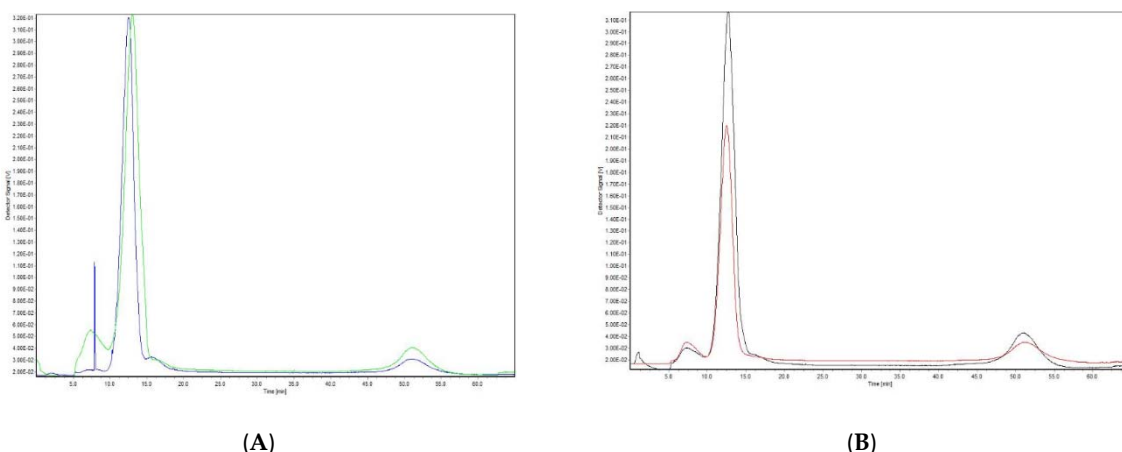


Figure 1. Fractograms of BVZ solution: (A) Avastin® diluted in a vehicle at $t = 0$ day (green) and at $t = 30$ days (blue); (B) Avastin® diluted in normal saline at $t = 0$ day (black) and at $t = 30$ days (red).

By CD analysis, BVZ secondary structure was maintained in aqueous solution (vehicle, normal saline, phosphate buffer, see Figure 2A, green, black and magenta line, in the order) after 24 h also when BVZ was present as an ion pair (BVZ:AOT 1:150) and when this ion pair was broken in pH 10.5 carbonate buffer (see Figure 2B, red and blue lines, respectively). All the spectra of BVZ in aqueous solutions have a similar shape, exhibiting a negative band with a minimum at 217 nm followed by a maximum at 202 nm. A similar profile is reported to be characteristic of the β -sheet type of structure [44].

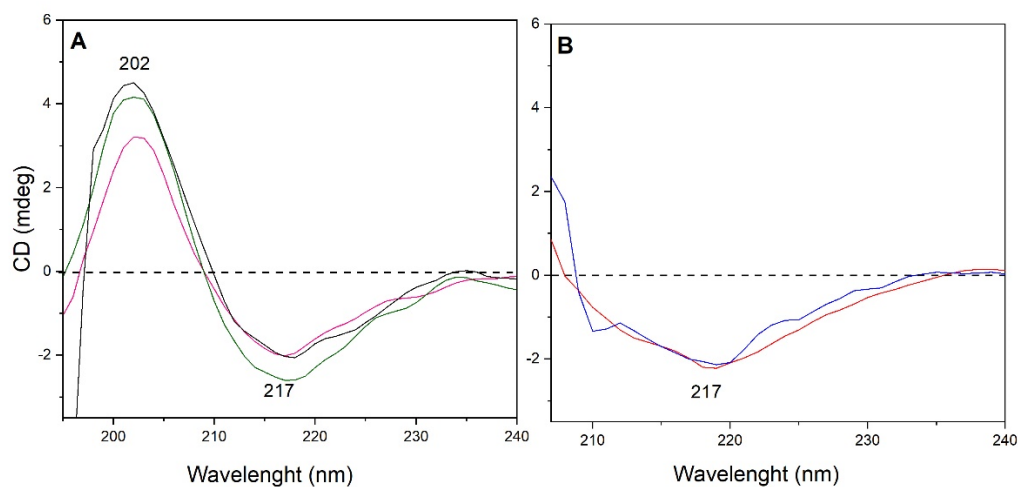


Figure 2. CD-UV spectra of BVZ (A) in a vehicle (green curve), normal saline (black curve), and phosphate buffer (magenta curve) and of BVZ (B) in the form of an ion pair (red curve) and after a break of ion pair (blue curve).

Further, the analysis of the spectra of BVZ as ion pair and when it was broken with the carbonate buffer (Figure 2B) is hindered by the presence of electrolytes rendering the sample nontransparent below 205 nm (see corresponding CD Absorbance spectra in Figure S1). However, the visible part of the spectra exhibits a shape similar to those of BVZ in aqueous solutions (Figure 2A), meaning the well-defined minimum at 217 nm and the similar shape of the “slope” between 220 and 240 nm. In addition, it is worth mentioning that the fitting of these spectra with the same algorithm indicated a similar number of β -sheet structures (ca. 43%).

3.2. BVZ Ion Pair Formation and Log P_{app}

Hydrophobic ion pairing of BVZ with AOT or CEF improved the lipophilicity of BVZ [45]. In Table 2, the yields (expressed as a percentage) of ion-pair formation and Log P_{app} values (\pm SD) in ethyl oleate/20% *w/w* Pluronic® F127 aqueous solution at pH 5.5 are reported. The yield was calculated by determining BVZ concentration in the supernatant, after ion pair precipitation, by SEC-HPLC analysis. The presence of BVZ in monomeric form was confirmed by AF4 (data not shown).

Table 2. Yield of ion-pair formation and log $P_{app} \pm$ SD of ion pairs.

Ion Pair	Yield (%)	Log $P_{app} \pm$ S.D.
BVZ	-	0.90 ± 0.02
BVZ–AOT (1:75)	90.0 ± 0.8	2.77 ± 0.08
BVZ–AOT (1:150)	91.7 ± 1.0	2.40 ± 0.07
BVZ–CEF (1:150)	76.0 ± 0.4	2.29 ± 0.08

The formation of the ion pair with AOT increases Log P_{app} of BVZ almost thrice. As CEF has many hydrophilic groups in its structure, the BVZ–CEF ion pair resulted less lipophilic than the BVZ–AOT one. As AOT has surfactant properties, at the higher concentration employed (BVZ:AOT 1:150 molar ratio), it can form micelles able to solubilize the BVZ phenomenon, which could explain the decrease of ion-pair oil partition at AOT concentrations higher than CMC. In fact, 1:75 BVZ:AOT showed greater lipophilicity than 1:150 BVZ:AOT.

3.3. Water-in-Oil ME Formulation Studies

The field of existence of the W/O ME systems that could present a change in viscosity by simple dilution by switching to a liquid crystal structure was studied. The pseudo-ternary phase diagram of the W/O system (Figure 3A) showed two distinct regions with the W/O ME transforming to lamellar liquid crystalline structure (LC) with increasing water content. The pseudo-ternary phase diagrams for blank ME regions were constructed using ethyl oleate as an oil (O), polysorbate 80 and lecithin mixture as a surfactant (TA) and water as the aqueous phase. For ME/LC regions containing BVZ, diluted Avastin® (8.33 mg/mL of BVZ) was used as an aqueous phase (Figure 3B). Each point was evaluated by using a couple of polarized lenses. We remarked that in the presence of BVZ, both the fields of the existence of LC and ME are reduced.

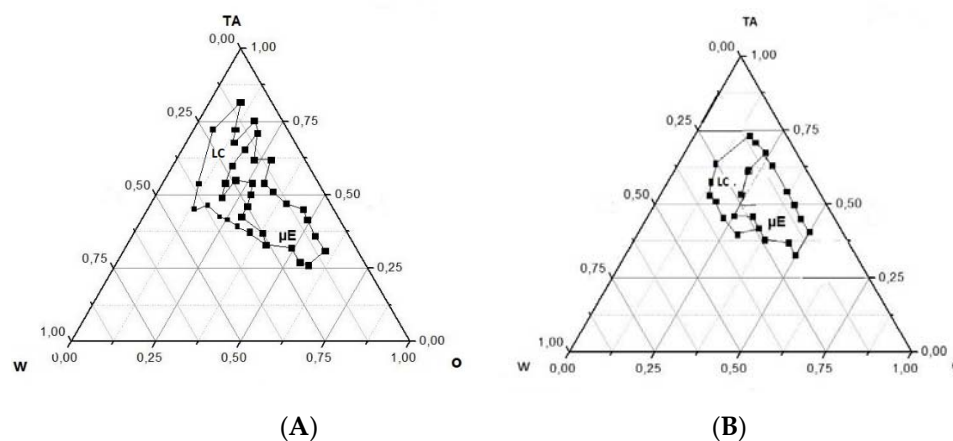


Figure 3. Pseudo-ternary phase diagram of the microemulsion (ME)–liquid crystal region (LC) system (A) without BVZ; (B) with BVZ.

3.4. Preparation of Microemulsion

After the identification of the ME region in the pseudo-ternary phase diagram, W/O ME formulations were selected at the desired component ratios to switch from the ME system to LC by dilution, miming the corneal environment. The preparation of selected W/O ME was performed in an easy way by putting the weighed components in a vial and stirring to form a clear ME. According to the pseudo ternary phase diagrams (Figure 3), liquid crystal systems were also prepared and observed using a couple of polarized lenses.

O/W ME (named PL1) was prepared by adding a 20% *w/w* Pluronic® F127 aqueous solution in oil and surfactants mixture. Oil, surfactant blend and aqueous phase were vortex-mixed for 10 min, and the resulting systems were left to equilibrate overnight at room temperature before conducting the characterization tests. Table 3 reports the composition of the tested formulations with and without BVZ. These formulations included W/O ME and LC formulations (named M1 and LC1) containing aqueous phase at 16% and 30% (*w/w*), respectively, with the latter being close to the W/O ME–LC phase boundary. BVZ was incorporated by replacing water (M2 and LC2) or Pluronic® F127 aqueous solution (PL2) with an Avastin® dilution. In the case of O/W ME containing BVZ/counter ion, the ion pair was added in the oil phase before ME preparation.

Table 3. Composition of the liquid systems formulated without BVZ or with BVZ as Avastin® diluted with a vehicle.

	M1	M2	LC1	LC2	PL1	PL2
	(mg)	(mg)	(mg)	(mg)	(mg)	(mg)
Ethyl oleate	313	313	313	313	17	17
Labrasol®	-	-	-	-	30	30
Epikuron® 200	220	220	220	227	-	-
Polysorbate 80	244	233	286	250	265	318
Water	150	-	350	170	-	-
Pluronic® F-127 solution	-	-	-	-	937	773
Avastin®	-	150 µl ¹	-	150 µl ¹	-	80 µl

¹ Avastin was previously diluted to 8.33 mg/mL of BVZ with a vehicle

The presence of monomeric BVZ in the ME systems was confirmed by AF4 analysis. It is possible to distinguish the peak of monomeric BVZ still remaining in the disperse system (Figure S2, Supplementary Materials).

3.5. Rheological Characterization and Viscosity Measurements

The rheological behavior at 25 °C of the W/O systems was studied. The conversion of Newtonian ME to non-Newtonian LC upon aqueous phase addition is shown in Figure 4A. In the M1 rheogram, the up curve is coincident with the down curve, showing time-independent viscosity, while the LC1 rheogram shows a thixotropic behavior. In Figure 4B, the rheological profile of PL1 at 18 °C is reported. It was not possible to characterize the rheological properties of PL1 at a temperature higher than that of gelation of Pluronic® F127 (32 °C), while the rotation of the spindle determined cavitation phenomena in the system, which hindered the correct measurements of shear stress.

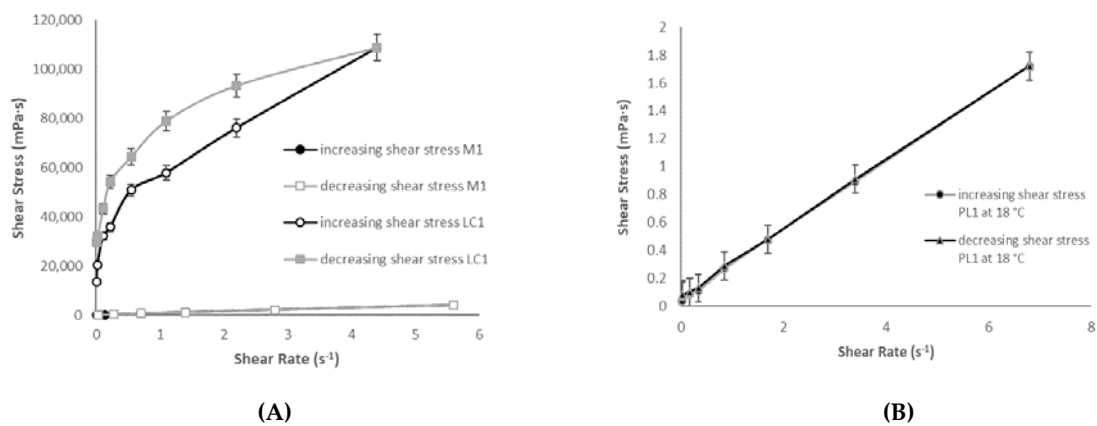


Figure 4. Rheological behavior of the W/O ME (M1) and LC system (LC1) at 25 °C (A) and of O/W ME (PL1) at 18 °C (B).

The viscosity values of the studied systems obtained at 0.08 s⁻¹ shear rate are reported in Table 4, and the PL1 viscosity as compared to that of 20% Pluronic®F127 solution at the same temperatures.

Table 4. Viscosity of colloidal systems formulated, measured at 0.08 s⁻¹.

Sample	Temperature (°C)	Viscosity × 10 ³ ± S.D. (mPa·s)
M1	25	0.89 ± 0.11
LC1	25	105.58 ± 3.50
PL1	18	1.25 ± 0.10
	32	3,604.03 ± 197.28
Pluronic® F127 gel	18	1.20 ± 0.12
	32	3,647.22 ± 231.00

The increase in viscosity of the W/O system is remarkable when M1 converts to LC1. Therefore, a highly viscous LC system, formed upon dilution of the M1 by the tear film, may remain on the cornea for a long time.

In PL1, being a thermosensitive system, thanks to the presence of Pluronic® F127, a significant viscosity increase was noted upon temperature enhancement (from 18 °C to 32 °C).

Pluronic® F127, able to form a thermoreversible gel in aqueous solution at 20% w/w (with gelation time = 1 min), maintained its ability in the ME formulations around body temperature, with a gelation time of 3 min when BVZ was in the external phase and of 1 min, 47 s when BVZ:AOT (1:150) ion pair was in the inner oil phase.

3.6. DSC Analysis

The possible impact of oil droplet addition upon Pluronic® F127 gelation must be investigated. The endothermic micellization process of Pluronic® F127 is usually analyzed by DSC. In this work, the possible impact of oil droplet addition on Pluronic® F127 micellization was investigated (Figure 5).

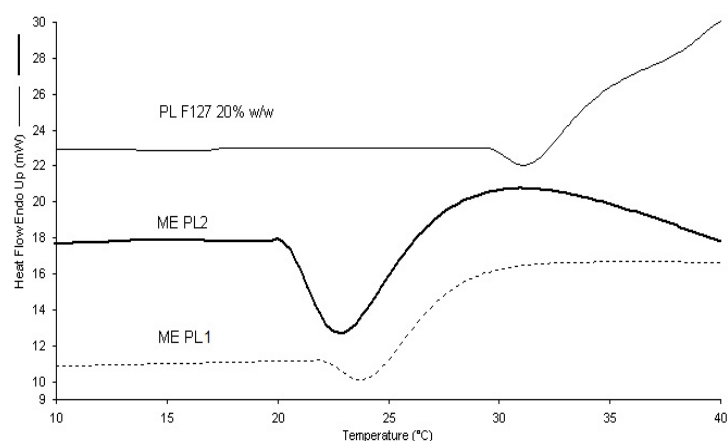


Figure 5. Thermograms of PL with (PL2) and without (PL1) BVZ, compared to thermogram of Pluronic® F127 solution.

Heat flow measurements performed during heating ramps were scrutinized in order to evaluate the possible loss of the thermal behavior related to micelle formation of Pluronic® F127 in the presence of oil droplets. The large endothermic peak was ascribed to the micellization of Pluronic® F127 unimers [46]. During heating, the rupture of hydrogen bonds of poly-(propylene oxide) (PPO) leads to an increase of hydrophobicity, while the poly-(ethylene oxide) (PEO) chains remain hydrophilic. Then, when the micellization is achieved, Pluronic® F127 micelles arrange themselves in a crystalline structure [47] at a distinct temperature. Gelling temperature coincided with the crystallization temperature, which is difficult to study by DSC because slightly endothermic. The temperature-dependent micellization behavior of Pluronic® F127 solution was maintained in PL1 and PL2 formulation. The micellization capacity of Pluronic® F127 in PL2 about 22 °C probably allows retaining BVZ to a greater extent, even if in the external phase of the ME.

3.7. Release of BVZ from PL2

In order to investigate the ion-pair formation influence on BVZ release from PL2, diffusion tests were performed. The percentage of released BVZ over time from PL2 compared to Pluronic® F127 solution at 32 °C is reported in Table 5. BVZ was released quickly and in a similar way (about 90% in 24 h) when incorporated in the polymeric gel or in PL2, as it is located in the external phase of the ME, where it is probably micellized into Pluronic® F127 chains as well as in Pluronic® F127 reference solution. When incorporated in PL2 as hydrophobic ion pairs, BVZ was released very slowly, almost 15–25% over 24 h. This behavior suggests that BVZ, in this case, is located in the inner oil phase of the ME. The release of BVZ hydrophobic ion pairs from PL2 was also tested at 18 °C. As at this temperature, PL2 viscosity is lower than at 32 °C, the release of BVZ was faster than from the viscous system.

Table 5. Percentage of BVZ (\pm S.D.), free and as ion pair, released from Pluronic® F127-containing systems vs. time.

Time (h)	Pluronic® F127 + BVZ at 32 °C	PL2 free BVZ at 32 °C	PL2 BVZ–AOT (1:150) at 32 °C	PL2 BVZ–CEF (1:150) at 32 °C	PL2 BVZ–AOT (1:150) at 18 °C	PL2 BVZ–CEF (1:150) at 18 °C
			release (%) \pm SD			
0	0	0	0	0	0	0
0.25	12.10 \pm 0.51	7.05 \pm 0.24	0	0	0	0
0.5	21.85 \pm 0.70	14.10 \pm 0.46	0	0	0	0
0.75	30.45 \pm 1.32	21.25 \pm 0.31	0	0	0	0
1	44.40 \pm 0.93	30.15 \pm 1.68	0	2.03 \pm 0.28	0	7.36 \pm 0.58

2	51.85 ± 1.70	41.95 ± 1.21	5.15 ± 0.75	14.17 ± 0.90	5.05 ± 0.70	28.83 ± 0.87
4	69.55 ± 1.95	52.85 ± 1.45	7.40 ± 0.76	16.85 ± 1.10	13.75 ± 1.43	45.23 ± 1.93
7	78.62 ± 1.18	70.35 ± 1.48	9.05 ± 0.88	21.65 ± 0.91	19.85 ± 1.27	59.69 ± 1.57
24	91.23 ± 1.81	89.20 ± 1.50	14.50 ± 1.12	25.15 ± 1.43	24.40 ± 1.41	68.50 ± 1.86

Comparing BVZ–AOT and BVZ–CEF ion pairs, the higher the value of Log P_{app} , the lower the release rate. Indeed, release results confirmed that the BVZ–CEF ion pair produced a faster release than the BVZ–AOT one, being less lipophilic. According to these results, 1:75 BVZ–AOT ion pair was not tested in release studies as the high value of Log P_{app} would probably produce a BVZ release too low for our purposes.

3.8. Corneal Opacity Tests

Irritant-induced opacity, which is experimentally determined by the amount of light transmission through the cornea, is an indicator of protein denaturation, swelling, vacuolization or damage in the epithelial and/or stromal layers. The evaluation of common standard irritants provides an empirical irritation scale, as reported by Battaglia et al. [48]. In this irritation classification, the samples result mild when opacity is <0.400 at $\lambda = 570$ nm. In Table 6, the increase of cornea absorbance (ΔAU) after contact with BVZ-containing ME was reported. After 1 min and 10 min exposition, a mild irritation effect was noted for all the systems under study. GBR buffer was used as a control.

Table 6. Increase of cornea absorbance (ΔAU) after contact with microemulsion systems and with glutathione bicarbonate Ringer (GBR) buffer.

Samples (Abs 0 min)	ΔAU 1 min	ΔAU 10 min
GBR buffer (0.153)	0.008 ± 0.001	0.009 ± 0.001
M2 (0.171)	0.035 ± 0.011	0.057 ± 0.015
PL2 (0.114)	0.019 ± 0.002	0.021 ± 0.003

3.9. Permeation and Accumulation of BVZ Through Rabbit Cornea

In Table 7, the percentage of BVZ diffused through the cornea and the percentage of BVZ accumulated in 24 h deposition are reported.

Table 7. Amount of permeated and accumulated BVZ after 24 h, expressed as a percentage, through the cornea, released from the ME systems under study.

Sample	% diffused BVZ in 24 h	% accumulated BVZ in 24 h
BVZ solution (Avastin®)	0.40 ± 0.11	5.16 ± 0.66
M2	0.56 ± 0.09	15.24 ± 0.95
LC2	0.70 ± 0.11	19.89 ± 0.83
PL2	1.56 ± 0.09	4.08 ± 0.37

Increasing the water content of the delivery system (from M2 to PL2), an increase in BVZ corneal permeation was noted. BVZ released by the liquid crystal system (LC2) accumulates on the cornea more than the other systems under study.

3.10. Adhesion Properties of W/O ME

To evaluate the adhesion properties of the M2 and LC2 formulation compared to a conventional solution (distilled water), the course of the systems on the hardened gel was timed. The flow rates (cm/s) of M2 and LC2 are reported in Table 8.

Table 8. Flow rate of water-in-oil (W/O) ME (M2) and LC (LC2) along a hardened gel simulant surface tension of tear fluid.

Sample	Flow Rate (cm·s ⁻¹)
Distilled water	4.81 ± 0.20
M2	0.08 ± 0.02
LC2	Not Detectable *

* under detection limits

PL2 was not tested because it was difficult to perform the study at 32 °C. The developed systems have a good adhesive capacity compared to water; therefore, they are probably able to remain on the cornea longer than an eye drop. In particular, the liquid crystal system is characterized by a high adhesive capacity, as it was not able to cross the gel, stopping halfway.

3.11. Effect of BVZ Released from O/W Systems on Cell Growth (Cell Growth Assay)

The cell growth assay was performed on ARPE-19 cells. This cell line was employed in this study as a model of retinal pigment epithelium (RPE) cells, able to secrete the VEGF [49]. The effect on cell growth of BVZ released from O/W ME (PL2) at the different times was tested at different concentrations determined as reported in the release studies. Cells were incubated for 48 h with each released sample diluted 1:100, and cell growth was determined by SRB assay (Figure 6).

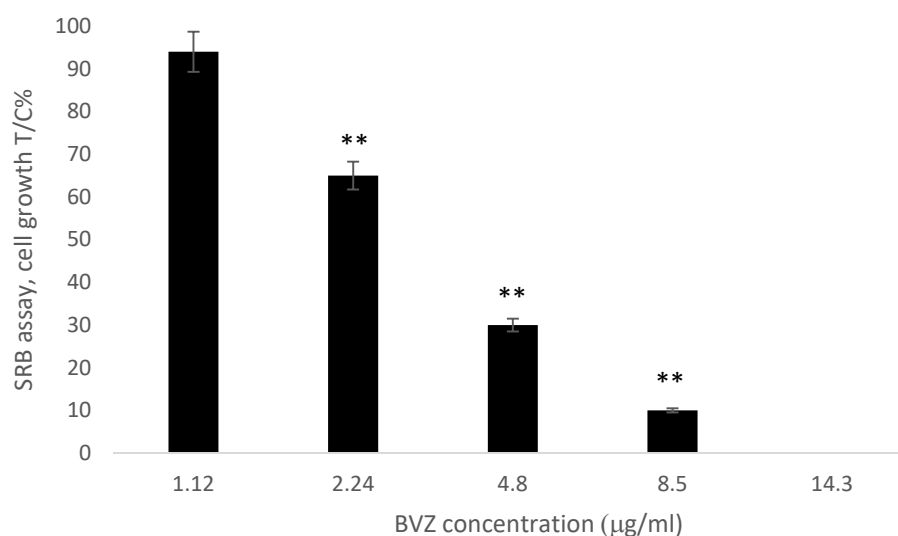


Figure 6. Effect of BVZ on ARPE-19 cell proliferation after 48 h of incubation. Cell growth is expressed as % T/C (mean optical density (OD) of treated cells/mean OD of control cells \times 100). Values are mean \pm SD ($n = 3$ wells/condition) of three independent experiments (** $p < 0.01$).

As shown in Figure 6, a significant decrease of ARPE-19 cell viability after 48 h of incubation was observed for BVZ at concentrations higher than 2.24 $\mu\text{g}/\text{m}$ (** $p < 0.01$). The effect of BVZ released from O/W ME was similar to the viability inhibition of BVZ commercial solution observed in a previous work [50]: at 5 $\mu\text{g}/\text{mL}$, the cell growth was decreased by 75%.

4. Discussion

The main goal of the present work was to develop BVZ-loaded MEs to be proposed as ophthalmic local delivery systems to promote BVZ corneal permeation and/or accumulation. MEs are thermodynamically stable disperse systems that are quite interesting for their supersolvent properties due both to the presence of oil and an aqueous phase and of a complex surfactant/cosurfactant mixture. These characteristics, together with the ability of the W/O microemulsions to evolve in liquid crystals upon water dilution, offer a plethora of possible drug carrying and drug release modalities, which are non-easily obtainable with other nanosystems.

Preliminary studies on BVZ stability were performed to evaluate in which aqueous solution was more appropriate to dilute Avastin®. Indeed, physicochemical instability of the antibody, which can lead to denaturation and/or aggregation, must be avoided; for this reason, it was necessary to assess the stability of the monomeric form of BVZ under

the conditions of use. The mixture of polysorbate 20, trehalose and phosphate salts in water was the most suitable for dilution while maintaining the stability of the monomeric BVZ, probably owing to the presence of polysorbate 20, which formed micelles able to stabilize BVZ. This hypothesis seems to be also confirmed by the stability of BVZ in normal saline, which was significantly lower at 1.25 mg/mL than at 5 mg/mL concentration: as 1.25 mg/mL solution was prepared to dilute a smaller volume of Avastin® than that used to prepare 5 mg/mL solution, polysorbate 20 (present in Avastin®) was diluted below its CMC value, determining consequent instability phenomena of BVZ. BVZ maintained its structure also when assembled in the ion pair, as shown with CD spectra. The fitting of the CD spectra (Figure 2) reveals the high relative amount of b-strand (ca. 45%), which indeed corresponds with the detailed analysis of the secondary structure of BVZ carried out by Ferreira et al. [51] and confirms the relative abundance of the β -sheets (ca. 47%).

These results are strongly supported by those obtained using three different analytical techniques (i.e., SEC-HPLC, AF4 Analysis, CD), which, though not interchangeable, can supply complementary information to assess BVZ moiety integrity after the production technologies reported in the present research. This was an important and absolutely nonobvious prerequisite to developing BVZ-containing microemulsions. In this research, O/W and W/O MEs were proposed for their in situ gel-forming properties and potential utilization for ocular drug delivery to reduce the frequency of instillations per day. Thanks to the construction of the pseudo-ternary phase diagram, it was possible to evaluate the appropriate dilution to obtain the corresponding LC system from the W/O ME.

A W/O ME was developed that was able to incorporate BVZ in the aqueous inner phase and to increase its viscosity once in contact with an aqueous environment, owing to the formation of liquid-crystalline structures in the system.

The field of existence of the W/O ME and its switching into an LC structure upon water dilution was investigated by pseudo-ternary phase diagrams systems. LC might form when W/O ME comes in contact with the physiological tear fluid and might influence both drug release and precorneal residence time. The reduced existence area of the W/O ME in the presence of BVZ can be related to a probable interaction of BVZ (even if located in the inner phase) with the W/O interface, perturbing, although not dramatically, the phase assessment. Diluting with Avastin® solution, of course, determined a variation of BVZ concentration dependent on added Avastin® volume, giving some supplementary information about the maximum amount of BVZ that it was possible to introduce in the studied W/O ME, but this was not the goal of the present research.

Furthermore, an O/W ME was proposed, containing a solution of Pluronic® F127, a polymer characterized by a sol–gel transition around 32 °C. This system has proven to be able to incorporate a commercial solution of BVZ, maintaining the temperature-sensitive characteristics of the polymer solution. BVZ maintained the monomeric form when incorporated in microemulsions, as shown with AF4 analysis (supplementary materials). As in the O/W microemulsion system, BVZ is probably located in the external phase, hydrophobic ion pairs of BVZ were also prepared. Hydrophobic ion pairing of BVZ with AOT or CEF proved to improve the lipophilicity of BVZ, necessary to incorporate it in the inner phase of O/W ME. Moreover, as CEF is one of the widely used antibiotics to prevent endophthalmitis, which might also occur during invasive procedures such as intravitreal injections or cataract surgery, we hypothesized that BVZ–CEF ion pair might play a double therapeutic action. On the other hand, AOT is a surfactant already widely studied as a counter ion of BVZ, which forms a highly water-insoluble ion pair [45]. Even if the use of the term lipophilicity can sound as not properly used, as no octanol/water partition was determined, it indicates the increase of ethyl oleate/water partition, as ethyl oleate is the oil phase of the ME, in, which we aimed to dissolve a quite hydrophilic molecule like BVZ.

The very low viscosity often exhibited by MEs is inappropriate for ophthalmic use, as they may easily be removed from the eye surface by lacrimation and/or nasolacrimal drainage. In the present research, ME's viscosity was enhanced by exploiting two different strategies: the addition of water to the W/O ME to turn it into a liquid crystal system and the introduction of a thermogelling polymer such as Pluronic®F127 in the aqueous phase of O/W ME.

Release studies performed on the different prepared systems allow us to deduce a number of conclusions.

First of all, BVZ release studies from PL2 confirmed the incorporation of BVZ ion pairs in the inner oil phase due to their increase in $\log P_{app}$ compared with BVZ.

When BVZ is introduced as ion pair in PL2, the release rate is slower than that obtained when BVZ alone was present, confirming the formation of ion pairs. Moreover, the formation of the BVZ–AOT ion pair and the introduction into the ME modifies the gelation time, decreasing it, thus stabilizing the ME. The release rate of BVZ as ion pairs from PL2 in 24 hours was very low and dependent on $\log P_{app}$ value; moreover, in some cases, lag time longer than two hours were observed. For these reasons, BVZ ion pair containing O/W ME seem to be not suitable for the topical corneal administration. On the other hand, these *in vitro* very slow releases are stimulating to plane further studies to exploit any possible way to the use of the BVZ-ion pair containing O/W ME as sustained (more than one month) BVZ delivery systems. The idea might be to propose them for intravitreal administrations.

BVZ aqueous solution has a limited ability to penetrate corneas with intact epithelium, and preliminary permeation tests through the cornea were required to verify the permeation capacity of BVZ from the liquid systems under study. Moreover, as in tube release studies, BVZ ion pairs showed a very slow release; they were not used in the corneal permeation studies.

The BVZ percentage diffused through the cornea from all the studied systems was, in general, very low; due to its high molecular weight, BVZ hardly permeates the corneal structure, which excludes macromolecules with a radius greater than 10Å . Regarding permeation, water percentage had an effect whereby, increasing water content of the delivery system from the W/O ME to O/W ME (M2 to PL2), the corneal permeation was increased. These results support the advantage of using BVZ containing O/W ME, probably related to their capability to enhance permeation. On the other hand, BVZ released by the liquid crystal system (LC2) accumulates on the cornea more than the other systems under study, proving to be an excellent topical BVZ release system. Presumably, *in vivo*, M2, upon contact with the tear fluid, could transform into the LC system (LC2) by changing its viscosity and therefore increasing the residence time on the cornea as well.

From the release tests, however, it was possible to evaluate the maintenance of the dose-dependent activity of the BVZ compared to the free BVZ solution on the ARPE-19 cell line.

Viscosity and rheology studies carried out on most ME formulations allowed to reinforce some hypothesis. The increase in viscosity upon water dilution (tear fluid in case of possible topical administration on the cornea) for the W/O ME, or with the temperature increase, typical of the ocular surface, for O/W ME, would allow prolonging *in situ* permanence of the BVZ release system. Both the proposed systems increase their viscosity, and therefore they could keep BVZ on the cornea, preventing or slowing down the washout due to eye drainage, improving its residence time. In addition, the results of adhesion tests confirmed a good adhesion capacity of the W/O systems. Moreover, MEs can increase the drugs' retention in the cornea by virtue of their solubilizing power, which allows the partitioning of the dissolved fraction of the drug into the epithelium, in addition to their nanometer size. As LC is a more rigid system than the ME, it passes to a less extent through the cornea, but it remains on the corneal surface and, after 24 h, the LC system allows a high BVZ accumulation, greater than the ME systems.

All the obtained results allowed to do an accurate screening on different ME and LC systems containing BVZ as such or as a hydrophobic ion pair, concluding that the different BVZ location, viscosity and release patterns may be exploited for several purposes and selecting those that can be proposed for topical corneal NV therapy.

5. Conclusions

The MEs studied in this research, both W/O and O/W, are able to change their viscosity under conditions that mimic the corneal environment (presence of tear fluid or temperature increase). Moreover, they incorporate BVZ, which is then able to permeate the cornea. A prolonged precorneal residence time could reduce the frequency of administration and promotes the crossing of the various ocular barriers. Therefore these systems can be considered a promising strategy for the treatment of the corneal NV secondary to a variety of the corneal diseases.

Supplementary Materials: The following are available online at www.mdpi.com/1999-4923/13/2/258/s1, Figure S1: CD absorbance spectrum of BVZ after breaking of ion pair in 190–240 nm region. The gray box is due to the region of the spectrum heavily affected by the presence of electrolytes and, thus rendering the CD signal impossible to analyze; Figure S2: Monomeric BVZ form in the ME systems, confirmed by AF4 analysis (a) in O/W ME (PL2) and (b) in the W/O ME (M2).

Author Contributions: Conceptualization, Elena Peira (E.P.) and Marina Gallarate (M.G.); methodology, Simona Sapino (S.S.), Simonetta Oliaro-Bosso (S.O.-B.) and Elena Peira (E.P.); software, Simona Sapino (S.S.); formal analysis, Giulia Chindamo (G.C.), Erica Rebba (E.R.); investigation, Giulia Chindamo (G.C.), Daniela Chirio (D.C.), Pavlo Ivanchenko (P.I.); data curation, Elena Peira (E.P.); writing—original draft preparation, Elena Peira (E.P.) and Daniela Chirio (D.C.); writing—reviewing and editing, Elena Peira (E.P.); supervision, Marina Gallarate (M.G.). All authors have read and agreed to the published version of the manuscript.

Funding: This work was supported by the University of Turin [Local Research Funds 2019, 2020]

Institutional Review Board Statement: Not applicable.

Informed Consent Statement: Not applicable.

Data Availability Statement: Please refer to suggested Data Availability Statements in the section “MDPI Research Data Policies” at <https://www.mdpi.com/ethics>.

Acknowledgments: This work is dedicated to the dearest memory of Professor Gianmario Martra, who taught P.I. and E.R. to get the things done. †Deceased 29 September 2020

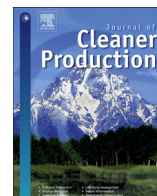
Conflicts of Interest: The authors declare no conflicts of interest.

References

1. Ferrara, N. Vascular endothelial growth factor as a target for anticancer therapy. *Oncologist* **2004**, *9*, 2–10.
2. Keating, G.M. Bevacizumab: A Review of Its Use in Advanced Cancer. *Drugs* **2014**, *74*, 1891–1925.
3. Aiello, L.P.; Avery, R.L.; Arrigg, P.G.; Keyt, B.A.; Jampel, H.D.; Shah, S.T.; Pasquale, L.R.; Thieme, H.; Iwamoto, M.A.; Park, J.E.; et al. Vascular endothelial growth factor in ocular fluid of patients with diabetic retinopathy and other retinal disorders. *N. Engl. J. Med.* **1994**, *331*, 1480–1487.
4. Mitchell, P.; Liew, G.; Gopinath, B.; Wong, T.Y. Age-related macular degeneration. *Lancet* **2018**, *392*, 1147–1159.
5. Michels, S.; Rosenfeld, P.J.; Puliafito, C.A.; Marcus, E.N.; Venkatraman, A.S. Systemic bevacizumab (Avastin) therapy for neovascular age-related macular degeneration twelve-week results of an uncontrolled open-label clinical study. *Ophthalmology* **2005**, *112*, 1035–1047.
6. Rosenfeld, P.J.; Moshfeghi, A.A.; Puliafito, C.A. Optical coherence tomography findings after an intravitreal injection of bevacizumab (Avastin®) for neovascular age-related macular degeneration. *Ophthalmic Surg. Lasers Imaging Retin.* **2005**, *36*, 331–333.
7. Rauck, B.M.; Friberg, T.R.; Mendez, C.A.M.; Park, D.; Shah, V.; Bilonick, R.A.; Wang, Y. Biocompatible reverse thermal gel sustains the release of intravitreal bevacizumab in vivo. *Investig. Ophthalmol. Vis. Sci.* **2014**, *55*, 469–470.

8. Bahar, I.; Yeung, S.N.; Sella, R.; Slomovic, A. Anterior segment uses of bevacizumab. *Curr. Opin. Ophthalmol.* **2012**, *23*, 303–316.
9. Murata, M.; Shimizu, S.; Horiuchi, S.; Taira, M. Inhibitory effect of triamcinolone acetonide on corneal neovascularization. *Graefes Arch. Clin. Exp. Ophthalmol.* **2006**, *244*, 205–209.
10. Benelli, U.; Ross, J.R.; Nardi, M.; Klintworth, G.K. Corneal neovascularization induced by xenografts or chemical cautery: Inhibition by cyclosporin A. *Investig. Ophthalmol. Vis. Sci.* **1997**, *38*, 274–282.
11. Ambati, B.K.; Jousseaume, A.M.; Ambati, J.; Moromizato, Y.; Guha, C.; Javaherian, K.; Gillies, S.; O'Reilly, M.S.; Adamis, A.P. Angiostatin inhibits and regresses corneal neovascularization. *Arch. Ophthalmol.* **2002**, *120*, 1063–1068.
12. Byun, Y.S.; Chung, S.K. The effect of methotrexate on corneal neovascularization in rabbits. *Cornea* **2011**, *30*, 442–446.
13. Habot-Wilner, Z.; Barequet, I.S.; Ivanir, Y.; Moisseiev, J.; Rosner, M. The inhibitory effect of different concentrations of topical bevacizumab on corneal neovascularization. *Acta Ophthalmol.* **2010**, *88*, 862–867.
14. Yoeruek, E.; Ziemssen, F.; Henke-Fahle, S.; Tatar, O.; Tura, A.; Grisanti, S.; Bartz-Schmidt, K.U.; Szurman, P. Safety, penetration and efficacy of topically applied bevacizumab: Evaluation of eyedrops in corneal neovascularization after chemical burn. *Acta Ophthalmol.* **2008**, *86*, 322–328.
15. Dastjerdi, M.H.; Sadrai, Z.; Saban, D.R.; Zhang, Q.; Dana, R. Corneal penetration of topical and subconjunctival bevacizumab. *Investig. Ophthalmol. Vis. Sci.* **2011**, *52*, 8718–8723.
16. Dastjerdi, M.H.; Al-Arfaj, K.M.; Nallasamy, N.; Hamrah, P.; Jurkunus, U.V.; Pineda, R.; Pavan-Langston, D.; Dana, R. Topical bevacizumab in the treatment of corneal neovascularization: Results of a prospective, open-label, noncomparative study. *Arch. Ophthalmol.* **2009**, *127*, 381–389.
17. Wakabayashi, T.; Oshima, Y.; Sakaguchi, H.; Ikuno, Y.; Miki, A.; Gomi, F.; Otori, Y.; Kamei, M.; Kusaka, S.; Tano, Y. Intravitreal bevacizumab to treat iris neovascularization and neovascular glaucoma secondary to ischemic retinal diseases in 41 consecutive cases. *Ophthalmology* **2008**, *115*, 1571–1580.
18. Saito, Y.; Higashide, T.; Takeda, H.; Ohkubo, S.; Sugiyama, K. Beneficial effects of preoperative intravitreal bevacizumab on trabeculectomy outcomes in neovascular glaucoma. *Acta Ophthalmol.* **2010**, *88*, 96–102.
19. Liu, J.; Xu, J.H.; Xu, W.; Liang, G.L.; Lou, J.X.; Wang, Y.; Wen, J.Q.; Cao, Y.B. Bevacizumab as adjuvant therapy in the management of pterygium: A systematic review and Meta-analysis. *Int. J. Ophthalmol.* **2017**, *10*, 1126–1133.
20. Peng, M.L.; Tsai, Y.Y.; Tung, J.N.; Chiang, C.C.; Huang, Y.C.; Lee, H.; Cheng, Y.W. Vascular endothelial growth factor gene polymorphism and protein expression in the pathogenesis of pterygium. *Br. J. Ophthalmol.* **2014**, *98*, 556–561.
21. Kim, S.W.; Ha, B.J.; Kim, E.K.; Tchah, H.; Kim, T.I. The effect of topical bevacizumab on corneal neovascularization. *Ophthalmology* **2008**, *115*, e33–e38.
22. Pandit, J.; Sultana, Y.; Aqil, M. Chitosan-coated PLGA nanoparticles of bevacizumab as novel drug delivery to target retina: Optimization, characterization, and in vitro toxicity evaluation. *Artif. Cells Nanomed. Biotechnol.* **2017**, *45*, 1397–1407.
23. Fangueiro, J.F.; Veiga, F.A.; Silva, M.; Souto, E.B. Ocular Drug Delivery—New Strategies for targeting anterior and posterior segments of the eye. *Curr. Pharm. Des.* **2016**, *22*, 1135–1146.
24. Mazet, R.; Yaméogo, J.B.G.; Wouessidjewe, D.; Choïnard L.; Gèze, A. Recent advances in the design of topical ophthalmic delivery systems in the treatment of ocular surface inflammation and their biopharmaceutical evaluation. *Pharmaceutics* **2020**, *12*, 570.
25. Arora, K.; Singhand, S.; Chaurasia, L. Ophthalmic drug delivery system—A concise review on its conventional and novel approaches. *Curr. Res. Pharm. Sci.* **2018**, *8*, 263–269.
26. Kesavan, K.; Gautam, N.; Bharti, S.K.; Mohan, P. Microemulsion systems: Prospective approach for superior drug delivery. *Drug Deliv. Lett.* **2017**, *7*, 157–169.
27. Gallarate, M.; Gasco, M.R.; Trotta, M.; Chetoni, P.; Saettone, M. Preparation and evaluation in vitro of solutions and o/w microemulsions containing levobunolol as ion-pair. *Int. J. Pharm.* **1993**, *100*, 219–225.
28. El Maghraby, G.M.; Bosela, A. Investigation of selfmicroemulsifying and microemulsion systems for protection of prednisolone from gamma radiation. *Pharm. Dev. Technol.* **2011**, *16*, 237–242.
29. Üstündağ-Okur, N.; Gökçe, E.H.; Eğriılmaz, S.; Özer, Ö.; Ertan, G. Novel ofloxacin-loaded microemulsion formulations for ocular delivery. *J. Ocul. Pharmacol. Therapeut.* **2014**, *30*, 319–332.
30. Gallarate, M.; Chirio, D.; Bussano, R.; Peira, E.; Battaglia, L.; Baratta, F.; Trotta, M. Development of O/W nanoemulsions for ophthalmic administration of timolol. *Int. J. Pharm.* **2013**, *440*, 126–134.
31. Bachu, R.D.; Stepanski, M.; Alzhrani, R.M.; Jung, R.; Boddu, S.H.S. Development and evaluation of a novel microemulsion of dexamethasone and tobramycin for topical ocular administration. *J. Ocul. Pharmacol. Therapeut.* **2018**, *34*, 312–324.
32. Üstündağ-Okur, N.; Çağlar, E.S.; Sıfaka, P.I. Novel ocular drug delivery systems: An update on microemulsions. *J. Ocul. Pharmacol. Therap.* **2020**, *36*, 342–354.
33. Mahlumba, P.; Choonara, Y.E.; Kumar, P.; Du Toit, L.C.; Pillay, V. Stimuli-responsive polymeric systems for controlled protein and peptide delivery: Future implications for ocular delivery. *Molecules* **2016**, *21*, 1002.
34. Gong, C.; Qi, T.; Wei, X.; Qu, Y.; Wu, Q.; Luo, F.; Qian, Z. Thermosensitive polymeric hydrogels as drug delivery systems. *Curr. Med. Chem.* **2013**, *20*, 79–94.
35. Kloud, L. Thermoresponsive hydrogels in biomedical applications: A seven-year update. *Eur. J. Pharm. Biopharm.* **2015**, *9*, 338–349.
36. Sapino, S.; Peira, E.; Chirio, D.; Chindamo, G.; Guglielmo, S.; Oliaro-Bosso, S.; Barbero, R.; Vercelli, C.; Re, G.; Brunella, V.; Riedo, C.; et al. Thermosensitive Nanocomposite Hydrogels for Intravitreal Delivery of Cefuroxime. *Nanomaterials* **2019**, *9*, 1461.

37. Steinhardt, R.A. Cornea Preservation Medium. U.S. Patent 7,087,369, 17 December 2003.
38. Casterton, P.L.; Potts, L.F.; Klein, B.D. A novel approach to assessing eye irritation potential using the bovine corneal opacity and permeability assay. *J. Toxicol. Cutaneous Ocul. Toxicol.* **1996**, *15*, 147–163.
39. Khattak, S.F.; Bhatia, S.R.; Roberts, S.C. Pluronic F127 as a Cell Encapsulation Material: Utilization of Membrane-Stabilizing Agents. *Tissue Eng.* **2005**, *11*, 974–983.
40. Camber, O. An in vitro model for determination of drug permeability through the cornea. *Acta Pharm. Suec.* **1985**, *22*, 335–342.
41. Muchtar, S.; Abdulrazik, M.; Frucht-Pery, J.; Benita, S. Ex-vivo permeation study of indomethacin from a submicronemulsion through albino rabbit cornea. *J. Control. Release* **1997**, *44*, 55–64.
42. Ubels, J.L.; Ditlev, J.A.; Clousing, D.P.; Casterton, P.L. Corneal permeability in a redesigned corneal holder for the bovine cornea opacity and permeability assay. *Toxicol. Vitro.* **2004**, *18*, 853–857.
43. Vichai, V.; Kirtikara, K. Sulforhodamine B colorimetric assay for cytotoxicity screening. *Nat. Protoc.* **2006**, *1*, 1112–1116.
44. Greenfield, N.J. Using circular dichroism spectra to estimate protein secondary structure. *Nat. Protoc.* **2006**, *1*, 2876–2890.
45. Battaglia, L.; Gallarate, M.; Peira, E.; Chirio, D.; Solazzi, I.; Giordano, S.M.; Gigliotti, C.L.; Riganti, C.; Dianzani, C. Bevacizumab loaded solid lipid nanoparticles prepared by the coacervation technique: Preliminary in vitro studies. *Nanotechnology* **2015**, *26*, 255102.
46. Pradines, B.; Djabourov, M.; Vauthier, C.; Loiseau, P.M.; Ponchel, G.; Bouchemal, K. Gelation and micellization behaviors of Pluronic®F127 hydrogel containing poly(isobutylcyanoacrylate) nanoparticles specifically designed for mucosal application. *Coll. Surf. B Biointerfaces* **2015**, *135*, 669–76.
47. Zhang, M.; Djabourov, M.; Bourgaux, C.; Bouchemal, K. Nanostructured fluids from pluronic® mixtures. *Int. J. Pharm.* **2013**, *454*, 599–610.
48. Battaglia, L.; D'Addino, I.; Peira, E.; Trotta, M.; Gallarate, M. Solid lipid nanoparticles prepared by coacervation method as vehicles for ocular cyclosporine. *J. Drug Deliv. Sci. Technol.* **2012**, *22*, 125–130.
49. Ford, K.M.; Saint-Geniez, M.; Walshe, T.; Zahr, A.; D'Amore, P.A. Expression and Role of VEGF in the Adult Retinal Pigment Epithelium. *Investig. Ophthalmol. Vis. Sci.* **2011**, *52*, 9478–9487.
50. Chirio, D.; Peira, E.; Sapino, S.; Chindamo, G.; Oliaro-Bosso, S.; Adinolfi, S.; Dianzani, C.; Baratta, F.; Gallarate, M. A new bevacizumab carrier for intravitreal administration: Focus on stability. *Eur. J. Pharm. Biopharm.* **2020**, submitted.
51. Ferreira, L.M.B.; Alonso, J.D.; Kiill, C.P.; Ferreira, N.N.; Buzzá, H.H.; Martins de Godoi, D.R.; de Britto, D.; Assis, O.B.G.; Seraphim, T.V.; Borges, J.C.; et al. Exploiting supramolecular interactions to produce bevacizumab-loaded nanoparticles for potential mucosal delivery. *Eur. Polymer. J.* **2018**, *103*, 238–250.



Chemistry behind leather: Life Cycle Assessment of nano-hydroxyapatite preparation on the lab-scale for fireproofing applications

Carlo Ingrao^a, Enrica Vesce^{a,*}, Rosalia S. Evola^a, Erica Rebba^b, Claudia Arcidiacono^c, Gianmario Martra^b, Riccardo Beltramo^a

^a Department of Management, University of Turin, Corso Unione Sovietica 218 Bis, 10134, Torino, Italy

^b Department of Chemistry, NIS Interdepartmental and INSTM Reference Centre, University of Turin, Via Pietro Giuria 7, 10125, Torino, Italy

^c Department of Agriculture, Food and Environment (Di3A), University of Catania, Via S. Sofia, 100 - 95123, Catania, Italy

ARTICLE INFO

Article history:

Received 12 May 2020

Received in revised form

13 August 2020

Accepted 14 August 2020

Available online 22 August 2020

Handling editor: Cecilia Maria Villas Bôas de Almeida

Keywords:

Leather manufacturing

Chemistry

Fireproof agent

Environmental sustainability

Life cycle assessment

Nano-hydroxyapatite

ABSTRACT

Human population has set in motion productive systems through which huge energy and resource flows are extracted and manipulated causing various negative externalities.

In this context, Life Cycle Assessment (LCA) may facilitate identifying the links between the product for which the company is responsible and the economic, environmental and social dimensions which it operates into. This research aims at contributing to assessment and improvement of sustainability of the chemistry behind leather manufacturing. This was done through LCA application to, explore the relevant environmental issues in the preparation of nano-hydroxyapatite (nano-HA) at the lab scale, a promising biomaterial for improving leather fireproof properties. The work is one of the first-time experiences of LCA application in this field, and so the authors believe that it may contribute to enhancement of the subject literature and knowledge. The effect on collagen matrix on leather has been investigated, indeed, only for Hydroxyapatite (HA), that is, the starting material for new nano-formulation.

Through their study, the authors found that the major production hotspots stay in the consumption of electricity and phosphoric acid (one of the two reagents), and in the acquisition of all input chemicals to the process. By doing so, the study may serve as the essential base for identification of new chemical formulations for improvement of the environmental sustainability associated with the process.

© 2020 Elsevier Ltd. All rights reserved.

1. Introduction

The extraction and transformation of raw materials into finished products imply huge challenges, and the unintended consequences of the associated activities are increasingly placing great demands and additional responsibilities on ways to take decisions in the manufacturing industries (Gbededo et al., 2018). It is now undisputed that industrial production processes imply consumption of fossil fuels causing, in turn, negative externalities. These mainly derives from the exploitation of non-renewable primary-energy resources and the emission of Greenhouse Gases (GHGs) and of other environmentally alarming gaseous pollutants (Arbolino et al., 2020). Previously published literature of the sector documented,

indeed, that manufacturing activities are contributing alarming degradation and pollution to the planet's natural resources and are generating harmful effects at the societal level (Gbededo et al., 2018).

Several studies highlighted that manufacturing activities cause release of pollutants, in a way that is leading to increased urgency to clean all of those environmentally-harmful sectors that Mani and Wheeler (1997) defined as 'dirty sectors'. These are pollution-intensive sectors that were identified as those incurring high levels of abatement expenditure per unit of output in the United States (US) and other Organisation for Economic Co-operation and Development (OECD) (Mani and Wheeler, 1998). Subsequently, five sectors emerged as leading candidates for the status of 'dirty industry', namely: 'Iron and Steel', 'Non-Ferrous Metals', 'Industrial Chemicals', 'Pulp and Paper', and 'Non-Metallic Mineral Products' (Mani and Wheeler, 1998). Furthermore, one more direct approach revealed leather manufacturing as one of the highest-rank sectors

* Corresponding author.

E-mail address: enrica.vesce@unito.it (E. Vesce).

on actual intensity of emissions per unit of output (Mani and Wheeler, 1998). This should be attributed mainly to tannery wastewaters presenting: remarkably high concentrations of chromium together with other inorganic compounds like chloride, ammonia, sulphide and sulphate; and a significant organic load (Rivela et al., 2004; Mwinyihija, 2010).

In this context, the European tannery industry is facing a number of challenges related to: the massive imports of raw materials from various countries; the size of companies (mainly small and medium); the increasing competition from the transition economies and developing countries; and the environmental impacts of the industry itself on water, terrestrial and atmospheric systems (Mwinyihija, 2010; Notarnicola et al., 2011).

Despite its ancient origin and the significant advancements throughout centuries, leather manufacturing still represents one of the most environmentally impacting industrial activities (Rosa et al., 2017).

Tanning is the process by which raw hides and skins are transformed into leather (Rivela et al., 2004) that is utilised, in turn, as intermediate industrial product with several applications in downstream sectors (Joseph and Nithya, 2009). Leather can be cut and assembled into shoes, clothing, furniture and many other items of daily use (Joseph and Nithya, 2009). It is expected that the market of leather goods will witness considerable growth during the period 2018–2022: consequently, there will be a revenue of almost USD 289 billion by 2022,¹ but there will be also the alarming risk of amplification of environmental issues.

Leather tanning and finishing processes are composed of several stages requiring consumption of large amounts of chemicals, auxiliaries, fuels, and energy but, mostly, of resources like freshwater, as well as generating liquid and solid wastes (Sreeram and Ramasami, 2003; Rivela et al., 2004).

Sustainability of tannery is hugely affected by the chemical industry, which today represents the fourth largest contributor to the European manufacturing sector (Arbolino et al., 2020), and is also hugely burdening from an environmental perspective. This is reflected on the tannery industry, because the latter provides usage of chemical products that are amongst the most polluting ones currently available in the market (Dixit et al., 2015; Rosa et al., 2017). Their application is strongly dependent upon the processing technologies that are utilised and the type of finished leather product that is obtained. It contributes, however, to generating emissions of organic compounds and to determining both the physical-chemical characteristics of the solid waste and the pollutant load of the wastewaters (Dixit et al., 2015). In line with this, Joseph e Nithya (2009) investigated 100 m²-leather manufacturing process reporting that 348 kg chemical substances were used in the tanning and finishing phases and that almost 70% of those were dangerous. Those substances are utilised to give specific attributes to leather in order to meet desired technological and aesthetics standards: flame resistance is one of those attributes. The use of fire retardants has contributed in the past few decades to reducing the fire incidence. Nowadays the main components of fire resistance agents are brominated flame-retardants (BFRs), and there are more than 75 different types that are commercially recognised today. In recent years, it has emphasised that BFR-treated products cause both emission and leaching of BFR compounds into the environment, with subsequent contamination of the atmosphere, and of soils and water bodies (Darnerud, 2003). These contaminants may then enter the food chain where they mainly occur in food of animal origin. Furthermore, chemicals may

cause other health effects, prompting many countries to ban or suspend their use in new consumer goods (Costa et al., 2008).

Hence, there is urgent need for cleaner approaches to leather Supply Chains (SCs), by developing and testing more environmental-friendly chemicals and technologies for leather manufacturing and processing (Krishnamoorthy et al., 2013; Shi et al., 2016), in an integrated, holistic approach to sustainability.

This study wishes to make a contribution in this sense, by exploring relevant environmental issues associated with preparation of nano-hydroxyapatite (nano-HA), for possible usage as fire-proof agent in leather applications. So, the study attempts to contribute to the sustainability assessment subject in chemical- and leather-product manufacturing, namely two of the most pollution-intensive industrial activities.

By doing so, the study could help meeting the recommendation from the International Union of Leather Technologists and Chemists Societies (IULTCS) about reducing the quantity of chemicals utilised, to achieve environmental improvements in leather manufacturing (IULTCS, 2018).

The study was motivated by nanomaterials being eco-friendly alternatives that are increasingly being utilised in the tannery industry, in that they add special characteristics to leather commodities, as documented by Sanchez-Olivares et al. (2014) and Jiang et al. (2015). Moreover, a key advantage of nano-HA over other conventional flame-retardants, like the brominated ones, is the natural compatibility towards the main leather component (i.e. collagen), as bone tissue is made primarily of nano-HA particles that are interspersed in a collagen matrix (Wang and Shan, 2019). That compatibility triggers interaction phenomena between leather and nano-HA, which contributes to making it effective as a fireproof agent. In this way, there would be mitigation of the volatilisation and leaching phenomena that, instead, are remarkable for conventional flame retardants, like the brominated ones, that are not covalently bounded to the products they are designed to protect (Usenko et al., 2016).

The study discussed in this paper investigates nano-HA preparation and was focussed upon the lab scale dimension, for assessment of environmental impacts and damages already at the earliest stages of material design and for identification of the hotspots, in line with Piccinno et al. (2016, 2018).

2. Review of previously published literature related to this paper's subject

2.1. Review development methods

This section was conceived to develop – and report findings from – a comprehensive review of the literature on the characteristics and methods of nanocomposite application in the various phases of leather manufacturing system. For this purpose, the bibliographical search was conducted by accessing Scopus which is acknowledged today as the largest abstract and citation database of peer-reviewed literature (Scopus, 2019). To make sure that a representative framework of innovation was provided, attention was addressed to studies published during the last ten years. Paper search was performed by using alternative combinations of the most representative key-words connected with the field investigated, namely “leather”, “leather treatment”, “leather industries”, “leather finishing”, “tanning”, “tanning process”, “nanomaterial”, “nanocomposite”, “hybrid nanocomposite”, and “nanoparticles”. Subsequently, paper collection was restricted even more on the basis of two criteria: the object analysed and the application field. First of all, only those papers dealing with materials considered to comply with the requirements established by European Commission (EC) in order to adopt a unique and science-based definition of

¹ Source: <https://www.technavio.com/report/global-leather-goods-market-analysis-share-2018> (accessed: Sep 15, 2019).

nanomaterial. The Commission Recommendation of October 2011 defines nanomaterial as a “natural, incidental or manufactured material containing particles, in an unbound state or as an aggregate or as an agglomerate and where, for 50% or more of the particles in the number size distribution, one or more external dimensions is in the size range 1 nm – 100 nm” (EC, 2011). Secondly, the innovation application field of scientific contributions chosen focuses on tanning, re-tanning, and finishing steps, the principal macro phases that constitute the tannery manufacturing cycle. The application of this criterion therefore led to exclusion of all papers that paid attention on the possible use of nanomaterials in treatments for the pollutant removal in leather post tanning wastewater: the contributions belonging to this line of research highlight the adsorbent power of nanomaterials that can be exploited in order to remove hexavalent chromium (Cr (VI)) and dyes from industrial wastewater, as for example documented by Acharya et al. (2018). Given the fact that in these cases the nanomaterials are not used directly on the leather to render some specific characteristics, the authors decided not to consider them in this review.

2.2. Discussion of findings from this review

The criterion according to which the review was set allowed the authors to select 53 papers, that are well representative of the research subject on nanomaterial application in the leather manufacturing sector.

The review allowed to understand that extensive research was conducted in this sector, and was focussed upon different nanomaterial types. These were classified by the authors into six main categories, depending upon the type of particle which they are composed of: titanium dioxide (TiO_2), silicon dioxide (SiO_2), zinc oxide (ZnO), silver (Ag), hydroxyapatite (Ha) and clay particles. Fig. 1 shows a percentage breakdown of papers reviewed per analysed nanomaterial type. During the review process, papers were found to be addressing SiO_2 and TiO_2 ; hence, the authors' choice to merge those papers in the category ' $\text{TiO}_2 - \text{SiO}_2$ ', as shown in Fig. 1.

Around 57% of the reviewed papers dealt with clay-based nanocomposites, with 30 contributions found out of the 53 found in total. Within this category Montmorillonite (MMT) based nanocomposites constitute the dominant subgroup as they were

investigated by authors 23 papers.

For all the other categories considered, the percentage of papers stays below 20%. Hydroxyapatite (HA) is the less assessed material category (5% of the 53 articles selected for this review). As a matter of fact, just the papers of Ershad-Langroudi and Mirmontahai (2013, 2015) and Selvaraju et al. (2017) were found, thereby testifying that little research has been done thus far in this content area and further is needed to contribute to making improvements and advancements.

HA should be considered as a promising innovative material for application in the leather manufacturing sector, although this review highlighted it to be the less studied than the other substances used for the preparation of nanomaterials. Hydroxyapatite is increasingly attracting the interest of experts in the field of chemistry for leather. Hydroxyapatite-based bio-nanocomposites were developed by Selvaraju et al. (2017), as alternatives to conventional tanning and re-tanning substances, as their application provides higher thermal stability and higher tear strength to treated leather. Moreover, Ha nanoparticles have been applied on historical goat leather by Ershad-Langroudi and Mirmontahai (2013, 2015) with the aim of exploring their effect on collagen matrix for a better conservation of historical bookbinding: after accelerating aging test, the comparison between treated with untreated leather samples allow to affirm that the nanoparticles treatment induces a better mechanical and thermal behaviours.

Just two (Selvaraju et al., 2017; Ma et al., 2014) of the 53 papers carried out assessments of the environmental impacts associated with nanomaterials' life cycles for sustainable innovation solutions. In particular, they considered standard parameters to measure the wastewater polluting load. In fact, the leather processing involves a huge amount of water that, if it not properly treated, becomes the main carrier of chemicals dispersion in the environment. The common standard parameter considered are Biochemical Oxygen Demand (BOD), Chemical Oxygen Demand (COD), Total Dissolved Solids (TDS), Total Suspended Solids (TSS) and Total Solids (TS); in the scientific contribution the value of parameters measured for the innovation is reduced compared to their value registered in case of conventional process.

So, it is the authors' opinion that such assessments are important but not enough to state whether new chemicals are sustainable in a holistic integrated approach. With a view to prevention, in the

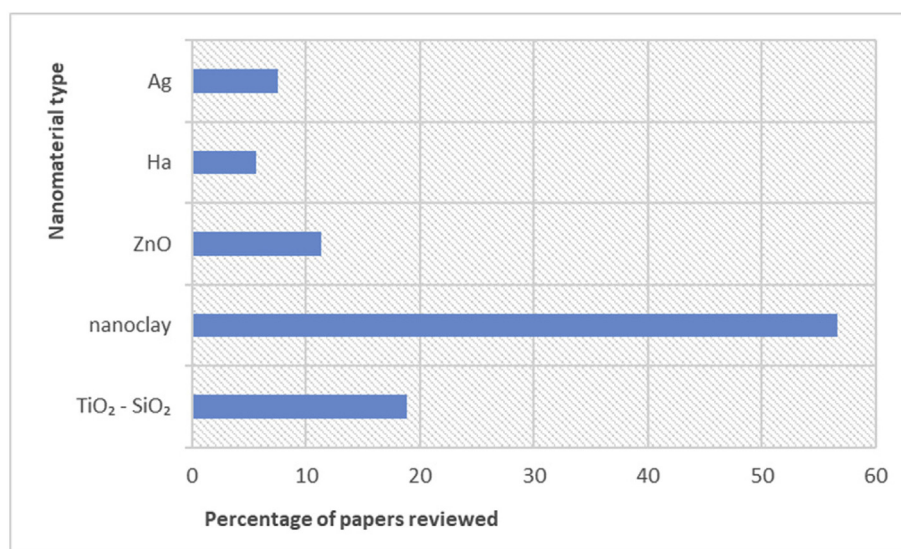


Fig. 1. The figure shows the distribution of the 53 papers reviewed per type of nanomaterial analysed.

initial phase of innovation development, it is always opportune to combine the conclusions on its functionality to the reflections on the possible impacts that innovation can cause along the entire SC for every sustainability's dimensions.

In this regard, LCA can be the valid tool to use for evaluation of the environmental performance of chemical innovations from a holistic point of view (Muñoz, 2012; Tufvesson et al., 2013; Pallas et al., 2018). However, comprehensive and detailed LCAs are consuming to be carried out, mainly owing to the widely recognised difficulties and limitations in the collection of reliable data as part of the Life Cycle Inventory (LCI) phase, that is, creating, analysing, and interpreting the material and energy flow throughout the system. This worsens when, especially in case of chemicals innovation, product and process are often very complex and its cycle involves many phases (Tufvesson et al., 2013; Hirschier et al., 2005) or even relevant data that are needed for the study development are covered by intellectual property rights and so cannot be delivered (Jiménez-González et al., 2000). In addition to this, there is a tendency to express LCA results on a percentage scale: this obscures inventories which could instead increase the collective knowledge of the processes (Jiménez-González et al., 2014). These and other related obstacles have limited the spread of the methodology in the chemistry field, especially in the case of fine chemicals and bioproducts as noted by Tufvesson et al. (2013), and have inevitably LCA practitioners to narrow the system boundaries to the unit operations for which it is possible to perform data collection. This is validated by Salieri et al. (2018) and Gavankar et al. (2012) asserting that LCAs in the nanomaterial field do not often cover full life cycles and are often of the 'cradle-to-gate' or 'gate-to-gate' type.

This has contributed to creating a gap in LCAs of chemical products for leather manufacturing applications, as also indirectly evidenced by the review conducted. This gap must be filled in, as in this way there would be improved evaluation of environmental aspects that are relevant and representative of chemical systems like the one investigated in this study (Beghetto et al., 2019).

To the authors' knowledge, there exists only one LCA of a chemical formulation specifically designed for the tanning process which, moreover, does not even concern nanomaterials: it was conducted on the lab scale by Rosa et al. (2017) and deals exclusively with the production phase. The object of the study is represented by a new defatting formulation (for usage in the hide degreasing sub-process), that includes a substance derived from natural sources and a reduced percentage of ethoxylated alcohols with respect to those commonly found in commercial products. The study allowed Rosa et al. (2017) to highlight the hotspots along the life cycle considered and thus provide a basis for improvement of formulation. The study discussed in this paper is added to that of Rosa et al. (2017) and may contribute to filling the aforementioned gap, especially in reference to the narrower branch of innovative nanocomposites, through investigation of nano-HA production on the lab-scale. Based upon findings from the review conducted, the study can be considered as the first one in this specific field of research, which can be read as a sign of its novelty and its potential of enriching the specialised literature and knowledge.

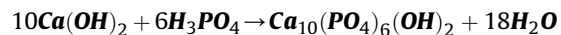
3. Materials and methods

3.1. Description of the lab-scale preparation process

Hydroxyapatite is an inorganic mineral that has been widely studied due to its chemical similarity with the mineral component of bones. In particular, it is present in the human body, in bones and teeth, and it represents the main constituent (about 50% of the dry weight of the bone matrix). The crystalline form has a reticular

structure (hexagonal structure, see SI) typical of apatites ($\text{Ca}_{10}(\text{PO}_4)_6(\text{OH})_2$) and, in its pure form, has a stoichiometric ratio Ca/P equal to 1.67. A classic preparation pathway reported was followed, according to Aina et al. (2012) and Sakhno et al. (2015), for the laboratory scale production of nano-HA. Commercially available reagents and solvents are used: calcium hydroxide ($\text{Ca}(\text{OH})_2$, Sigma-Aldrich, 96%), phosphoric acid (H_3PO_4 , Sigma-Aldrich, 85%), ammonium hydroxide solution (NH_4OH , Sigma Aldrich) and distilled water.

The reaction is a typical stoichiometric neutralisation reaction:



In particular, calcium hydroxide ($\text{Ca}(\text{OH})_2$) was stirred in distilled water, phosphoric acid (H_3PO_4) diluted in distilled water was added dropwise to the suspension. The pH was regulated by addition of ammonium hydroxide solution (NH_4OH), as necessary. After adding of all the acid solution, the suspension was left under stirring and, further, left still overnight in the mother solution.

The synthesised particles were then centrifuged (4000 rpm, 5 min), separated from supernatant, re-dispersed in water, and then centrifuged again in order to remove unreacted reagents (3 times, 4000 rpm, 5 min); finally, particles were oven-dried at 50 °C overnight or dried on air until removal of residual water; the reaction yield is 99.6%.

The washing water is treated with hydrochloric acid (HCl, Sigma-Aldrich, 37%) in order to neutralise the non-reacted hydroxide ammonium solution.

The prepared nano-HA at laboratory scale was used for the application on leather samples; the minimal required amount of nano-HA for the application to one leather sample (ca. 30 × 40cm) is ca. 8–10 g; each synthesis allows to produce ca.10 g. So, a few batches were prepared and for this reason, one of the important aspects to consider in the production of nano-HA, is the reproducibility of the procedure. For this sake, the detailed characterisation of all the prepared samples with High-Resolution Transmission Electron Microscopy (HR-TEM), X-ray Powder Diffraction (XRPD) and adsorption volumetry were performed (see details in the appendix).

3.2. Assessment of energy and environmental issues

Life Cycle Assessment is now accepted to be an environmental management tool for the holistic, systematic and multidisciplinary qualification and quantification of the environmental impacts and damages associated with the life of cycles of products and services (Pieragostini et al., 2016; Dassisti et al., 2016). Life Cycle Assessment was applied in this study according to the International Standards 14040 and 14044 (ISO, 2006) and so was articulated in the following phase: Goal and Scope Definition; Life Cycle Inventory (LCI); Life Cycle Impact Assessment (LCIA); and Life Cycle Interpretation. These phases are interlinked, with all of them playing key roles for the consistency of the study and for the reliability of the results obtained. The methodological application of each of those phases for the here-investigated system was addressed in the following sections.

3.2.1. Goal and scope definition

This study was conducted to address the environmental criticalities that are associated with synthetic chemistry for nano-HA preparation: for this purpose, LCA application was experienced on the lab scale, and was presented in this paper. This was done because the currently available literature acknowledges LCA as a valid tool to estimate, already at the design/lab phase, the environmental impact associated with wide range of products:

chemicals are amongst those. In particular, the system investigated was that of the preparation of nano-HA to be utilised as fireproof agent in leather products.

As part of this phase, the Functional Unit (FU) and the system boundaries were clearly defined following [Hischier and Walser \(2012\)](#), in collaboration with the chemistry-lab technicians who have given support to this author team for the LCA development. The FU is the key element that represents the unit of product and provides a reference through which inputs are linked to outputs and to the related impacts. The system boundaries establish which unit operations should be considered when assessing the life cycle of a product ([Arzoumanidis et al., 2013](#); [Ingrao et al., 2018a](#)). Those operations generally describe the extraction of resources, the production of materials and energy sources, and other processes characterising the system investigated. Included amongst those is the treatment of process wastes and of the main product when it reaches the end of its useful life ([Ingrao et al., 2018a](#)). Following previously published LCAs, both the FU and the system boundaries were defined in this study to: be consistent with the aim and scope of the study; best represent the system under investigation; facilitate data collection; and enable comparisons with equal function chemicals. Together with the lab technicians and following [Hischier and Walser \(2012\)](#), the FU was chosen considering the system service, that is, producing 10 g nano-Ha for finishing a given surface of leather sample, as reported in section 3.1 (ca. 30×40 cm).

The system boundaries were set at the lab exit-gate and included: the preparation of both input materials, auxiliaries and electricity from resource extraction; their transformation into the finished product (10 g nano-HA) through a set of steps including magnetic stirring, centrifugation, and drying. They can be found depicted in [Fig. 2](#).

3.2.2. Life Cycle Inventory

Life Cycle Inventory is accepted to be the core phase of any LCA, as it involves compilation, qualification and quantification of both input and output data which, then, are elaborated into environmental impacts and damages. So, it is understood that, without data availability, LCA is not doable, especially when it is of attributional type and so is oriented to system level decision ([Ekvall et al., 2016](#); [Ingrao et al., 2017](#)).

The inputs are represented by the materials and energy sources that are utilised in the system investigated, whilst the outputs are the material emissions in air, water and soil, as well as the exploitation of natural and primary-energy resources. For the LCA development, primary data were recorded in collaboration with the lab technicians, and regarded both inputs and outputs as associated with the synthesis process. This made it possible for the authors of this paper to have adequate access to the LCI data, as recommended by [Hischier and Walser \(2012\)](#). In particular, considering the great benefit of integrating LCA with scientifically-based information sources and calculation tools ([Pieragostini et al., 2016](#); [Dassisti et al., 2016](#)), the electricity consumed for magnetic stirring and centrifugation was measured during the process execution with the support of Scatol8®². [Fig. 3](#) shows the data that have been inventoried for the study development. In the figure, the amounts reported for NH_4OH (1.05 g) and HCl (2.85 g) correspond to 6 and 2.4 ml, respectively. This is the reason why the amount of discharge water is equal to 1032.4 ml, namely almost 1028 g. Additionally, the amount of discharge water contains an almost negligible quantity of chemical waste, which is represented by a 3.32 mg ensemble of unreacted substances ($\text{Ca}(\text{OH})_2$ and H_3PO_4). As shown in [Fig. 2](#), to make the whole water dischargeable and safe for human health, those substances were treated through a neutralisation process providing application of the aforementioned HCl . That is when it is disposed of in lab sinks, that convey it to the municipal sewer

system and, then, to the municipal wastewater treatment plant.

Transports for raw material supply were also accounted for and depicted in [Fig. 4](#): the transport flow was calculated and resulted to be equal to a total of 13.65 kgkm. In addition to this, from the figure there is evidence that no transport of ultra-pure water was accounted for, because the water is produced locally through a distillation plant serving all laboratories working within the Department of Chemistry of University of Turin (Italy). Therefore, the modelling of the life cycle of the distillation plant was excluded from the assessment due to the huge difficulty of collecting primary data to be referred to the laboratory in question and, then, to the synthesis process carried out within it. In addition to this, supportive secondary data were not found in Ecoinvent, nor the authors believed it was the case of using low-quality data for a simplified LCA of the distillation plant's life cycle, because that would have meant compromising the reliability of the entire assessment. By the way, negligible uncertainties in the results are expected, because negligible (compared with the other input items of the investigated system) is expected to be the environmental impact of the share of distillation plant associated with the synthesis activity of the laboratory considered in this study.

For the study development, secondary data were used to model the production of those material and energy inputs. This was done by extrapolating them from database of acknowledged scientific relevance and value, as is Ecoinvent. In this study, those data were represented by the production of the raw materials depicted in [Fig. 2](#) and of the related transports ([Fig. 4](#)), and were modelled by accessing the Ecoinvent database: the modules were reported in [Table 1](#).

As shown in [Table 1](#), the NH_4OH was modelled as liquid ammonia (NH_3) through the related module contained in Ecoinvent: a different amount was used, however, for the assessment. It was calculated considering that, based upon information provided by the lab technicians, the NH_3 content in the NH_4OH is 28%. In the light of this, a consumption value of 0.294 g was calculated and assigned to the ammonia production module.

3.2.3. Life Cycle Impact Assessment

This phase was developed according to [De Benedetto and Klemes \(2009\)](#) by aggregating the material output flows (emitted substances and resources consumed), already quantified in the LCI phase, in a limited set of 'midpoint categories', also known as Impact Categories (ICs). The next step was about grouping the aforementioned ICs into Damage Categories (DCs), with the latter representing the quality changes which the life cycle of the product causes to the environment ([Jolliet et al., 2003](#); [Ingrao et al., 2019 a,b](#)). A generalised version of the assessment framework was depicted in [Fig. 5](#), using [Jolliet et al. \(2003\)](#).

It can, so, be asserted that the ICs are the environmental aspects through which the output inventories affect the DCs. For instance, by looking at [Fig. 5](#) it is understood that S_1 , S_2 , and S_3 flow into IC_a which is one amongst the ICs that are associated with DC_a . By doing so, those substances get allocated to – and so damage – DC_a , along with the ensemble of substances that are allocated to IC_b and IC_c .

For this study, the LCIA was extended to the 'endpoint approach', that is, by considering the phases of 'normalisation' and 'weighing'.

So, the allocation framework shown in [Fig. 5](#), and the related step-by-step conversion factors (from characterisation to weighing, passing through damages-assessment and normalisation) are clearly dependent from the LCIA method that is decided to use. To carry out this study, the authors used the one provided by Impact 2002+, as implemented and described by [Jolliet et al. \(2003\)](#).

In the midpoint approach, equivalent indicators were used to quantify LCIA results in the form of specific characterisation values; these were expressed as: kgCO_2 eq for 'Global Warming'; MJ primary

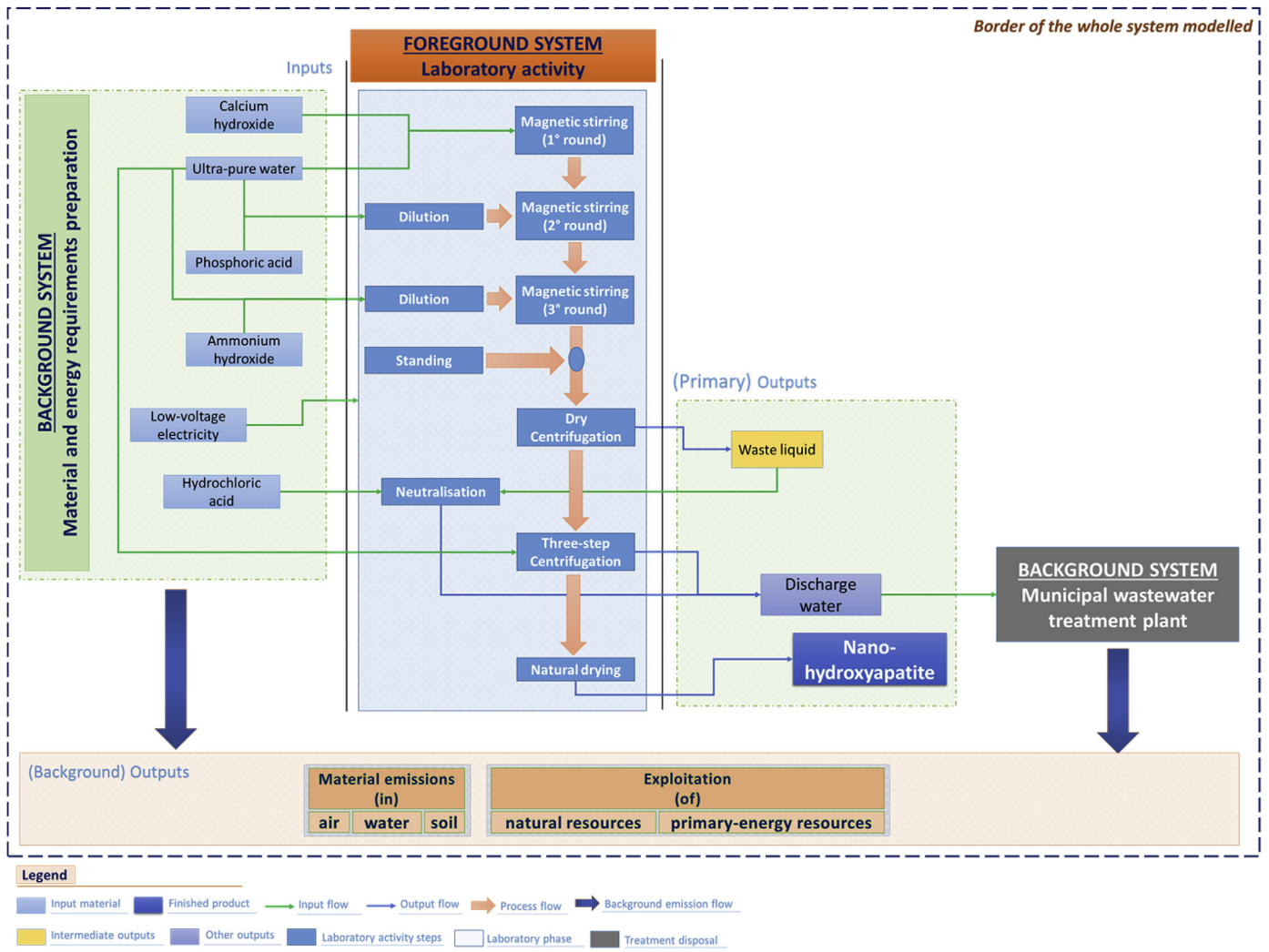


Fig. 2. The figure shows boundaries of the system that has been assessed in this study.

for 'Non-renewable Energy'; and kgPM_{2.5}, eq for 'Respiratory Inorganics'.

As a standardised practice in LCA, end-weighting was based upon estimation of results from the study, through equivalent numerical parameters that are known as 'weighing points' or 'damage points' or 'eco-points' or, more simply, 'points'. End-weighting has always been an issue of controversy (López-Mesa et al., 2009) because, as De Benedetto and Klemes (2009) indicate, it is not always based upon science, but often upon social or political considerations. However, it was used in this study because, according to Ingrao et al. (2018b), it enables practitioners to represent quantitatively the environmental damage overall associated with a given system favouring, in turn, comparison amongst systems, on the same point scale.

The endpoint analysis was then narrowed to the damage point associated with each and every background material and energy commodity utilised, and with both the emission of pollutants and the exploitation of primary-energy resources. This made it possible to highlight the most environmentally burdening ones, as the base to find room for improvement, in line with the objectives of this study.

Finally, the end-weighting results were reported also in reference to both ICs and DCs, so making it possible to identify the most

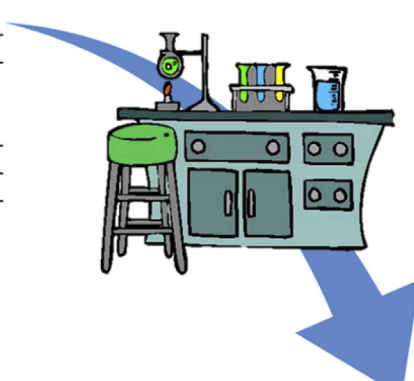
important ones on a unique point scale and, hence, the most representative of the system investigated.

4. Results and discussions

The endpoint LCIA showed the environmental damage associated with the system investigated to be quantified in 37.18 μ pt, with the highest contributions staying in the production and consumption of electricity (23.345 μ pt) and in the production of H₃PO₄ (9.304 μ pt), as both demanded for the process, and in the transport mix for acquisition of all chemical substances utilised (2.564 μ pt); these three items contributed together 94.71% of the total environmental damage. With regard to production of the chemicals utilised, H₃PO₄ is the most environmentally harmful one, whilst far lesser contributions were found in the production of Ca(OH)₂, HCl, and NH₃, equal to a total of 1.276 μ pt, which is just 3.43% of the total damage. On average, such should be attributed mainly to the combined effect of the little amounts in stake of those substances and of the environmental impact associated with the specific production processes on equal amount of substance produced.

Results per DCs from the endpoint phase were shown in Table 2 in the terms of damages-assessment values and were graphed in Fig. 6 as weighing points.

ITEM	QUANTITY	UNIT
INPUTS		
<i>Raw materials</i>		
Calcium hydroxide +	14.33	g
Phosphoric acid (85%) Ultra-pure water	424	g
<i>Auxiliairies</i>		
Hydro	1.05	g
Ultra-pure water	600	g
Hydrochloric acid	2.85	g
<i>Energy</i>		
Low-voltage electricity	127.61	Wh



ITEM	QUANTITY	UNIT
OUTPUTS		
<i>Finished product (FU of the study)</i>		
Nano-hydroxyapatite	10	g
<i>Waste streams</i>		
Discharge water (to municipal wastewater treatment)	1027.9	g

Fig. 3. In the figure, there can be found depicted the inventory dataset that has been used for the environmental impact assessment.

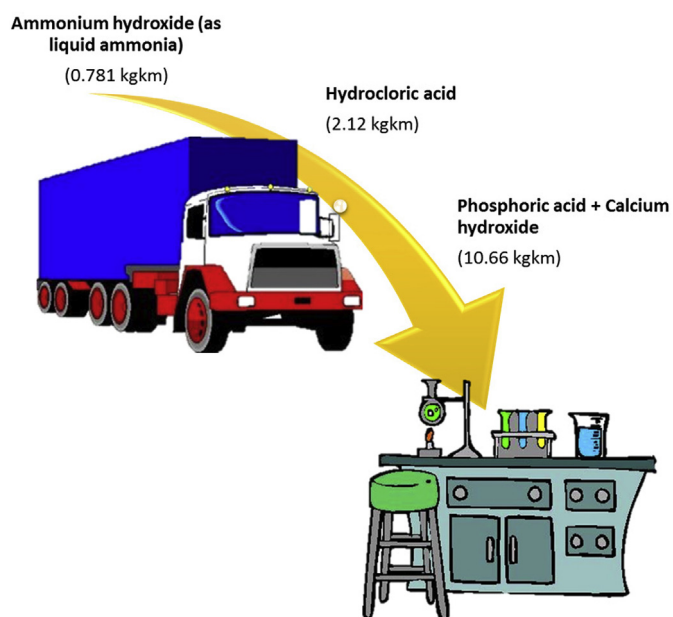


Fig. 4. In the figure, all flows related to raw material supply to the lab were depicted.

From the figure, it is confirmed that, along with H_3PO_4 production, the major environmental impacts stay in the electricity consumption, and in the road transports for the acquisition of all the chemical substances utilised in the process. So, there is evidence that, in the light of their environmental relevancy, these two items cannot be neglected for creation of reliable models of lab-

scale processes. However, their accounting could tend to divert the focus of the analysis from the process core-substances, mainly because of the little amounts in stake as a classic of synthesis processes. Just think that, the damage caused by electricity consumption is nearly two times and a half bigger already than the production of the most impactful substance, namely phosphoric acid.

Furthermore, from Fig. 6 it can be concluded that the most affected damage categories are, in line with the inventory dataset, 'Human health' (HH), 'Resources' (R), and 'Climate change' (CC), with damage values equal to a total of 12.39, 11.688, and 11.19 μ pt. 'Ecosystem Quality' (EQ) is the DC suffering the lowest damage, as the latter resulted in a value of 2.059 μ pt.

The end-weighting assessment was extended to the most environmentally damaging: material emissions (in air, and soil) striking DCs like 'Climate Change', 'Human Health' and 'Ecosystem Quality'; and primary-energy resources affecting the damage category 'Resources'. These were extrapolated from the output inventory pack of the system investigated, and were reported in Table 3. They are the output streams that most largely contribute to the damage value associated with the membership DCs, and so were considered by this author team as highly representative of the lab process under study. This is proven, indeed, by their overall incidences being: 97.16% for 'Resources'; 97.79% for 'Climate Change'; 94.78% for 'Human Health'; and 84.29% for 'Ecosystem Quality'. In this damage category, the percentage contribution is lower than the others, because higher is the number of damaging substances and so more distributed is its total damage (2.059 μ pt), with many slightly or negligibly contributing environmental aspects.

Average contributions to the damage from the three most impacting processes were calculated based upon values of Table 3

Table 1

In this table, the main Ecoinvent modules used for the modelling of the system were listed along with the related descriptions.

Input item	Ecoinvent module	Dataset description
	Modelled as	
Calcium hydroxide	Lime, hydrated, packed {RoW} production Alloc Def, S	The dataset includes processes like milling, sieving, filtering, packing, and storing
Phosphoric acid	Phosphoric acid, industrial grade, without water, in 85% solution state {RER} purification of wet-process phosphoric acid to	This module refers to concentration of acid after purification to 85% H3PO4 content. The dataset includes raw materials, processing chemicals and processing energy, direct emissions to water from process, disposal of solid process waste to landfill and of spent solvent to incineration, estimations on of raw materials transport to the plant.
Ultra-pure water	Water, ultrapure {RoW} production Alloc Def, S	The module refers to production of ultrapure water including materials, energy uses, infrastructure and emissions.
Ammonium hydroxide	Ammonia, liquid {RoW} ammonia production, steam reforming, liquid Alloc Def, S	The dataset considers the manufacturing process starting with natural gas, air and electricity, plus auxiliaries, energy, transportation, infrastructure and land use, as well as wastes and emissions into air and water. Transport of the raw materials, auxiliaries and wastes is included, whilst the delivery phase of the finished product is not incorporated in the module, mainly because it was considered as pertaining to the downstream utilisation.
Hydrochloric acid	Hydrochloric acid, without water, in 30% solution state {RER} benzene chlorination Alloc Def, S	The module provides production of hydrochloric acid, in 30% solution state, from benzene chlorination; the dataset includes materials, energy uses, infrastructure and emissions.
Electricity	Electricity, low voltage transformation from medium to low voltage Alloc Def, S	This dataset describes the transformation from medium to low voltage as well as the distribution of electricity at low voltage. Included are the electricity production in Italy and from imports, the transmission network as well as direct SF6-emissions to air. Electricity losses during low-voltage transmission and transformation from medium-voltage are accounted for.
Transport mean	Transport, freight, lorry 3.5–7.5 metric ton, EURO 5 {RER} transport, freight, lorry 3.5–7.5 metric ton, EURO 5 Alloc Def, S	Inventory refers to the entire transport life cycle. For road infrastructure, expenditures and environmental interventions due to construction, renewal and disposal of roads have been allocated based on the Gross tonne kilometre performance. Expenditures due to operation of the road infrastructure, as well as land use have been allocated based on the yearly vehicle kilometre performance. For the attribution of vehicle share to the transport performance a vehicle life time performance of 540000 vkm/vehicle has been assumed. Included processes are the followings: operation of vehicle; production, maintenance and disposal of vehicles; construction and maintenance and disposal of road.

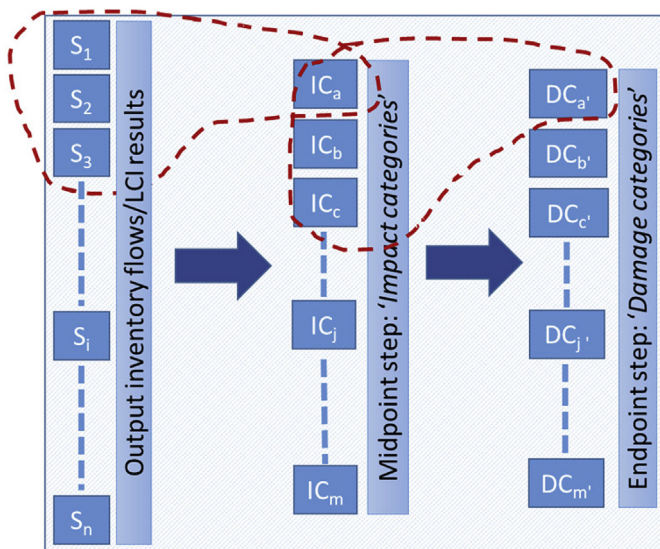


Fig. 5. The figure shows a generalised version of the LCIA framework, that was elaborated by the authors using the relevant information pack contained in Jolliet's et al. (2003). Aside from the LCI, CI and DI acronyms that have already been given in the text, 'S' refers to the given substance emitted or resource consumed.

and were reported in Table 4 for each DC. From Table 4 there is evidence that, for electricity consumption, comparable incidences were found for R, CC, and EQ, whilst a lower value (41.20%) was recorded for HH. This is because ion-arsenic emission is the item, amongst those affecting HH, as listed in Table 3, to be generated by electricity consumption only for 1.46% and, almost entirely (nearly 97%) by H₃PO₄ production. The latter explains the higher contribution to damage (47.94%) exhibited by H₃PO₄ production for HH

Table 2

This table shows 'Damages assessment' values for each damage category considered. Values were extrapolated from Impact 2002 + LCIA, as referred to FU of the system.

Damage category	Damage-assessment	
	Value	UM
Human health	8.68E-8	DALY
Climate change	110.791	kg CO ₂ eq
Resources	1.776	Primary-energy MJ
Ecosystem quality	0.0282	PDF m ² y

compared with the other damage categories, for which more or less comparable percentages were recorded (8.57%–15.67%).

Finally, the freight-transport mix affects the four DCs with relatively close values, especially for HH, R, and CC. The highest value in correspondence to EQ should be attributed to major contribution (49.72%) of the transport mix to the emission of zinc into soil.

From Table 4, it is confirmed that those are the most environmentally relevant items of the synthesis process investigated, with overall contributions to damage in the range of 82%–95%. The lowest one is for EQ, because for this DC the contribution made by the total of the other items is largely higher (17.74%) than that for the other DCs (5.02%–5.56%, as shown in Table 4). This is 15% of the damage associated with EQ (2.059 µpt) is due to the treatment of the discharge water generated by the process that, however, is not relevant for the other DCs.

Each of the substances reported in Table 3 was addressed in terms of output inventory amount, and characterisation and damages assessment: values were extrapolated from the LCIA conducted in Simapro using Impact 2002+, and were reported in Table 5.

Considering results shown in Table 5, it seems that the most environmentally relevant ICs are 'Non-renewable Energy', 'Global

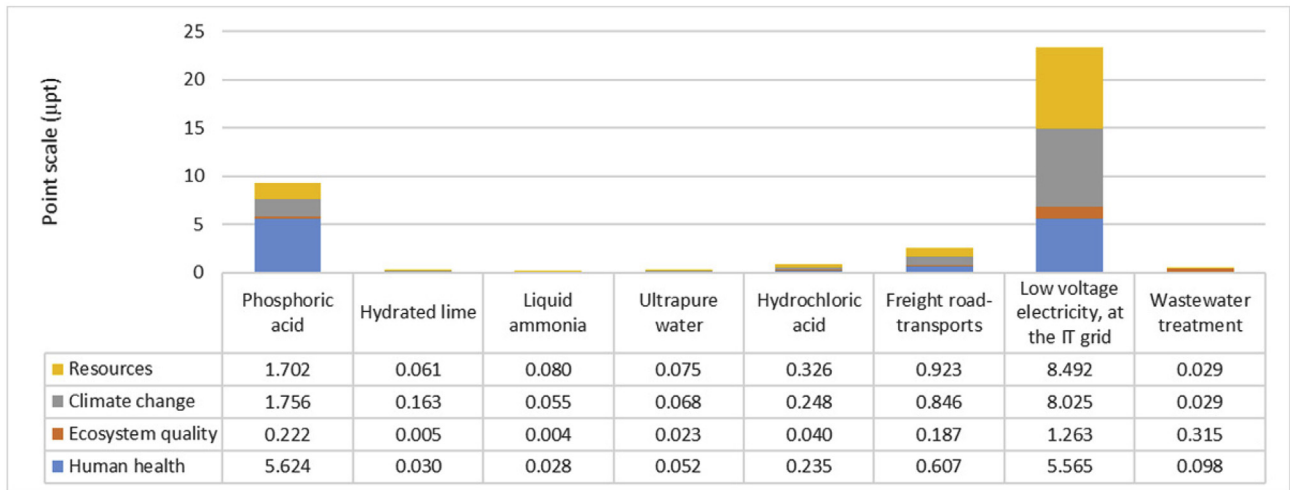


Fig. 6. In the figure, weighing results per damage category were reported on a μpt scale.

Table 3

Results from the weighing step as related to the most environmentally damaging emitted substances and resources consumed, compared to the total damages associated with the related affected damage categories. Those can be clearly obtained by summing up the contributions from the included substances: those highlighted and the minor ones hidden in the category 'Others'.

Emitted substance	Emission compartment	TOTAL Lab process phases								
		Phosphoric acid	Hydrated lime	Liquid ammonia	Ultrapure water	Hydrochloric acid	Freight transport mix	Low voltage electricity	Wastewater treatment	
Weighing points ($\mu\text{pt}/\text{FU}$)										
CLIMATE CHANGE										
Carbon dioxide, fossil	Air	10.94	1.715	0.161	0.054	0.067	0.241	0.829	7.85	0.026
Others		0.25	0.041	2.094E-03	1.095E-03	1.321E-03	6.771E-03	0.0175	0.175	2.998E-03
HUMAN HEALTH										
Sulphur dioxide	Air	5.140	2.901	0.006	0.005	0.014	0.067	0.068	2.069	0.010
Nitrogen oxides		3.125	0.590	0.014	0.008	0.014	0.059	0.340	2.085	0.017
Particulates, with grain size < 2.5 μm		2.280	0.942	0.008	0.012	0.016	0.074	0.144	1.075	0.009
Arsenic, ion	Water	1.057	1.024	1.48E-04	1.85E-04	0.001	0.007	0.005	0.015	0.004
Others	Air/water/soil	0.638	0.17	2.15E-03	3.76E-03	0.01	0.03	0.05	0.32	0.06
ECOSYSTEM QUALITY										
Copper	Soil	0.501	6.169E-03	8.943E-05	3.831E-05	4.952E-04	2.756E-03	4.663E-03	4.530E-01	3.373E-02
Aluminium		0.376	2.553E-02	7.868E-04	1.321E-03	5.197E-04	7.555E-03	2.458E-02	1.224E-01	1.937E-01
Aluminium	Air	0.296	5.087E-02	2.621E-03	4.762E-04	1.238E-03	8.402E-03	6.107E-03	2.256E-01	9.864E-04
Chromium	Soil	0.236	2.456E-03	4.279E-05	1.698E-05	2.455E-04	9.229E-04	7.823E-04	2.313E-01	3.819E-04
Zinc		0.222	1.410E-02	2.185E-04	1.732E-04	2.407E-04	3.370E-03	1.104E-01	1.775E-02	7.582E-02
Nitrogen oxides	Air	0.104	1.955E-02	4.564E-04	2.603E-04	4.592E-04	1.969E-03	1.126E-02	6.913E-02	5.490E-04
Others	Air/water/soil/resources	0.324	0.103	1.249E-03	1.428E-03	1.977E-02	1.475E-02	2.945E-02	0.144	9.843E-03
RESOURCES										
Natural gas	Resources	5.713	0.556	0.005	0.057	0.014	0.070	0.072	4.394	0.004
Crude oil		3.041	0.557	0.049	0.020	0.007	0.051	0.739	1.613	0.006
Hard coal		1.712	0.226	8.10E-04	1.35E-03	1.46E-02	5.87E-02	3.52E-02	1.371	4.53E-03
Uranium		1.429	0.254	5.140E-03	1.433E-03	2.799E-02	0.101	6.573E-02	0.962	1.243E-02
Others		0.332	0.108	5.171E-04	6.678E-04	1.236E-02	4.527E-02	1.117E-02	0.152	1.512E-03

Table 4

The average contributions to damage exhibited by the three most damaging items within the synthesis process investigated were calculated based upon values of Table 2 and were shown in this table per each DC considered. The percentage associated with the 'other items of the system' were extrapolated by difference.

DC	Total damage (μpt)	Most impacting items in the synthesis process investigated			
		Electricity consumption	Phosphoric acid production	Freight-transport mix	Other items of the systems
Average contribution to damage (%)					
Human health	12.39	41.20	47.94	5.38	5.48
Resources	11.688	71.34	15.01	8.09	5.56
Climate change	11.19	71.74	15.67	7.57	5.02
Ecosystem quality	2.059	61.95	8.57	11.74	17.74

Table 5
In this table, substances and resources from Table 3 were classified based upon: amounts from output inventory analysis; characterisation; and damages assessments. All values reported were referred to the FU of the system investigated, namely 10 g nano-HA.

Substance/resource	Emission compartment	Output inventory		Characterisation		IC	Damages assessment		DC
		Amount	UM	Value	UM eq		Value	UM eq	
Aluminium	air	3.959	mg	1.953	kg TEG water	Aquatic ecotoxicity	0.00406	PDF*m ² *y	EQ
Aluminium	soil	835.232	µg	0.501	kg TEG soil	Terrestrial ecotoxicity	0.00516	PDF*m ² *y	
Arsenic, ion	water	23.389	µg	2.92	kg TEG water	Aquatic ecotoxicity	7.49E-9	DALY	HH
				0.633	kg TEG soil	Terrestrial ecotoxicity			
				0.00244	kg C ₂ H ₃ Cl	Non-carcinogens			
				0.000235		Carcinogens			
Carbon dioxide, fossil	air	108.341	g	108.341	g CO ₂	Global warming	108.341	g CO ₂	CC
Chromium	soil	3.931	µg	0.00176	kg TEG water	Aquatic ecotoxicity	6.99E-5	PDF*m ² *y	EQ
				0.00883	kg TEG soil	Terrestrial ecotoxicity			
Copper	soil	122.978	µg	2.514	kg TEG water	Aquatic ecotoxicity	0.00686	PDF*m ² *y	
				0.852	kg TEG soil	Terrestrial ecotoxicity			
Crude oil	resources	10.092	g	0.462	Primary-energy	Non-renewable Energy	0.462	Primary-energy	R
Hard coal		13.626	g	0.26	MJ		0.26	MJ	
Natural gas		19.506	dm ³	0.786			0.786		
Nitrogen oxides	air	248.757	mg	3.17E-5	kg PM _{2.5}	Respiratory inorganics	2.22E-8	DALY	HH
				0.00137	kg SO ₂	Terrestrial acidification/nitrification	0.00142	PDF*m ² *y	EQ
				0.000174		Aquatic acidification			
Particulates, with grain size < 2.5 µm	air	23.097	mg	2.31E-5	kg PM _{2.5}	Respiratory inorganics	1.62E-8	DALY	HH
Sulphur dioxide	air	667.606	mg	5.21E-5			3.65E-8		
Uranium	resources	387.966	µg	0.217	Primary-energy	Non-renewable Energy	0.217	Primary-energy	R
					MJ			MJ	
Zinc	soil	64.952	µg	0.0907	kg TEG water	Aquatic ecotoxicity	0.00304	PDF*m ² *y	EQ
				0.384	kg TEG soil	Terrestrial ecotoxicity			

Table 6

In this table, the ICs being most environmentally relevant of the system investigated were reported, based upon results from characterisation (midpoint) and weighing (endpoint). All values reported were referred to the system's FU.

Impact category	Weighing		Characterisation	
	Mpt		Value	UM eq
Non-renewable energy	11.680		1.775	Primary-energy MJ
Global warming	11.190		0.111	kg CO ₂ eq
Respiratory inorganics	10.578		1.072E-4	kg PM _{2.5} eq
Terrestrial ecotoxicity	1.814		3.142	kg TEG soil
Non-carcinogens	1.269		3.214E-3	kg C ₂ H ₃ Cl eq
Carcinogens	0.311		7.887E-4	
Terrestrial acidification/nitrification	0.158		2.075E-3	kg SO ₂ eq

Warming', 'Respiratory Inorganics', 'Terrestrial Ecotoxicity', 'Non-Carcinogens', 'Carcinogens', and 'Terrestrial acidification/nitrification': these were detailed with results both at the endpoint and midpoint level (Table 6). In this regard, it should be underscored that, though appearing in Table 5, 'Aquatic ecotoxicity' was not included in that field of ICs and so cannot be found in Table 6, because, based upon endpoint results, its damage point was far lower than those of the ICs considered. Furthermore, it should be observed that, as also pointed out by Ingrao et al. (2019b), 'Aquatic acidification' is a midpoint indicator only and, so, does not take part in the damage-oriented evaluation that characterises the endpoint

approach. This means that the damage value associated with 'Nitrogen oxides' (0.00142 PDF*m²*y) was obtained through elaboration just of the characterisation result related just to its impact to 'Terrestrial acidification/nitrification'.

To complement results shown in Table 6, Fig. 7 was elaborated to report on the association between the impact categories contemplated by the method and the material and energy items composing the synthesis process investigated.

According to this author team, the output inventory pack presented and discussed thus far can be considered as environmental aspects being highly significant and representative of the system investigated. Therefore, they could serve as the starting base to identify environmental impact indicators that can be used for potential development and improvement of labelling systems.

Finally, results are more or less in line with the subject literature as reviewed in section 2 of this manuscript and, in particular, with Rosa et al. (2017), in terms of main impacting items (e.g. input material production, energy source, and transport), and main impact and damage categories. Differences may be found as resulting from different chemical products investigated, different methodological aspects, and different background conditions.

² Scatol8 per la Sostenibilità srl (briefly, Scatol8 srl) is an academic spin-off of the University of Turin and an innovative start-up of Regione Piemonte. It works in the fields of clean technologies along with of energy and environmental monitoring. Its activity concerns the development, production and marketing of innovative products and services with a high technological value, and more specifically the development, production and marketing of integrated electronic systems and networks for the collection of variables - in particular environmental - and data analysis through intelligent dashboard, primarily intended as for agricultural, commercial and industrial activities. Additional information is available at: <http://scatol8.net/>.

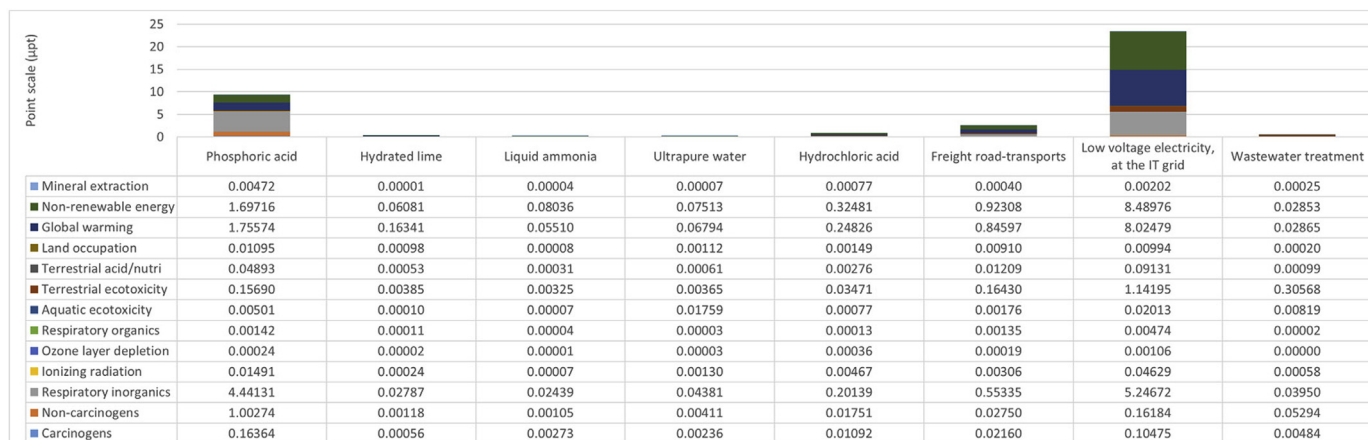


Fig. 7. In the figure, weighing results per impact category were reported on a μpt scale.

5. Conclusions and future perspectives

Over the course of the last years, the leather sector has been increasingly expanding to meet new challenging requests from sectors like those business-to-business and business-to-commerce: developing water and fireproof leather commodities is one of those. This paper is focussed upon assessing the environmentally damaging impacts of a chemical formulation designed on the lab scale to give fire resistance to leather products, with the final aim of orienting industrial production towards sustainability. The innovation must contribute to reduction of the economic and environmental costs of the production process, whilst improving the overall quality and functionality of the product. In line with the framework suggested by Piccinno et al. (2016, 2018), lab-scale assessments are the first step towards industrialisation, and are recommended to test any innovation, especially when a set of feasible alternatives is available. From this perspective, the study here-presented is one of the fews (e.g., Rosa et al., 2017) on application of LCA to lab-scale chemistry processes. In particular, it investigates the synthesis of nano-HA useable in the tannery industry with finishing and tanning functions. Based upon findings from the study, electricity consumption, H_3PO_4 production, as well as the transports for acquisition of the chemicals utilised in the processes, are the three most environmentally damaging items. From laboratory to industrial scale, electricity consumption and transport may have a not-fully proportional impact compared with the increase in the quantity of chemicals. This awareness, based upon LCIA results may lead to foster more attention paid upon H_3PO_4 supply chain rather than upon electricity consumption, in terms of making strategies oriented to process optimisation and innovation.

The study is the first essential step of a full research designed by the authors to investigate the field of nano-materials in the tannery sector on the lab- and industry scale, in comparison with preparation of nano-HA particles using organic wastes like eggshell and fish bones. The comparative assessment will be then extended to conventional flame-retardants as currently available in the market.

CRedit authorship contribution statement

Carlo Ingrao: Conceptualization, Investigation, Methodology, Data curation, Software, Supervision, Writing - original draft. **Enrica Vesce:** Conceptualization, Investigation, Methodology, Data curation, Writing - original draft. **Rosalia S. Evola:** Conceptualization, Investigation, Methodology, Data curation, Writing - original

draft. **Erica Rebba:** Investigation, Methodology, Data curation, Writing - original draft. **Claudia Arcidiacono:** Writing - review & editing. **Gianmario Martra:** Writing - review & editing. **Riccardo Beltramo:** Writing - review & editing.

Declaration of competing interest

The authors declare that they have no known competing financial interests or personal relationships that could have appeared to influence the work reported in this paper.

Acknowledgements

This work is the result of the project “Nanomaterials for sustainable leather products (NanoSusLeather)” funded by Compagnia di San Paolo, Progetto di Ateneo 2016 (CSTO 165920 - Linea 2). In this regard, the authors wish to thank Kemia Tau S.r.L. for being part of the project and for supporting its development by providing all the information and data needed for the environmental modelling and assessment.

The study was developed under the agreement signed between the Department of Management of University of Turin, and the Department of Agriculture, Food and Environment (Di3A) of University of Catania.

Appendix A. Supplementary data

Supplementary data to this article can be found online at <https://doi.org/10.1016/j.jclepro.2020.123837>.

References

- Acharya, R., Naik, B., Parida, K.M., 2018. Adsorption of Cr (VI) and textile dyes on to mesoporous silica, titanate nanotubes, and layered double hydroxides. *Nanomater. Wet Process. Textiles* 219–260.
- Aina, V., Lusvardi, G., Annaz, B., Gibson, I.R., Imrie, F.E., Malavasi, G., Menabue, L., Cerrato, G., Martra, G., 2012. Magnesium- and strontium-co-substituted hydroxyapatite: the effects of doped-ions on the structure and chemico-physical properties. *J. Mater. Sci. Mater. Med.* 23 (12), 2867–2879.
- Arbolino, R., Boffardi, R., Ioppolo, G., 2020. An insight into the Italian chemical sector: how to make it green and efficient. *J. Clean. Prod.* 264, 121674.
- Arzoumanidis, I., Petti, L., Raggi, A., Zamagni, A., 2013. Life cycle assessment for the agri-food sector. In: Salomone, R., Clasadonte, M.T., Proto, M., Raggi, A. (Eds.), *Product-oriented Environmental Management Systems (POEMS)*. Springer Science+Business Media, Dordrecht, The Netherlands, pp. 105–122.
- Beghetto, V., Agostinis, L., Gatto, V., Samiolo, R., Scrivanti, A., 2019. Sustainable use of 4-(4, 6-dimethoxy-1, 3, 5-triazin-2-yl)-4-methylmorpholinium chloride as metal free tanning agent. *J. Clean. Prod.* 220, 864–872.
- Costa, L.G., Giordano, G., Tagliaferri, S., Caglieri, A., Mutti, A., 2008. Polybrominated

- diphenyl ether (PBDE) flame retardants: environmental contamination, human body burden and potential adverse health effects. *Acta Biomed.* 79 (3), 172–183.
- Darnerud, P.O., 2003. Toxic effects of brominated flame retardants in man and in wildlife. *Environ. Int.* 29 (6), 841–853.
- Dassisti, M., Intini, F., Chimienti, M., Starace, G., 2016. Thermography-enhanced LCA (Life Cycle Assessment) for manufacturing sustainability assessment. The case study of an HDPE (High Density Polyethylene) net company in Italy. *Energy* 108, 7–18.
- De Benedetto, L., Klemes, J., 2009. The Environmental Performance Strategy Map: an integrated LCA approach to support the strategic decision-making process. *J. Clean. Prod.* 17, 900–906.
- Dixit, S., Yadav, A., Dwivedi, P.D., Das, M., 2015. Toxic hazards of leather industry and technologies to combat threat: a review. *J. Clean. Prod.* 87, 39–49.
- Ershad-Langroudi, A., Mirmontahai, A., 2013. Hydroxyapatite nanoparticles and polyethylene glycol treatment of historical leather—mechanical properties. *J. Am. Leather Chem. Assoc.* 108 (12), 449–456.
- Ershad-Langroudi, A., Mirmontahai, A., 2015. Thermal analysis on historical leather bookbinding treated with PEG and hydroxyapatite nanoparticles. *J. Therm. Anal. Calorim.* 120 (2), 1119–1127.
- Ekvall, T., Azapagic, A., Finnveden, G., Rydberg, T., Weidema, B.P., Zamagni, A., 2016. Attributional and consequential LCA in the ILCD handbook. *Int. J. Life Cycle Assess.* 21, 293–296.
- European Commission EC, 2011. Commission recommendation 2011/696/EU, of 18 October 2011, on the definition of nanomaterial. *Off. J. European Union L275*, 38–40.
- Gavankar, S., Suh, S., Keller, A.F., 2012. Life cycle assessment at nanoscale: review and recommendations. *Int. J. Life Cycle Assess.* 17 (3), 295–303.
- Gbededo, M.A., Liyanage, K., Garza-Reyes, J.A., 2018. Towards a Life Cycle Sustainability Analysis: a systematic review of approaches to sustainable manufacturing. *J. Clean. Prod.* 184, 1002–1015.
- Hischier, R., Hellweg, S., Capello, C., Primas, A., 2005. Establishing life cycle inventories of chemicals based on differing data availability. *Int. J. Life Cycle Assess.* 10 (1), 59–67.
- Hischier, R., Walsler, T., 2012. Life cycle assessment of engineered nanomaterials: state of the art and strategies to overcome existing gaps. *Sci. Total Environ.* 425, 271–282.
- Ingrao, C., Facchiongo, N., Di Gioia, L., Messineo, A., 2018b. Food waste recovery into energy in a circular economy perspective: a comprehensive review of aspects related to plant operation and environmental assessment. *J. Clean. Prod.* 184, 869–892.
- Ingrao, C., Facchiongo, N., Valenti, F., De Pascale, G., Di Gioia, L., Messineo, A., Arcidiacono, C., 2019b. Tomato puree in the Mediterranean region: an environmental Life Cycle Assessment, based upon data surveyed at the supply chain level. *J. Clean. Prod.* 233, 292–313.
- Ingrao, C., Gigli, M., Siracusa, V., 2017. An attributional Life Cycle Assessment application experience to highlight environmental hotspots in the production of foamy polylactic acid trays for fresh-food packaging usage. *J. Clean. Prod.* 150, 93–103.
- Ingrao, C., Licciardello, F., Pecorino, B., Muratore, G., Zerbo, A., Messineo, A., 2018a. Energy and environmental assessment of a traditional durum-wheat bread. *J. Clean. Prod.* 171, 1494–1509.
- Ingrao, C., Selvaggi, R., Valenti, F., Matarazzo, A., Pecorino, B., Arcidiacono, C., 2019a. Life cycle assessment of expanded clay granulate production using different fuels. *Resour. Conserv. Recycl.* 141, 398–409.
- International Union of Leather Technologists and Chemists Societies IULTCS, 2018. IUE Environment documents. Available at: <http://www.iultcs.org/environment-ue.php> (accessed: Jan-Mar 2020).
- Jiang, Y., Li, J., Li, B., Liu, H., Li, Z., Li, L., 2015. Study on a novel multifunctional nanocomposite as flame retardant of leather. *Polym. Degrad. Stabil.* 115, 110–116.
- Jiménez-González, C., Kim, S., Overcash, M.R., 2000. Methodology for developing gate-to-gate life cycle inventory information. *Int. J. Life Cycle Assess.* 5 (3), 153–159.
- Jiménez-González, C., Overcash, M.R., 2014. The evolution of life cycle assessment in pharmaceutical and chemical applications – a perspective. *Green Chem.* 16 (7), 3392–3400.
- Jolliet, O., Manuele, M., Raphael, C., Sebastian, H., Jerome, P., Gerald, R., Rosenbaum, R., 2003. Impact 2002p: a new life cycle impact assessment methodology. *Int. J. Life Cycle Assess.* 8, 324–330.
- Joseph, K., Nithya, N., 2009. Material flows in the life cycle of leather. *J. Clean. Prod.* 17 (7), 676–682.
- Krishnamoorthy, G., Sadulla, S., Sehgal, P.K., Mandal, A.B., 2013. Greener approach to leather tanning process: D-Lysine aldehyde as novel tanning agent for chrome-free tanning. *J. Clean. Prod.* 42, 277–286.
- T. López-Mesa, B., Pitarch, Á., Tomás, A., Gallego, T., 2009. Comparison of environmental impacts of building structures with in situ cast floors and with precast concrete floors. *Build. Environ.* 44, 699–712.
- Ma, J., Lv, X., Gao, D., Li, Y., Lv, B., Zhang, J., 2014. Nanocomposite-based green tanning process of suede leather to enhance chromium uptake. *J. Clean. Prod.* 72, 120–126.
- Mani, M., Wheeler, D., 1998. In search of pollution havens? Dirty industry in the world economy, 1960 to 1995. *J. Environ. Dev.* 7 (3), 215–247.
- Muñoz, I., 2012. LCA in Green Chemistry: a new subject area and call for papers. *Int. J. Life Cycle Assess.* 17, 517–519.
- Mwinyihija, M., 2010. Main pollutants and environmental impacts of the tanning industry. In: Mwinyihija, M. (Ed.), *Ecotoxicological Diagnosis in the Tanning Industry*. Springer, Cham, pp. 17–35.
- Notarnicola, B., Puig, R., Raggi, A., Fullana, P., Tassielli, G., De Camillis, C., Rius, A., 2011. Life cycle assessment of Italian and Spanish bovine leather production systems. *Afinidad* 68 (553), 167–180.
- Pallas, G., Peijnenburg, W.J., Guinée, J.B., Heijungs, R., Vijver, M.G., 2018. Green and clean: reviewing the justification of claims for nanomaterials from a sustainability point of view. *Sustainability* 10 (3), 689.
- Piccinno, F., Hischier, R., Seeger, S., Som, C., 2016. From laboratory to industrial scale: a scale-up framework for chemical processes in life cycle assessment studies. *J. Clean. Prod.* 135, 1085–1097.
- Piccinno, F., Hischier, R., Seeger, S., Som, C., 2018. Predicting the environmental impact of a future nanocellulose production at industrial scale: application of the life cycle assessment scale-up framework. *J. Clean. Prod.* 174, 283–295.
- Pieragostini, C., Mussati, M.C., Aguirre, P., 2016. On process optimization considering LCA methodology. *J. Environ. Manag.* 96 (1), 43–54.
- Rivela, B., Moreira, M.T., Bornhardt, C., Méndez, R., Feijoo, G., 2004. Life Cycle Assessment as a tool for the environmental improvement of the tannery industry in developing countries. *Environ. Sci. Technol.* 38, 1901–1909.
- Rosa, R., Pini, M., Neri, P., Corsi, M., Bianchini, R., Bonanni, M., Ferrari, A.M., 2017. Environmental sustainability assessment of a new degreasing formulation for the tanning cycle within leather manufacturing. *Green Chem.* 19 (19), 4571–4582.
- Sakhno, Y., Ivanchenko, P., Iafisco, M., Tampieri, A., Martra, G., 2015. A step toward control of the surface structure of biomimetic hydroxyapatite nanoparticles: effect of carboxylates on the {010} P-rich/Ca-rich facets ratio. *J. Phys. Chem. C* 119 (11), 5928–5937.
- Salieri, B., Turner, D.A., Nowack, B., Hischier, R., 2018. Life cycle assessment of manufactured nanomaterials: where are we? *NanoImpact* 10, 108–120.
- Sanchez-Olivares, G., Sanchez-Solis, A., Calderas, F., Medina-Torres, L., Manero, O., Di Blasio, A., Alongi, J., 2014. Sodium montmorillonite effect on the morphology, thermal, flame retardant and mechanical properties of semi-finished leather. *Appl. Clay Sci.* 102, 254–260.
- Scopus, 2019. Available at: <https://www.scopus.com/> (accessed: Jan-Mar 2020).
- Selvaraju, S., Ramalingam, S., Rao, J.R., 2017. Preparation and application of biodegradable nanocomposite for cleaner leather processing. *J. Clean. Prod.* 158, 225–232.
- Shi, J., Puig, R., Sang, J., Lin, W., 2016. A comprehensive evaluation of physical and environmental performances for wet-white leather manufacture. *J. Clean. Prod.* 139, 1512–1519.
- Sreeram, K.J., Ramasami, T., 2003. Sustaining tanning process through conservation, recovery and better utilization of chromium. *Resour. Conserv. Recycl.* 38 (3), 185–212.
- Tufvesson, L.M., Tufvesson, P., Woodley, J.M., Börjesson, P., 2013. Life cycle assessment in green chemistry: overview of key parameters and methodological concerns. *Int. J. Life Cycle Assess.* 18 (2), 431–444.
- Usenko, C.Y., Abel, E.L., Hopkins, A., Martinez, G., Tijerina, J., Kudela, M., Norris, N., Joudeh, L., Bruce, E.D., 2016. Evaluation of common use brominated flame retardant (BFR) toxicity using a zebrafish embryo model. *Toxics* 4 (3), 21.
- Wang, Y.Z., Shan, Z.H., 2019. The penetration and accumulation of hydroxyapatite and the hydrothermal stability of collagen matrix material. *Mater. Chem. Phys.* 226, 257–262.

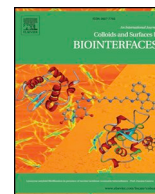
Glossary

- BOD:** Biochemical Oxygen Demand
CC: Climate Change, damage category
COD: Chemical Oxygen Demand
DC: Damage Category
EC: European Commission
EQ: Ecosystem Quality, damage category
FU: Functional Unit
HH: Human Health, damage category
HR-TEM: High-Resolution Transmission Electron Microscopy
IC: Impact Category
IULTCS: International Union of Leather Technologists and Chemists Societies
LCA: Life Cycle Assessment
LCI: Life Cycle Inventory
LCIA: Life Cycle Impact Assessment
LCSA: Life Cycle Sustainability Assessment
OECD: Organisation for Economic Co-operation and Development
REACH: Registration, Evaluation, Authorisation and Restriction of Chemicals regulation
RR: Resources, damage category
SC: Supply Chain
SVHC: Substances of Very High Concern
TDS: Total Dissolved Solids
TS: Total Solids
TSS: Total Suspended Solids
US: United States
XRPD: X-ray Powder Diffraction

Nomenclature

Ag: Silver
BFR: Brominated Flame-Retardant
Ca(OH)₂: Calcium Hydroxide
Cr(VI): Hexavalent chromium
Ha: Hydroxyapatite
HCl: Hydrochloric Acid
H₃PO₄: Phosphoric Acid

MMT: Montmorillonite
Nano-Ha: Nano-Hydroxyapatite
NH₃: Ammonia
NH₄OH: Ammonium Hydroxide solution
SiO₂: Silicon Dioxide
TiO₂: Titanium Dioxide
ZnO: Zinc Oxide



Protocols

Towards the control of the biological identity of nanobiomaterials: Impact of the structure of {0110} surface terminations of nanohydroxyapatite on the conformation of adsorbed proteins

Federico Catalano^{a,1,2}, Pavlo Ivanchenko^{a,*,1}, Erica Rebba^a, Yuriy Sakhno^{a,3}, Gabriele Alberto^a, Galyna Dovbeshko^b, Gianmario Martra^a

^a Department of Chemistry and Interdepartmental Nanostructured Interfaces and Surfaces (NIS) Centre, University of Torino, via P. Giuria 7, Torino, 10125, Italy

^b Institute of Physics of the National Academy of Science of Ukraine, 46 Nauky Ave, Kyiv 03028, Ukraine

ARTICLE INFO

Keywords:

Nanohydroxyapatite
Surface structure
Adsorbed protein
Protein conformation
Biological identity
IR spectroscopy
CD-UV spectroscopy
Zeta-Potential

ABSTRACT

High-resolution transmission electron microscopy, ζ -potential and in-situ IR spectroscopy of adsorbed CO were combined for elucidating the ratio between {0110}_{Ca-rich}: {0110}_{P-rich} terminations of {0110} facets, i.e. the surfaces with the highest morphological importance, in two nanohydroxyapatite samples. Bovine serum albumin was found to form at least a monolayer on the surface left accessible to protein molecules by the agglomeration of nanoparticles when suspended in the buffered incubation medium. Noticeably, the conformation of adsorbed proteins appeared sensitive to the ratio between the two types of {0110} terminations, also resulting in a difference in the surface exposed toward the exterior by the adsorbed protein layer(s).

1. Introduction

Hydroxyapatite – Ca₁₀(PO₄)₆(OH)₂ (hereafter referred to as HA) is among the most abundant mineral components of human bones and teeth [1–4]. HA is considered as an important bioactive and bioresorbable biomaterial widely used for bone tissue engineering, bone filling and substitution applications in orthopedics and dentistry [5–8]. Since the concept of biological surface science was established [9–11], the surface of biomaterials has been recognized to play a significant biological role, being the location of interaction with host biological media. Indeed, the analysis of various failed implants in the last decades indicated that failure mainly originates at the tissue/biomaterial interface [12]. Hence, a deep understanding of the biomaterial surface characteristics, in particular to elucidate the relationship between the types of surface terminations and the fate of the interactions with biomolecules, is mandatory to attain an increasingly higher level of control over biomaterials-host tissue interactions. The role of surfaces is further amplified in the case of nanobiomaterials; among them is nanosized hydroxyapatite, mimicking apatite nanocrystals in natural bone and teeth [13]. For instance, nanosizing and hierarchical structuring

down to nanoscale of synthetic hydroxyapatite was found to have a beneficial effect on the response elicited in osteoblasts [14–16]. HA nanoparticles (NPs) can easily be prepared with different morphologies, namely needle-like [17–20] or plate-like [21,22]. Their surface/interface properties have been studied with a large variety of techniques (HR-TEM, MIR, NIR, NMR, ζ -potential) [23–26], combined with computational studies [27–29], allowing a precise knowledge of the atomic distribution of the exposed surfaces. Focusing on the types of surface facets, recent advances resulting from XRD [30] and HR-TEM investigations [31,32] indicated that, independently on the hexagonal or platelet morphology, the prevailing surfaces are often of the {0110} type, corresponding to both lateral facets of hexagonal HA nanoparticles and basal facets of platelets. Noticeably, {0110} surfaces are considered good models of the prevailing facets exposed by nanoapatite crystals in bone [33]. However, it is known that {0110} can exhibit different terminations depending on the specific interruption of the ...-A-B-A-A-B-A-B-A-... sequence along the axis normal to the {0110} crystal plane family, where A and B correspond to layers with Ca₃(PO₄)₂ and Ca₄(PO₄)₂(OH)₂ composition, respectively. As a consequence, three different types of {0110} terminations are possible, indicated as

* Correspondence author.

E-mail address: pavlo.ivanchenko@unito.it (P. Ivanchenko).

¹ These authors contributed equally to the work.

² Present address: Electron Microscopy Facility, Italian Institute of Technology (IIT), via Morego 30, 10163, Genova, Italy.

³ Present address: Plant & Soil Sciences Department, 154a Townsend Hall, 531 S. College Avenue, Newark, DE 19713, USA.

stoichiometric HA {0110} (upmost three layers: ...-A-B-A), HA {0110} _Ca-rich (upmost three layers: ...-A-A-B) and HA {0110} _P-rich (upmost three layers: ...-B-A-A). The labels Ca-rich and P-rich stem from a Ca/P ratio higher and lower than bulk Ca/P ratio of 1.67, respectively [28].

Refinement of synthetic procedures resulting in micro- and nanoHA particles with defined shape and size [22], have led to studies on the adsorption of amino acids [34–36], peptides [35,37], proteins [38–40], and DNA [41,42], aimed at understanding complex biomolecule adsorption phenomena [43]. Indeed, adsorption depends on a number of parameters related to the incubation conditions (i.e. temperature [44], pH and ionic strength [45], buffering agent [46]), the biomolecule(s) (i.e. charge size and structural rigidity [47,48], as well as cooperative behavior of proteins [49]) and textural and structural features of the adsorbing surfaces. Focusing on this latter aspect, Lin et al. provided evidence of the beneficial effect of surface nanotexture of HA bioceramics on the adsorption of specific plasma proteins [15]. As far as the surface texture, in terms of crystallographic facets exposed, the Kandori group investigated extensively the different behavior towards protein adsorption of {0001} surfaces with respect to {0110}. They were found to preferentially adsorb basic (e.g. lysozyme) and acid (e.g. BSA) proteins, respectively. [50–52] However, the recent awareness of the possible presence of different types of {0110} terminations raises the question about any specific behavior towards protein adsorption. Indeed, differences in the adsorption on {0110} _Ca-rich and {0110} _P-rich terminations of other types of biomacromolecules, namely DNA, were revealed by a combined experimental and computational study [42]. Similar observations were made in the case of the computational investigation of HA surfaces with the simple amino acid glycine [53].

Here we report the results of an experimental study of the adsorption of bovine serum albumin (BSA), widely used to investigate the interaction of nanobiomaterials with proteins, on two nanoapatites, both preferentially exposing {0110} surfaces (by high resolution transmission electron microscopy, HR-TEM) but with significantly different Ca-rich/P-rich terminations. The relative amount of these terminations was determined by analyzing IR spectra of adsorbed CO using the method developed in ref [54]. Aspects dealing with protein coverage were analyzed, taking into consideration the agglomeration state of apatite nanoparticles in the incubation experiments. Finally, the impact of the different Ca-rich/P-rich terminations ratio on the secondary structure of adsorbed proteins was determined by circular dichroism-UV spectroscopy (CD-UV).

2. Experimental Section

2.1. Materials

All solvents and reagents [calcium hydroxide $\text{Ca}(\text{OH})_2$, phosphoric acid H_3PO_4 , magnesium chloride hexahydrate $\text{MgCl}_2 \cdot 6\text{H}_2\text{O}$, ammonia, HEPES buffer, BSA] were high-purity Sigma-Aldrich products and used as received. MilliQ water was used throughout. High-purity CO (Praxair) was used for IR measurements without any additional purification, except liquid nitrogen trapping.

2.2. Preparation of HA NPs

In order to prepare 0.01 mol of hydroxyapatite, 0.10 mol of calcium hydroxide and 0.06 mol of phosphoric acid were combined. Calcium hydroxide was stirred magnetically in 200 ml of MilliQ water for 20 min until a homogeneous suspension was obtained. Phosphoric acid (diluted with 200 ml of MilliQ water) was added dropwise to this suspension over 45 min, with continuous stirring, keeping the pH above 10.5 by addition of ammonia solution, as necessary. The solution was stirred for a further 2 h, and then left overnight. The product was filtered under suction and dried at ambient conditions. For HA-LT (LT = low temperature) all the synthesis steps were carried out at 298 K, while for HA-HT (HT = high temperature) the temperature was kept at 368 K.

2.3. High resolution transmission Electron microscopy (HR-TEM)

HR-TEM images were obtained with a 3010 Jeol instrument operated at 300 kV. Samples were prepared by spreading a droplet of an aqueous suspension of nanoparticles on a copper grid coated with a lacey carbon film and then waiting for liquid evaporation. As apatite samples might evolve under the electron beam, potentially leading to further crystallization and/or loss of bulk water [55–57], TEM analysis was carried out under low-illumination conditions to avoid significant modification to the materials.

2.4. X-ray diffraction (XRD)

XRD patterns of HA powders were recorded with an Analytical X'Pert Pro equipped with a PIXcel detector powder diffractometer using $\text{Cu K}\alpha$ radiation ($k = 1.5418 \text{ \AA}$) generated at 45 kV and 40 mA. For the diffracted beam an automatic-variable anti-scatter slit with an irradiated length of 10 mm was used. The 2θ range was from 5° to 80° with a step size (2θ) of 0.039 and a counting time of 3 s.

2.5. Specific surface area (SSA_{BET}) measurements

Specific surface areas of HA nanoparticles were measured by N_2 adsorption-desorption isotherms at 77 K using a Micromeritics ASAP 2020 instrument and SSA was calculated by the Brunauer-Emmett-Teller (BET) method.

2.6. IR measurements

Infrared measurements were performed on powders pressed in self-supporting pellets and placed in a cell, equipped with KBr windows, allowing the collection of spectra at ca. 100 K (by liquid N_2 cooling). The cell was connected to a conventional vacuum line (residual pressure = 1×10^{-5} mbar, 1 mbar = 100 Pa) to perform all thermal treatments and adsorption-desorption experiments in situ. The spectra were collected at a resolution of 4 cm^{-1} with a Bruker IFS28 spectrometer, equipped with a DTGS detector. Each set of measurements (150 scans) was carried out on three different samples of each material, and data were normalized with respect to both the SSA for a comparative analysis and to the intensity of a pattern in the $2200\text{--}1900 \text{ cm}^{-1}$ range (due to a combination and overtone of vibrational modes of bulk phosphate groups) to render differences in intensity independent of differences in the thickness of the pellets. Spectra of adsorbed CO are reported in Absorbance, after subtraction of the spectra of the sample before CO admission. The IR spectra at the highest CO coverage were analyzed in terms of linear combination of the theoretical spectra of $(\text{CO})_n\text{-Ca}^{2+}$ adducts ($4 \geq n \geq 1$) calculated for CO on different HA surface terminations (from ref. [54], see Fig. S1 in the Supporting Information, hereafter SI). In summary, for each structure i of carbonyl adducts (containing from 1 to 4 CO molecules) computed in ref. [54], the CO stretching IR spectrum $S_i(\nu)$ was computed as a linear combination of Gaussian functions $G(\nu - \nu_j)$, each one centered at the j th CO B3LYP rescaled frequency value ν_j , and a 15 cm^{-1} full width at half-maximum (FWHM), weighted by the corresponding calculated IR intensity (I_j)

$$S_i(\nu) = \sum_j G(\nu - \nu_j) \quad (1)$$

Hence, at this level, the only guess was the FWHM value adopted, which was consistent with the FWHM = 15 cm^{-1} of the νCO band at very low CO coverage, where only monocarbonyls, producing a single band, should be overwhelmingly present.

A linear combination $T(\nu)$ of all the computed $S_i(\nu)$ spectra represents the resulting spectrum in which, however, the weights w_i of each $S_i(\nu)$ have to be, somehow, determined

$$T(\nu) = \sum w_i S_i(\nu) \quad (2)$$

The criterion adopted to choose the weights w_i has been to run a nonlinear regression between the experimental IR spectrum and the computed $T(\nu)$ one, by keeping constant the relative ratios of the computed I_j intensities within the same case i , while changing their absolute values.

2.7. Dynamic light scattering (DLS)

For DLS measurements a 90Plus Particle Size Analyzer (Brookhaven Instruments) was used (laser wavelength 663 nm, detection angle 90° , temperature 293 K). HA NPs were suspended (0.5 mg ml^{-1}) in bare HEPES (pH 7.4) and in BSA solutions buffered with HEPES. Moreover, DLS measurements were also performed on HA NPs carrying proteins irreversibly adsorbed toward dilution (namely protein hard corona, hereafter referred to “irreversibly adsorbed proteins”), separated by centrifugation from the BSA incubation solutions and resuspended in bare HEPES (see “Adsorption of BSA on HA samples” section for the detailed procedure). HEPES and buffered BSA solutions were the relevant media for this study, but in order to attain the highest dispersion of HA NPs, samples were also suspended in 0.1 M sodium citrate solution and stirred at 348 K for 24 h, to properly evaluate the NPs agglomeration occurring in other media. Moreover, DLS data of BSA solutions were acquired, for the sake of comparison. For each suspension condition, DLS measurements were performed in triplicate and results reported as mean values of hydrodynamic diameters (D_h) \pm standard deviation.

2.8. ζ -potential

The ζ -potential of samples (BSA in buffer, nanoparticles in the relevant dispersion media and NPs carrying the irreversible fraction of adsorbed proteins) was measured by electrophoretic light scattering (ELS) with a Zetasizer Nano-ZS (Malvern Instruments). Data are reported for each sample as mean values of triplicate experiments.

2.9. Adsorption of BSA on HA samples

For both types of HA, a series of 6 suspensions, repeated in triplicate, were prepared (25 mg of powder in 2.5 ml of HEPES) and sonicated for 15 min at 298 K. An equal volume of BSA solution in HEPES were added for each sample obtaining, in a final volume of 5 ml, a series of incubation solutions with different initial protein concentration: 0.1, 0.5, 1.0, 2.5, 5, and 7.5 mg ml^{-1} . Samples rotated end-over-end for 15 min at 298 K, were then centrifuged for 20 min (10,000 rpm, 298 K) to separate powders from the incubation media. Incubation times long up to 1 h were tested, but no significant changes in amount of adsorbed proteins and DLS values were obtained (Fig. S2 in the SI). In order to desorb toward dilution the fraction of reversibly adsorbed BSA, pellets underwent several re-suspension/centrifugation cycles with fresh buffer and were then re-suspended in 5.0 ml of HEPES for spectrophotometric analyses.

2.10. Quantification of adsorbed BSA

Adsorption curves of BSA on HA NPs were obtained by spectrophotometric measurement of the difference in the absorbance value at $\lambda = 280 \text{ nm}$ (Cary 300 Bio, Varian) to evaluate the protein concentration before and after contact with the powders. The specific aim was to obtain quantitative information on both the reversibly and irreversibly adsorbed protein components. The supernatants resulting from the first centrifugation after incubation of HA NPs in the BSA buffered solutions were analyzed spectrophotometrically, to determine the concentration/amount of proteins remained in solution. These values were used for plotting relevant physical-chemical parameters as a function of the actual concentration of BSA in solution in equilibrium with the adsorbed one. The amount of BSA in solution was subtracted from the

initial amount of proteins before contacting NPs in the incubation systems, thus resulting in the total (reversible + irreversible) amount of adsorbed proteins. Finally, for each sample, the supernatants obtained by the subsequent washing procedure (re-suspension/centrifugation cycles) were merged and the absorbance at 280 nm was measured in order to estimate the amount of reversibly adsorbed proteins. These values, subtracted from the total amount, gave the amount of irreversibly adsorbed proteins. Results are reported as the mean value of at least three separate experiments \pm standard deviation.

2.11. Circular dichroism spectroscopy (CD-UV)

A solution of 0.1 mg ml^{-1} of BSA in MilliQ water (HEPES buffer is not transparent in the range of 180–210 nm for CD measurements) was prepared, and an aliquot was heated for 15 min at 373 K (with PTC-423S Peltier heating/cooling system in a tapped cuvette to prevent evaporation). Both solutions were scanned in the far-UV spectral range (180–300 nm, 4 accumulations, path length 0.1 cm, bandwidth 1 nm, scanning speed of 50 nm min^{-1}) using a Jasco J-815 spectropolarimeter equipped with a Xe arc lamp. Samples of HA NPs carrying the irreversible fraction of adsorbed BSA were suspended in MilliQ water and diluted in order to minimize the scattering due to particle suspension, attaining a final powder concentration of 0.5 mg ml^{-1} just before acquiring spectra. BSA concentration in each suspension was then determined and adjusted to obtain the same nominal concentration of irreversibly adsorbed BSA per volume (see details in the SI). Deconvolution of CD spectra was performed with CDNN software (Version 2.1, Copyright (C) 1997 Gerald Böhm) to estimate the relative percentage of secondary structures, considering the maximum number (33) of reference spectra in the software database. The effectiveness of this deconvolution method was confirmed also by the agreement of results obtained for native and thermally treated BSA in solution with literature data.

3. Results and discussion

3.1. Structure, morphology and size of HA NPs

Both HA-HT and HA-LT, exhibited XRD patterns (Fig. S3) typical of single phase hexagonal hydroxyapatite (JCPDS 9–432).

In HR-TEM images (Fig. 1), heavily affected by a tight agglomeration of nanoparticles on the support, both HA-HT (panel A) and HA-LT (panel B) in most cases produced elongated 2D projections on the image plane, with a different contrast (of the mass-thickness type) dependent on their width (normal to the elongation direction): narrower the width, higher the contrast (darker the particle image). This suggests that nanoparticles might exhibit an elongated plate-like shape, with size (length \times width \times thickness) of ca. $150\text{--}100 \text{ nm} \times 40\text{--}20 \text{ nm} \times 5\text{--}10 \text{ nm}$. Such dimensions are in agreement with a SSA_{BET} of 76 and $73 \text{ m}^2 \text{ g}^{-1}$ measured for HA-HT and HA-LT, respectively. For nanoparticles properly oriented with respect to the electron beam lattice fringes due to $\{01\bar{1}0\}$ planes of hexagonal hydroxyapatite phase appeared. It was noted that these fringes run along the main side of the projection of NPs on the image plane indicating that both HA-HT and HA-LT nanoparticles are elongated along the c -axis. Moreover, the main borders of the nanoparticle projection appeared parallel to the lattice fringes, indicating that they correspond to the lateral view of $\{01\bar{1}0\}$ facets.

3.2. Types of HA surface terminations

The information provided by HR-TEM can be limited from a statistical point of view, and the sensitivity of HA nanoparticles to the exposure to the electron beam can prevent in a large extent the possibility to image details useful for the recognition of the structure of surfaces. Thus, a method based on the analysis of the IR spectra of adsorbed CO was used to obtain insights on the relative amount of the

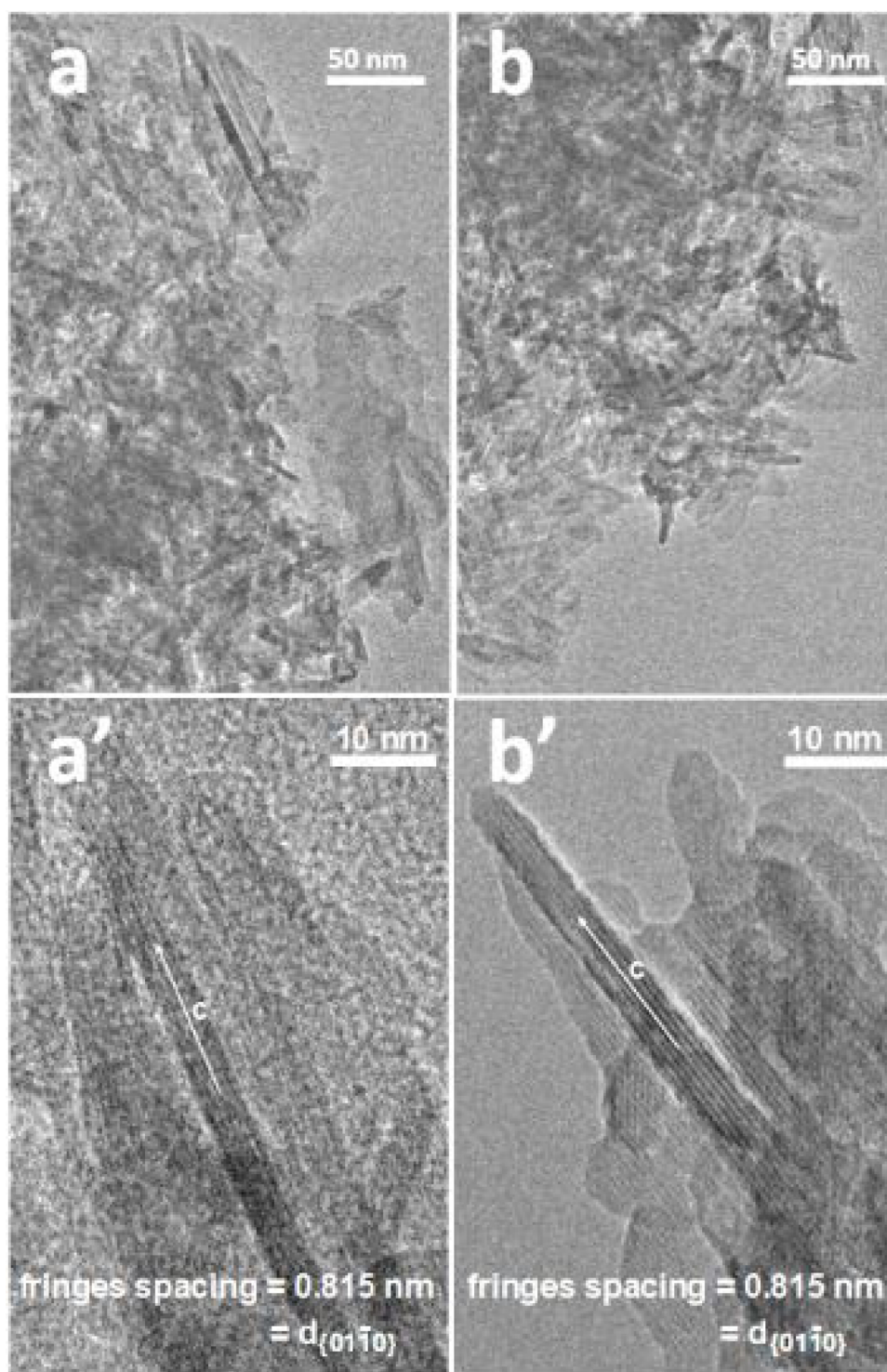


Fig. 1. Representative HR-TEM images of HA-HT (panels (a), (a')), HA-LT (panels (b), (b')). Original magnifications: (a), (b) 35k \times ; (a'), (b') 200k \times .

different types of surface terminations exposed by HA nanoparticles [32,54]. In each of these measurements, milligrams of material are analyzed, instead of some hundreds of nanoparticles inspected by TEM, and the experimental conditions adopted allow CO molecules to probe the local structure of all Ca^{2+} ions exposed to the surfaces of nanoparticles. Fig. S4 shows the IR spectra of CO dosed on HA-HT and HA-LT (panels A and B, respectively) in order to saturate their capacity toward the adsorption of probe molecules on surface Ca^{2+} sites. The whole series of spectra collected at decreasing CO for both HA samples is reported in Fig. S5 in the SI. The spectra at saturated CO coverage

were compared with the unbiased sum (black dotted spectrum) of theoretical spectra (S_x curves, $4 \geq x \geq 1$), each with weight = 1, due to all possible $\text{Ca}^{2+}-(\text{CO})_n$ adducts ($4 \geq n \geq 1$) calculated for carbon monoxide on {0001}, stoichiometric {01 $\bar{1}$ 0} reacted (R) with water, {01 $\bar{1}$ 0} Ca-rich and {01 $\bar{1}$ 0} P-rich surface terminations [54]. The huge misfit clearly indicated that only some of the carboxylic adducts might have been formed on the surface of the two HA samples. A nonlinear regression between the computed sum and the experimental IR spectra was then run. In both cases the best fit resulted from the combination of components due only to carboxylic adducts on {01 $\bar{1}$ 0} Ca-rich and

Table 1
{0110}₋ Ca-rich: {0110}₋ P-rich ratio of HA-HT and HA-LT.

Material	{0110} ₋ Ca-rich : {0110} ₋ P-rich
HA-HT	2.00 ± 0.06 : 1.00 ± 0.04
HA-LT	1.00 ± 0.05 : 2.20 ± 0.06

{0110}₋ P-rich surfaces, whereas the coefficient of all other theoretical spectra approached a value close to zero, indicating that the other types of surfaces contribute in a very minor extent to nanoparticle terminations. Noteworthy, the relative amount of {0110}₋ Ca-rich and {0110}₋ P-rich terminations appeared reversed in the two samples: *ca.* 2:1 for HA-HT and *ca.* 1:2 for HA-LT (Table 1). These reversed ratios are also in agreement with the results of ζ -potential measurements, i.e. of the assessment of the average surface charge of the two nanoparticle samples. On the basis of the findings of del Valle et al. [42], a larger relative amount of {0110}₋ Ca-rich terminations, which expose Ca²⁺, OH⁻ and PO₄³⁻ is consistent with the more negative ζ -potential measured for HA-HT (-16.7 mV) than for HA-LT (-12.3 mV), where {0110}₋ P-rich terminations should be the more abundant.

3.3. Agglomeration status and ζ -potential of HA-NPs in BSA solutions

The hydrodynamic diameter (Dh) of HA NPs suspended in HEPES buffer in their bare form and carrying irreversibly adsorbed proteins was measured by DLS. Mass distribution data resulting from the average of 3 measurements are reported in Fig. 2, panel A. The whole set of raw data of BSA in HEPES and of HA NPs in the various suspension conditions considered are reported in Fig. S6 and S7, respectively, in the SI.

The highest dispersion of HA NPs was pursued and best results were found by using a citric acid solution with pH adjusted to 6.5 by NaOH addition. In this condition, HA-HT exhibited a bimodal distribution with Dh values of *ca.* 100 and 400 nm (panel A, black dashed lines a, a', respectively; ratio in mass 1:2, see Fig. S7 in the SI), whilst for HA-LT the distribution appeared monomodal, with an average Dh of *ca.* 380 nm (panel A, green dashed line b). The Dh value around 100 nm found for HA-HT, is similar to the size of primary particles observed by HR-TEM, indicating that the suspension medium used allows a monodispersion of the nanoparticles. Consequently, the Dh values around 380/400 nm indicated that *ca.* 2/3 of HA-HT and the whole HA-LT sample are constituted by aggregates of multiple nanoparticles.

Hence, the citric acid solution appeared a good suspension medium for attaining a high dispersion of HA nanoparticles. This behavior likely resulted from the adsorption of citrate anions, that were reported to strongly interact with the surface of apatite nanocrystals [30,33]. As a consequence, this medium was not considered for studying the adsorption of BSA, in order to avoid the interference of citrate ions in this phenomenon.

When suspended in HEPES buffer, both single and aggregated NPs of HA-HT underwent a large agglomeration, as indicated by the appearance of a monomodal distribution with an average Dh of *ca.* 1.6 μ m. In the case of HA-LT the agglomeration was so extended to result in the flocculation of the system (amount of agglomerates remained in suspension too low to produce a detectable signal in DLS measurements).

HEPES buffered solutions of BSA were then added to HA-LT and HA-HT suspended in HEPES buffer. Dh was measured in two conditions, and equivalent results were obtained: i) with unadsorbed proteins still present in the suspension (thus before any centrifugation), ii) after removing them, by separating NPs with irreversibly adsorbed BSA and re-suspending them in HEPES buffer (see Fig. S8 in the SI). The second condition was also used for the ζ -potential measurements, to avoid contribution from non-adsorbed proteins.

An overall dispersive effect of BSA molecules was observed. In the

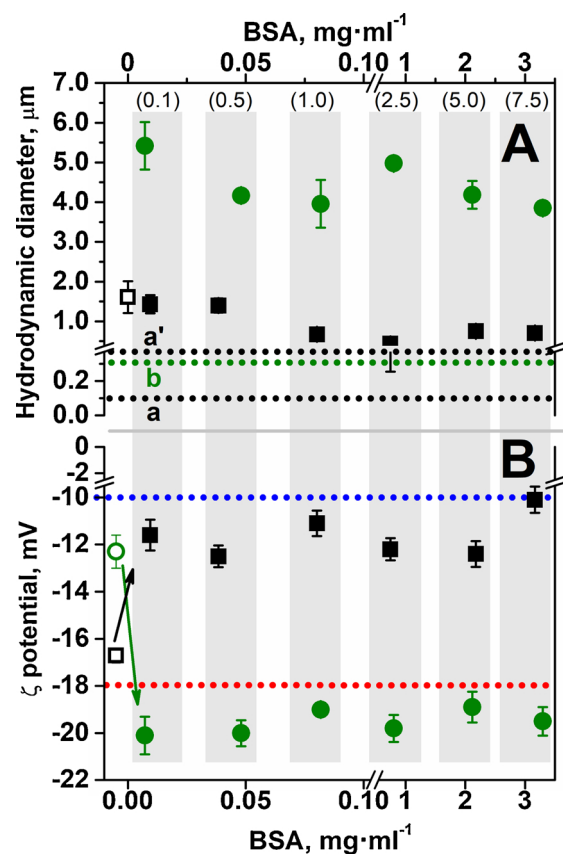


Fig. 2. Panel (a): hydrodynamic diameter (Dh) of HA-HT (color code: black squares), HA-LT (color code: green circles) suspended in: (i) solution of sodium citrate 0.1 M ((a), (a') and (b) dotted lines), (ii) HEPES buffer (HA-HT: empty symbols; HA-LT: agglomerates too large in size to be measured) and (iii) re-suspended in HEPES after incubation with BSA solution with different concentrations (full symbols) and removal of BSA adsorbed reversibly upon dilution (see Experimental). Panel (b): ζ -potential of: (i) native and thermally treated BSA in solution (upper blue and lower red dotted lines, respectively) and (ii) HA-HT and HA-LT NPs in bare form (empty symbols) and with irreversibly adsorbed BSA (full symbols), as in panel (a) (again, values reported on the X-axis: concentration of BSA in solution in equilibrium with the adsorbed one). Values reported on the X-axis: concentration of BSA in solution in equilibrium with the adsorbed one, at the end of the incubation. Values in brackets over grey bars are initial concentrations of BSA solutions. (For interpretation of the references to color in the Figure, the reader is referred to the web version of this article).

case of HA-HT, a slight decrease of Dh occurred for NPs incubated in 0.1 and 0.5 mg ml⁻¹ protein solutions, whilst Dh more than halved for incubation in more concentrated BSA solutions. In any case, a dispersion as high as in the citrate solution was not attained. Protein molecules also acted as dispersing agents toward HA-LT agglomerates, which however, remained very large in size, from *ca.* 5.5 to 4 μ m.

The dispersive effect of proteins toward agglomeration of both types of HA NPs appeared qualitatively similar to observations in a previous work for silica nanoparticles [58]. This behavior was interpreted in terms of diffusion of protein molecules within interparticle spaces in the initial agglomerates, which are then partly disrupted.

The incomplete redispersion indicates that the diffusion process did not reach the core of agglomerates. Consequently, DLS is actually measuring the size of the fragments of agglomerates that resisted the diffusion of BSA molecules, carrying adsorbed proteins on the surface accessible to BSA molecules.

Complementary aspects of the HA NPs-BSA interaction were studied by measuring the ζ -potential of HA-HT and HA-LT suspended in HEPES buffer in their bare form or when carrying on their surface the

hard protein corona. Data are shown in Fig. 2, panel B, where also the ζ -potential values of BSA in HEPES buffer in the native state (blue dotted line) and after thermal treatment (red dotted line) are reported for the sake of comparison.

As reported above, ζ -potential values measured for bare HA-HT and HA-LT were -16.7 and -12.3 mV, respectively. Noticeably, an opposite evolution of ζ -potential occurred as a consequence of the presence of irreversibly adsorbed proteins: by incubation with the less concentrated BSA HEPES buffered solution (0.1 mg ml^{-1}), the ζ -potential measured for HA-HT increased from -16.7 mV to -12.1 mV ($\Delta\zeta = +4.6$ mV), whereas for HA-LT it decreased from -12.3 mV to -20.1 mV ($\Delta\zeta = -7.8$ mV). By incubation with more concentrated BSA solutions, up to an equilibrium concentration of ca. 3.0 mg ml^{-1} (initial BSA concentration 7.5 mg ml^{-1}), ζ -potential changed in a more limited way, remaining in the $-12.0/-10.0$ mV range for HA-HT, and $-20.1/-18.0$ mV range for HA-LT. Noteworthy, the ζ -potential values of the BSA on HA-HT system and of the BSA on HA-LT one are similar to those of native and thermally treated BSA in solution, respectively (dotted lines in Fig. 2B).

Such opposite behavior clearly indicated that the adsorption of BSA molecules is significantly influenced by the different $\{01\bar{1}0\}$ -Ca-rich: $\{01\bar{1}0\}$ -P-rich terminations ratio between the two HA samples. The ζ -potential of a protein-on-NPs system depends on both protein coverage and structure. Thus, these aspects were also investigated.

3.4. Amount of adsorbed BSA and surface coverage

Total and irreversibly adsorbed amounts of BSA per unit mass of the two materials, with dependence on the initial concentration of the protein incubation solutions, are shown in Fig. 3A. For each type of HA NPs, the two sets of data appeared almost coincident, indicating that the overwhelming part of BSA adsorption had an irreversible character. Nevertheless, in no case a complete adsorption of BSA present in the incubation medium occurred. Thus, for the sake of simplicity, only data dealing with the irreversibly adsorbed amounts were further considered.

The next step was the evaluation of the surface coverage, assuming a BSA molecule should occupy an area of ca. $9.0 \times 5.5 \text{ nm}^2$ when adsorbed in a “side-on” manner (a conservative choice with respect to the “end-on” mode, resulting in the occupation of a smaller $5.5 \times 5.5 \text{ nm}^2$ area) [59]. As far as the surface area of HA NPs for protein adsorption is considered, the SSA_{BET} values (then measured by N_2 adsorption on dry powders) were used, and the results obtained are reported in Fig. 3, panel B, in terms of relative coverage with respect to a theoretical monolayer of “side-on” adsorbed BSA molecules. The data sets appeared quite similar for both HA-HT and HA-LT, exhibiting a progressive increase of the coverage up to 0.6 for BSA initial concentration as large as 1.0 mg ml^{-1} , and then exhibiting oscillations in the 0.4–0.7 θ value range for higher BSA initial concentrations.

Noteworthy, the incubation with BSA solutions at different initial concentrations up to 1 mg/ml resulted in a different dispersion of HA NPs agglomerates (Fig. 2, panel A). Thus, it must be considered that each of the three first points in the adsorption isotherms in Fig. 3 results from an incubation condition where two parameters are different with respect to the other points: not only the initial/equilibrium protein concentration, but also the size of the HA NPs agglomerates, i.e. the amount of surface area available for protein adsorption. Hence, the linear trend of the initial part of the isotherms cannot be interpreted on the basis of the usual models developed for the protein adsorptions on substrates not changing in size in dependence on the protein concentration.

However, it must be considered that an extensive agglomeration of both types of HA nanoparticles occurred in HEPES buffer, and that the partial redispersion attained when BSA was added witness for the limited diffusion of proteins within the agglomerates. Thus, the surface per unit of mass of HA actually available for the adsorption of BSA

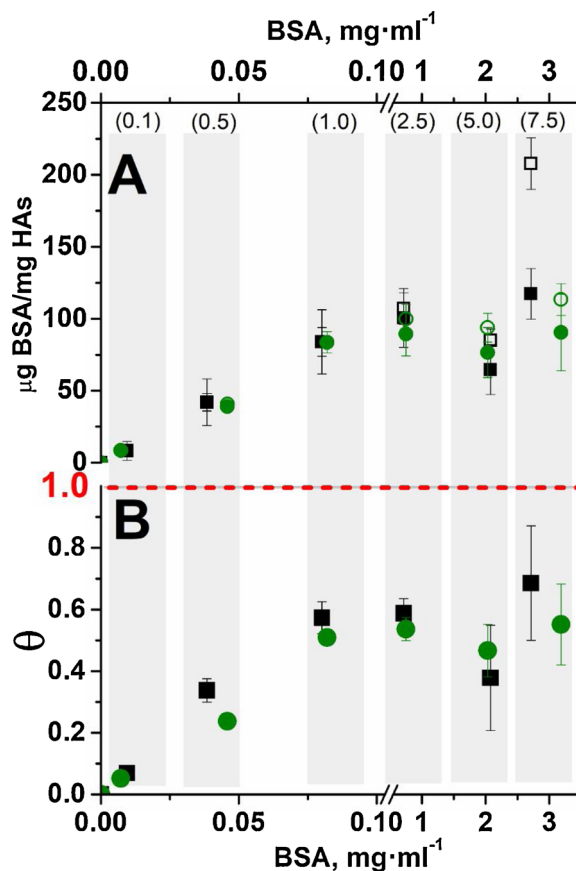


Fig. 3. Panel (a): amount of total (empty symbols) and irreversibly (full symbols) adsorbed BSA on HA-HT (black squares) and HA-LT (green circles) after incubation in different BSA solutions with different protein concentrations reported per mass of HA powder. Evaluation of HA surface coverage by irreversibly adsorbed BSA by considering: panel (b) the SSA measured by the BET method. Red dashed line, $\theta = 1$: theoretical monolayer, for BSA adsorption in the side-on mode [59]. Values reported on the X-axis: concentration of BSA in solution in equilibrium with the adsorbed one, at the end of the incubation. Values in brackets over grey bars are initial concentrations of BSA solutions. (For interpretation of the references to color in the Figure, the reader is referred to the web version of this article).

molecules should have been significantly lower with respect the SSA_{BET} . As a consequence, in both HA-HT and HA-LT agglomerated the protein coverage should be higher than what reported in Fig. 3, panel B. In a previous study dealing with adsorption of BSA on spherical SiO_2 NPs [58], the high homogeneity in shape and size of nanoparticles resulted in the agglomeration of nanoparticles in a hexagonal array, and this allowed for a reasonable estimation of the mass present in the agglomerates and of their external surface area, accessible to BSA molecules. The different shape of HA nanoparticles and the unknown shape and structure of agglomerates prevented a similar analysis in the present case. Nevertheless, it must be considered that the ζ -potential of a protein-NP system results from the combined contribution adsorbed proteins and the part of the surface of nanoparticles still uncoated by them. Thus, the dependence of ζ -potential and of surface coverage from the protein concentration in the incubation suspensions should be similar, whereas this was not the case for BSA on HA-HT and HA-LT. The trend of protein coverage calculated on the basis of the SSA_{BET} was characterized by an almost linear increase by increasing up to 1.0 mg ml^{-1} the BSA concentration of the incubations solutions (Fig. 3, panel B). Conversely, a steep change of ζ -potential occurred when passing from bare nanoparticles to the presence of irreversibly adsorbed protein by contact with a 0.1 mg ml^{-1} BSA solution, and then more limited changes occurred for proteins-NPs systems resulting from the

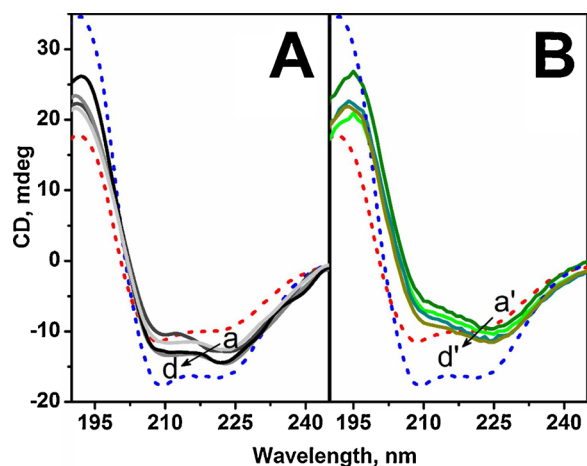


Fig. 4. CD-UV spectra of BSA irreversibly adsorbed on HA-HT and HA-LT (panels (a) and (b), respectively) incubated in protein solutions at different initial concentration: (a),(a') 0.1, (b),(b') 0.5, (c),(c') 2.5, (d),(d') 7.5 mg ml^{-1} . Spectra are compared with those of BSA solutions in native form and after thermal treatment at 373 K for 15 min (blue and red dashed curves, respectively). (For interpretation of the references to color in the Figure, the reader is referred to the web version of this article).

suspension in more concentrated BSA solutions (Fig. 2, panel B). This behavior suggests that, for each type of HA material, the extent of the surface of agglomerated nanoparticles coated by irreversibly adsorbed proteins should have been almost constant along the series of protein-NPs systems resulting from incubations in BSA solutions with different protein concentration.

Confirmatory evidence of these proposals was obtained by CD-UV spectroscopy, also providing insights on the conformation of adsorbed proteins.

3.5. CD-UV of BSA irreversibly adsorbed on HA

CD-UV spectra of proteins irreversibly adsorbed on HA-HT and HA-LT (curves a–d and a'–d', respectively) are reported in Fig. 4. In order to properly relate possible changes in the intensity of the CD-UV signals to structural modification due to adsorbed proteins, spectral intensities were normalized with respect to the same protein content (for details, see Fig. S9 and related comment in the SI). Moreover, spectra of adsorbed proteins are compared with those of BSA in solution in both native and thermally treated forms (blue and red dashed curves, respectively). The latter was of interest as a case where protein underwent changes in the secondary structure, without aggregation.

The CD-UV spectrum of native BSA in solution exhibits the usual profile characterized by one positive signal at 192 nm and a negative partner at 208 nm (resulting from the exciton coupling splitting of the $\pi \rightarrow \pi^*$ transition) and a negative component at 222 nm due to the $n \rightarrow \pi^*$ transition [60,61]. Following thermal treatment, the total intensity of these signals decreased and also a change in their relative intensity occurred. Spectra were deconvoluted (CDNN software; results in Table 2) and the relative amount of α -helix, β -sheet and unordered secondary motifs found for native BSA appeared fully consistent with literature values [62].

As expected, the relative amount of α -helices decreased in favor of random coils (and in a minor extent of β -turns) for thermally treated BSA, whereas the relative amount of β -sheets remained almost unchanged, indicating that aggregation among proteins, resulting in the formation of intermolecular β -sheets-like structure, did not occur.

Considering irreversibly adsorbed proteins, the spectra of BSA on HA-HT (panel A, curves a–d) appeared located between those of native and thermally treated BSA. Moreover, they are very similar to each other, independently on the concentration of BSA in the incubation

solution. The main difference with respect to the spectra of BSA in solution was a change in the relative intensity of minima at 208 and 222 nm. Such a change appeared even more evident for spectra of BSA irreversibly adsorbed on HA-LT, all located over the spectrum of thermally treated BSA (panel B, curves a'–d'). These spectral behaviors clearly indicated that important changes in the relative amount of secondary structural motifs occurred in adsorbed proteins. By spectral analysis, an increase in β -sheet content deconvolution (Table 2, column 4) was found for BSA adsorbed on HA-HT and HA-LT, almost doubled with respect to proteins in solution in both their native and thermally treated forms. This finding, accompanied by a significant decrease in the 208/222 nm intensity ratio (Table 3), monitors the formation of intermolecular β -sheets, as observed for BSA assembly resulting from the interaction with cationic lipids [63], or the adsorption of amyloid proteins on Teflon particles [64].

The occurrence of protein-protein interactions among BSA molecules adsorbed on HA-HT and HA-LT can then be inferred. This can account for the formation of at least a protein monolayer on the parts accessible to BSA of the surface of nanoparticles forming the agglomerates. This finding confirms that the sub-monolayer protein coverage calculated by taking into consideration the SSA_{BET} was underestimated (Fig. 3, panel B): when HA nanoparticles are agglomerated, their specific surface area accessible to proteins is lower than that measured by N_2 adsorption on dry powders. The formation of at least a BSA monolayer, likely occurring for all the BSA concentrations considered, should result from the combined increase of the amount of proteins in solution and of the protein-induced partial disagglomeration of nanoparticles, with a consequent increase of the surface area available for protein adsorption.

Another important feature is constituted by the different content in random coils (Table 2, column 6) and α -helices (Table 2, column 3) between BSA adsorbed on HA-HT and HA-LT.

In the case of BSA on HA-HT, the random coil content (11–17 %) changed in a limited extent with respect to native BSA in solution (12 ± 2 %), whereas it increased significantly for BSA on HA-LT (27–30 %). Accordingly, the α -helix content of BSA on HA-LT (38–40 %) decreased in a larger extent with respect to native BSA in solution (69 ± 3 %), than for BSA on HA-HT (55.63 %). In addition, it must be considered that, in both cases, a part of the decrease in intensity of the spectroscopic features due to α -helices is due to the protein-protein interactions responsible for β -sheet-like signals. Because the protocol for protein adsorption on the two HA NPs types was the same, the difference in random coil content points to a role of the ratio between $\{01\bar{1}0\}$ -Ca-rich and $\{01\bar{1}0\}$ -P-rich surface terminations in determining possible intramolecular conformational changes of adsorbed proteins.

Changes in secondary structure detected by CD-UV for native and thermally treated BSA in solution resulted in a change in the protein ζ -potential (Fig. 2B). Hence, the different conformation of BSA adsorbed on HA-HT and HA-LT can be related to the different ζ -potential of the two protein-NPs systems (Fig. 2B). CD-UV data indicated that at least a protein monolayer was attained for both systems even when the agglomerates of HA nanoparticles were contacted with the BSA solution with initial concentration of 0.1 mg ml^{-1} . Hence, the ζ -potential measured was mainly due only to the protein layer(s), without any significant contribution from the underlying HA surface. In the case of BSA on HA-HT, the protein adsorption did not result in a significant change in the relative amount of unordered secondary structure, and the increase in the relative amount of β -sheet-like motifs monitors the occurrence of protein-protein interactions. Thus it can be proposed that BSA on HA-HT basically maintained their native structure, and the parts of the polypeptidic chain exposed towards the exterior contribute to the measured ζ -potential. Conversely, CD-UV spectra indicated that conformational changes occurred for BSA adsorbed on HA-LT. Because also in this case, the surface of agglomerates of HA nanoparticles is completely covered by adsorbed proteins, the measured ζ -potential should result from the ionizable chemical groups exposed towards the exterior

Table 2

Relative amount of secondary structures obtained by deconvolution of CD-UV spectra of BSA in solution (native and thermal treated forms) and irreversibly adsorbed on HA-HT and HA-LT incubated in protein solutions at different initial concentrations.

Sample (BSA)	BSA, mg·ml ⁻¹ (initial concentration)	α-helix (%)	β-sheet (%)	β-turn (%)	random coil (%)
solution	0.1	69 ± 3	9 ± 2	10 ± 1	12 ± 2
solution (373 K)	0.1	48 ± 2	10 ± 2	16 ± 1	27 ± 2
BSA on HA-HT	0.1	55 ± 3	18 ± 1	10 ± 1	17 ± 2
	0.5	63 ± 2	18 ± 1	8 ± 1	11 ± 1
	2.5	56 ± 3	17 ± 1	10 ± 1	17 ± 2
	7.5	59 ± 3	18 ± 1	10 ± 1	13 ± 1
BSA on HA-LT	0.1	40 ± 1	20 ± 1	11 ± 1	30 ± 1
	0.5	40 ± 2	21 ± 1	10 ± 1	27 ± 2
	2.5	38 ± 2	21 ± 1	10 ± 1	30 ± 1
	7.5	40 ± 2	21 ± 1	9 ± 1	28 ± 2

Table 3

Ratio between CD values at 208 and 222 nm (CD₂₀₈/CD₂₂₂) calculated for CD-UV spectra of BSA in solution and adsorbed on HA NPs.

CD ₂₀₈ /CD ₂₂₂ > 1		CD ₂₀₈ /CD ₂₂₂ < 1	
BSA in solution		adsorbed BSA	
native BSA	1.07	0.89, 0.87, 0.78, 0.88	panel A, spectra a-d
heated at 373 K	1.16	0.64, 0.59, 0.61, 0.68	panel B, spectra a'-d'

by protein molecules. Owing to the differences in secondary structure, the amount and nature of these groups can be different from those determining the ζ-potential of BSA on HA-HT.

4. Conclusions

The collection of the results presented above point at two principal insights, one relevant for the methodologies to be adopted for the investigation of the adsorption of proteins on nanomaterials, and the other for the sensitivity of protein adsorption to surface features of nanomaterials.

As far as the methodological aspect is concerned, our data indicate that an important aspect of the protein adsorption on nanoparticles, such as the protein surface coverage, cannot be determined taking into consideration the specific surface area of nanoparticles as measured by N₂ adsorption on dry powders (the so-called BET method). Conversely, it must be considered that nanoparticles can agglomerate in the incubation medium, thus the surface available for the adsorption of proteins is only that of nanoparticles exposed at the surface of agglomerates.

Passing to the impact of the protein-nanoparticles interaction on the protein secondary structure, it can be concluded that even differences in the atomic arrangement of surface termination of the same crystallographic type affect the conformation of adsorbed proteins. This insight extends to proteins what found by del Valle et al. [42] when studying the interaction of DNA with nano-HA, and adds a step to the elucidation of the effect of hierarchical nanostructuring of HA bioceramics on protein adsorption [15].

CRedit authorship contribution statement

Federico Catalano: Investigation, Methodology, Formal analysis, Writing - original draft. **Pavlo Ivanchenko:** Investigation, Formal analysis, Writing - review & editing, Visualization. **Erica Rebba:** Investigation. **Yuriy Sakhno:** Data curation, Visualization. **Gabriele Alberto:** Methodology. **Galyna Dovbeshko:** Funding acquisition, Supervision. **Gianmario Martra:** Conceptualization, Writing - review & editing, Supervision, Funding acquisition.

Declaration of Competing Interest

The authors declare that they have no known competing financial interests or personal relationships that could have appeared to influence the work reported in this paper.

Acknowledgment

This work has been supported by the CSP-UniTo project “Nanomaterials for sustainable leather products - NanoSusLeather” – CSTO165920 (Italy). F.C acknowledges the University of Torino (Italy) and its Department of Chemistry for supporting his post-doc position (code A03.128/2015/XVIII). E.R acknowledges Kemia Tau S.R.L for supporting her PhD.

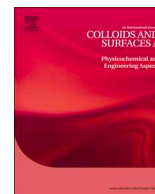
Appendix A. Supplementary data

Supplementary material related to this article can be found, in the online version, at doi:<https://doi.org/10.1016/j.colsurfb.2020.110780>.

References

- [1] S.J. Eppell, W. Tong, J. Lawrence Katz, L. Kuhn, M.J. Glimcher, Shape and size of isolated bone mineralites measured using atomic force microscopy, *J. Orthop. Res.* 19 (2001) 1027–1034, [https://doi.org/10.1016/S0736-0266\(01\)00034-1](https://doi.org/10.1016/S0736-0266(01)00034-1).
- [2] P. Fratzl, H.S. Gupta, E.P. Paschalis, P. Roschger, Structure and mechanical quality of the collagen–mineral nano-composite in bone, *J. Mater. Chem.* 14 (2004) 2115–2123, <https://doi.org/10.1039/B402005G>.
- [3] M.J. Olszta, X. Cheng, S.S. Jee, R. Kumar, Y.Y. Kim, M.J. Kaufman, E.P. Douglas, L.B. Gower, Bone structure and formation: a new perspective, *Mater. Sci. Eng. R Rep.* 58 (2007) 77–116, <https://doi.org/10.1016/j.mser.2007.05.001>.
- [4] R.A. Young, W.E. Brown, Structure of biological minerals, in: G.H. Nancollas (Ed.), *Biological Mineralization and Demineralization: Report of the Dahlem Workshop Biological Mineralization and Demineralization*, Springer, Berlin Heidelberg, Berlin, 1982, pp. 101–141.
- [5] S.V. Dorozhkin, Calcium orthophosphates in nature, biology and medicine, *Materials (Basel)*. 2 (2009) 399–498, <https://doi.org/10.3390/ma2020399>.
- [6] F.H. Jones, Teeth and bones: Applications of surface science to dental materials and related biomaterials, *Surf. Sci. Rep.* 42 (2001) 75–205, [https://doi.org/10.1016/S0167-5729\(00\)00011-X](https://doi.org/10.1016/S0167-5729(00)00011-X).
- [7] H. Liu, T.J. Webster, Nanomedicine for implants: a review of studies and necessary experimental tools, *Biomaterials*. 28 (2007) 354–369, <https://doi.org/10.1016/j.biomaterials.2006.08.049>.
- [8] N. Roveri, B. Palazzo, *Hydroxyapatite nanocrystals as bone tissue substitute*, *Nanotechnologies Life Science*, Wiley-VCH Verlag GmbH & Co., KGaA, 2007.
- [9] D.G. Castner, B.D. Ratner, Biomedical surface science: foundations to frontiers, *Surf. Sci.* 500 (2002) 28–60, [https://doi.org/10.1016/S0039-6028\(01\)01587-4](https://doi.org/10.1016/S0039-6028(01)01587-4).
- [10] B. Kasemo, Biological surface science, *Surf. Sci.* 500 (2002) 656–677, [https://doi.org/10.1016/S0039-6028\(01\)01809-X](https://doi.org/10.1016/S0039-6028(01)01809-X) doi:Pii S0039-6028(01)01809-X.
- [11] M. Tirrell, E. Kokkoli, M. Biesalski, The role of surface science in bioengineered materials, *Surf. Sci.* 500 (2002) 61–83, [https://doi.org/10.1016/S0039-6028\(01\)01548-5](https://doi.org/10.1016/S0039-6028(01)01548-5).
- [12] W.B. Greene, L.S. Dias, R.E. Lindseth, M.A. Torch, Musculoskeletal problems in association with cloacal exstrophy, *J. Bone Joint Surg. Am.* 73 (1991) 551–560, <https://doi.org/10.2106/00004623-199173040-00012>.
- [13] P. Wang, L. Zhao, J. Liu, M.D. Weir, X. Zhou, H.H.K. Xu, Bone tissue engineering via nanostructured calcium phosphate biomaterials and stem cells, *Bone Res.* 2 (2015) 14017, <https://doi.org/10.1038/boneres.2014.17>.
- [14] S.V. Dorozhkin, Nanosized and nanocrystalline calcium orthophosphates, *Acta*

- Biomater. 6 (2010) 715–734, <https://doi.org/10.1016/j.actbio.2009.10.031>.
- [15] K. Lin, L. Xia, J. Gan, Z. Zhang, H. Chen, X. Jiang, J. Chang, Tailoring the nanostructured surfaces of hydroxyapatite bioceramics to promote protein adsorption, osteoblast growth, and osteogenic differentiation, *ACS Appl. Mater. Interfaces* 5 (2013) 8008–8017, <https://doi.org/10.1021/am402089w>.
- [16] T.J. Webster, R.W. Siegel, R. Bizios, Osteoblast adhesion on nanophase ceramics, *Biomaterials* 20 (1999) 1221–1227, [https://doi.org/10.1016/S0142-9612\(99\)00020-4](https://doi.org/10.1016/S0142-9612(99)00020-4).
- [17] Y. Deng, H. Wang, L. Zhang, Y. Li, S. Wei, In situ synthesis and in vitro biocompatibility of needle-like nano-hydroxyapatite in agar-gelatin co-hydrogel, *Mater. Lett.* 104 (2013) 8–12, <https://doi.org/10.1016/j.matlet.2013.03.145>.
- [18] H. Ito, Y. Oaki, H. Imai, Selective synthesis of various nanoscale morphologies of hydroxyapatite via an intermediate phase, *Cryst. Growth Des.* 8 (2008) 1055–1059, <https://doi.org/10.1021/cg070443f>.
- [19] C. Shuai, P. Feng, Y. Nie, H. Hu, J. Liu, S. Peng, Nano-hydroxyapatite improves the properties of β -tricalcium phosphate bone scaffolds, *Int. J. Appl. Ceram. Technol.* 10 (2013) 1003–1013, <https://doi.org/10.1111/j.1744-7402.2012.02840.x>.
- [20] X. Yao, H. Yao, G. Li, Y. Li, Biomimetic synthesis of needle-like nano-hydroxyapatite templated by double-hydrophilic block copolymer, *J. Mater. Sci.* 45 (2010) 1930–1936, <https://doi.org/10.1007/s10853-009-4182-4>.
- [21] L. Bertineti, A. Tampieri, E. Landi, C. Ducati, P.A. Midgley, S. Coluccia, G. Martra, Surface structure, hydration, and cationic sites of nanohydroxyapatite: UHR-TEM, IR, and microgravimetric studies, *J. Phys. Chem. C* 111 (2007) 4027–4035, <https://doi.org/10.1021/Jp066040s>.
- [22] M. Sadat-Shojai, M.T. Khorasani, E. Dinpanah-Khoshdargi, A. Jamshidi, Synthesis methods for nanosized hydroxyapatite with diverse structures, *Acta Biomater.* 9 (2013) 7591–7621, <https://doi.org/10.1016/j.actbio.2013.04.012>.
- [23] M. Aizawa, A.E. Porter, S.M. Best, W. Bonfield, Ultrastructural observation of single-crystal apatite fibres, *Biomaterials* 26 (2005) 3427–3433, <https://doi.org/10.1016/j.biomaterials.2004.09.044>.
- [24] L. Bertineti, C. Drouet, C. Combes, C. Rey, A. Tampieri, S. Coluccia, G. Martra, Surface characteristics of nanocrystalline apatites: effect of Mg surface enrichment on morphology, surface hydration species, and cationic environments, *Langmuir* 25 (2009) 5647–5654, <https://doi.org/10.1021/la804230j>.
- [25] C. Jäger, T. Welzel, W. Meyer-Zaika, M. Epple, A solid-state NMR investigation of the structure of nanocrystalline hydroxyapatite, *Magn. Reson. Chem.* 44 (2006) 573–580, <https://doi.org/10.1002/mrc.1774>.
- [26] M. Rouahi, E. Champion, O. Gallet, A. Jada, K. Anselme, Physico-chemical characteristics and protein adsorption potential of hydroxyapatite particles: influence on in vitro biocompatibility of ceramics after sintering, *Colloids Surf. B Biointerfaces* 47 (2006) 10–19, <https://doi.org/10.1016/j.colsurfb.2005.11.015>.
- [27] N. Almora-Barrios, K.F. Austen, N.H. De Leeuw, Density functional theory study of the binding of glycine, proline, and hydroxyproline to the hydroxyapatite (0001) and (010) surfaces, *Langmuir* 25 (2009) 5018–5025, <https://doi.org/10.1021/la803842g>.
- [28] R. Astala, M.J. Stott, First-principles study of hydroxyapatite surfaces and water adsorption, *Phys. Rev. B* 78 (2008), <https://doi.org/10.1103/PhysRevB.78.075427>.
- [29] N.H. de Leeuw, Resisting the onset of hydroxyapatite dissolution through the incorporation of fluoride, *J. Phys. Chem. B* 6 (2004) 1809–1811, <https://doi.org/10.1021/jp036784v>.
- [30] J.M. Delgado-Lopez, R. Frison, A. Cervellino, J. Gomez-Morales, A. Guagliardi, N. Masciocchi, Crystal size, morphology, and growth mechanism in bio-inspired apatite nanocrystals, *Adv. Funct. Mater.* 24 (2014) 1090–1099, <https://doi.org/10.1002/adfm.201302075>.
- [31] C.A. Ospina, J. Terra, A.J. Ramirez, M. Farina, D.E. Ellis, A.M. Rossi, Experimental evidence and structural modeling of nonstoichiometric (010) surfaces coexisting in hydroxyapatite nano-crystals, *Colloids Surf. B Biointerfaces* 89 (2012) 15–22, <https://doi.org/10.1016/j.colsurfb.2011.08.016>.
- [32] Y. Sakhno, P. Ivanchenko, M. Iafisco, A. Tampieri, G. Martra, A step toward control of the surface structure of biomimetic hydroxyapatite nanoparticles: Effect of carboxylates on the {010} P-rich/Ca-rich facets ratio, *J. Phys. Chem. C* 119 (2015) 5928–5937, <https://doi.org/10.1021/jp510492m>.
- [33] Y.Y. Hu, A. Rawal, K. Schmidt-Rohr, Strongly bound citrate stabilizes the apatite nanocrystals in bone, *Proc. Natl. Acad. Sci. U. S. A.* 107 (2010) 22425–22429, <https://doi.org/10.1073/pnas.1009219107>.
- [34] R. Goobes, G. Goobes, W.J. Shaw, G.P. Drobny, C.T. Campbell, P.S. Stayton, Thermodynamic roles of basic amino acids in statherin recognition of hydroxyapatite, *Biochemistry* 46 (2007) 4725–4733, <https://doi.org/10.1021/bi602345a>.
- [35] A. Rimola, M. Aschi, R. Orlando, P. Ugliengo, Does adsorption at hydroxyapatite surfaces induce peptide folding? Insights from large-scale B3LYP calculations, *J. Am. Chem. Soc.* 134 (2012) 10899–10910, <https://doi.org/10.1021/ja302262y>.
- [36] A. Rimola, M. Corno, C.M. Zicovich-Wilson, P. Ugliengo, Ab initio modeling of protein/biomaterial interactions: glycine adsorption at hydroxyapatite surfaces, *J. Am. Chem. Soc.* 130 (2008) 16181–16183, <https://doi.org/10.1021/ja806520d>.
- [37] A.A. Sawyer, K.M. Hennessy, S.L. Bellis, Regulation of mesenchymal stem cell attachment and spreading on hydroxyapatite by RGD peptides and adsorbed serum proteins, *Biomaterials* 26 (2005) 1467–1475, <https://doi.org/10.1016/j.biomaterials.2004.05.008>.
- [38] K. Kandori, M. Mukai, A. Yasukawa, T. Ishikawa, Competitive and cooperative adsorptions of bovine serum albumin and lysozyme to synthetic calcium hydroxyapatites, *Langmuir* 16 (2000) 2301–2305, <https://doi.org/10.1021/la990642a>.
- [39] K. Kandori, K. Murata, T. Ishikawa, Microcalorimetric study of protein adsorption onto calcium hydroxyapatites, *Langmuir* 23 (2007) 2064–2070, <https://doi.org/10.1021/la062562n>.
- [40] M.L. Wallwork, J. Kirkham, J. Zhang, D.A. Smith, Binding of matrix proteins to developing enamel crystals: an atomic force microscopy study, *Langmuir* 17 (2001) 2508–2513, <https://doi.org/10.1021/la001281r>.
- [41] M. Brundin, D. Figdor, G. Sundqvist, U. Sjögren, DNA binding to hydroxyapatite: a potential mechanism for preservation of microbial DNA, *J. Endod.* 39 (2013) 211–216, <https://doi.org/10.1016/j.joen.2012.09.013>.
- [42] L.J. del Valle, O. Bertran, G. Chaves, G. Revilla-López, M. Rivas, M.T. Casas, J. Casanovas, P. Turon, J. Puiggali, C. Alemán, DNA adsorbed on hydroxyapatite surfaces, *J. Mater. Chem. B* 2 (2014) 6953–6966, <https://doi.org/10.1039/C4TB01184H>.
- [43] K. Nakanishi, T. Sakiyama, K. Imamura, On the adsorption of proteins on solid surfaces, a common but very complicated phenomenon, *J. Biosci. Bioeng.* 91 (2001) 233–244, [https://doi.org/10.1016/S1389-1723\(01\)80127-4](https://doi.org/10.1016/S1389-1723(01)80127-4).
- [44] M. Mohsen-Nia, M. Massah Bidgoli, M. Behrashi, A. Mohsen Nia, Human serum protein adsorption onto synthesis nano-hydroxyapatite, *Protein J.* 31 (2012) 150–157, <https://doi.org/10.1007/s10930-011-9384-3>.
- [45] D.T.H. Wassell, R.C. Hall, G. Embery, Adsorption of bovine serum albumin onto hydroxyapatite, *Biomaterials* 16 (1995) 697–702, [https://doi.org/10.1016/0142-9612\(95\)99697-K](https://doi.org/10.1016/0142-9612(95)99697-K).
- [46] E. Mavropoulos, A.M. Costa, L.T. Costa, C.A. Achete, A. Mello, J.M. Granjeiro, A.M. Rossi, Adsorption and bioactivity studies of albumin onto hydroxyapatite surface, *Colloids Surf. B Biointerfaces* 83 (2011) 1–9, <https://doi.org/10.1016/j.colsurfb.2010.10.025>.
- [47] W. Norde, A.C.I. Anusiemi, Adsorption, desorption and re-adsorption of proteins on solid surfaces, *Colloids Surf.* 66 (1992) 73–80, [https://doi.org/10.1016/0166-6622\(92\)80122-I](https://doi.org/10.1016/0166-6622(92)80122-I).
- [48] M. Rabe, D. Verdes, S. Seeger, Understanding protein adsorption phenomena at solid surfaces, *Adv. Colloid Interface Sci.* 162 (2011) 87–106, <https://doi.org/10.1016/j.cis.2010.12.007>.
- [49] Q. Luo, J.D. Andrade, Cooperative adsorption of proteins onto hydroxyapatite, *J. Colloid Interface Sci.* 200 (1998) 104–113, <https://doi.org/10.1006/jcis.1997.5364>.
- [50] K.K. Kandori, A. Fudo, T. Ishikawa, Study on the particle texture dependence of protein adsorption by using synthetic micrometer-sized calcium hydroxyapatite particles, *Colloids Surf. B Biointerfaces* 24 (2002) 145–153, [https://doi.org/10.1016/S0927-7765\(01\)00227-2](https://doi.org/10.1016/S0927-7765(01)00227-2).
- [51] K. Kandori, H. Hamazaki, M. Matsuzawa, S. Togashi, Selective adsorption of acidic protein of bovine serum albumin onto sheet-like calcium hydroxyapatite particles produced by microreactor, *Adv. Powder Technol.* 25 (2014) 354–359, <https://doi.org/10.1016/j.apt.2013.05.016>.
- [52] K. Kandori, M. Saito, H. Saito, A. Yasukawa, T. Ishikawa, Adsorption of protein on non-stoichiometric calcium-strontium hydroxyapatite, *Colloids Surfaces A, Int. J. Pavement Eng. Asph. Technol.* 94 (1995) 225–230, [https://doi.org/10.1016/0927-7757\(94\)02969-5](https://doi.org/10.1016/0927-7757(94)02969-5).
- [53] E. Jimenez-Izal, F. Chiatti, M. Corno, A. Rimola, P. Ugliengo, Glycine adsorption at nonstoichiometric (010) hydroxyapatite surfaces: a B3LYP study, *J. Phys. Chem. C* 116 (2012) 14561–14567, <https://doi.org/10.1021/jp304473p>.
- [54] F. Chiatti, M. Corno, Y. Sakhno, G. Martra, P. Ugliengo, Revealing hydroxyapatite nanoparticle surface structure by CO adsorption: a combined B3LYP and infrared study, *J. Phys. Chem. C* 117 (2013) 25526–25534, <https://doi.org/10.1021/Jp4086574>.
- [55] G. Celotti, A. Tampieri, S. Sprio, E. Landi, L. Bertineti, G. Martra, C. Ducati, Crystallinity in apatites: how can a truly disordered fraction be distinguished from nanosize crystalline domains? *J. Mater. Sci. Mater. Med.* 17 (2006) 1079–1087, <https://doi.org/10.1007/s10856-006-0534-7>.
- [56] A. Meldrum, L.M. Wang, R.C. Ewing, Electron-irradiation-induced phase segregation in crystalline and amorphous apatite: a TEM study, *Am. Mineral.* 82 (1997) 858–869, <https://doi.org/10.2138/am-1997-9-1003>.
- [57] L. Wang, S. Wang, R. Ewing, A. Meldrum, R. Birtcher, P. Newcomer Provencio, W. Weber, H. Matzke, Irradiation-induced nanostructures, *Mater. Sci. Eng. A* 286 (2000) 72–80, [https://doi.org/10.1016/S0921-5093\(00\)00677-8](https://doi.org/10.1016/S0921-5093(00)00677-8).
- [58] F. Catalano, G. Alberto, P. Ivanchenko, G. Dovbeshko, G. Martra, Effect of silica surface properties on the formation of multilayer or submonolayer protein hard corona: albumin adsorption on pyrolytic and colloidal SiO₂ nanoparticles, *J. Phys. Chem. C* 119 (2015) 26493–26505, <https://doi.org/10.1021/acs.jpcc.5b07764>.
- [59] K. Rezwan, L.P. Meier, M. Rezwan, J. Vörös, M. Textor, L.J. Gauckler, Bovine serum albumin adsorption onto colloidal Al₂O₃ particles: a new model based on zeta potential and UV-vis measurements, *Langmuir* 20 (2004) 10055–10061, <https://doi.org/10.1021/la048459k>.
- [60] S. Beychok, Circular dichroism of biological macromolecules, *Science* 154 (80-) (1966) 1288–1299, <https://doi.org/10.1126/science.154.3754.1288>.
- [61] W. Moffitt, J. Yang, The optical rotatory dispersion of simple polypeptides, I, *Proc. Natl. Acad. Sci. U. S. A.* 42 (1956) 596–603, <https://doi.org/10.1073/pnas.42.9.596>.
- [62] C.E. Giacomelli, W. Norde, The adsorption-desorption cycle. Reversibility of the BSA-silica system, *J. Colloid Interface Sci.* 233 (2001) 234–240, <https://doi.org/10.1006/jcis.2000.7219>.
- [63] D.M. Charbonneau, H.A. Tajmir-Riahi, Study on the interaction of cationic lipids with bovine serum albumin, *J. Phys. Chem. B* 114 (2010) 1148–1155, <https://doi.org/10.1021/jp910077h>.
- [64] C.E. Giacomelli, W. Norde, Influence of hydrophobic teflon particles on the structure of amyloid β -peptide, *Biomacromolecules* 4 (2003) 1719–1726, <https://doi.org/10.1021/bm034151g>.



Solid silica nanoparticles as carriers of fluorescent squaraine dyes in aqueous media: Toward a molecular engineering approach

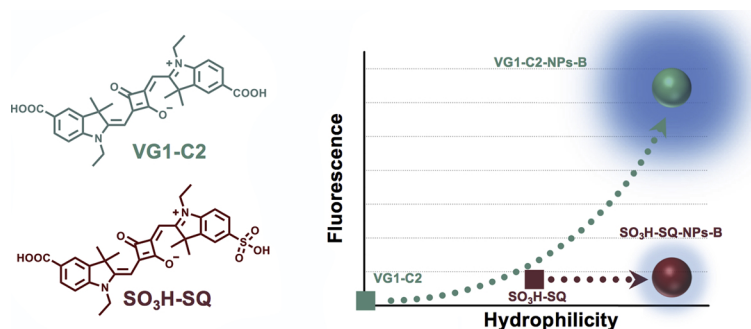


Gabriele Alberto^{a,*}, Nadia Barbero^{a,*}, Carla Divieto^b, Erica Rebba^a, Maria Paola Sassi^b, Guido Viscardi^a, Gianmario Martra^a

^a Department of Chemistry, NIS Interdepartmental and INSTM Reference Centre, University of Torino, Via Pietro Giuria 7, 10125, Torino, Italy

^b Italian National Institute for Metrological Research INRIM, Strada delle Cacce 91, 10135, Torino, Italy

GRAPHICAL ABSTRACT



ARTICLE INFO

Keywords:

Squaraines in water
Hybrid dye-silica solid nanoparticles
Fluorescence
Tissue optical window

ABSTRACT

Hybrid squaraine-SiO₂ nanoparticles extremely homogeneous in size (50 ± 2 nm), and with photoluminescent emission in the optical tissue window, were prepared by using the reverse microemulsion technique. Three different high quantum-yield squaraine dyes were used and the photophysical behavior of the prepared samples were qualitatively and quantitatively studied, by steady state and time-resolved photoluminescence, in order to establish structure-property relationships useful for the optimization of the preparation method. These squaraine dyes are insoluble in water and suffer a severe decrease of quantum yield if derivatized with polar groups. The role of the hydrophilicity of the dye-APTS adduct in ruling its dispersion in the nascent silica matrix was confirmed, and the possibility to improve the tuning of the process by proper administration of the adduct with the co-surfactant was demonstrated.

1. Introduction

Organic dyes with absorption in the optical tissue window from 600 to 850 nm, where both the advantages of low absorption by tissues and negligible self-fluorescence of biological molecules are present, have

emerged as a promising tool for bioanalytical or biologically related applications and for *in vivo* fluorescence imaging. Polymethine dyes [1], such as cyanines and squaraines, offer numerous advantages such as their easiness in designing new molecules with the desired photochemical properties simply by elongating the central bridge and/or

* Corresponding authors.

E-mail addresses: gabriele.aberto@unito.it (G. Alberto), nadia.barbero@unito.it (N. Barbero), c.divieto@inrim.it (C. Divieto), erica.rebba@unito.it (E. Rebba), m.sassi@inrim.it (M.P. Sassi), guido.viscardi@unito.it (G. Viscardi), gianmario.martra@unito.it (G. Martra).

<https://doi.org/10.1016/j.colsurfa.2019.01.052>

Received 9 November 2018; Received in revised form 25 January 2019; Accepted 27 January 2019

Available online 29 January 2019

0927-7757/ © 2019 Elsevier B.V. All rights reserved.

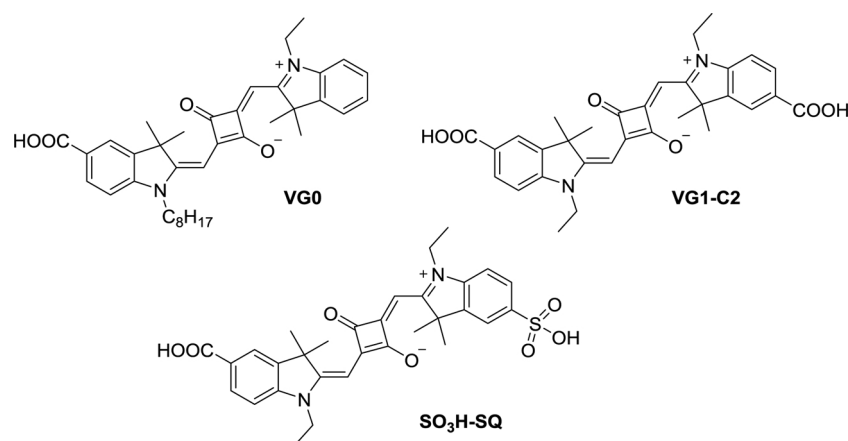


Fig. 1. Structures of VG0, VG1-C2 and SO₃H-SQ.

tuning the lateral functional groups [2–4]. In this manner, dyes with absorption and emission spectra properly located in the optical tissue window are obtained [5–8]. Cyanines and squaraines have both their own pros and cons, however squaraines, resulting from the di-condensation between squaric acid and electron rich molecules, are typically characterized by a pH stability and photostability significantly higher than those found for cyanines [9,10]. Unfortunately, squaraines are poorly soluble in aqueous media, and the consequent easy formation of non-fluorescent aggregates heavily limited their adoption as fluorescent markers for biological applications [11]. Moreover, the usual strategy used in organic chemistry targeting, i.e. the introduction of a group ionizable in water, such as a sulfonic moiety, is detrimental, because once dissolved in water, such derivatized squaraine dyes show a very low quantum yield with respect to pristine fluorophores dissolved in less polar media [12]. In order to overcome these problems, the incorporation of these hydrophobic dyes in carriers appeared to be a mandatory step for their dispersion in physiological conditions. As far as molecular carriers are concerned, a proposed approach is the encapsulation of the dye inside a permanently interlocked rotaxane molecule, also increasing the resistance to chemical and photochemical degradation [13], or in micelles [14]. Moreover, SQ-based self-assembly in hydrophobic phospholipid bilayers of liposomes were successfully used for *in vivo* imaging [15]. Squaraine dyes have also been encapsulated in polymeric nanoparticles [16] or polymer dots [17] for biomedical applications in order to prevent aggregation in physiological environments. In the domain of inorganic carriers, a possibility is the intercalation of photoactive compounds into hydrotalcite (layered double hydroxides; LDH) [18], or they can be loaded inside porous or nonporous amorphous silica nanoparticles, depending on the specific application. Silica NPs can be categorized as mesoporous or nonporous (solid) NPs, both having an amorphous silica structure. In general, amorphous silica NPs are particularly interesting because of their unique properties such as hydrophilic surface, versatile surface functionalization, excellent biocompatibility, ease of large-scale synthesis, and low cost production [19]. When multifunctional nanoplatforms are pursued, the materials of interest are mesoporous silica nanoparticles, used as such, for instance for photodynamic therapy [20], or wrapped with graphene oxide sheets, to protect the squaric ring from possible nucleophilic attack of molecular components of *in-vitro* and *in-vivo* biological media [21]. When imaging is the intended application, a relevant nanocarrier is constituted by solid non-porous silica nanoparticles (NPs), highly protecting encapsulated dye molecules [22–24]. Hybrid dye doped nonporous amorphous solid silica NPs can be prepared by hydrolysis and polycondensation of a silicon alkoxide, such as tetraethylorthosilicate (TEOS), and fluorophores derivatized with an alkoxy silane moiety, allowing the encapsulation of dye molecules in the nascent silica matrix. The process can be carried out in homogeneous

solution [25], i.e. exploiting the so-called Stöber method, or in reverse microemulsion [26]. In both cases, the condensation reaction among molecular precursors of silica typically occurs by addition of a basic agent, and this can prevent the production of silica NPs hybridized with dyes as penta/hepta-methine cyanines, which do not resist a high pH. Conversely, squaraines do not suffer this limitation, and then appear as relevant organic dyes to be vehiculated in aqueous media by entrapment in silica NPs. Despite the complexity of the synthesis procedure, the microemulsion method can be preferred to the Stöber one, owing to the possibility to obtain particles with a very narrow size distribution, thus simplifying at least one aspect of the complex combination of parameters affecting the behavior of nanomaterials in biological media. Moreover, previous research works devoted to the encapsulation of three methine cyanines [27,28] allowed to highlight that the dispersion of these visible dye molecules throughout the nascent silica matrix is ruled by the relative hydrophilicity of TEOS and the dye-3-aminopropyltriethoxysilane (APTS) adduct. This molecular feature affects the relative kinetic of the partition of TEOS and the dye-APTS adducts in the water pool inside reverse micelles [13]. Avoiding aggregation of dyes within the nanocarrier is mandatory to preserve photoemission performances. To the best of our knowledge, no examples of squaraine dyes encapsulated in non-porous amorphous silica NPs have been reported so far.

This was the basis of the present work, devoted to the elucidation of molecular aspects and preparation procedures relevant for the production of photoluminescent hybrid squaraines-SiO₂NPs. To this aim, three squaraine dyes with different chemical structures and degree of hydrophilicity (Fig. 1) were used to synthesize silica NPs by the reverse microemulsion method. Each sample was characterized in terms of size and morphology by electronic transmission microscopy and their photophysical properties were investigated by UV-vis absorption and steady-state/time-resolved photoemission spectroscopy in order to define structure-property relationships useful for the optimization of the photoemission performances.

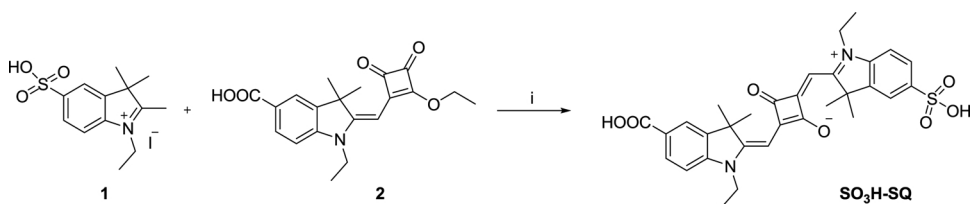
2. Experimental details

2.1. Syntheses: chemicals and procedures

All reagents and solvents, of a highly pure grade, were purchased from Sigma Aldrich, Fluka, Merck or Riedel de Haen and were used without any further purification.

2.1.1. Synthesis of squaraines

VG0 and VG1-C2 were prepared as previously described [2]. For the synthesis of SO₃H-SQ a modified procedure as reported in the literature [2,29] was followed. An equimolar mixture (0.84 mmol) of



Scheme 1. Synthesis of $\text{SO}_3\text{H-SQ}$. Experimental conditions: (i) toluene/butanol (1:1), MW, 25 min, 160°C .

compound **1** and **2** (Scheme 1) were introduced into a 20 ml microwave reaction vial with toluene and butanol (18 ml, 1:1), sealed with a crimp cap and heated in the microwave system (single-mode Biotage Initiator 2.5) at 160°C for 25 min. The green precipitate which is formed is washed with diethyl ether and further purified by a semi-preparative HPLC system (by Schimatzu, equipped with SCL 10Avp, SPD 10Avp, a LC8A pump and a Phenomenex column Synergi Fusion-RP $4\ \mu$, 150×21.20 mm) using an isocratic flow of methanol with formic acid (1%, v/v) to obtain $\text{SO}_3\text{H-SQ}$ (105 mg, yield = 22%) as a green powder.

^1H NMR (200 MHz, D_2O), δ : 8.01–7.72 (m, 6H), 7.15 (s, 1H), 6.91 (s, 1H), 4.42 (m, 2H), 3.79 (m, 2H), 1.47 (s, 12H), 1.14 (s, 6H). The compound solubility proved too low to record a ^{13}C NMR spectrum. Elemental Analysis: $\text{C}_{31}\text{H}_{32}\text{N}_2\text{O}_7\text{S}$; calcd. C, 64.57; H, 5.59; N, 4.86; O, 19.42; S, 5.56; found C, 64.46; H, 5.52; N, 4.83; O, 19.12; S, 5.35. MS (ESI) $[\text{M} - \text{H}]^-$ 575.60.

2.1.2. Synthesis of squaraine-silane derivatives

The *N*-Hydroxysuccinimide (NHS) active esters of the two non-symmetrical squaraines VG0 and $\text{SO}_3\text{H-SQ}$ were synthesized by reacting 0.02 mmol of each fluorophore with NHS (0.08 mmol) and *N,N*-Dicyclohexylcarbodiimide (DCC, 0.08 mmol) in dimethylformamide (DMF, 2.0 ml) and stirring for 4 h at 80°C ; in the case of the symmetrical VG1-C2, 0.16 mmol of both NHS and DCC were used due to the presence of two carboxyl groups. Reactions were monitored by mass spectrometry until complete conversion and then the product was separated through dilution in diethyl ether and filtration to obtain products as powders.

Squaraine-silane derivatives were then prepared by adding 3-aminopropyltriethoxysilane (APTS; $46.0\ \mu\text{mol}$, $10\ \mu\text{L}$ for VG0-NHS and $\text{SO}_3\text{H-SQ-NHS}$; $92.0\ \mu\text{mol}$, $20\ \mu\text{L}$ for VG1-C2-NHS) to squaraine-NHS solutions in 0.5 ml of anhydrous DMF and stirring the mixture for 24 h at room temperature; reactions were monitored by thin layer chromatography until complete disappearance of former NHS esters. The obtained squaraine-silane derivatives (hereafter X-APTS, where X is the squaraine code) were then used without further purification in order to avoid the occurrence of self-polymerization.

Schemes of the syntheses are shown in the Supporting Information (hereafter SI).

2.1.3. Synthesis of squaraine-loaded silica NPs

Hybrid squaraine-silica NPs were prepared by the reverse microemulsion technique already reported in previous works [27,28,30]. Briefly, a water in oil microemulsion was prepared by mixing cyclohexane (75.0 ml), Triton X-100 (18.85 g), *n*-hexanol (18.0 ml) and distilled water (5.4 ml); the mixture was gently stirred for ca. 30 min and then 0.05 ml of a 0.01 M squaraine-APTS in DMF was added; after further 15 min, TEOS (1.0 ml, 4.5 mmol) and NH_4OH (28–30%, 0.7 ml) were added to start the NPs formation. Reaction was stirred for 16 h at room temperature and then was stopped by adding 50.0 ml of acetone; particles were extracted from the supernatant by centrifugation (10k rpm, r.t.) and washed twice in ethanol and several times in distilled water by resuspension and centrifugation cycles until complete removal of the surfactant. Finally, squaraine-loaded silica NPs (hereafter X-NPs, where X is the squaraine code) were stored as suspensions in distilled water at room temperature in the dark until needed.

In order to attain possible optimization of the preparation technique, in two cases the hybrid NPs preparation protocol was changed

(vide infra) and the resulting materials were labeled as X-NPs-B.

For solvatochromic experiments, NPs stored as water suspensions were first centrifuged at 10k rpm for 20 min and then resuspended using acetone. Then, NPs were washed twice by centrifugation/resuspension cycles in order to completely remove water and, finally, the concentration of the final suspensions was adjusted to $1\ \text{mg}\ \text{ml}^{-1}$.

2.2. Methods

2.2.1. Characterization of dyes

Thin-layer chromatography was performed on silica gel 60 F254 plates. ESI-MS spectra were recorded using a LCQ Thermo Advantage Max spectrometer, with electrospray interface and ion trap as mass analyzer. The flow injection effluent was delivered into the ion source using nitrogen as sheath and auxiliary gas. ^1H NMR (200 MHz) spectra were recorded on a Bruker Avance 200 NMR.

2.2.2. UV-vis absorption spectroscopy

UV-VIS electronic absorption spectra of the squaraine in solution and of the supernatants derived from nanoparticle extraction from the microemulsion mixture were measured by a Cary 300 Bio spectrophotometer (Varian, Santa Clara, CA, USA), using quartz cuvettes (1 cm pathway length).

For the determination of absorption coefficients, every dye was weighed, (7.0–10.0 mg), and diluted to 10.0 ml in a flask using DMSO. From this solution, 0.25 ml were taken and diluted to 25.0 ml with the proper solvent (mother solution). Three dilutions were prepared by diluting 1.0, 2.5 and 5.0 ml of this solution to 25.0 ml. Those solutions were analyzed by UV-vis spectroscopy. Absorbance at the λ_{max} for every diluted solution was plotted vs. dye concentration and a linear fitting was performed. The slope of the plot is the molar absorption coefficient (ϵ). The determination was made, in duplicate, by preparing two separate concentrated dye mother solutions in DMSO. The $\log\epsilon$ obtained from the two separate data sets was compared: if their difference was less or equal to 0.02 respect to their average, the data were considered acceptable and the average of the two values was taken as the official value. Otherwise, a further concentrated dye mother solution in DMSO was prepared, the whole procedure was repeated and the $\log\epsilon$ data were compared.

2.2.3. UV-vis photoemission spectroscopy

Photoluminescence and excitation spectra in steady state mode were acquired using a Horiba Jobin Yvon Fluorolog 3 TCSPC fluorimeter equipped with a 450-W Xenon lamp and a Hamamatsu R928 photomultiplier.

The absolute quantum yield of each dye in solution was determined combining Quanta- ϕ with Fluorolog 3. The reported values are the average of three measurements using three different dye solutions.

Fluorescence lifetimes were measured by the time correlated single photon counting method (Horiba Jobin Yvon) using a 560 nm Horiba Jobin Yvon NanoLED as excitation source and an impulse repetition frequency of 1 MHz positioned at 90° with respect to a TBX-04 detector. Lifetimes were calculated using DAS6 decay analysis software.

2.2.4. High resolution transmission electron microscopy (HRTEM)

Size and morphology of NPs were analyzed with a 3010 Jeol microscope operating at 300 kV. A droplet of each nanoparticle water

suspension (1.0 mg ml^{-1}) was spread on a copper grid coated with a carbon film and then water was allowed to slowly evaporate in order to limit particle agglomeration. Size distribution was evaluated by measuring at least 300 nanoparticles and the mean diameters were calculated as $d_m = \sum d_i n_i / \sum n_i$ (n_i = number of particles of diameter d_i); results were reported as $d_m \pm \text{stdv}$.

3. Results and discussion

3.1. Synthesis of squaraines and squaraine-silane derivatives

VG0 and VG1-C2 squaraines were prepared via a microwave condensation reaction based on a previously reported procedure [2] while SO₃H-SQ was synthesized by a microwave-assisted condensation of 5-sulfo-indolenine salt 1 [29] and carboxymisquarate 2 [2] (see Scheme 1).

Squaraine-silane derivatives were prepared via a previously reported method [12] through the NHS ester modification of the squaraine carboxylic group and subsequent reaction with APTS (see Scheme S2 in the SI for SO₃H-SQ modification).

3.2. Photophysical properties of squaraines in solution

The photophysical behaviour of each squaraine dye in solution was investigated together with the determination of the correspondent molar decadic absorption coefficient and absolute quantum yield by means of absorption and both steady-state and time-resolved photoemission spectroscopies (see Table 1).

The UV–vis absorption spectra (see Fig. 2) of the squaraine dyes show absorption maxima between 630 nm and 646 nm with high molar extinction coefficients ($\log \epsilon$ around 5.40 in organic solvents and 4.51 in water). The main absorption peak is associated to the $\pi \rightarrow \pi^*$ HOMO–LUMO transitions, mainly localized on the squarainic core [31,32], while the shoulder at higher energy is due to the HOMO–LUMO + 1 transition. When excited within the absorption band at room temperature, the three types of squaraines emit a luminescence spectrum almost specular to the absorption one, with maxima ranging from 639 to 656 nm, thus with small Stokes shifts as expected for squaraine dyes [33].

Fluorescence lifetime and quantum yield of VG0 in methanol and VG2-C1 in acetone are in the ranges typical for squaraines in organic media [34]. Also the much lower τ and Φ of SO₃H-SQ is in agreement with the twisting relaxation process, expected for indolenine-based squaraines, connected with an increase of the excited state dipole moment, resulting in an enhancement of nonradiative losses in polar solvents [35,36].

3.3. Shape, size and dye-content of squaraine loaded silica NPs

Representative TEM micrographs of the three squaraine-NPs samples are shown in Fig. 3, where the highly regular spherical shape (upper panels) and quite homogeneous size of NPs around a mean diameter of 50 nm (lower panels) can be appreciated. Hence, on the

Table 1

Main optical characteristics of VG0 in methanol, VG1-C2 in methanol and acetone and SO₃H-SQ in water.

	λ_{abs} (nm)	$\log \epsilon$	λ_{em} (nm)	τ (ns)	ϕ
VG0 ^a	635	5.39	645	0.28 (100%)	0.15
VG1-C2 ^a	639	5.47	647	0.46 (100%)	0.12
VG1-C2 ^b	646	5.40	656	0.99 (100%)	0.27
SO ₃ H-SQ ^c	631	4.51	639	0.11 (100%)	0.023

^a in methanol.

^b in acetone.

^c in water.

basis of the TEOS-to-SiO₂ conversion yield, the density of NPs (ca. $2.2 \text{ g} \cdot \text{cm}^{-3}$) [28] and the calculated average nanoparticle volume, the total number of NPs obtained by each preparation was estimated.

As a second step, for each sample the total amount of squaraine molecules associated to NPs was calculated as the difference between their initial amount and that remained in the reaction media after the accomplishment of the formation of NPs, as determined spectrophotometrically after the separation of NPs by centrifugation. This was possible because no squaraine degradation products were detected in the UV–vis spectra of the post-reaction liquid medium. Thus, the average number of dye molecules per nanoparticle was calculated (Table 2). Apparently, the VG0-APTS adduct was unable to participate to the formation of NPs, whereas this was the case for ca. 45% and 65% of VG1-C2-APTS and SO₃H-SQ-APTS species present in the relevant reaction media, resulting in ca. 50 and 70 dye molecules-per-NP, respectively.

The lack of encapsulation of VG0-APTS in the silica matrix should be rationalized in terms of a so poor hydrophilicity of this squaraine derivative to prevent its transfer into the water pool in the core of reverse micelles, and thus this squaraine derivative will be no longer considered. Conversely, the presence of two triethoxysilane moieties in VG1-C2-APTS counterbalance enough the hydrophobicity of the squaraine motif to allow this derivative to reach the water pools and participate to hydrolysis and condensation with TEOS during the formation of NPs. As expected, a stronger effect resulted from the presence of the sulphonic group in SO₃H-SQ-APTS, which was involved in the formation of NPs in a larger extent. However, the rate of transfer into the micelles of neither VG1-C2-APTS nor SO₃H-SQ-APTS was high enough to allow all the dye derivative to participate to the reaction before the accomplishment of the formation of the NPs.

Apparently, the amount of squaraine molecules per NP was too low for allowing a characterization of molecules entrapped in the silica matrix also by FT-IR spectroscopy, even using highly concentrated self-supporting pellets of hybrid nanoparticles.

3.4. Photoemission properties and location of the entrapped squaraines

In order to evaluate any possible modification of the photophysical behaviour of the entrapped fluorophores, steady state photoemission and excitation spectra of hybrid VG1-C2-NPs and SO₃H-SQ-NPs were recorded in suspension and compared to the data obtained for the correspondent dye derivatives in solution (Fig. 4). Data obtained for VG1-C2 and VG1-C2-APTS were similar, indicating that the derivatization did not modify significantly the photophysical behaviour of the dye. SO₃H-SQ was only soluble in water, and this prevented a comparison with SO₃H-SQ-APTS in the same medium, because of the sensitivity of the derivative to hydrolysis. Thus, the pristine VG1-C2 and SO₃H-SQ were considered for the comparisons with their derivative associated to NPs.

For both types of hybrid NPs, excitation instead of absorption in transmission was recorded because the lower sensitivity of the latter did not allow to record spectra with an acceptable signal-to-noise ratio at suspension concentrations low enough to avoid light scattering.

In Fig. 4 panel A, excitation and photoemission spectra of VG1-C2 in solution and VG1-C2-NPs in suspension are reported; acetone was used as solution and suspension medium due to the low solubility of VG1-C2 in water. It can be clearly observed that both excitation and emission signals of the NPs are identical to the correspondent ones of the fluorophore in solution suggesting that no modifications of the energies and relative probabilities of the electronic transitions occurred due to the association with the inorganic matrix. On the contrary, in the case of SO₃H-SQ (Fig. 4, panel B), where the hydrophilicity of the dye allowed to use water as medium for both the molecule in solution and the hybrid NP suspension, the association of dye derivatives with silica produced a decrease of the energies of absorption and fluorescence transitions as indicated by the 9 nm red shift of both signals. The

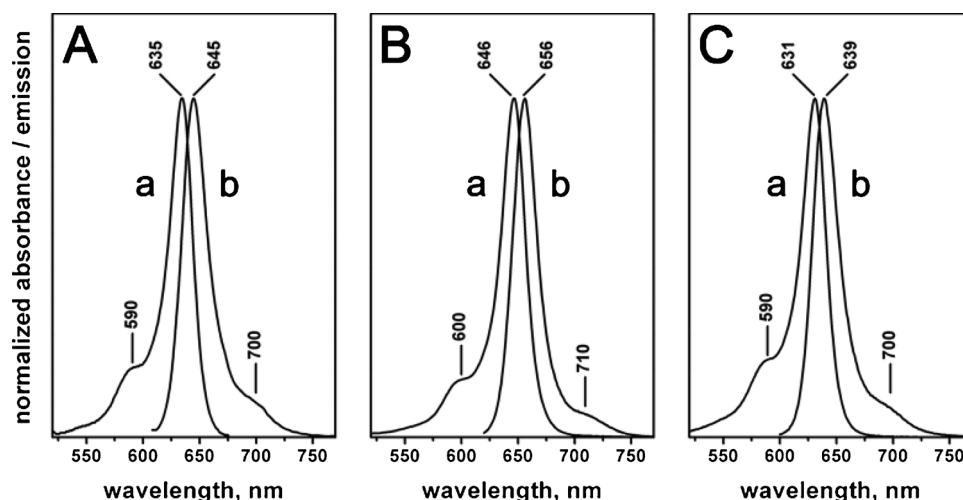


Fig. 2. Absorption (a) and emission spectra ($\lambda_{\text{ex}} = 590 \text{ nm}$) (b) of VG0 in methanol (panel A), VG1-C2 in acetone (panel B) and SO₃H-SQ in water (panel C).

coincidence of the shape of the spectra profiles exhibited by both dye/hybrid NPs pairs allowed to exclude the occurrence of intra-particle autoabsorption effects. Hence, as the framework of amorphous silica is apolar [37] the red-shift observed for SO₃H-SQ-NPs should be reasonably assigned to a solvatochromic effect due to the decrease of the polarity of the environment experienced by entrapped squaraine derivatives with respect to the ones in water solution. The solvatochromic behavior of the SO₃H-SQ in solution were reported in Fig. S1 in the SI for the sake of comparison.

Time-resolved photoemission measurements were also carried out, and the results are listed in Table 3, compared with relevant cases of squaraine derivatives in solution. The targeted suspension medium for hybrid NPs is water, but also acetone was considered because of its lower polarity, thus useful to reveal possible solvatochromic effects due to dye molecules not entrapped in the bulk of NPs. For all suspensions of hybrid NPs, bi-functional equations were necessary to fit the decay

Table 2

Yields of entrapment of squaraine-APTS molecules in silica NPs.

	Yield of Squaraine-APTS molecules entrapment (%)	Squaraine-APTS molecules per NP (n')
VG0-NPs	0	0
VG1-C2-NPs	46	47
SO ₃ H-SQ-NPs	66	68
VG1-C2-NPs-B	41	42
SO ₃ H-SQ-NPs-B	63	65

curves, indicating that for both VG1-C2-APTS and SO₃H-SQ-APTS derivatives two different scenarios of interaction with the silica host are present. For VG1-C2-APTS, independently on the suspension medium, one fluorescence lifetime (τ_F^1) is slightly longer than what found for the molecular form in acetone solution, whereas the other (τ_F^2) appears

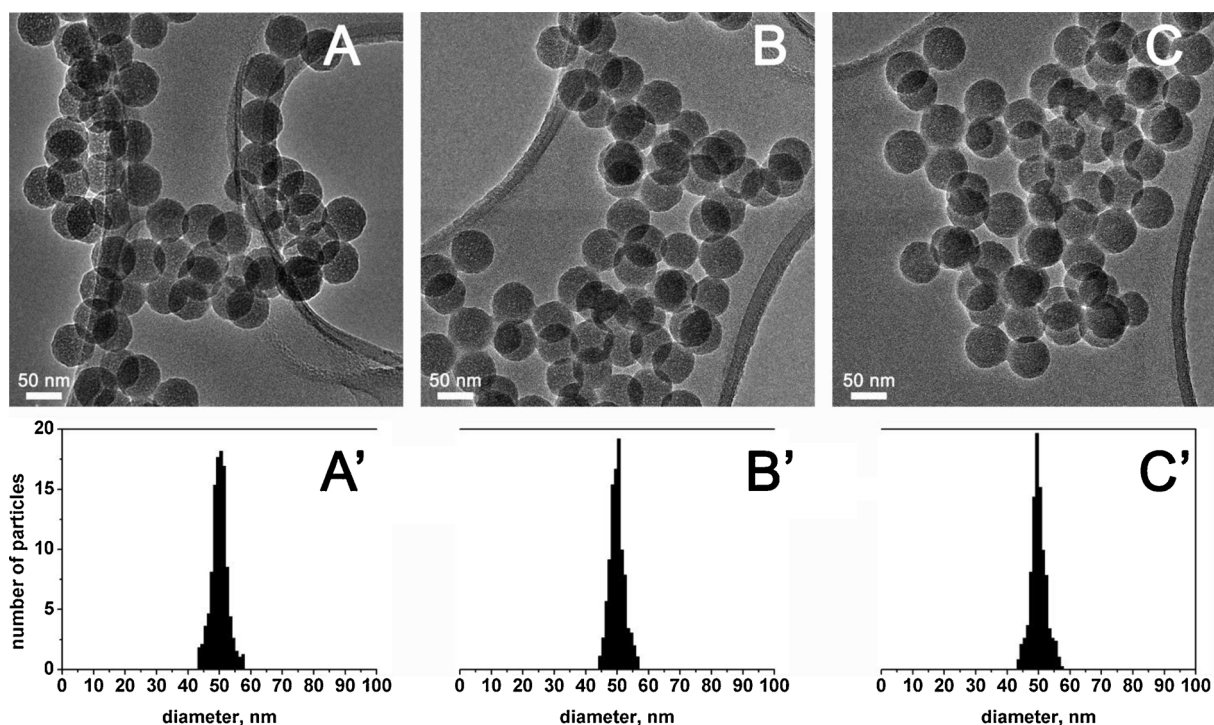


Fig. 3. Representative TEM images of VG0-NPs (A), VG1-C2-NPs (B) and SO₃H-SQ-NPs (C) and correspondent size distribution histograms. Original magnification of images: 500,000 \times . Scale bar: 50 nm.

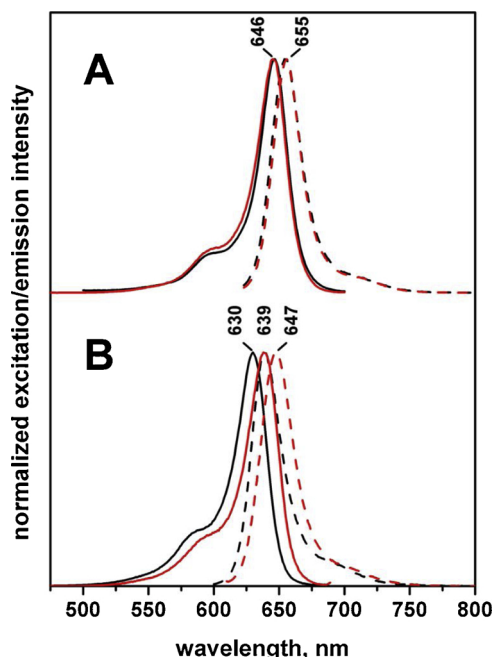


Fig. 4. Panel A: excitation (solid curves, $\lambda_{em} = 655$ nm) and photoemission (dashed curves, $\lambda_{exc} = 590$ nm) spectra of VG1-C2 in acetone solution (black curve, $5.0 \cdot 10^{-6}$ M) and VG1-C2-NPs in acetone suspension (red curve, $3.0 \cdot 10^{-8}$ mg \cdot ml⁻¹); Panel B: excitation (solid curves, $\lambda_{em} = 640$ nm) and photoemission (dashed curves, $\lambda_{exc} = 590$ nm) spectra of SO₃H-SQ in water solution (black curve, $5.0 \cdot 10^{-6}$ M) and SO₃H-SQ-NPs in water suspension (red curve, $3.0 \cdot 10^{-8}$ mg \cdot ml⁻¹). All spectra were normalized with respect to the maximum for the sake of clarity (For interpretation of the references to colour in this figure legend, the reader is referred to the web version of this article).

Table 3

Emission decay times ($\lambda_{exc} = 560$ nm) of: VG1-C2 in acetone solution ($5 \cdot 10^{-7}$ M); VG1-C2-NPs and VG1-C2-NPs-B in acetone and water suspension (0.1 mg ml⁻¹); SO₃H-SQ in water solution ($1 \cdot 10^{-6}$ M); SO₃H-SQ-NPs and SO₃H-SQ-NPs-B in water and acetone suspension (0.1 mg ml⁻¹).

	Medium	τ_F^0 (ns)	% τ_F^0 (ns)	τ_F^1 (ns)	% τ_F^1 (ns)	χ^2
VG1-C2	acetone	0.99	100	—	—	1.01
VG1-C2-NPs	acetone	1.19	21	2.42	79	1.12
	water	1.06	31	2.37	69	1.04
SO ₃ H-SQ-NPs	acetone	1.10	15	2.38	85	1.08
	water	0.80	21	2.31	79	1.02
SO ₃ H-SQ	water	0.11	100	—	—	1.03
VG1-C2-NPs-B	acetone	1.35	25	2.44	75	1.04
	water	1.02	43	2.19	57	1.13
SO ₃ H-SQ-NPs-B	acetone	1.21	35	2.62	65	1.07
	water	0.99	46	2.38	54	1.02

increased of ca. 2.5 times with respect to that comparative form. In the case of SO₃H-SQ-APTS, the association with the silica matrix resulted in two lifetimes both significantly longer than for the molecular form in water solution, with an increase of ca. 7–10 and ca. 20 times, for τ_F^0 and τ_F^1 , respectively. For both types of hybrid dye-SiO₂ NPs, the relative population of fluorescent molecules showing the longer lifetime is the more abundant by far.

For hybrid dye-NPs, the increase of fluorescence lifetime is the result of the decrease in rotational/twisting degrees of freedom, and in possible detrimental effects due to the interaction with highly polar media, such as water. Thus, data obtained for SO₃H-SQ-NPs indicate that SO₃H-SQ derivatives should be not simply anchored on the surface of NPs. Because of the similarity of τ_F^1 values, significantly longer than the fluorescence lifetime of VG1-C2-APTS in acetone solution, the same should occur at least for the most abundant fraction of fluorescent dyes

in VG1-C2-NPs. Conversely, the other fraction should experience an interaction with its environment with more limited differences with respect of acetone as solvent.

Noticeably, the time resolved photoemission behavior of both VG1-C2-NPs and SO₃H-SQ-NPs appeared sensitive to the suspension medium, with a slight increase of both τ_F^0 and τ_F^1 and, more significantly, with the transfer of ca. a 10% of fluorescent molecules between the relative abundances of dyes showing different fluorescence lifetime.

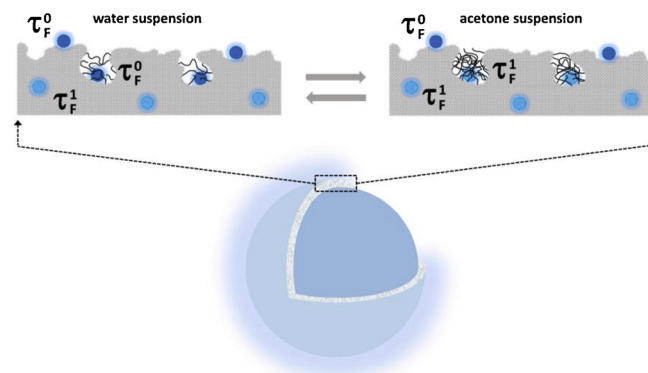
For both VG1-C2-NPs and SO₃H-SQ-NPs, fluorescent dyes showing the longer lifetime are candidate to be depicted as well entrapped in the silica matrix; however, their sensitivity to the suspension medium, and in particular their change in relative abundance, pose a problem.

In this respect, it is useful to remind that silica NPs prepared by the microemulsion or Stöber methods are characterized by the presence of domains, extended from the surface towards the interior, of non-completely condensed silica, resulting in a mass fractal structure sensitive to changes in the external environment [38,39]. Moreover, H/D isotopic exchange indicated that such domains can be infiltrated by water molecules [21]. Therefore, although the sensitivity of the measurement technique did not allow to distinguish more than two relative abundances of fluorescent dyes for each type of hybrid NPs, the obtained data could be explained by assuming the presence of three ensembles of fluorescent dyes in the NPs (Scheme 2):

- a most abundant fraction, characterized by the longer fluorescent lifetime, τ_F^1 (ca.70% and 80% for VG1-C2-NPs and SO₃H-SQ-NPs, respectively), well constrained by the silica matrix, likely in its fully condensed part, insensitive to changes in suspension medium
- a fraction of ca. 20% for VG1-C2-NPs and 15% for SO₃H-SQ-NP, showing the shorter fluorescent lifetime τ_F^0 , located at/near the nanoparticle surface and less constrained by the silica matrix independently on the type of suspension medium
- a fraction, ca. 10% and 6% for VG1-C2-NPs and SO₃H-SQ-NPs, respectively, located in not fully condensed parts of silica matrix more sensitive to the nature of the suspension medium, where fluorescent dyes are less constrained when these parts are infiltrated by water.

3.5. Dyes in solution vs hybrid NPs: comparison of fluorescence intensity

Because of the direct proportionality between fluorescence lifetime and quantum yield [40], the measured increase of fluorescence lifetime for all dye fractions in SO₃H-SQ-NPs and the most abundant one for VG1-C2-NPs appears the basis for expecting an increase in fluorescence intensity of hybrid NPs suspensions with respect to the squaraine derivatives in solutions, for equivalent dye molar concentrations. Hence, the following experimental procedure was used for VG1-C2 and SO₃H-SQ-based systems, differing only for the suspension medium, as described in the previous section. On the basis of the calculated number of



Scheme 2. Distribution of dye molecules in the NPs explaining the different sensitivity to the suspension medium.

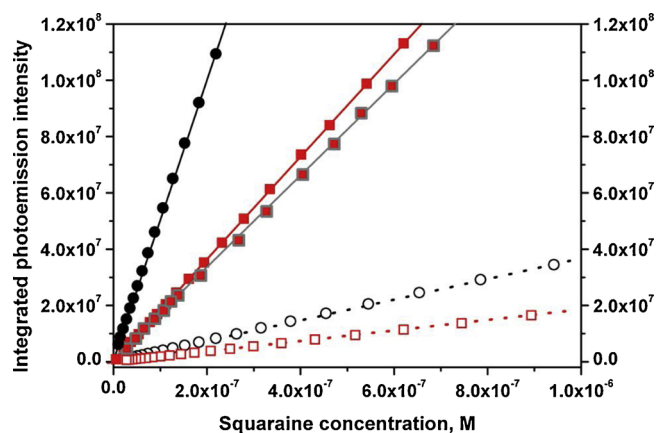


Fig. 5. Comparison of the integrated intensities of photoemission spectra ($\lambda_{\text{exc}} = 590$ nm) of VG1-C2 in acetone solution (black solid dots), VG1-C2-NPs in acetone and water suspension (red solid squares and grey bordered red squares, respectively), $\text{SO}_3\text{H-SQ}$ in water solution (black empty dots) and $\text{SO}_3\text{H-SQ-NPs}$ in water suspension (red empty squares) (For interpretation of the references to colour in this figure legend, the reader is referred to the web version of this article).

squaraine per nanoparticle (Table 2), a series of suspensions at known dye concentration was prepared for both VG1-C2-NPs and $\text{SO}_3\text{H-SQ-NPs}$, as well as a series of solutions of VG1-C2 and $\text{SO}_3\text{H-SQ}$ in the same concentration range. The photoemission spectra were recorded, strictly using the same excitation conditions, and the integrated intensities of photoemission spectra were plotted with respect to the correspondent concentration values (Fig. 5). A straight linear dependence was obtained, clearly indicating that the measurements were affected by neither light scattering nor inter-particle auto-absorption effects.

In agreement with the absolute quantum yields (Table 1), solutions of the two squaraines produces significantly different fluorescence outputs, with VG1C2 (black solid dots) showing integrated intensities of photoemission spectra ca. 13 times higher than SO_3HSQ (black empty dots). For hybrid NPs, the integrated intensities of photoemission spectra of VG1-C2NPs in both acetone (red solid squares) and water (grey bordered red squares) suspensions are ca. 35% and 30%, respectively, of what obtained for VG1C2 solutions (black solid dots), and the relative decrease is limited to ca. 50% when comparing the $\text{SO}_3\text{H-SQ-NPs}/\text{SO}_3\text{HSQ}$ pair (red empty squares and black empty dots, respectively).

Such lower fluorescence intensity should be due to a decrease of the decadic absorption coefficient of squaraines and/or a quenching of a part of them when linked to/entrapped in the silica matrix. Non-light-scattering suspensions of hybrid NPs were too diluted to allow the recording of absorbance spectra, and then no insights were obtained for the first possibility.

Focusing on fluorescence quenching, if occurred it might be of the concentration type, resulting from the formation of aggregates of squaraine derivatives when involved in the growth of NPs. In particular, $\text{SO}_3\text{H-SQ-APTS}$, highly hydrophilic and then easily transferred from the oil phase to the inner water pool of reverse micelles, could have formed aggregates in the first steps of the reaction, whereas the contrary might have occurred for VG1-C2-APTS, definitely less hydrophilic and then involved in the reaction when the nanoparticle formation was almost accomplished.

Based on these hypotheses, two additional samples were prepared by modifying the synthesis procedure with an opposite target, depending on the squaraine derivative considered. Thus, to dilute in time the entering of $\text{SO}_3\text{H-SQ-APTS}$ in the micelles, the adduct was dosed in the reaction medium in small aliquots at regular time intervals (0.01 ml every 10 min) during the first hour of the NPs synthesis. Conversely, VG1-C2-APTS was added to the microemulsion as solution in *n*-hexanol,

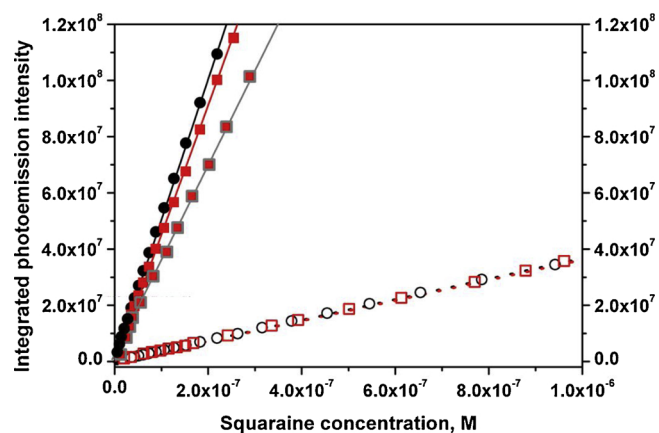


Fig. 6. Comparison of the integrated photoemission intensities ($\lambda_{\text{exc}} = 590$ nm) of VG1-C2 in acetone solution (black solid dots), VG1-C2-NPs-B in acetone and water suspension (red solid squares and grey bordered red squares, respectively), $\text{SO}_3\text{H-SQ}$ in water solution (black empty dots) and $\text{SO}_3\text{H-SQ-NPsB}$ in water suspension (red empty squares). (For interpretation of the references to colour in this figure legend, the reader is referred to the web version of this article).

i.e. the co-surfactant of micelles, in order to facilitate its partition at the boundary between the oil and water phases. In this way, the shortening of the diffusion path should allow this squaraine derivative to be involved not only in late steps of the formation of NPs. These two samples were labeled as $\text{SO}_3\text{H-SQ-NPs-B}$ and VG1-C2-NPs-B.

As for the previous cases, the amount of dyes effectively associated with NPs was calculated, and values very close to the ones already found for the previous corresponding hybrid NPs were obtained (Table 2). The same occurred for steady-state and time resolved photoemission data (Fig. S2 in the SI and Table 3, respectively). Conversely, the integrated intensity of the photoemission spectra of dye equimolar $\text{SO}_3\text{H-SQ}$ solutions/hybrid NPs suspensions in water appears almost coincident, while the values obtained for VG1-C2-NPs-B in acetone and water suspensions are ca. 90% and 70%, respectively of those measured with VG1C2 in acetone solutions (Fig. 6). Thus, the second set of hybrid NPs shows a definitely better performance as photoemitters with respect to the first one (see Fig. 5).

Apparently, the strategies adopted to affect the entrapment of squaraine derivatives on/in the silica NPs were successful, at least partly. In fact, if all dye molecules in hybrid NPs were fluorescent, based on the measured increase in photoemission lifetime, the fluorescence intensity of their suspensions should exceed that of equimolar dye solutions by far. A specific investigation in this respect will be the object of a future investigation.

4. Conclusion

The preparation of hybrid squaraines-silica nanoparticles has been achieved successfully by the reverse microemulsion method. They show, in aqueous suspension, a photoluminescence emission intensity, per dye molecule, equivalent to parent water insoluble squaraine molecules, when in organic solution. Such achievement stems from the adopted molecular engineering approach, based on the hypothesis that the relative hydrophobicity of dye-3-aminopropyltriethoxysilane (APTS) adducts and tetraethylorthosilicate (TEOS) is a key parameter ruling the distribution of fluorophores within the nascent silica matrix. Such hypothesis, developed in previous studies on the preparation of hybrid cyanine- SiO_2 nanoparticles [21], and recently assumed also by other researchers [41], has been here confirmed also for squaraines. In addition, the possibility to improve the tuning of the process by administering the squaraine-APTS adduct with the co-surfactant has been demonstrated. This is the first report, at the best of our knowledge, on

molecular factors ruling the dispersion of squaraines in nonporous amorphous silica nanoparticles, but the number of dye molecules per nanoparticles and likely their photoluminescent fraction are significantly lower with respect what obtained with cyanine dyes [19,21]. Thus, the future steps of this research will be aimed to overcome this gap, targeting brighter hybrid squaraine-SiO₂ nanoparticles.

Acknowledgments

This work was supported by the Fondazione Cassa di Risparmio di Torino, Italy (STemMRef project, cod. ID 48853) and by Compagnia di San Paolo - Università di Torino (NanoSusLeather project).



Appendix A. Supplementary data

Supplementary material related to this article can be found, in the online version, at doi:<https://doi.org/10.1016/j.colsurfa.2019.01.052>.

References

- [1] S. Luo, E. Zhang, Y. Su, T. Cheng, C. Shi, A review of NIR dyes in cancer targeting and imaging, *Biomaterials* 32 (2011) 7127–7138, <https://doi.org/10.1016/j.biomaterials.2011.06.024>.
- [2] N. Barbero, C. Magistris, J. Park, D. Saccone, P. Quagliotto, R. Buscaino, C. Medana, C. Barolo, G. Viscardi, Microwave-assisted synthesis of near-infrared fluorescent indole-based squaraines, *Org. Lett.* 17 (2015) 3306–3309, <https://doi.org/10.1021/acs.orglett.5b01453>.
- [3] W. Sun, S. Guo, C. Hu, J. Fan, X. Peng, Recent development of chemosensors based on cyanine platforms, *Chem. Rev.* 116 (2016) 7768–7817, <https://doi.org/10.1021/acs.chemrev.6b00001>.
- [4] D. Saccone, S. Galliano, N. Barbero, P. Quagliotto, G. Viscardi, C. Barolo, Polymethine dyes in hybrid photovoltaics: structure-properties relationships, *Eur. J. Org. Chem.* 2016 (2016) 2244–2259, <https://doi.org/10.1002/ejoc.201501598>.
- [5] L. Serpe, S. Ellena, N. Barbero, F. Foglietta, F. Prandini, M.P. Gallo, R. Levi, C. Barolo, R. Canaparo, S. Visentin, Squaraines bearing halogenated moieties as anticancer photosensitizers: synthesis, characterization and biological evaluation, *Eur. J. Med. Chem.* 113 (2016) 187–197, <https://doi.org/10.1016/j.ejmech.2016.02.035>.
- [6] J. Atchison, S. Kamila, H. Nesbitt, K.A. Logan, D.M. Nicholas, C. Fowley, J. Davis, B. Callan, A.P. McHale, J.F. Callan, Iodinated cyanine dyes: a new class of sensitizers for use in NIR activated photodynamic therapy (PDT), *Chem. Commun.* 53 (2017) 2009–2012, <https://doi.org/10.1039/C6CC09624G>.
- [7] B. Ciubini, S. Visentin, L. Serpe, R. Canaparo, A. Fin, N. Barbero, Design and synthesis of symmetrical pentamethine cyanine dyes as NIR photosensitizers for PDT, *Dyes Pigm.* 160 (2019) 806–813, <https://doi.org/10.1016/j.dyepig.2018.09.009>.
- [8] S.M. Usama, S. Thavornpradit, K. Burgess, Optimized heptamethine cyanines for photodynamic therapy, *ACS Appl. Bio Mater.* 1 (2018) 1195–1205, <https://doi.org/10.1021/acsabm.8b00414>.
- [9] H. Zollinger, *Color Chemistry, second ed.*, VCH, Weinheim, 1991.
- [10] L.I. Markova, E.A. Terpetchnik, L.D. Patsenker, Comparison of a series of hydrophilic squaraine and cyanine dyes for use as biological labels, *Dyes Pigm.* 99 (2013) 561–570, <https://doi.org/10.1016/j.dyepig.2013.06.022>.
- [11] A.J. McKerrow, E. Bunzel, P.M. Kazmaier, Aggregation of squaraine dyes: structure–property relationships and solvent effects, *Can. J. Chem.* 73 (1995) 1605–1615, <https://doi.org/10.1139/v95-200>.
- [12] I.A. Karpenko, A.S. Klymchenko, S. Gioria, R. Kreder, I. Shulov, P. Villa, Y. Me, M. Hibert, D. Bonnet, Squaraine as a bright, stable and environment-sensitive far-red label for receptor-specific cellular imaging, *Chem. Commun.* 51 (2015) 2960–2963, <https://doi.org/10.1039/C4CC09113B>.
- [13] E. Arunkumar, N. Fu, B.D. Smith, Squaraine-derived rotaxanes: highly stable, fluorescent near-IR dyes, *Chem. – A Eur. J.* 12 (2006) 4684–4690, <https://doi.org/10.1002/chem.200501541>.
- [14] S. Sreejith, J. Joseph, M. Lin, N.V. Menon, P. Borah, Near-infrared squaraine dye encapsulated micelles for in vivo fluorescence and photoacoustic bimodal imaging, *ACS Nano* 9 (2015) 5695–5704, <https://doi.org/10.1021/acs.nano.5b02172>.
- [15] F. Wu, H. Wang, Nano-confinement of squaraine dye assemblies: new photoacoustic and near-infrared fluorescence dual-modal imaging probes in vivo, *Bioconjug. Chem.* 25 (2014) 2021–2029, <https://doi.org/10.1021/bc5003983>.
- [16] J. Lee, A.G. White, D.R. Rice, B.D. Smith, In vivo imaging using polymeric nanoparticles stained with near-infrared chemiluminescent and fluorescent squaraine catenane endoperoxide, *Chem. Commun.* 49 (2013) 3016–3018, <https://doi.org/10.1039/c3cc40630j>.
- [17] I. Wu, J. Yu, F. Ye, Y. Rong, M.E. Gallina, B.S. Fujimoto, Y. Zhang, Y. Chan, W. Sun, X. Zhou, C. Wu, D.T. Chiu, Squaraine-based polymer dots with narrow, bright near-infrared fluorescence for biological applications, *J. Am. Chem. Soc.* 137 (2015) 173–178, <https://doi.org/10.1021/ja5123045>.
- [18] E. Conteroso, I. Benesperi, V. Toson, D. Saccone, N. Barbero, L. Palin, C. Barolo, V. Gianotti, M. Milanesio, High-throughput preparation of new photoactive nanocomposites, *ChemSusChem*. 9 (2016) 1279–1289, <https://doi.org/10.1002/cssc.201600325>.
- [19] L. Tang, J. Cheng, Nonporous silica nanoparticles for nanomedicine application, *Nano Today* 8 (2013) 290–312, <https://doi.org/10.1016/j.nantod.2013.04.007>.
- [20] I. Miletto, A. Fraccarollo, N. Barbero, C. Barolo, M. Cossi, L. Marchese, E. Gianotti, Mesoporous silica nanoparticles incorporating squaraine-based photosensitizers: a combined experimental and computational approach, *Dalton Trans.* 47 (2018) 3038–3046, <https://doi.org/10.1039/c7dt03735j>.
- [21] S. Sreejith, Y. Zhao, Graphene oxide wrapping on squaraine-loaded mesoporous silica nanoparticles for bioimaging, *J. Am. Chem. Soc.* 134 (2012) 17346–17349, <https://doi.org/10.1021/ja305352d>.
- [22] S. Santra, D. Dutta, B.M. Moudgil, Functional dye-doped silica nanoparticles for bioimaging, diagnostics and therapeutics, *Food Bioprod. Process.* 83 (2005) 136–140, <https://doi.org/10.1205/fbp.04400>.
- [23] L. Accomasso, E.C. Rocchietti, S. Raimondo, F. Catalano, G. Alberto, A. Giannitti, V. Minieri, V. Turinetti, L. Orlando, S. Saviozzi, G. Caputo, S. Geuna, Fluorescent silica nanoparticles improve optical imaging of stem cells allowing direct discrimination between live and early-stage apoptotic cells, *Small* 8 (2012) 3192–3200, <https://doi.org/10.1002/sml.201200882>.
- [24] C. Liu, H. Yu, Q. Li, C. Zhu, Y. Xia, Brighter, more stable, and less toxic: a host–guest interaction-aided strategy for fabricating fluorescent silica nanoparticles and applying them in bioimaging and biosensing at the cellular level, *ACS Appl. Mater. Interfaces* 10 (2018) 16291–16298, <https://doi.org/10.1021/acsami.8b03034>.
- [25] D.R. Larson, H. Ow, H.D. Vishwasrao, A.A. Heikal, U. Wiesner, W.W. Webb, U.V. Park, V. Pennsly, Silica nanoparticle architecture determines radiative properties of encapsulated fluorophores, *Chem. Mater.* 20 (2008) 2677–2684.
- [26] F.J. Arriagada, Synthesis of Nanosize Silica in a nonionic water-in-oil microemulsion: effects of the water / surfactant molar ratio and Ammonia concentration, *J. Colloid Interface Sci.* 211 (1999) 210–220.
- [27] I. Miletto, A. Gilardino, P. Zamburlin, S. Dalmazzo, D. Lovisolio, G. Caputo, G. Viscardi, G. Martra, Highly bright and photostable cyanine dye-doped silica nanoparticles for optical imaging: photophysical characterization and cell tests, *Dyes Pigm.* 84 (2010) 121–127, <https://doi.org/10.1016/j.dyepig.2009.07.004>.
- [28] G. Alberto, I. Miletto, G. Viscardi, G. Caputo, L. Latterini, S. Coluccia, G. Martra, Hybrid cyanine - silica nanoparticles: homogeneous photoemission behavior of entrapped fluorophores and consequent high brightness enhancement, *J. Phys. Chem. C*. 113 (2009) 21048–21053.
- [29] A.J. Winstead, G. Nyambura, R. Matthews, D. Toney, S. Oyaghire, Synthesis of quaternary heterocyclic salts, *Molecules* 18 (2013) 14306–14319, <https://doi.org/10.3390/molecules181114306>.
- [30] G. Alberto, G. Caputo, G. Viscardi, S. Coluccia, G. Martra, Molecular engineering of hybrid dye – silica fluorescent nanoparticles: influence of the dye structure on the distribution of fluorophores and consequent photoemission brightness, *Chem. Mater.* 24 (2012) 2792–2801, <https://doi.org/10.1021/cm301308g>.
- [31] J.-H. Yum, P. Walter, S. Huber, D. Rentsch, T. Geiger, F. Nüesch, F. De Angelis, M. Grätzel, M.K. Nazeeruddin, Efficient far red sensitization of nanocrystalline TiO₂ films by an unsymmetrical squaraine dye, *J. Am. Chem. Soc.* 129 (2007) 10320–10321, <https://doi.org/10.1021/ja0731470>.
- [32] J. Park, N. Barbero, J. Yoon, E. Dell'Orto, S. Galliano, R. Borrelli, J.-H. Yum, D. Di Censo, M. Grätzel, M.K. Nazeeruddin, C. Barolo, G. Viscardi, Panchromatic symmetrical squaraines: a step forward in the molecular engineering of low cost blue-greenish sensitizers for dye-sensitized solar cells, *Phys. Chem. Chem. Phys.* 16 (2014) 24173–24177, <https://doi.org/10.1039/C4CP04345F>.
- [33] R. Borrelli, S. Ellena, C. Barolo, Theoretical and experimental determination of the absorption and emission spectra of a prototypical indolenine-based squaraine dye, *Phys. Chem. Chem. Phys.* 16 (2014) 2390–2398, <https://doi.org/10.1039/c3cp54298j>.
- [34] J. Park, C. Barolo, F. Sauvage, N. Barbero, C. Benzi, P. Quagliotto, S. Coluccia, D. Di Censo, M. Grätzel, M.K. Nazeeruddin, G. Viscardi, Symmetric vs. Asymmetric squaraines as photosensitizers in mesoscopic injection solar cells: a structure–property relationship study, *Chem. Commun.* 48 (2012) 2782, <https://doi.org/10.1039/c2cc17187b>.
- [35] G. Gude, W. Rettig, Radiative and nonradiative excited state relaxation channels in squaric acid derivatives bearing differently sized donor substituents: a comparison of experiment and theory, *J. Phys. Chem. A* 104 (2000) 8050–8057, <https://doi.org/10.1021/jp000139w>.
- [36] F. Momicchioli, A.S. Tatikolov, G. Ponterini, Electronic structure and photochemistry of squaraine dyes: basic theoretical analysis and direct detection of the photoisomer of a symmetrical squarylium cyanine, *Photochem. Photobiol. Sci.* 3 (2004) 396–402.
- [37] A.P. Legrand, *The Surface Properties of Silicas*, John Wiley, New York, 1998.
- [38] M. Szekeres, J. Tóth, I. Dékány, Specific surface area of stoichiometric determined by, *Langmuir* 18 (2002) 2678–2685, <https://doi.org/10.1021/la011370j>.
- [39] F. Catalano, G. Alberto, P. Ivanchenko, G. Dovbeshko, G. Martra, Effect of silica surface properties on the formation of multilayer or submonolayer protein hard corona: albumin adsorption on pyrolytic and colloidal SiO₂ nanoparticles, *J. Phys. Chem. C* 119 (2015) 26493–26505, <https://doi.org/10.1021/acs.jpcc.5b07764>.
- [40] J.R. Lakowicz, *Principles of Fluorescence Spectroscopy*, (2006).
- [41] V. Kabanov, D.J. Press, R.P.S. Huynh, G.K.H. Shimizu, B. Heyne, Assessment of encapsulated dyes' distribution in silica nanoparticles and their ability to release useful singlet oxygen, *Chem. Commun.* 54 (2018) 6320–6323, <https://doi.org/10.1039/c8cc03413c>.

Solvent-free synthesis of Ser–His dipeptide from non-activated amino acids and its potential function as organocatalyst

Marco Fabbiani¹  · Erica Rebba² · Marco Pazzi² · Marco Vincenti² · Ettore Fois¹ · Gianmario Martra² 

Received: 18 September 2017 / Accepted: 27 October 2017 / Published online: 11 November 2017
© Springer Science+Business Media B.V., part of Springer Nature 2017

Abstract Short homopeptides (up to 3-mer) of serine and histidine, as well as Ser–His and His–Ser hetero-dipeptides, are produced from non-activated amino acids by using facile chemical vapor deposition and TiO₂ nanoparticles as catalyst. The assessment of the formation of peptides is based on spectroscopic data such as in situ FT-IR and mass spectrometry. Evidence of the capability of Ser–His to promote hydrolysis of peptide bonds in hexaglycine is provided, contributing to the debate on the effectiveness of this dipeptide as an organocatalyst.

Keywords FT-IR of adsorbed species · Peptides · Serine · Histidine · CVD

Introduction

Peptide synthesis promotes interest in several aspects of modern chemistry research, from the crescent employment of peptide-based pharmaceuticals [1, 2], the needs for green synthesis [3, 4], to the implications in prebiotic chemistry [5]. Catalytic methods represent a promising approach, in alternative to the well-established solid

Electronic supplementary material The online version of this article (<https://doi.org/10.1007/s11164-017-3198-7>) contains supplementary material, which is available to authorized users.

✉ Marco Fabbiani
mfabbiani@uninsubria.it

✉ Gianmario Martra
gianmario.martra@unito.it

¹ Department of Science and High Technology, University of Insubria, Via Valleggio 9, 22100 Como, Italy

² Department of Chemistry, University of Torino, Via P. Giuria 7, 10125 Turin, Italy

phase peptide synthesis (SPPS) [6, 7], for the possibility to avoid reagent activation steps and to carry out the reaction using mild conditions [8]. Heterogeneous catalysis has lately drawn attention, and surface-catalyzed peptide bond formation is of particular interest in synthetic biochemistry and shows great potential in synthesizing different kinds of peptides [9, 10]. Taking inspiration from possible prebiotic chemistry scenarios, non-activated amino acids (aa) can be adsorbed as zwitterions from aqueous solution on different materials. Typically, oxides are good candidates as approximations to mineral surfaces and after the adsorption, are heated for water removal, simulating wet and dry cycles that can occur in hydrothermal systems [9, 11]. Exploiting this method, short homopeptides of glycine [10, 12], alanine [9, 13], valine [14] and asparagine [15] have been synthesized. Noteworthy, the most abundant product was diketopiperazine (DKP) when silica was used as a catalyst for generating glycine [12] and alanine [9]. The adsorption from aqueous solution of different aa was also investigated, mainly focusing on competitive aspects but, to the best of our knowledge, the subsequent possible reaction to form heteropeptides was not explored. On the other hand, chemical vapor deposition (CVD) represents an alternative approach where aa are initially sublimated in the presence of the catalyst, in a dry state. Non-ionic, non-activated aa molecules adsorb and react on the catalyst surface and the produced peptides are later washed away, passing into solutions. Indeed, aa polymerization via a sublimation process was demonstrated to be an effective method to produce glycine oligomers up to 16 or 11 units long on titanium dioxide and silica, respectively, with DKP being a minor product [16]. This procedure can be potentially applied to other aa capable to sublimate at lower than the decomposition temperature, a property exhibited by 14 of the 20 proteinogenic aa [17]. Moreover, heteropeptides can be obtained in principle by sublimating the aa of interest in the proper sequence. On this basis, here we report a proof-of-principle study of the production of homo- and heteropeptides produced by sublimating serine (Ser) and histidine (His) on TiO₂ nanoparticles, exploiting the CVD method, carried out using a cell for in situ infrared (IR) measurements in a controlled atmosphere as the reactor, set up for the oligomerization of Gly [16]. The interest regarding the possibility to prepare peptides containing Ser and His stems from the presence of these aa in the catalytic triad (together with Asp) found in many enzymes such as chymotrypsin, subtilisin and phospholipase A2 [18]. Serine hydrolases comprise approximately 1% of the genes in the human proteome [19]. Short peptides can be considered minimalistic form of enzymes, for organic synthesis and prebiotic chemistry [20]. The catalytic activity of Ser–His dipeptide has been reported for the first time by the group of Zhao [21, 22], showing different cases of hydrolytic activity towards proteins [23, 24] and nucleic acids [25–27]. Nevertheless, MacDonald et al. [28] recently reported a different conclusion on the activity of Ser–His, assessing a non-statistical significance in the hydrolysis of sterically hindered esters and amides. As a contribution to the debate, we tested the hydrolytic activity of Ser–His produced by CVD towards a simple, model oligopeptide, namely hexaglycine (6-Gly).

Materials and methods

The commercial TiO₂ P25 from Evonik (ca. 80% anatase and 20% rutile, specific surface area $\approx 50 \text{ m}^2/\text{g}$) was used as catalyst. L-Ser, L-His, L-His–L-Ser and 6-Gly powders were purchased from Sigma-Aldrich, while D₂O (99.9% D) was purchased from Euriso-top.

Titanium dioxide thermal treatment

The titanium dioxide powder was compressed into a self-supporting pellet (optical thickness ca. $10 \text{ mg}/\text{cm}^2$) and thermally treated in vacuum (residual pressure $1.0 \times 10^{-5} \text{ mbar}$) to remove previously adsorbed molecules and water. The samples were heated inside the cell under dynamic vacuum from room temperature to 723 K (ca. 5 K/min) and outgassed at this temperature for 1 h. To compensate for the reductive effect on TiO₂ produced by this dehydration/dehydroxylation treatment, 6 mbar of O₂ were admitted in the cell, and kept in contact with the samples for 1 h at 723 K. The system was subsequently let to cool down to 473 K in O₂ and finally outgassed until reaching room temperature. The treated samples appeared perfectly white, as expected for stoichiometric TiO₂.

Sublimation of amino acids

The cell with the treated TiO₂ was transferred into a nitrogen filled glovebox for the introduction of the aa. The aa powders were also compressed into self-supporting pellets (ca. 150 mg) and moved close to the TiO₂ pellet. The cell was then connected to a vacuum line for the subsequent sublimation process where the TiO₂/aa system was outgassed. The sublimation process was the same as described by Martra et al. [16] in their supporting information for the glycine aa. Briefly, the aa and the oxide pellets were placed close to each other within a section of the IR cell, acting as a reactor, and heated up in static vacuum to the sublimation temperature of the aa. A liquid nitrogen trap was present during the whole sublimation process in order to remove generated water from the system. Typical sublimation steps can last from 20 to 60 min and can be repeated until the aa pellet was consumed. Ser was adsorbed at 433 K, while His sublimations were carried out at 473 K. For the heteropeptides experiments, after the first aa was sublimated, the cell was moved into a nitrogen-filled glovebox and the aa pellet was replaced with the other one; then the sublimation of the second aa was carried out. For these experiments, each aa sublimation lasted 1 h.

CO₂ coverage evaluation

In order to monitor the degree of coverage of the titanium dioxide surface by aa molecules, linearly adsorbed CO₂ was employed as the probe molecule. A mixture of ¹²CO₂ and ¹³CO₂ was specifically prepared in a ratio of 9:1 and the IR signal of the isotopically labelled molecule was monitored. After each experimental step,

oxide thermal treatment and sublimation steps, CO₂ mixture at 50 mbar was dosed in the cell with the previously outgassed samples and left in contact for 10 min, after which an IR spectrum was collected. The system was then outgassed for 20 min to remove CO₂ pressure. Some carbonates and bicarbonates formed during this analysis for the reaction of the linearly adsorbed CO₂ with the basic sites of titanium dioxide: beside being a minor component, these species are removed during the temperature ramping of the subsequent sublimation step. We found this method to be effective with Ser, while in the case of His, probably due to the basicity of the side chain, the procedure was not reliable. For this latter aa, coverage estimations were made comparing the optical density of the titanium dioxide pellet with one used in a serine experiment and correlate those values to obtain the percentage of surface coverage.

Infrared measurements

The whole experimental work was monitored by means of in situ IR spectroscopy. The spectra were collected at beam temperature (b.t., ca. 323 K) with a resolution of 4 cm⁻¹, averaging 100 scans to attain a good signal-to-noise ratio, in a Bruker Vector 22 equipped with a LaDTGS detector.

Products extraction and mass spectrometry analysis

At the end of the spectroscopic measurements, the samples were removed from the cell, manually ground in an agate mortar and suspended in 0.5 mL of Milli-Q water (Millipore system). The suspension was shaken for 15 min by a vortex mixer and then centrifuged for 5 min at 10 k rpm. After removal of the supernatant, the solid was treated a second time with the same volume of water. The two aliquots of the aqueous solutions were then mixed, and analyzed by high-resolution mass spectrometry (HR-MS). The washed samples were dried under flowing nitrogen, pelletized and inserted into the IR cell for subsequent measurements carried out after outgassing at b.t. and admission/outgassing of D₂O at 20 mbar, until invariance of the spectra.

HR-MS analyses of the washing solutions were performed using an LTQ Orbitrap mass spectrometer (Thermo Scientific) equipped with an atmospheric pressure interface and an electrospray ionization (ESI) source. The source voltage was set to 4.48 kV. The heated capillary temperature was maintained at 538 K. The tuning parameters adopted for the ESI source were: capillary voltage 0.02 V, tube lens 24.77 V; for ions optics: multipole 0 offset – 4.28 V, lens 0 voltage – 4.36 V, multipole 0 offset – 4.28 V, lens 1 voltage – 13.69 V, gate lens voltage – 8.84 V, multipole 1 offset – 18.69 V and front lens voltage – 5.09 V. Mass accuracy of recorded ions (vs. calculated) was ± 1 mmu (without internal calibration). Samples, with addition of 100 μL of a 0.1 M HCOOH aqueous solution, were delivered directly to the mass spectrometer via a Hamilton microliter syringe at constant flow (10 μL/min).

Ser–His hydrolysis test towards hexaglycine

A 0.5-mL volume of 10 ppm hexaglycine (6-Gly) solution was mixed with 0.5 mL (thus halving the 6-Gly concentration) of (1) solution of His–Ser dimer purchased from Sigma–Aldrich, (2) washing solutions from adsorption of His–Ser sequence on TiO₂ experiment and (3) washing solutions from adsorption of Ser–His sequence on TiO₂ experiments. The samples were stirred for 10 min with the vortex system and then incubated at 298 K for 12 h. After incubation, samples were analyzed by HR-MS. A solution of 6-Gly alone was incubated as well and analyzed as a 6-Gly stability control test towards hydrolysis in water.

Results and discussion

Formation of homopeptides of Ser and His

The possible formation of homopeptides of Ser and His via the catalytic CVD method was monitored by in situ IR spectroscopy. The results are reported in Fig. 1,

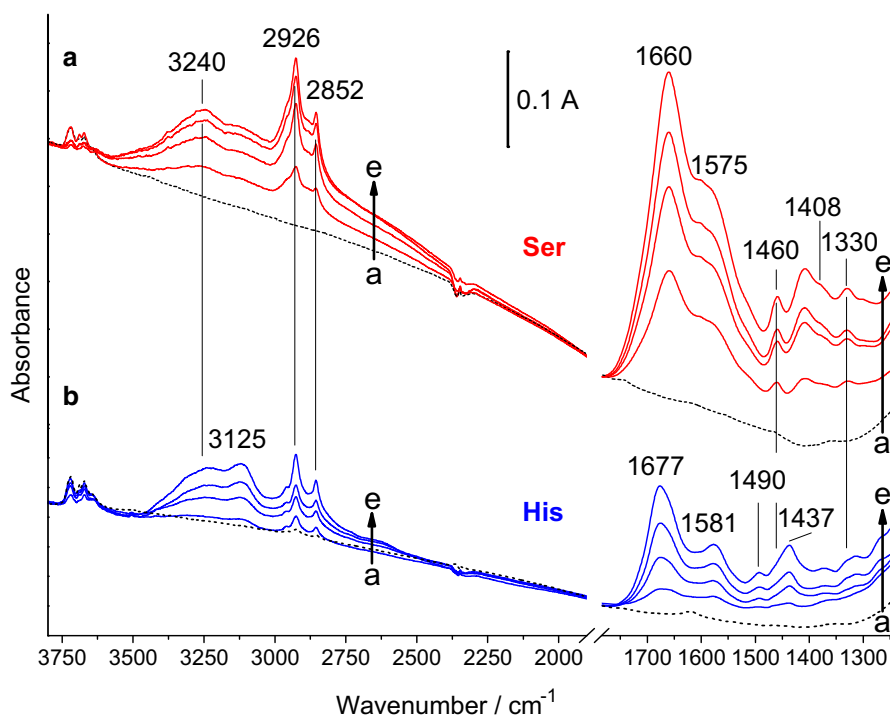


Fig. 1 IR spectra resulting from the adsorption of Ser (section a) and His (section b) from vapor phase on TiO₂ P25. The intensity of the spectra is normalized with respect to the optical thickness (mg cm^{-2}) of the self-supporting pellets used for the measurements. Curve a: TiO₂ P25 dried by outgassing at 723 K; curves b–e: after exposure to Ser or His vapors for 30, 60, 90 and 120 min, respectively

where curve a is the spectrum of bare titania, exhibiting only the typical pattern of weak bands in the range from 3750 to 3600 cm^{-1} due to surface hydroxy groups [29]. In the type of TiO_2 nanoparticles used, $-\text{OH}$ groups occupy only a minor fraction of surface sites; thus, is not surprising if their IR signals are perturbed to a limited extent by increasing the amount of adsorbed aa. Conversely, the important feature in the spectrum of bare TiO_2 is the absence of the band at ca. 1620 cm^{-1} due to the deformation mode (δ) of H_2O molecules, indicating the catalyst is fully dehydrated before the contact with aa. Passing to the systems resulting from the adsorption of aa on the catalyst, Ser is dosed on TiO_2 nanoparticles until attaining a surface coverage of $\sim 70\%$ (see Fig. S1, in the Electronic Supporting Material, hereafter ESM), as estimated by the competitive CO_2 adsorption method (see the Materials and methods section). In the case of His, only a surface coverage of $\sim 30\%$ was achieved after the same time of contact with aa vapor, likely because the lower propensity of this aa toward sublimation. The stepwise contact with Ser (section a) or His (section b) vapors resulted in the appearance and progressive growth of signals in the 1680–1620- and 1560–1530- cm^{-1} ranges, which can be easily recognized as amide I and amide II bands, respectively, typical of peptide species. The weaker signal at 1330 cm^{-1} (that resisted H/D isotopic exchange, vide infra) might result from the deformation (δ) mode involving the $\text{C}_\alpha\text{--H}$ bond [30]. Noteworthy, these bands are already present after the adsorption of the first aa doses, indicating that the formation of peptides is almost independent from the surface coverage. However, evidence of the role of TiO_2 as catalyst promoting aa condensation is obtained by comparison with a control test. We carried out sublimation of each aa in the absence of the titanium dioxide pellet: the film formed by the aa condensed on the inner walls of the cell was dissolved in water and the resulting solutions were analyzed by HR-MS. Only Ser and His monomers were found (Figs. 3b and 4b), indicating that the formation of peptides in the vapor phase during aa sublimation, followed by their adsorption on TiO_2 nanoparticles, can be excluded. Focusing on IR data, another feature common to Ser/ TiO_2 and His/ TiO_2 spectra is the broad band at 3240 cm^{-1} , assignable to the stretching mode (ν) of the N–H moiety of peptide bonds involved in weak H bonding [31]. Two narrow bands at 2926 and 2852 cm^{-1} are due to the ν_{asym} and ν_{sym} $-\text{CH}_2$ groups present in both aa with the partner δCH_2 mode producing the signal at 1460 cm^{-1} (resolved band in the Ser/ TiO_2 spectra, section a; high-frequency shoulder of the signal at 1437 cm^{-1} in the His/ TiO_2 spectra, section b) [32]. Conversely, the main distinctive feature of the Ser/ TiO_2 spectra (section a) is the broad band spread over the 3500–2250- cm^{-1} range, assignable to the νOH mode of H-bonded hydroxy group of the side chain of Ser, whilst νCH and $\nu\text{CN}/\delta\text{CH}$ of the imidazole group of the His side chain are responsible for signals at 3125 and 1490 cm^{-1} , respectively, in the His/ TiO_2 spectra (section b) [31]. The ν_{sym} of COO^- groups might produce the signals at 1408 and 1423 cm^{-1} in Ser/ TiO_2 and His/ TiO_2 spectra, respectively, the ν_{sym} of COO^- likely contributing to the pattern in the 1650–1540- cm^{-1} range [33]. The deprotonation of carboxylic groups (aa molecules in vapor phase are in a non-ionic form) could be accompanied by the protonation of $-\text{NH}_2$ moieties, as observed for the adsorption of Gly vapors on hydroxyapatite [34]. Thus, the contribution of δ_{asym} and δ_{sym} $-\text{NH}_3^+$

modes in the 1650–1550-cm⁻¹ range cannot be excluded, as well as the contribution of the partner νNH₃⁺ modes in the range from 3200 to 2800 cm⁻¹ [33].

IR data provided strong suggestion for the formation of peptides, but do not contain information about the number of terms present in such possibly formed species. The catalyst pellets which reacted with Ser or His were then washed with water, and the resulting aqueous solutions were analyzed by HR-MS. As a complementary investigation, the washed catalysts were recovered, dried and pelletized. These samples were then analyzed by IR spectroscopy in a controlled atmosphere, to evaluate the relative amount of adsorbed species removed by washing. Since the absorption in the 1750–1500-cm⁻¹ range is the targeted signal, the interference of the δH₂O band, expected at ~ 1620 cm⁻¹, due to water molecules left adsorbed on the catalyst surface after washing should be avoided. The solution adopted is an isotopic exchange by adsorption/desorption cycles of D₂O vapors before the collection of IR spectra. In order to carry out a consistent comparison of the state of the surface before and after the washing procedure, the catalyst samples reacted with aa were hydrated in the IR cell by adsorption/desorption of H₂O, and then underwent an isotopic exchange by adsorption/desorption of D₂O. We collected IR spectra after both steps, in order to monitor separately the effects of hydration and H/D exchange on aa-derived adsorbed species. The results are depicted in Fig. 2, where curves in panels a/b and a'/b' are the spectra of Ser/TiO₂ and His/TiO₂ before/after washing, respectively. For both systems, the initial hydration resulted in an increase in intensity and a downshift of ~ 10 cm⁻¹ of the band initially at 1660 cm⁻¹ for Ser/TiO₂, or 1677 cm⁻¹ for His/TiO₂ (panels a, a', curves a, b). This evolution was only partly due to the additional contribution of the δH₂O signal at ca. 1620 cm⁻¹, because it was affected to a quite limited extent by the subsequent H/D exchange (panels a, a', curve c). Thus, the increase in intensity and downshift of the amide I band might be ascribed to a strengthening of H bonding involving the C=O group of formed peptide species. Additional expected effects of the H/D exchange were a further downshift of the amide I band, and the fading of the amide II band, initially contributing to the signal over the 1600–1500-cm⁻¹ range and then converted in a component of the complex spectral profile in the 1500–1350-cm⁻¹ region. Moreover, the deformation modes of –NH₃⁺ moieties were also downshifted by the conversion in –ND₃⁺ groups, while the band at 1195 cm⁻¹ appearing in the spectra after the treatment for isotopic exchange was due to the deformation mode of D₂O molecules left adsorbed on the catalyst surface after outgassing at b.t. The spectral profiles of catalyst samples reacted with the aa, washed in H₂O and isotopically exchanged by contact with D₂O appeared significantly decreased in intensity and changed in shape (panels b, b', curve d). On the basis of the ratio between the integrated intensity of the absorption in the 1700–1500-cm⁻¹ range, the effectiveness of washing in removing aa-derived species from the catalyst surface was evaluated to be ~ 65 and ~ 80% for Ser/TiO₂ and His/TiO₂, respectively.

As anticipated above, the solutions resulting from the washing procedure were analyzed by HR-MS. Two other samples were also analyzed, as “blanks”. The first one was an aqueous solutions of Ser, in order to assess the ESI analysis to be ineffective towards the formation of peptides, as conversely occurred in other ESI

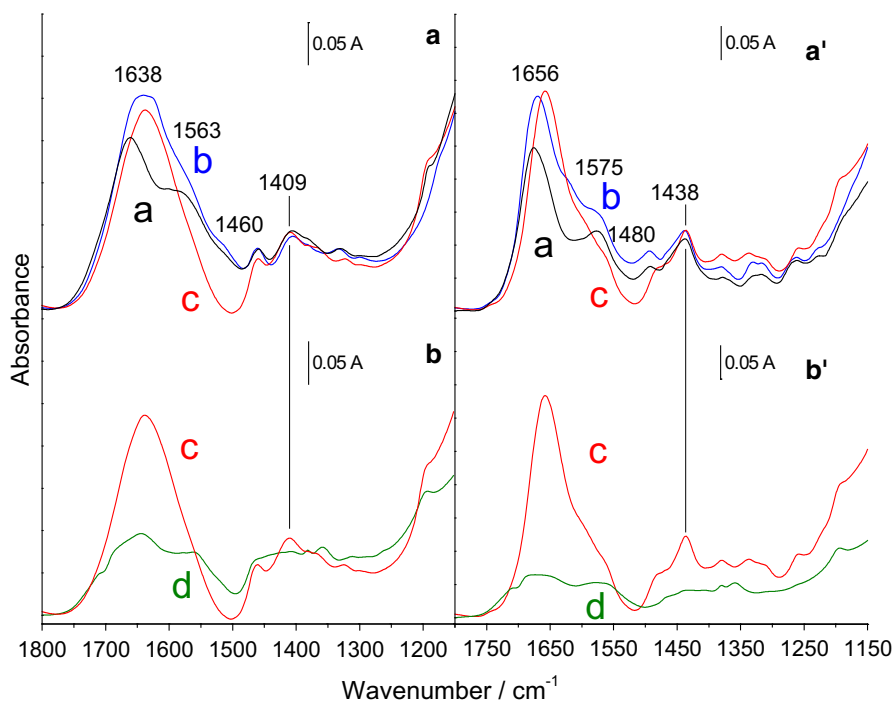


Fig. 2 IR spectra comparing the signals from the sublimated Ser and His samples (panels a and a', respectively) with the ones after the washing procedure (panels b and b'). Curve a: 2 h of Ser sublimation at 433 K; curve b: outgassed sample after subsequent contact with H₂O vapor at 20 mbar; curve c: outgassed sample after subsequent contact with D₂O vapor at 20 mbar; curve d: outgassed sample after contact with D₂O vapor at 20 mbar after the washing procedure

conditions [35]. The second was the film of Ser condensed on the inner wall of the IR cell dissolved in water, when the sublimation of aa was carried out in the absence of the catalyst. In this case, the rationale was the assessment of the absence of peptide formation during sublimation, independently on the presence of titania nanoparticles. The results are shown in Fig. 3: in the two blank tests, only Ser in monomeric form was detected (panels a and b), whereas cyclic and linear (the most abundant) Ser dipeptides, as well as Ser tripeptide were present in the aqueous solutions resulting from washing the catalyst contacted with Ser vapors (panel c). Even though the cyclic dimer (diketopiperazine, 2S_{DKP}) is present, the signal at $m/z = 175$ and the detection of the linear dimer (2S), positioned at $m/z = 193$, means that further monomer addition is possible. Indeed, the signal at $m/z = 280$ was found for the Ser linear trimer (3S).

The equivalent set of data for His is depicted in Fig. 4. Also, in this case, blank tests indicated that peptides are formed neither during the ESI analysis (panel a), nor in vapor phase during sublimation (panel b). However, when His is sublimated in the presence of the catalyst, cyclic (2H_{DKP}, $m/z = 275$) and linear (2H, $m/z = 293$) dipeptides and linear tripeptide (3H, $m/z = 430$) were formed (panel c). In this case,

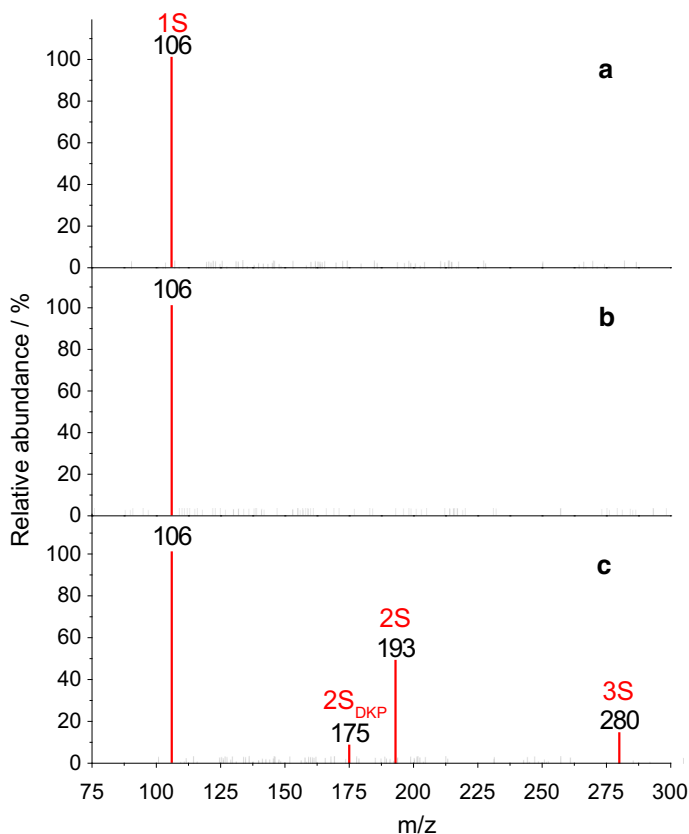


Fig. 3 ESI-MS spectra of: **a** Ser aqueous solution (10 ppm); **b** Ser collected from the inner wall of the IR cell after sublimation at 433 K in the absence of the catalyst and dissolved in water; **c** aqueous solution resulting from washing the catalyst contacted with Ser vapors for 2 h at 433 K. Numbers on the bars are the m/z values, without decimal digits, for the sake of simplicity. Original HR-MS spectra with complete m/z values are reported in Fig. S2 in the ESM

the cyclic dimer seemed to be favored, probably due to the influence of the bulkier side chain with respect to the Ser side chain.

Using the same experimental procedure employed for the production of homopeptides, consecutive sublimations of Ser and His, and vice versa (IR spectra in Fig. S4 in the ESM), are carried out to obtain heteropeptides (see Materials and methods section). Figure 5 shows the results of the HR-MS analysis of the final washing solutions. In both cases, homopeptides of Ser and His prevail by far; however, hetero-dipeptides Ser–His or His–Ser ($m/z = 243$) or Ser–Ser–His trimer ($m/z = 330$) were also present in relative amounts of ~ 10 and $\sim 5\%$, respectively, in comparison with the most abundant species, which in both experiments was His in monomeric form ($m/z = 156$).

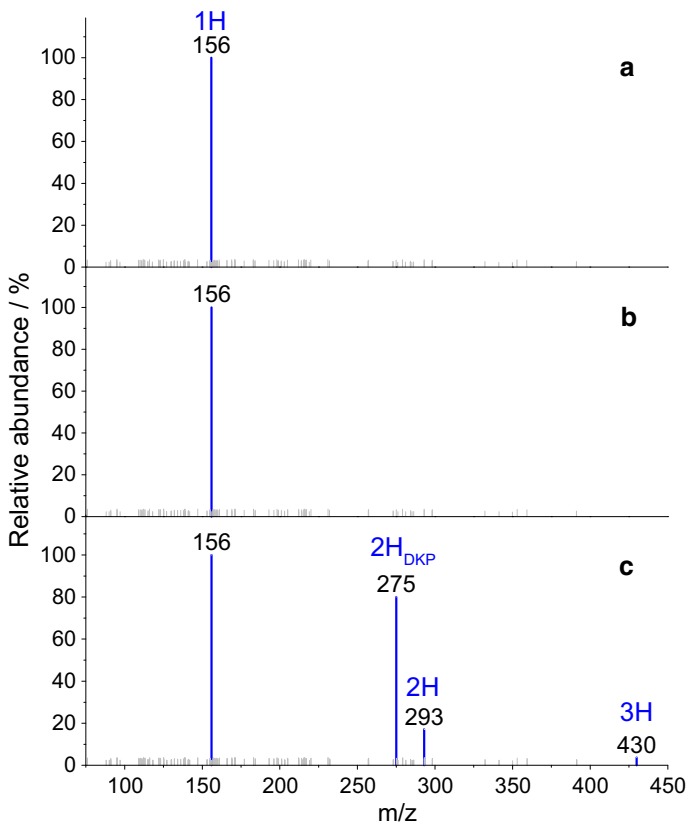


Fig. 4 ESI-MS spectra of: **a** His aqueous solution (10 ppm); **b** His collected from the inner wall of the IR cell after sublimation at 473 K in the absence of the catalyst and dissolved in water; **c** aqueous solution resulting from washing the catalyst contacted with His vapors for 2 h at 473 K. Numbers on the bars are the m/z values, without decimal digits, for the sake of simplicity. Original HR-MS spectra with complete m/z values are reported in Fig. S3 in the ESM

Ser–His activity as peptide bond hydrolase towards hexaglycine

Using the procedure described in the Materials and methods section, the potential hydrolysis activity of Ser–His towards 6-Gly was tested. The results obtained during two blank tests and using as organocatalyst the peptide mixtures obtained by washing pellets of TiO_2 catalyst contacted with Ser/His and His/Ser vapors are compared in Fig. 6. The first blank sample is the starting solution of hexaglycine, which, as far as Gly-related ESI signals are concerned, produced only the signal $m/z = 361$ of 6-Gly, providing evidence of the stability of this oligopeptide towards self-hydrolysis in the adopted condition (panel a). In the second blank test, 6-Gly was incubated in solution with commercial His-Ser peptide ($m/z = 243$): again, no evidence of any hydrolysis of hexaglycine was found (panel b). In the two cases of 6-Gly incubated with the solutions of catalytically produced peptides (panels c, d), in addition to the signals for hexaglycine, Ser and His in monomeric form ($m/$

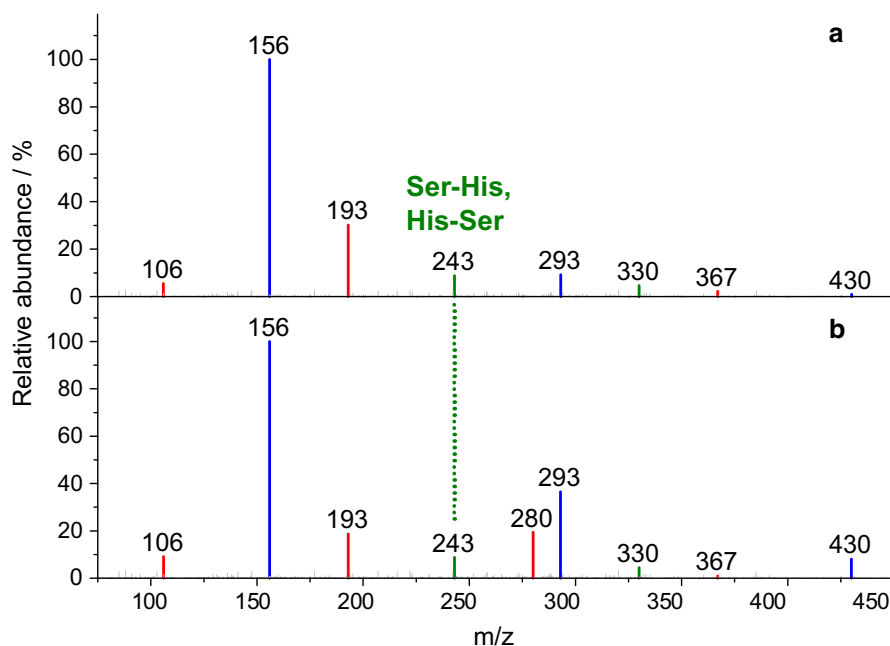


Fig. 5 ESI-MS spectra of the aqueous solution resulting from washing the TiO_2 catalyst consecutively reacted with: **a** Ser/His, or **b** His/Ser. Color code: red, Ser monomer and homopeptides (as in Fig. 3); blue, His monomer and homopeptides (as in Fig. 4); green, Ser-His/His-Ser and Ser-Ser-His heteropeptides. Numbers on the bars are the m/z values, without decimal digits, for the sake of simplicity. Original HR-MS spectra with complete m/z values are reported in Fig. S5 and S6 in the ESM. (Color figure online)

$z = 106$ and 156 , respectively), Ser-based homopeptides ($m/z = 193$, 2-Ser; 367 , 3-Ser), His-based homopeptides ($m/z = 293$, 2-His; 430 , 3-His) and Ser-His and His-Ser heteropeptides ($m/z = 243$) were found. Moreover, the signal due to glycine in monomeric form ($m/z = 76$) was detected. Hence, a hydrolysis of 6-Gly apparently occurred, although two contradictory scenarios seemed to be present. Data in panel c deals with the system where the heteropeptide expected to have been produced is His-Ser, found ineffective towards 6-Gly hydrolysis in the relevant bank test (panel b), whilst data in panel d, dealing with the system where the heteropeptide expected to have been produced is Ser-His, appear to be in agreement with the hydrolysis activity proposed for this peptide [23, 25].

A possible rationalization is as follows: when Ser and His (or vice-versa) were consecutively adsorbed on the catalyst, the carboxylic group of both aa monomers were activated by the interaction with the surface. It could then react with the amino group of any other neighboring aa, resulting in the formation of both Ser-His and His-Ser peptides (other than in the formation of homopeptides). Finally, the discussion of the hydrolytic mechanism of 6-Gly is outside the scope of this report. Nevertheless, it can be noticed that the presence at the end of the incubation of both unreacted hexamer and of product Gly in monomeric form as the only hydrolysis

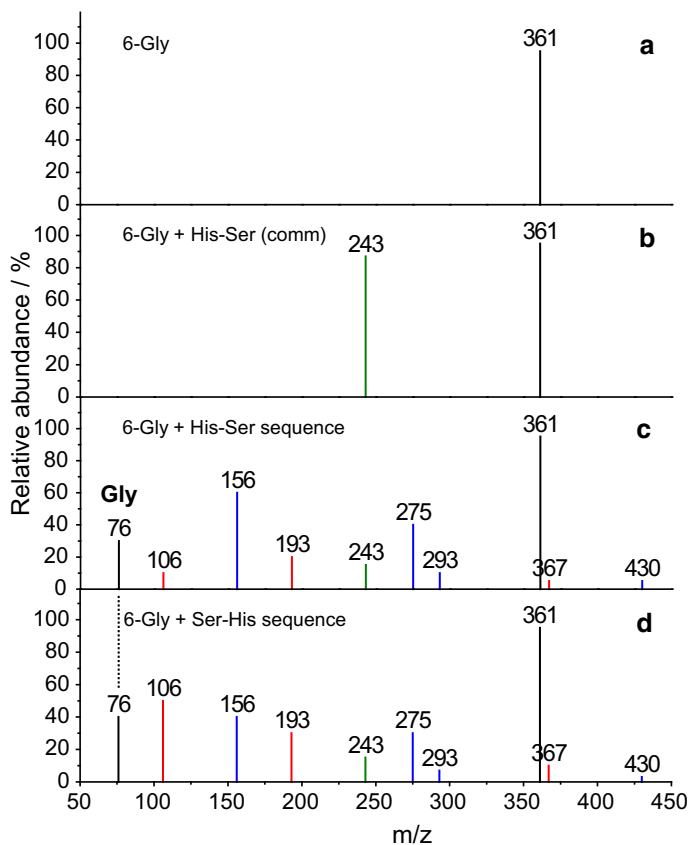


Fig. 6 ESI-MS spectra of: **a** 10 ppm of 6-Gly solution as such, then mixed in a 1:1 ratio in vol with **b** a 10 ppm commercial His-Ser solution; **c** washing solution from adsorption of His-Ser sequence on TiO_2 ; **d** washing solution from adsorption of Ser-His sequence on TiO_2 . Numbers on the bars are the m/z values, without decimal digits, for the sake of simplicity. Original HR-MS spectra with complete m/z values are reported in Fig. S7 to S10 in the ESM

product suggests that once the hydrolysis of a peptide bond occurred, the subsequent hydrolysis of the shorter peptides produced might be quite fast.

Conclusions

The collection of results reported and commented upon above allows us to conclude that short homopeptides of Ser and His (up to 3 terms), and of Ser-His and His-Ser heteropeptides can be produced by adsorbing vapors of these amino acids on TiO_2 nanoparticles. The pros of the method adopted for the synthesis of these peptides are the absence of chemical activation of amino acids and the absence of solvent. However, the main con is the (still) lack of selectivity. In particular, in the formation of hetero-dipeptides, the attainment of the desired sequence is not guaranteed to be

an indication of reactants in the correct sequential order. Furthermore, a contribution to the debate on the hydrolase activity of Ser–His is provided, in terms of evidence of activity in promoting the hydrolysis of hexaglycine. The origin of discrepancy with the absence of any significant hydrolytic activity reported by MacDonald et al. [28] can be the absence of significant electronic and steric effects of H atoms as lateral chains in the oligopeptide used in this work. On the other hand, it will be interesting to investigate if the hydrolytic activity of Ser–His towards biomacromolecules reported by the group of Zhao [23, 25] shows any selectivity towards peculiar positions along the polymeric sequence.

Acknowledgements This work was carried out in the frame of the project DAMA_RILO_16_01, funded by the University of Torino.

References

1. T. Uhlig, T. Kyrianiou, F.G. Martinelli, C.A. Oppici, D. Heiligers, D. Hills, X.R. Calvo, P. Verhaert, *EuPA Open Proteom.* **4**, 58–69 (2014)
2. K. Fosgerau, T. Hoffmann, *Drug Discov. Today* **20**, 122–128 (2015)
3. V.R. Pattabiraman, J.W. Bode, *Nature* **480**, 471–479 (2011)
4. M. Rodriguez-Garcia, A.J. Surman, G.J.T. Cooper, I. Suárez-Marina, Z. Hosni, M.P. Lee, L. Cronin, *Nature* **6**, 8385 (2015)
5. J.-F. Lambert, *Orig. Life Evol. Biosph.* **38**, 211–242 (2008)
6. A.R. Mitchell, *Pept. Sci.* **90**, 175–184 (2008)
7. J.M. Collins, K.A. Porter, S.K. Singh, G.S. Vanier, *Org. Lett.* **16**, 940–943 (2014)
8. T. Mohy El Dine, W. Erb, Y. Berhault, J. Rouden, J. Blanchet, *J. Org. Chem.* **80**, 4532–4544 (2015)
9. C. Guo, J.S. Jordan, J.L. Yarger, G.P. Holland, A.C.S. *Appl. Mater. Interfaces* **9**, 17653–17661 (2017)
10. T. Georgelin, M. Akouche, M. Jaber, Y. Sakhno, L. Matheron, F. Fournier, C. Méthivier, G. Martra, J.-F. Lambert, *Eur. J. Inorg. Chem.* **2017**, 198–211 (2017)
11. E.-I. Imai, H. Honda, K. Hatori, K. Matsuno, *Orig. Life Evol. Biosph.* **29**, 249–259 (1999)
12. M. Meng, L. Stievano, J.-F. Lambert, *Langmuir* **20**, 914–923 (2004)
13. U. Shanker, B. Bhushan, G. Bhattacharjee, *Origins Life Evol. Biospheres* **42**, 31–45 (2012)
14. Y. Furukawa, T. Otake, T. Ishiguro, H. Nakazawa, T. Kakegawa, *Orig. Life Evol. Biosph.* **42**, 519–531 (2012)
15. T. Munegumi, N. Tanikawa, *Orig. Life Evol. Biosph.* (2017). <https://doi.org/10.1007/s11084-017-9547-0>
16. G. Martra, C. Deiana, Y. Sakhno, I. Barberis, M. Fabbiani, M. Pazzi, M. Vincenti, *Angew. Chem. Int. Ed.* **53**, 4671–4674 (2014)
17. D. Gross, G. Grodsky, *J. Am. Chem. Soc.* **77**, 1678–1680 (1955)
18. O.D. Ekici, M. Paetzel, R.E. Dalbey, *Prot. Sci.* **17**, 2023–2037 (2008)
19. G.M. Simon, B.F. Cravatt, *J. Biol. Chem.* **285**, 11051–11055 (2010)
20. K.L. Duncan, R.V. Uljijn, *Biocatalysis* **1**, 67 (2015)
21. S. Hatfield, Y. Li, Y. Zhao, R. Wan, M. McMills, J. Li, X. Chen, *FASEB J.* **14**, A1323 (2000)
22. Y.S. Li, Y.F. Zhao, S. Hatfield, R. Wan, Q. Zhu, X.H. Li, M. McMills, Y. Ma, J. Li, K.L. Brown, C. He, F. Liu, X.Z. Chen, *Bioorg. Med. Chem.* **8**, 2675–2680 (2000)
23. J. Chen, R. Wan, H. Liu, C.M. Cheng, Y.F. Zhao, *Lett. Pept. Sci.* **7**, 325–329 (2000)
24. H.L. Du, Y.T. Wang, L.F. Yang, W.X. Luo, N.S. Xia, Y.F. Zhao, *Lett. Pept. Sci.* **9**, 5–10 (2002)
25. Y. Ma, X. Chen, M. Sun, R. Wan, C. Zhu, Y. Li, Y. Zhao, *Amino Acids* **35**, 251–256 (2008)
26. M. Sun, Y. Ma, S.H. Ji, H.N. Liu, Y.F. Zhao, *Bioorg. Med. Chem. Lett.* **14**, 3711–3714 (2004)
27. P.Y. Chen, Y. Liu, X. Gao, N.S. Xu, J. Niu, S.Y. Liu, Y.F. Zhao, *Phosphorus Sulfur Silicon Relat. Elem.* **186**, 933–935 (2011)
28. M.J. MacDonald, L.D. Lavis, D. Hilvert, S.H. Gellman, *Org. Lett.* **18**, 3518–3521 (2016)
29. C. Deiana, E. Fois, S. Coluccia, G. Martra, *J. Phys. Chem. C* **114**, 21531–21538 (2010)

30. P.I. Haris, D. Chapman, *Biopolymers* **37**, 251–263 (1995)
31. K. Hasegawa, T.-A. Ono, T. Noguchi, *J. Phys. Chem. B* **104**, 4253–4265 (2000)
32. N.B. Colthup, L.H. Daly, S.E. Wiberley, *Introduction to Infrared and Raman Spectroscopy*, 3rd edn. (Academic Press, San Diego, 1990), pp. 215–233
33. L.J. Bellamy, S. Krimm, *Journal of Polymer Science: Polymer Letters Edition* (Wiley, New York, 1975)
34. A. Rimola, Y. Sakhno, L. Bertinetti, M. Lelli, G. Martra, P. Ugliengo, *J. Phys. Chem. Lett.* **2**, 1390–1394 (2011)
35. P. Yang, R. Xu, S.C. Nanita, R.G. Cooks, *J. Am. Chem. Soc.* **128**, 17074–17086 (2006)